ACOUSTO-OPTIC FILTER DEVICE USING PROTON-EXCHANGED WAVEGUIDES

A thesis submitted to the Faculty of Engineering

of the University of Glasgow

for the degree of

Doctor of Philosophy

by

Joseph Francis Duffy, B.Sc.

December 1986

ProQuest LLC.
789 East Eisenhower Parkway
P.O. Box 1346
Ann Arbor, MI 48106 – 1346

TO MY MOTHER

ACKNOWLEDGMENTS

I would like to thank Professor J. Lamb for provision of the excellent research facilities in the Department of Electronics and Electrical Engineering.

I am indebted to Professor R. M. De La Rue for his close supervision of my work and for his advice and many useful suggestions as I prepared this thesis.

I am indebted to Dr. S. Al-Shukri for her collaboration and support during this project and I wish her every success in her new job.

I would like to thank Hughes Microelectronics Ltd. and the S.E.R.C. for the provision of the C.A.S.E. award. In particular, I would like to thank Mr. J. West at Hughes for the help and encouragement. I would also like to thank the members of staff of this department who have helped me in the past three years especially, Dr. J. Wilkinson, Dr. J. Arnold and Prof. P.J.R. Laybourn.

Mr. R. Hutchins provided much encouragement, especially in my first year, and I would like to thank him for all his efforts.

The technical advice and assistance available in this department is of a very high standard and I would like to thank Mr G. Boyle, Mrs. L Hobbs, Mr. J. Young, Mr. R. Harkins, Mr. K. Piechowaik, Mr. J. Clark and Mr. K. Melvin for their very valuable help. In addition, the help of Mr. H. Anderson and all the workers of the mechanical workshop is greatly appreciated.

The collaboration with Dr. G.A.D. Briggs and his co-workers at the University of Oxford was both fruitful and enjoyable and I would like to thank them for their efforts and for the help they gave me.

I would also like to thank Dr. H. Davie, Dr. M. Macauley and Dr. D. Muir for allowing me access to their laboratory to use the

word processing facilities in the preparation of this work.

I have had many interesting discussions with my colleagues in this department and I would like to thank each and every one of them (especially Mr. M.A. Grant and Dr. M.A. McBean) for three enjoyable years.

I would like to thank Mrs. J. Wink for typing this thesis.

Finally I would like to thank my family who have given me so much encouragement during the past three years and without whom this thesis would not have been possible. I would especially like to thank Gillian for her efforts to keep me sane.

SUMMARY

This thesis describes an investigation of the acoustic and optical properties of waveguides fabricated by proton-exchange from dilute melts.

Initially a narrow-band acousto-optic filter, based on the Integrated Optical Spectrum Analyser, is investigated. The device is proposed to detect and separate two acoustic frequencies and it was envisaged that the angular separation of the acoustically diffracted optical beams could be performed within a channel waveguide structure. However, analysis has indicated the impracticality of the device when operational requirements are considered.

The dilute melt proton-exchange process for waveguide fabrication on $LiNbO_3$ substrates is characterised. The waveguides have step-index profiles and are stable immediately after exchange. The waveguide depth increases as a $t^{1/2}$ function of exchange time, so a temperature dependent diffusion coefficient can be assigned and this coefficient fits an Arrhenius law. In comparison with pure melt proton-exchange waveguides, dilute melt waveguides exhibit less in-plane scattering and Rutherford Back-Scattering Spectrometry (RBS) measurements indicate a significantly lower level of latice disorder. Close agreement is found between optical measurements of waveguide depth (assuming a step-index profile) and RBS data for a range of melt dilutions, thus supporting the step-index model as an appropriate profile for the refractive index. Multi-mode waveguides are fabricated on Y-cut $LiNbO_3$ substrates without surface damage, though short post annealing is necessary to relieve induced strain.

Planar optical waveguides are fabricated on X-cut and Z-cut $LiTaO_3$ substrates from dilute melts without the need for prolonged post annealing. High quality waveguides with low in-plane scattering levels are produced. The refractive index change is similar to that achieved with titanium indiffused $LiNbO_3$ and RBS measurements indicate a region of lattice disorder similar to that observed with $LiNbO_3$.

A line-focus-beam Scanning Acoustic Microscope is used to investigate the acoustical properties of dilute melt proton-exchanged $LiNbO_3$ waveguides. Substantial changes (as much as 5%) in the surface acoustic wave (SAW) propagation velocity due to proton-exchange are observed on all three major-axis crystal cuts, with both increases and decreases in velocity occurring, depending on propagation direction. Changes in acoustic attenuation are also observed. A simple model is used to calculate the 'true' velocity change for a proton-exchange region without the infulence of a virgin $LiNbO_3$ base and the acoustic anisotropy exhibited by the X- and Y-cut $LiNbO_3$ appears greater than that of virgin $LiNbO_3$.

A theoretical analysis based on the quasi-static approximation is used to determine the overlap integral between the acoustic and optical waves in proton-exchange waveguides. The overlap integral falls with variations in index profile from step-index to graded-index and the domination of the acousto-optic interaction by the electro-optic effect is emphasized. The analysis indicates that shallow (~3μm) step-index waveguides are required for maximum interaction efficiency and that prolonged annealing results in reduced interaction efficiencies.

Acousto-optic devices are fabricated on dilute melt proton-exchanged $LiNbO_3$ and $LiTaO_3$ waveguides using simple, non-optimal, electrode structures. For 7.5 minutes exchange in 0.5% dilute melt on X-cut $LiNbO_3$ at $220^{\circ}C$, 87% diffraction efficiency is measured for an input power of 640mW. Similarly, for an untuned X-cut $LiTaO_3$ device, fabricated in 0.5% dilute melt for 4 hours at $230^{\circ}C$, 22% diffraction efficiency is demonstrated. The thermo-optic behaviour on both $LiNbO_3$ and $LiTaO_3$ is observed indicating that there is no apparent difference between proton-exchanged waveguides and those produced by titanium indiffusion.

The findings of this thesis will be useful in the development of high index, low loss acousto-optic and integrated-optic waveguide devices, which have numerous applications in optical signal processing systems.

TABLE OF CONTENTS

ACKNOWLEDGMENTS.....i

SUMMARY.....iii

CONTENTS.....v

1. Introduction.....1

1.1. General Introduction.....1
1.2. The Integrated Optical Spectrum Analyser.....2
1.3. Simplified Acousto-optic Filter Device.....3
1.4. Choice of Waveguide Substrate.....5
1.5. Choice of Fabrication Process.....6
1.6. Proton-exchange in Pure Melts.....7
1.7. Proton-exchange in Dilute Melts.....8
References to Chapter 1.....10

2. Acousto-optic Filtering Using Channel Waveguides.....15

2.1. Introduction.....15
2.2. Fundamentals of Acousto-optic Interaction.....15
2.3. Acousto-optic Interaction in Channel Waveguides.....20
2.4. Waveguide Horns in Integrated Optical Devices.....21
2.5. Analysis of Mode Conversion in Channel Waveguides using an Acoustic Grating.....23
2.6. Investigations of Mode Filtering using the Beam Propagation Method.....27
2.7. Fabrication of channel waveguide tapers.....29
2.7.1. Introduction.....29
2.7.2. Diffusion mask fabrication.....29
2.7.3. Substrate cleaning.....30
2.7.4. Aluminium deposition.....30
2.7.5. Delineation of resist pattern and 'aluminium etch'.....30
2.8. Design and fabrication of waveguide tapers.....32

2.8.1. Design of shadow mask.....32
2.8.2. Waveguide fabrication.....32
2.9. Analysis of Taper Behaviour.....33
2.10. Discussion.....34
References to Chapter 2.....35

3. Characterisation of Dilute Melt Proton-exchange Waveguides.39

3.1. Introduction.....39
3.2. Waveguide Fabrication Procedure.....40
3.3. Optical Characterisation.....42
3.3.1. Introduction.....42
3.3.2. Lithium Niobate Waveguides.....43
3.3.3. Lithium Tantalate Waveguides.....47
3.4. Material Analysis.....50
3.5. In-plane Scattering Measurements.....53
3.6. Dilute Melt Proton-exchanged Waveguides on Y-cut $LiNbO_3$.....55
3.7. Discussion.....59
References to Chapter 3.....61

4. Analysis of Proton-exchanged Waveguides Using the Scanning Acoustic Microscope.....66

4.1. Introduction.....66
4.2. Acousto-optic Proton-exchange.....66
4.3. Material Characterization by Line-Focus-Beam Acoustic Microscope.....67
4.3.1. Line-Focus-Beam Acoustic Microscope.....67
4.3.2. Principle of Material Characterisation.....69
4.4. Waveguide Fabrication Conditions.....72
4.5. Line-Focus-Acoustic Measurements on $LiNbO_3$: Results and Analysis.....74
4.6. Discussion.....76
References to Chapter 4.....78

5. Analysis of the Acousto-optic Overlap in Proton-exchange Waveguides....82

5.1. Introduction....82
5.2. Elastic Waves in Solids....83
5.3. Propagation of Elastic Waves....84
5.3.1. Basic Elastic Equations....84
5.3.2. Surface Waves Solutions....86
5.4. Effect of Elastic Waves on the Refractive Index of a Medium....87
5.4.1. Photoelastic Effect....88
5.4.2. The Electro-optic Effect....89
5.5. Interaction of a Surface Acoustic Wave and a Guided Optical Wave....90
5.6. Implementation of Overlap Analysis....93
5.6.1. Introduction....93
5.6.2. Derivation of Elastic and Electric Field Equations....93
5.6.3. Determination of the Optical Field Profile....95
5.7. Results and Analysis....97
5.7.1. Overlap Integral for Waveguides with Graded-index Profiles....97
5.7.2. Overlap Integral for Waveguides with Step-index Profiles....99
5.8. Conclusions....101
Appendix 5.1 Equations for displacement and electrical waves in YZ-$LiNbO_3$....102
Appendix 5.2 Piezoelectric Stress and Strain Relationships for Trigonal Class-3m Crystals....104
Appendix 5.3 Application of Boundary Conditions at a Stress Free Surface....107
References to Chapter 5....108

6. Acousto-optic Surface Acoustic Wave Devices: Design and Operation....112

6.1. Introduction....112

6.2. Acousto-optic Interaction using Surface Acoustic Waves....112
6.3. Design of the Interdigital Transducer....113
6.4. Fabrication of Interdigital Transducer....116
6.5. Characterisation of an IDT....117
6.6. Optical Bench Arrangement....117
6.7. Acousto-optic Measurements....118
6.7.1. Lithium Niobate....120
6.7.2. Lithium Tantalate....124
6.8. Thermo-optic Behaviour....125
6.8.1. Experimental Arrangement....126
6.8.2. Lithium Niobate....126
6.8.3. Lithium Tantalate....128
6.9. Discussion....129
Appendix 6.1 Exact Determination of Design Parameters for IDT on XZ and YZ $LiNbO_3$ and $LiTaO_3$....130
References to Chapter 6....131

7. Conclusions....136

References to Chapter 7....142

CHAPTER 1. Introduction

1.1. General Introduction

Acousto-optic signal processing is based on the interaction of optical waves with electrically induced acoustic waves and the resultant optical diffraction is directly related to the frequency of the acoustic wave. Many signal processing applications such as convolution, correlation and spectrum analysis have been demonstrated[1,2]. Initially, acousto-optic devices were designed using bulk wave interaction. However, the non-confinement of the optical and acoustic waves necessitated large drive powers to achieve efficient acousto-optic interaction. With the advent of guided optical waves and the associated integrated optics[3,4] technology low power acousto-optic devices using surface acoustic waves (SAW) were designed.[5] This technology has allowed the design of very small devices, incorporating complicated electrode structures and optical waveguides, specifically designed to match external sources and detectors.

Integrated optical devices are particularly attractive for optical filtering applications and wide band spectrum analysers have been developed [6] which utilize waveguide lenses to separate and focus the diffracted beams. This thesis describes an investigation of the development of a narrow band optical filter, based on the integrated optical spectrum analyser, which is required to detect and separate two acoustic frequencies, i.e. the device is to perform frequency shift key (FSK) demodulation. It was envisaged that angular separation of the acoustically diffracted optical beams could be performed within a channel waveguide structure and that waveguide lenses would no longer be required.

Due to its strong piezoelectric properties, low acoustic losses and its suitability for waveguide fabrication, Lithium Niobate ($LiNbO_3$) was chosen as the substrate material for the acousto-optic device. Optical waveguides[7] have been fabricated and a detailed investigation of the suitability of such waveguides for acousto-optic devices has been performed. Emphasis has been

placed upon the differences between pure melt[8] and dilute melt proton-exchange waveguides and, in particular, the acousto-optic diffraction efficiency is shown to be improved by using dilute melts.

1.2. The Integrated Optical Spectrum Analyser

Integrated optics is concerned with light guided in surface waveguides on solid substrates, and with optical devices to control and process light signals propagating in these guides. A typical single-mode planar waveguide has a depth of 0.6μm, while both channel waveguides and electrode structures can be defined using standard photolithographic techniques. One such device, the Integrated Optical Spectrum Analyser (IOSA)[6], utilises acousto-optic Bragg diffraction to perform frequency filtering operations. The signal to be analysed is converted, using a piezoelectric transducer, into a surface acoustic wave which propagates across the optical waveguide and locally perturbs the refractive index. The sinusoidally varying refractive index change creates a moving phase or diffraction grating. Light, propagating in the waveguide, is diffracted by the grating, in the plane of the waveguide, at an angle proportional to frequency of the acoustic wave. The diffracted beams are focussed, typically by a waveguide lens, onto a range of photodetectors and the resultant signal from the photodetectors can be directly related to the frequency components of the electrical signal. For wide-band operation with many frequency channels, complicated beam-steering transducers[9] and photodetector arrays are necessary. To obtain high-resolution performance from an IOSA, collimation and focussing of the guided optical wave are required. In addition, for diffraction limited operation, aberration-free waveguides and waveguide lenses are necessary.

Low loss optical waveguides can be fabricated on single crystal Lithium Niobate ($LiNbO_3$) by the titanium indiffusion method and this, along with its strong acoustic and piezoelectric properties has made this material the best choice for IOSA fabrication. Two of the waveguide lenses which have been used to focus guided light in planar waveguides are the thin-film

waveguide lens[10] and the waveguide geodesic lens[11]. Thin-film waveguide lenses defined by increasing the effective index of the guide have been fabricated on titanium indiffused $LiNbO_3$ waveguides. However, the relatively small index change possible with these waveguides (+0.03) has meant that short focal length lenses have been very difficult to fabricate[6]. (With the advent of the high index proton-exchanged $LiNbO_3$ waveguides[8], however, short focal length thin-film waveguide lenses are now being designed[12,13,14].) Waveguide geodesic lenses are waveguide-covered depressions where the focussing effect is determined by the curvature of the depressions. IOSA which were designed, contained geodesic lenses which performed the collimation and focussing of the beam. However, to reach the initial operating targets (i.e., 100 resolvable frequency components in a bandwidth of 400MHz), geodesic lenses with 10mm diameter and focal lengths of 18.5mm are required[15]. Fabrication of such high quality lenses requires extensive manufacturing facilities and extremely accurate polishing techniques. The expense incurred in producing these lenses has been a major drawback in the development of the IOSA and it was hoped that a simple integrated optical device could be designed which would perform the acousto-optic filtering function without the use of expensive waveguide lenses.

1.3. Simplified Acousto-optic Filter Device

The design of the F.S.K. demodulator proposed for this work was based generally on the IOSA but with a few important simplifications. It was proposed that the device would only have narrow band operation, removing the need for complicated wide-band acoustic transducers, and the binary behaviour of the system would remove the need for large detector arrays. In addition, the principle aim of the device was to separate two diffracted beams, which were very close together, without the use of expensive geodesic lenses.

In 1976, Millar et al.[16] demonstrated, in sandwich ribbon fibres, that it was possible to excite, individually, all the transverse modes of a waveguide, from the lowest upwards, by varying the input coupling angle in the plane of the waveguide.

In the experiment, the optical wave was launched into the waveguide initially with wavefronts perpendicular to the guide axis exciting the zero-order fundamental mode. As the angle of the wavefronts was changed, relative to the guide axis, each transverse mode was individually excited. It was proposed to apply this same principle of mode selection to the present application where the phase variation would result from the angular deflection of the acoustic grating.

Consider a channel waveguide with a waveguide branch of equal width aligned at an angle equal to twice the Bragg angle of the acoustic grating (see Figure 1.1(a)). Without the application of the acoustic grating, optical power propagates down the main waveguide with minimal coupling into the waveguide branch. On application of an acoustic grating, aligned at the Bragg angle relative to the waveguide axis (see Figure 1.1(b)), optical power propagating as a single transverse mode of the main waveguide will be deflected into the branch. For operation of the grating exactly at the Bragg frequency, it is assumed that the single transverse mode of the main waveguide will excite the single transverse mode of the branch. (This simple analysis neglects any fringing effects.) If the acoustic frequency is altered, then the fundamental mode, deflected from the main waveguide, will enter the branch with its wavefronts tilted with respect to the guide axis and multiple transverse modes will be excited. If the wavefronts are tilted far enough (i.e. $\Delta\alpha \sim \lambda_0/d$ where d is the waveguide width), then it will be possible to predominately excite the adjacent transverse mode. Thus, ideally a channel waveguide device could be designed whose output was either a single or a 1st order transverse mode and this output could be directly related to one of two acoustic frequencies.

For two acoustic signals separated by a small frequency difference, the resultant separation between two deflected beams would be very small and the modal mismatch at the branch input would be negligible. To obtain the maximum possible angular separation between two such beams over a small area, the acousto-optic interaction width needs to be maximised. In acousto-optic channel waveguide devices, the acousto-optic interaction width is

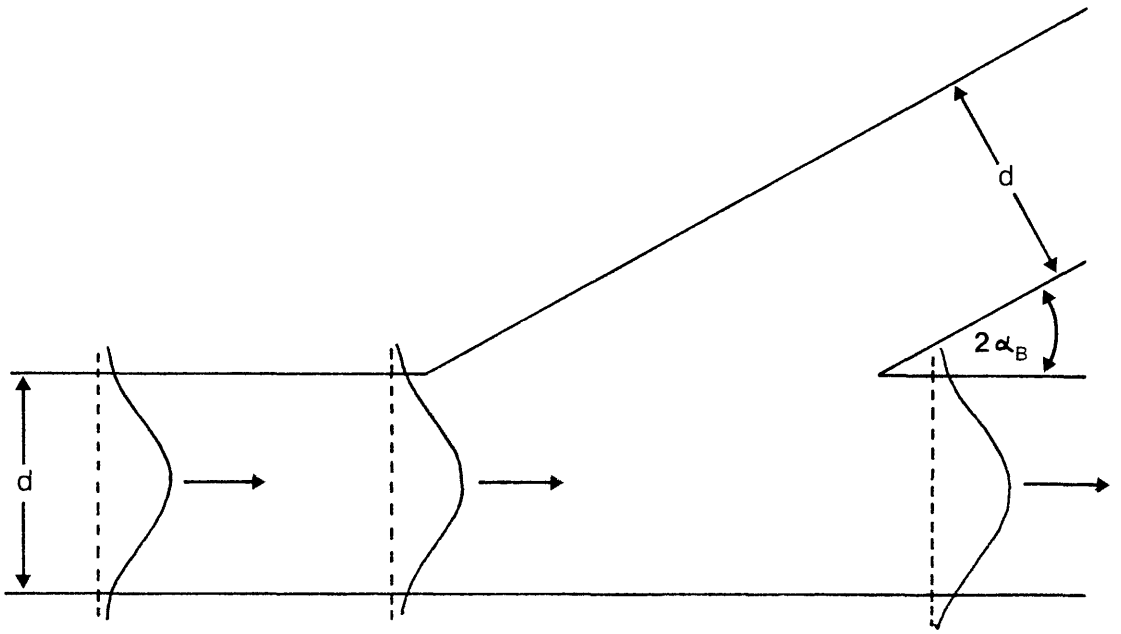

Figure 1.1 (a) Branch waveguide structure: In the absence of a coupling grating, optical power is assumed to propagate in the main waveguide only.

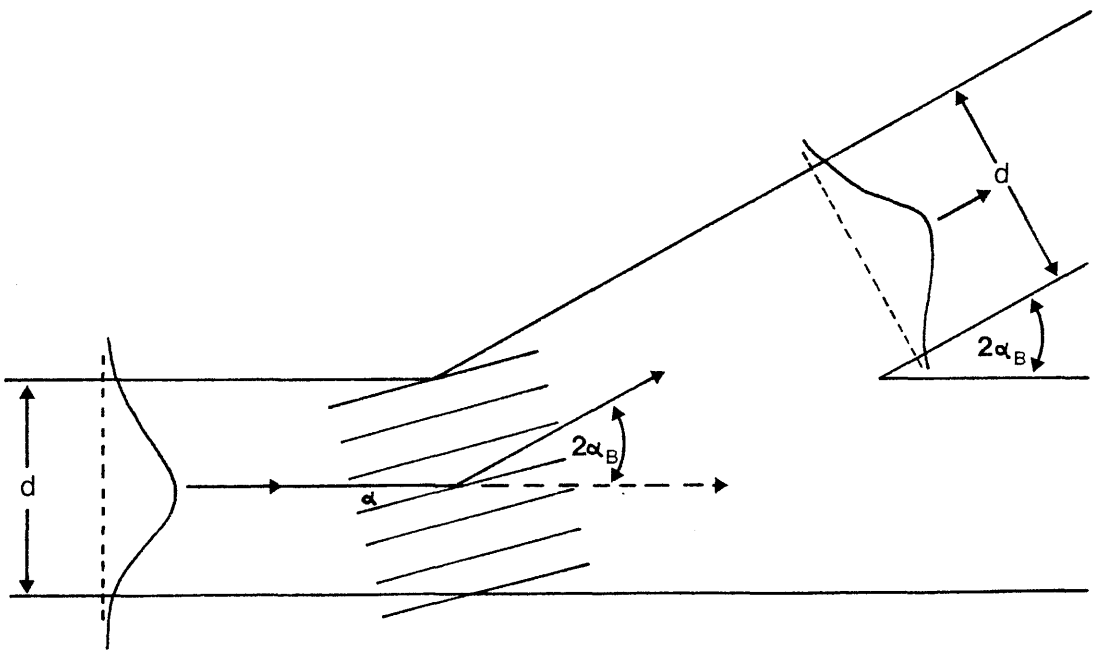

Figure 1.1 (b) Branch waveguide structure: For operation of the acoustic grating at the Bragg angle optical power is deflected into the branch.

limited by the width of the waveguide. However, increases in the channel width would make single transverse mode propagation very difficult since the guided wave would be very sensitive to slight imperfections in the waveguide and multiple modes could easily be excited.

Previously[17], single mode propagation in highly multimoded channel waveguides has been achieved by using adiabatic waveguide tapers which transfer optical power from single-mode to multimode waveguides with minimal power loss to higher order modes. Such a structure would be required at the input to the device, if single-mode propagation were to be achieved at the acousto-optic interaction region. In addition, if the waveguides were highly multimoded, many unwanted modes would be excited in the interaction region and would propagate in the waveguide branch. Therefore, it was proposed to place a waveguide taper, changing from a wide multimode region to a narrow region, at the output of the branch waveguide so that unwanted higher order modes would be radiated from the taper as successive cut-off widths were reached. The deflected light beams, preferably of low order, would enter the wide section of the taper and as they propagate down its length, the small angle between the beams would be increased in inverse proportion to the guide narrowing. The output section of the waveguide taper would support two modes and separation and detection of these two modes could be performed using prism coupling[18].

It was proposed that such a device would provide frequency filtering for a channel separation of 800KHz. This thesis investigates the practicalities of such a device. In particular, the use of waveguide tapers as mode strippers is investigated and the principle of mode excitation using an acoustic wave is observed.

1.4. Choice of Waveguide Substrate

For many years, $LiNbO_3$ has been looked upon as the ideal material for acousto-optic devices both for its low acoustic attenuation and the ease with which low loss optical waveguides

can be fabricated. In addition, along certain crystal axes, $LiNbO_3$ has a very large electro-mechanical coupling coefficient and many acousto-optic devices have utilized these properties[5,6,9]. Y-cut $LiNbO_3$, with Z-propagating acoustic waves has been the most favoured crystal orientation for acousto-optic devices, utilizing the maximum electro-mechanical coupling coefficient for efficient generation of acoustic waves, though X-cut material with its slightly reduced coupling coefficient [19] has also been used.

Lithium Tantalate ($LiTaO_3$) is another material with favourable electro-optic and acoustic properties[19] but fabrication of waveguide devices on $LiTaO_3$ has been limited due to the difficulties involved in fabricating optical waveguides. Previously waveguide fabrication has been performed using thermal outdiffusion[20], copper indiffusion[21,22], and titanium indiffusion[23] but temperatures involved in these methods were in excess of the Curie temperature of the crystal. This resulted in a disruption of the aligned ferro-electric fields and on each occasion the crystal required to be repoled. Recently with the advent of proton-exchange, it has been possible to fabricate low-loss optical waveguides on $LiTaO_3$ at temperatures well below the Curie temperature.

In this work, a comparison is made between waveguides fabricated on Y- and X-cut $LiNbO_3$ and $LiTaO_3$ in terms of waveguide quality and suitability for acousto-optic interaction. Active acousto-optic devices are fabricated on both $LiNbO_3$ and $LiTaO_3$, with conditions being optimised for maximum diffraction efficiency.

1.5. Choice of Fabrication Process

The most firmly established method for fabricating waveguides in $LiNbO_3$ substrates is the indiffusion of titanium ions and most integrated optical waveguide devices, including integrated optical acoustic devices, have been fabricated using this technique. However, titanium indiffused waveguides do have some limitations. Such waveguides are very susceptible to the photorefractive effect

at short wavelengths and, more importantly, the relatively low index change (+0.03) restricts the device design possibilities to some extent, due to the resultant weak confinement of the optical mode.

Waveguide fabrication on $LiNbO_3$ by proton-exchange[8] has been shown to produce step-index waveguides with index changes as high as +0.12 for the extraordinary index at $\lambda_o = 0.6328\mu m$. This large index change results in strong confinement of the optical wave and means that complicated waveguide devices such as the optical ring resonator[24] can be fabricated on $LiNbO_3$. More importantly, the large index change available means that short focal length planar waveguide lenses can now be designed[12,13,14]. In addition the proton-exchange process allows the fabrication of waveguides on $LiTaO_3$ [25,26], which was not possible using titanium indiffusion. The index change, in this case, is comparable with $Ti:LiNbO_3$.

Proton-exchange has been chosen as the main waveguide fabrication process for the work of this thesis and an investigation is carried out into the acousto-optic properties of proton exchanged waveguides.

1.6. Proton-exchange in Pure Melts

When $LiNbO_3$ is placed in a melt of benzoic acid, optical waveguides are formed by the process of proton-exchange where lithium ions are lost from the surface of the crystal and are substituted by protons[8]. The waveguides immediately produced have a step-like refractive index profile but are of poor optical quality, suffering from severe in-plane scattering and index instabilities. Furthermore Y-cut $LiNbO_3$ suffers considerable surface damage after only a few minutes immersion[27,28]. This places severe limitations on the waveguides in terms of acousto-optic performance since Y-cut waveguides are often preferred for such devices and improved in-plane scattering is very important to their dynamic range. A reduced electro-optic activity has also been reported which could severely effect the diffraction efficiency of a proton-exchanged acousto-optic device[29,30].

To overcome the problems of in-plane scattering and index instabilities the waveguides were annealed at temperatures higher than the exchange temperatures[31,32]. This resulted in an overall reordering of the structure of the guiding layer and reduced in-plane scattering. Prolonged annealing, however, forces the hydrogen atoms deeper and deeper into the substrate and results in a graded index profile and a multimoded waveguide. Dawar et al.[33] demonstrated 72% acousto-optic diffraction efficiency in a Y-cut $LiNbO_3$ waveguide fabricated in a pure melt for 3 minutes at 210°C and annealed for 15 minutes at 400°C in wet flowing O_2. To improve the poor in-plane scattering performance, the waveguide was annealed further. However, it was noticed that the acousto-optic diffraction efficiency fell with increased annealing. This reduction has been attributed to a change in the index profile from a step to a graded profile resulting in a reduction in the acousto-optic overlap efficiency.

These problems associated with pure melt proton-exchange waveguides have tended to limit their use for acousto-optic devices and an improved fabrication technique has been sought.

1.7. Proton-exchange in Dilute Melts

When a small percentage of lithium benzoate is added to the pure benzoic acid melt, the rate at which lithium atoms leave the host substrate is considerably reduced and the protons diffuse in more evenly, forming stronger, more stable, bonds[34,35,36]. Figure 1.2 shows a comparison between Rutherford Back-Scattering Spectrometry (RBS)* data[37] obtained on an X-cut $LiNbO_3$ waveguide exchanged in a pure melt and one exchanged in a 0.5% dilute melt. The position of the step-change indicates the exchange depth and it can be seen that the 0.5% dilution has reduced the speed of exchange by a factor of 5, resulting in a stable waveguide with a step-index profile[26].

The reduction in process speed is of immediate value where single mode waveguides are desired as it permits more accurate control of the waveguide properties. Another advantage of using

* See section 3.4.

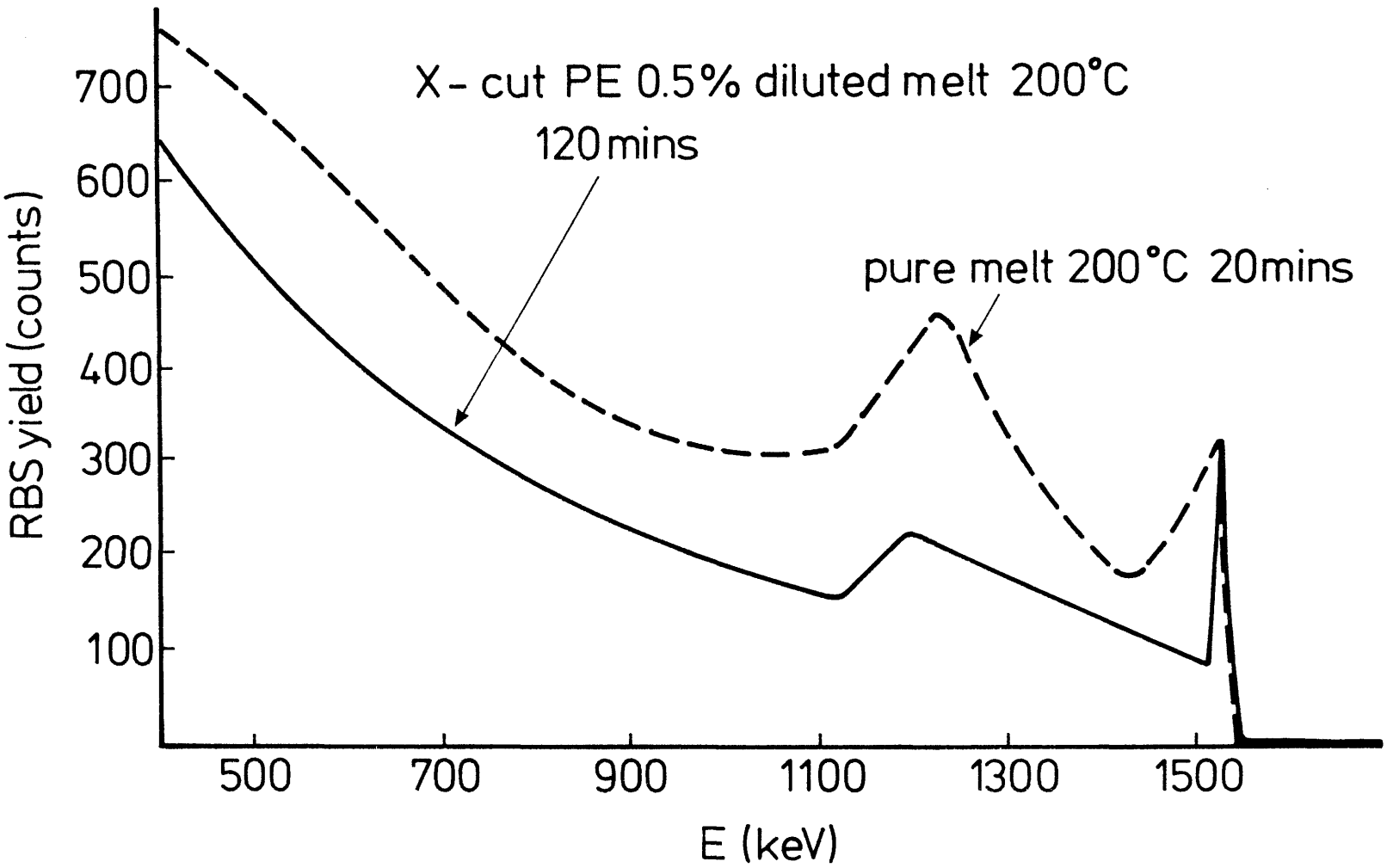

Figure 1.2 RBS data for proton – exchange on X – cut $LiNbO_3$

dilute melts is that, unlike pure-melt proton-exchange, long fabrication times can be used to produce single and multimode waveguides on Y-cut $LiNbO_3$[7]. Figure 1.3 also compares the level of structural disorder, given in terms of RBS yield, of waveguides fabricated in pure and dilute melts to similar depths. It can be seen that the dilute-melt waveguides have substantially reduced structural disorder and this in turn leads to them having far better in-plane scattering performance.

The potential advantages of the dilute melt process for acousto-optical devices, in terms of step-index profile and index stability, are immediate. Prolonged post exchange annealing to improve stability and in-plane scattering performance is no longer required, though a very short post-annealing process has been found to be very beneficial and reports of the preservation of electro-optic activity[38] lead to the belief that performance superior to pure-melt devices can be achieved.

Dilute melt proton-exchange has been chosen for waveguide fabrication in this thesis. A characterisation of the fabrication process has been made and acousto-optic devices have been fabricated on both $LiNbO_3$ and $LiTaO_3$. Comparisons between the properties of pure melt and dilute melt proton-exchange waveguides have been made and it is shown that much improved waveguide quality and device performance is achieved by using dilute melts.

References to Chapter 1.

1. D. Casasent, 'Coherent optical pattern recognition', Proc. IEEE, Vol. 67, No. 5, pp.813-825, 1979.

2. W.T. Rhodes, 'AO signal processing: convolution and correlation', Proc. IEEE, Vol. 89, No. 1, pp.65-79, 1981.

3. P.K. Tien, 'Integrated optics and new wave phenomena in optical waveguides', Reviews of Mod. Phys., Vol. 49, No. 2, pp.361-420, 1977.

4. P.J.R. Laybourn and J. Lamb, 'Integrated Optics - a tutorial review', The Radio and Electronic Eng., Vol. 51, No. 7/8, pp.397-413, 1981.

5. R.V. Schmidt, 'Acousto-optic interactions between guided optical waves and surface acoustic waves', IEEE Trans. Sonics and Ultrasonics, Vol. SU-23, No. 1, pp.22-33, 1976.

6. M.K. Barnoski, B. Chen, T.R. Joseph, J.Y. Lee and O.G. Raimer, 'Integrated-optic Spectrum Analyser', IEEE Trans. Circuits and Systems, Vol. CAS-26, No. 12, pp.1113-1124, 1979.

7. S.M. Al-Shukri, J.F. Duffy, R.M. De La Rue, M.N. Armenise, C. Canali and A. Carnera, 'Proton-exchange optical waveguides on lithium niobate: devices, characterisation and future prospects', Proc. Soc. Photo-opt. Inst. Eng., Vol. 578, pp.2-6, 1985.

8. J.L. Jackel, C.R. Rice and J.J. Veselka, 'Proton-exchange for high-index waveguides in $LiNbO_3$' Appl. Phys. Letts., Vol. 41, No. 7, pp.607-608.

9. C.S. Tsai, 'Guided-wave A.O. Bragg modulators for wide-band integrated optical communications and signal processing', IEEE Trans. on Circuits and Systems, Vol. CAS-26, No. 12, pp.1072-1098, 1979.

10. W.H. Southwell, 'Index profiles for generalized Lunenberg lenses and their uses in planar optical waveguides', J. Opt. Soc. Amer., Vol. 67, pp.1010-1014, 1977.

11. B. Chen and O.G. Ramer, 'Diffraction limited geodesic lenses for integrated optical circuits', IEEE J. Quant. Elect., Vol. QE-15, pp.853-860, 1979.

12. D.Y. Zang and C.S. Tsai, 'Single-mode waveguide microlenses and microlens arrays fabrication in $LiNbO_3$ using titanium indiffused proton-exchange technique', Appl. Phys. Letts. Vol. 46, No. 8, pp.703-705, 1985.

13. D.Y. Zang and C.S. Tsai, 'Titanium-indiffused proton-exchanged waveguide lenses in $LiNbO_3$ for optical information processing', Appl. Opts., Vol. 25, No. 14, pp.2264-2271, 1986.

14. P.J.R. Laybourn and G.C. Righini, 'New design of thin-film lens', Elect. Letts., Vol. 22, No. 6, pp.343-344, 1986.

15. G.F. Doughty, R.B. Wilson, J. Singh, R.M. De La Rue and S. Wright', Aspheric geodesic lenses in an integrated optics spectrum analyser', Proc. Soc. Photo-opt. Instm. Eng., Vol. 235, pp.35-41, 1980.

16. C.A. Millar, R.H. Hutchins and P.J.R. Laybourn, 'Modes of a 3-dimensional sandwich-ribbon optical waveguide', Microwaves, Optics and Acoustics, Vol. 1, No. 1, pp.27-33, 1976.

17. A.F. Milton and W.K. Burns, 'Mode coupling in optical waveguide horns', IEEE J. Quant. Elect., Vol. QE-13, No. 10, pp.825-835, 1977.

18. P.K. Tien and R. Ulrich, 'Theory of prism-film coupler and thin-film light guides', J. Opt. Soc. Amer., Vol. 60, No. 10, pp.1325-1337, 1970.

19. A.J. Slobodnik, Jr., 'Surface acoustic waves and SAW

materials', Proc. IEEE, Vol. 64, No. 5, pp.581-595, 1976.

20. I.P. Kaminow and J.R. Carruthers, 'Optical waveguiding layers in $LiNbO_3$ and $LiTaO_3$', Appl. Phys. Letts., Vol. 22, No. 7, pp.326-328, 1973.

21. J. Noda, T. Saku and N. Uchida, 'Fabrication of optical waveguiding layer in $LiTaO_3$ by Cu diffusion', Appl. Phys. Letts., Vol. 25, No. 5, pp.308-310, 1974.

22. Y. Okamura, S. Yamamoto and T. Makimoto, 'Electro-optic guided-to-radiation mode conversion in Cu-diffused $LiTaO_3$ waveguide with periodic electrodes', Appl. Phys. Lett., Vol. 32, No. 3, pp.161-163, 1978.

23. G.L. Tangonan, M.K. Barnoski, J.F. Lotspeich and A. Lee, 'High optical power capabilities of Ti:diffused $LiTaO_3$ waveguide modulator structures', Appl. Phys. Letts., Vol. 30, No. 5, pp.238-239, 1977.

24. A. Mahapatra and W.C. Robinson, 'Integrated-optic ring resonators made by proton-exchange in lithium niobate', Appl. Opts., Vol. 24, No. 15, pp.2285-2286, 1986.

25. W.B. Spillman, Jr., N.A. Stanford and R.A. Soref, 'Optical waveguides in $LiTaO_3$ formed by proton-exchange', Opts. Letts., Vol. 8, No. 9, pp.497-499, 1983.

26. S.M. Al-Shukri, J.F. Duffy, R.M. De La Rue, G. Mazzi, A. Carnera and M.N. Armenise, 'Single mode planar and stripe waveguides by proton-exchange in lithium tantalate and lithium niobate', Proc. Soc. Photo-Opt. Inst. Eng., Vol. 651, pp. 20-25, 1986.

27. M. Goodwin and C. Stewart, 'Proton-exchanged optical waveguides in Y-cut $LiNbO_3$', Elect. Letts., Vol. 19, No. 6, pp.223-225, 1983.

28. A. Campari, C. Ferrari, G. Mazzi, C. Summonte, S.M. Al-

Shukri, A.L. Dawar, R.M. De La Rue and A.C.G. Nutt, 'Strain and surface damage induced by proton-exchange in Y-cut $LiNbO_3$', J. Appl. Phys., Vol. 58, No. 12, pp.4521-4524, 1985.

29. K.K. Wong, R.M. De La Rue and S. Wright, 'Electro-optic waveguide frequency translator in $LiNbO_3$ fabricated by proton-exchange', Opt. Letts., Vol. 7, No. 11, pp.456-458, 1982.

30. R.A. Becker, 'Comparison of guided wave interferometric modulators fabricated on $LiNbO_3$ via Ti:indiffusion and proton-exchange', Appl. Phys. Letts., Vol. 43, No. 2, pp.131-133, 1983.

31. S.M. Al-Shukri, A.L. Dawar, R.M. De La Rue, A.C.G. Nutt, M. Taylor, J.R. Tobin, G. Mazzi, A. Carnera and C. Summonte, 'Analysis of annealed proton-exchanged waveguides in $LiNbO_3$ by optical waveguide measurements and microanalytical techniques', Proc. 7th Topical Meeting on Integrated and Guided Optics, Orlando, Florida, U.S.A., PDP 71-4, April 1984.

32. C. Canali, A. Carnera, G. Della Mea, R.M. De La Rue, A.C.G. Nutt and J.R. Tobin, 'Proton-exchanged $LiNbO_3$ waveguides: materials analysis and optical characteristics', Proc. Soc. Photo-opt. Inst. Eng., Vol. 460, paper 7, 1984.

33. A.L. Dawar, S.M. Al-Shukri and R.M. De La Rue, 'Guided wave acoustooptic interaction in proton-exchanged Y-cut $LiNbO_3$', Appl. Phys. Letts., Vol. 48, No. 23, pp.1579-1581, 1986.

34. J.L. Jackel, C.E. Rice and J.J. Veselka, 'Composition control in proton-exchanged $LiNbO_3$', Elect. Letts., Vol. 19, No. 10, pp.387-388, 1983.

35. M. de Micheli, J. Botineau, S. Neveu, P. Sibillot, D.B. Ostrowsky and M. Papuchon, 'Independent control of index and profiles in proton-exhcnaged lithium niobate guides', Opt. Letts., Vol. 8, No. 2, pp.114-115, 1983.

36. J.L. Jackel and C.E. Rice, 'Short and long term stability in proton-exchanged $LiNbO_3$ waveguides', Proc. Soc. Photo-opt. Inst. Eng., Vol. 460, pp.43-48, 1984.

37. C. Canali, A. Carnera, G. Della Mea, P. Mazzoldi, S.M. Al-Shukri, A.C.G. Nutt and R.M. De La Rue, 'Structural characterisation of proton-exchanged $LiNbO_3$ optical waveguides', J. Appl. Phys., Vol. 59, No. 8, pp.2643-2649, 1986.

38. K.K. Wong, N.J. Parsons, A.R. Oldroyd and A.C. O'Donnell, 'High quality optical waveguides in $LiNbO_3$ by dilute melt proton-exchange', Proc. IOOC/ECOC '85, pp.59-62, Venice, 1985.

CHAPTER 2. Acousto-optic Filtering Using Channel Waveguides

2.1. Introduction

This chapter discusses some of the fundamentals of acousto-optic interaction and outlines the important considerations when the interaction is applied to optical filtering. In addition, previous applications of acousto-optic interaction in channel waveguide structures are discussed and simple theoretical calculations are performed to assess suitable waveguide widths and acoustic frequencies for the successful design of the optical filter. The design of optical waveguide tapers for adiabatic transfer of optical power between waveguides of varying widths is discussed and a computer analysis is performed to investigate the effects of phase variations at the wide input to the waveguide. Finally waveguide tapers have been fabricated on lithium niobate substrates using the method of dilute melt proton-exchange. A description of the fabrication procedure and the simple experiments which were performed on the waveguide tapers to investigate their behaviour and optical properties is presented.

2.2. Fundamentals of Acousto-optic Interaction

Acousto-optic devices which use Bragg interaction have applications as beam deflectors and modulators, and for mode-locking and Q-switching of lasers. In general, devices where the optical and acoustic waves interact in the bulk of a solid material are used, but integrated optical devices using the interaction between surface acoustic waves (SAW) and guided optical waves have also received attention. The acoustic waves originate from piezoelectric acoustic transducers and the interaction efficiency is determined, in part, by the properties of the acoustic material and the operation of the transducer.

An acoustic wave, excited by a single frequency electrical input applied to an acoustic transducer, forms a sinusoidal refractive index grating as it propagates through the crystal. Light incident upon the moving grating will, in general, be diffracted into a number of discrete beams in a manner similar to

that of a fixed grating. If, however, the acoustic wave is wide enough and the light beam is incident at the Bragg angle α_B, then the reflections from the acoustic grating add constructively in one direction and only a single diffracted beam is produced[1], see Figure 2.1. This diffracted light beam is frequency-shifted by the acoustic wave. The total angle between the diffracted beam and the incident beam is $2\alpha_B$ where α_B is given by

$$\sin\alpha_B = \frac{\lambda}{2\lambda_a} \qquad \ldots.2.1$$

where λ is the optical wavelength in the interaction medium and λ_a the acoustic wavelength. λ can be written as λ_o/n, where λ_o is the free space wavelength and n the refractive index of the medium. λ_a can be written as V/f, where V is the acoustic wave velocity in the medium and f the frequency of the externally applied r.f. signal. Thus for small angles, equation 2.1 can be re-expressed as

$$\alpha_B = \frac{\lambda f}{2V} \qquad \ldots.2.2$$

and, up to a frequency of ~1.5GHz, the diffraction angle is to a good approximation linearly proportional to the acoustic frequency. For acoustic propagation along the Z axis of a Y-cut $LiNbO_3$ crystal (i.e. 'YZ-$LiNbO_3$') with $\lambda_o = 0.6328\mu m$, $V=3494 ms^{-1}$, f=425MHz and n=2.23 then $\alpha_B = 0.989^o$.

Acousto-optic interaction takes place either in the Bragg regime where only one diffracted light beam is obtained, or in the Raman-Nath regime[2] where many diffraction orders result. A simple criterion to determine the region of operation is to assume that interaction is in the Bragg regime when the optical beam traverses at least one acoustic wavefront[3], that is

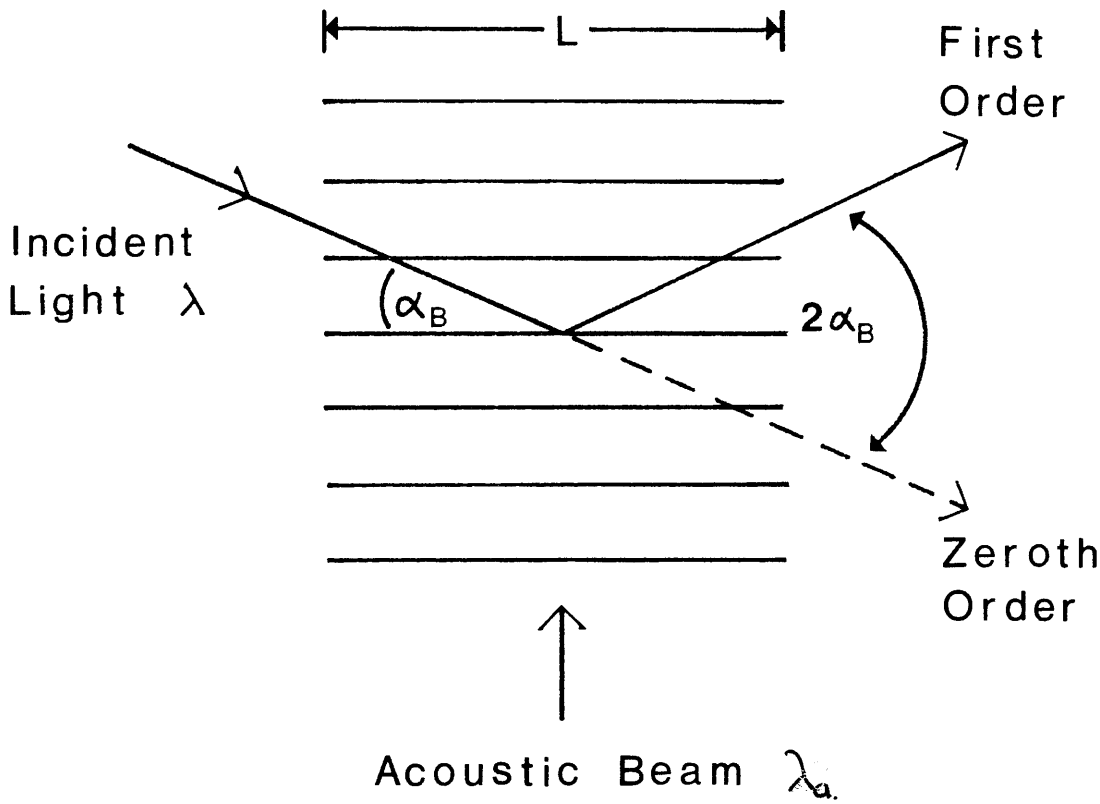

$$\alpha_B \approx \frac{\lambda}{2\lambda_a}$$

Figure 2.1 Acousto – optic Bragg diffraction

in the small angle approximation

$$\frac{L\sin\alpha_B}{\lambda_a} >= 1 \qquad \ldots.2.3$$

where L is defined in Figure 2.1 as the acoustic beam width. This criterion can be expressed more formally in terms of phase variations as[4]

$$Q = \frac{2\pi\lambda L}{\lambda_a^2} \qquad \ldots.2.4$$

where multiple diffraction occurs for Q<1. From Klein and Cook[4] an approximate lower limit is placed on Bragg interaction of $Q=4\pi$, below which a transition region between multiple scattering and Bragg interaction exists. For Q greater than or equal to 4π, equations 2.3 and 2.4 are identical.

For bulk interaction in the Bragg regime and at the Bragg angle, the ratio of optical power in the first order diffracted beam to that remaining in the undeflected beam is given by[1]

$$\frac{I_1}{I^0} = \sin^2\left\{\frac{\pi L}{\lambda}\left(\frac{M_2 P_s}{2}\right)^{1/2}\right\} \qquad \ldots.2.5$$

where P_s is the power density of the acoustic wave and M_2 is a Figure of Merit which is characteristic of the interaction medium. M_2 is given by[5]

$$M_2 = \frac{n^6 p^2}{\rho V^3} \qquad \ldots.2.6$$

where p is the photoelastic constant, ρ the density of the medium and V the velocity of the acoustic wave.

Equation 2.5 is a particular expression for acousto-optic bulk interaction operating in the Bragg regime and at the Bragg angle. For guided wave interaction an additional non-dimensional parameter (between the value of 0 and 1), representing the overlap between the optical and acoustic waves, is included[6]. Thus for acousto-optic Bragg interaction the diffraction efficiency can be simply related to the acoustic power by a relationship of the form:-

$$\eta = \frac{I_1}{I_0} = \sin^2 \{ \text{const } (P_{ac}^{1/2}) \} \qquad \ldots.2.7$$

One of the main applications of acousto-optic devices is as optical beam deflectors where the important considerations are the number of possible resolvable deflection angles and the frequency bandwidth over which the linear relationship, between the acoustic frequency and the deflection angle, holds. In an acousto-optic device, the maximum number of resolvable deflection angles, N, is defined[7] as the ratio of the maximum range of deflection angles to the angular spread of the optical beam. From equation 2.2, the maximum range of deflection angles is determined by the maximum frequency range, Δf, through the relationship

$$\Delta\alpha_{def} = \frac{\lambda \, \Delta f}{V} \qquad \ldots.2.8$$

while the angular spread of the optical beam, of diameter D, is given by

$$\theta = \lambda/D \qquad \ldots.2.9$$

Thus, the maximum number of resolvable deflection angles is given by

$$N = \Delta\alpha_{def}/\theta$$

$$= D/V\ \Delta f$$

$$= \tau\ \Delta f \qquad \ldots.2.10$$

where τ is the transit time of the sound wave through the light beam, and $\tau\Delta f$ is referred to as the time bandwidth product of the device. For a proton-exchanged $LiNbO_3$ waveguide device which resolved 100 separate channels over a frequency bandwidth of 400MHz, τ would equal $2.5\ 10^{-7}$ s and an optical beam width of 0.872mm would be required. Where, according to the Rayleigh criterion, two images are resolved when the central maximum in the diffraction pattern due to one image is situated at a point corresponding to the first minimum in the diffraction pattern of the other.

N can be maximised either by increasing the width of the optical beam or by increasing the frequency bandwidth of the acoustic wave (i.e. bandwidth over which the Bragg angle is maintained). However, a simple increase in the acoustic frequency will result in a reduced interaction efficiency, since the optical beam will no longer be incident at the Bragg angle, and special beam steering transducer structures[8,9,10] are required which maintain the Bragg angle over a wide frequency range. Such transducer structures have been used in the integrated optical spectrum analyser where, in addition, an input collimating lens is used to increase the width of the optical beam in the interaction medium[11]. The aim of the present application was to design a simple narrowband acousto-optical filter which did not require complex electrode structures or expensive collimating and Fourier Transform lenses.

For modulator devices which only require only one deflection angle, the speed of operation is limited by the acoustic-transit time τ. In this case τ can be reduced by focussing the light beam to a small width in the interaction medium. Efficiency is achieved by focussing the acoustic beam so that the acoustic and optical diffraction spreads are approximately equal. In the present

application, two deflected optical beams were required so focussing of the optical and acoustic beams was not performed. Acousto-optic interaction will occur within a channel waveguide structure, the width of which determines the optical beam width and the fundamental frequency between two resolvable positions.

2.3. Acousto-optic Interaction in Channel Waveguides

The greatest potential of integrated optics lies with devices in which light is guided by strip or channel waveguides, with confinement in both dimensions transverse to the direction of propagation. With such devices, the problems experienced with planar waveguides of mode matching to other devices or fibre systems are greatly reduced. Optical deflection in channel waveguides has been performed electro-optically using a static Bragg grating in an X-type switch[12]. The grating was formed by an interdigital electrode structure placed over the interaction section of two optical waveguides. The interaction width was maximised by using tapered sections which expanded the single mode waveguides to a width of 30μm. With 30 Volts applied to the electrodes 48% of the optical power was transferred from one guide to the other.

A similar switch, using an acoustic Bragg grating, was first demonstrated by Tsai et al.[13] in 1980. Here, two identical multimode Ti-indiffused:$LiNbO_3$ channel waveguides, crossed at an angle equal to twice the Bragg angle. The experiment was performed using 20μm wide channel waveguides intersecting at an angle of $2\alpha_B=3^o$. The acoustic frequency was 634MHz and the fundamental waveguide mode was excited using a prism coupler[14]. 97% depletion of optical power from one waveguide was demonstrated, however, it could not be demonstrated that this light was coupled into the other waveguide. Experiments on a single mode version of the same structure were reported by Von Helmolt et al.[15] where 6% deflection efficiency was obtained with an acoustic frequency of 629MHz and an intersection angle of 3.5^o. The relatively low efficiency in this device was attributed to the short interaction length between the acoustic and optical beams, resulting in a relatively low Q value of 7.6. The value of interaction length, L,

in cross channel waveguide structures of this type is directly related to the width, d, of the channel waveguide ($L=d/\sin\alpha$)[15]. Tapered waveguide sections could be used to expand the width of the channel waveguides, as in the electro-optic Bragg switch[12]. This design has been proposed[16], see Figure 2.2, but to date no experimental results have been reported.

Von Helmolt[17] also demonstrated the use of acousto-optic channel waveguide devices for modulation and directional coupling. A Mach-Zender interferometic design was used to provide intensity modulation with the relative phase shifts, between the adjacent arms of the structure, being induced by a surface acoustic wave. In the experiment 1.2 rad. r.f. phase shift was achieved with 20mW of acoustic power. A SAW driven waveguide directional coupler has also been demonstrated in which 100% modulation of the transferred power was achieved for an acoustic power of 8mW. One of the advantages of these later devices is that during fabrication only parallelism between waveguide and IDT is necessary and that one SAW can drive up to 14 directional couplers[17] (assuming that the SAW attenuation is low). These devices can be used primarily in optical communication systems where signal transfer and modulation are required. However, the acousto-optic diffraction efficiency is severely limited by the waveguide width and such devices could only be used to deflect light in one direction and are not sensitive enough to provide any kind of frequency filtering within the guide walls.

2.4. Waveguide Horns in Integrated Optical Devices

Waveguide horns or tapers are used in integrated optics to alter the dimensions of channel waveguides and either to couple from planar waveguides to channel waveguides or to aid end-fire or prism coupling of laser power to channel waveguides[18,19]. In cases such as the electro-optic Bragg switch[12] or the static grating coupler[20], the tapers are used to expand narrow single-mode channel waveguides while still retaining most of the power in the fundamental transverse mode. Tapers are designed so that power loss, as a result of the taper action, is kept to a minimum. To provide this, the taper performance must be as close as possible

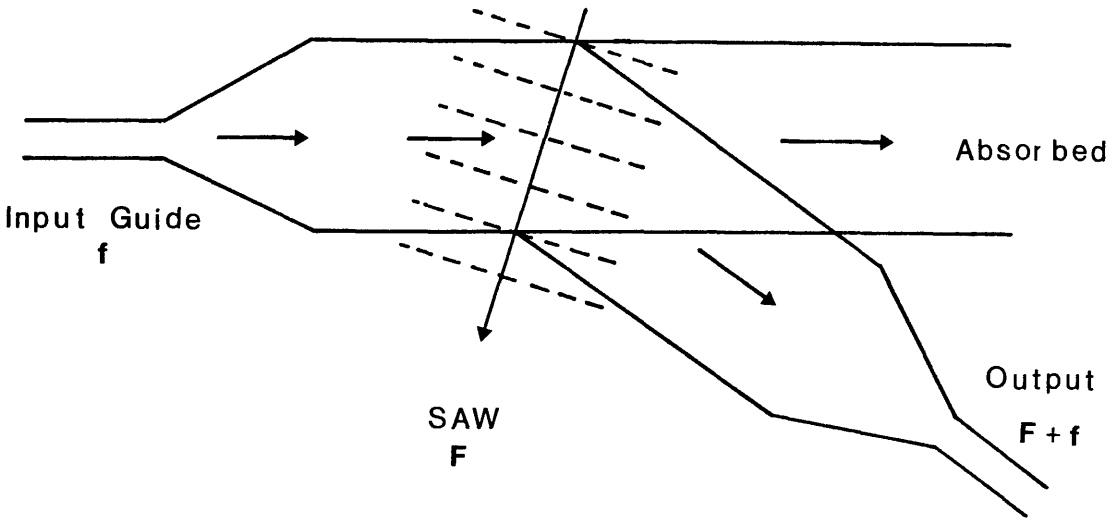

Figure 2.2 Proposed acousto – optic channel waveguide modulator (after 17).

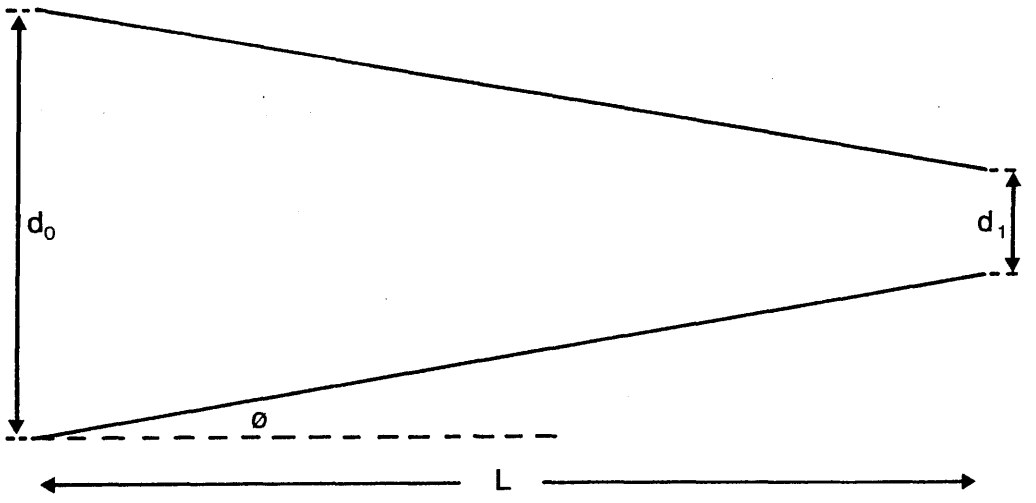

$$\tan\text{ø} = \left(\frac{d_0 - d_1}{2L}\right)$$

Figure 2.3 Linear taper of length L and angle ø

to an adiabatic transfer of power, i.e., the lowest order mode must propagate through the structure without cumulative power transfer to higher order local modes, since the largest source of power loss is radiation of higher order modes as successive cut-off dimensions are reached. Previous investigations into the design of waveguide tapers have dealt mostly with transition from a single mode to a multimode waveguide using the step analysis proposed by Marcuse[21]. However, as in a lossless situation modal coupling follows the rules of reciprocity, the results obtained can be related to tapers acting in the other direction.

Winn and Harris[22] applied coupled mode theory to the problem of an expanding linear waveguide taper, where they constructed a 3-dimensional structure and computed results for changes in taper angle and waveguide length. A schematic diagram of a linear taper is given in Figure 2.3. In the analysis, the authors considered waveguides which supported only one depth mode, stipulating that, for efficient taper coupling, there should be no cross coupling between depth and transverse modes[22] as a result of the taper action. In addition, only tapers which were symmetrical about a centre axis were considered so that any coupling which might occur would only be between modes of the same parity, i.e. asymmetric modes will couple only with asymmetric modes and symmetric modes couple only with symmetric modes[22,23]. Coupling structures with widths varying from 3μm to 50μm were considered[22] and results indicated a dramatic increase in the mode coupling as the horn angle varied from 1.3° to 3.0°. The authors concluded that very long shallow tapers were required for low loss performance and suggested that a reduction in taper length might be achieved by using exponential shaped tapers. Nelson[24] however, concluded that any improvement would be modest and suggested the use of linear tapers, with a maximum taper angle of 1°, to ensure efficient coupling. This design should ensure that during coupling at least 90% of the optical power remained in the fundamental mode.

Burns and Milton[25] used coupled mode theory to investigate the use of shorter parabolic shaped tapers and developed equations from which values of the taper angle and length necessary to

ensure low loss power transfer could be obtained. The equations require that the spreading of the waveguide walls is slower than the diffraction spread of the lowest order mode, thus ensuring, in the analogous ray optics interpretation, that the mode interacts with the waveguide walls and propagates along the waveguide. The approximation however, assumes a small index change between the waveguide and the substrate and this could result in the design being unsuitable for proton-exchange waveguides where large index changes (~ +0.12) are possible.

Baets and Lagasse[26] used the Beam Propagation Method (BPM) to assess the behaviour of tapered waveguides. Their results for gentle linear tapers agreed with those mentioned previously, however it was shown that in some cases steep taper transitions would radiate more power than abrupt transitions. The authors also noted that for transition ratios of ~10, linear tapers were suitable but for larger ratios, improvement in coupling performance might be found by using exponential or parabolic tapers.

For the experiments discussed later in this chapter, linear waveguide tapers were used, with an initial width of 2μm and expanding to 10μm at various taper angles up to 1.0°. Simple experiments have been performed examining the behaviour of the waveguides as the input coupling conditions were altered.

2.5. Analysis of Mode Conversion in Channel Waveguides using an Acoustic Grating

In chapter one of this thesis, a narrowband frequency filter based on an acousto-optic channel waveguide device was proposed. Light propagating as the fundamental mode in a channel waveguide would be diffracted into a waveguide branch at an angle such that either the fundamental or the first order transverse mode of the branch waveguide was excited, see Figure 2.4. The phase mismatch required to excite two adjacent modes in a channel waveguide would result from the variation in angular diffraction and this variation would be related to the acoustic frequency. A waveguide

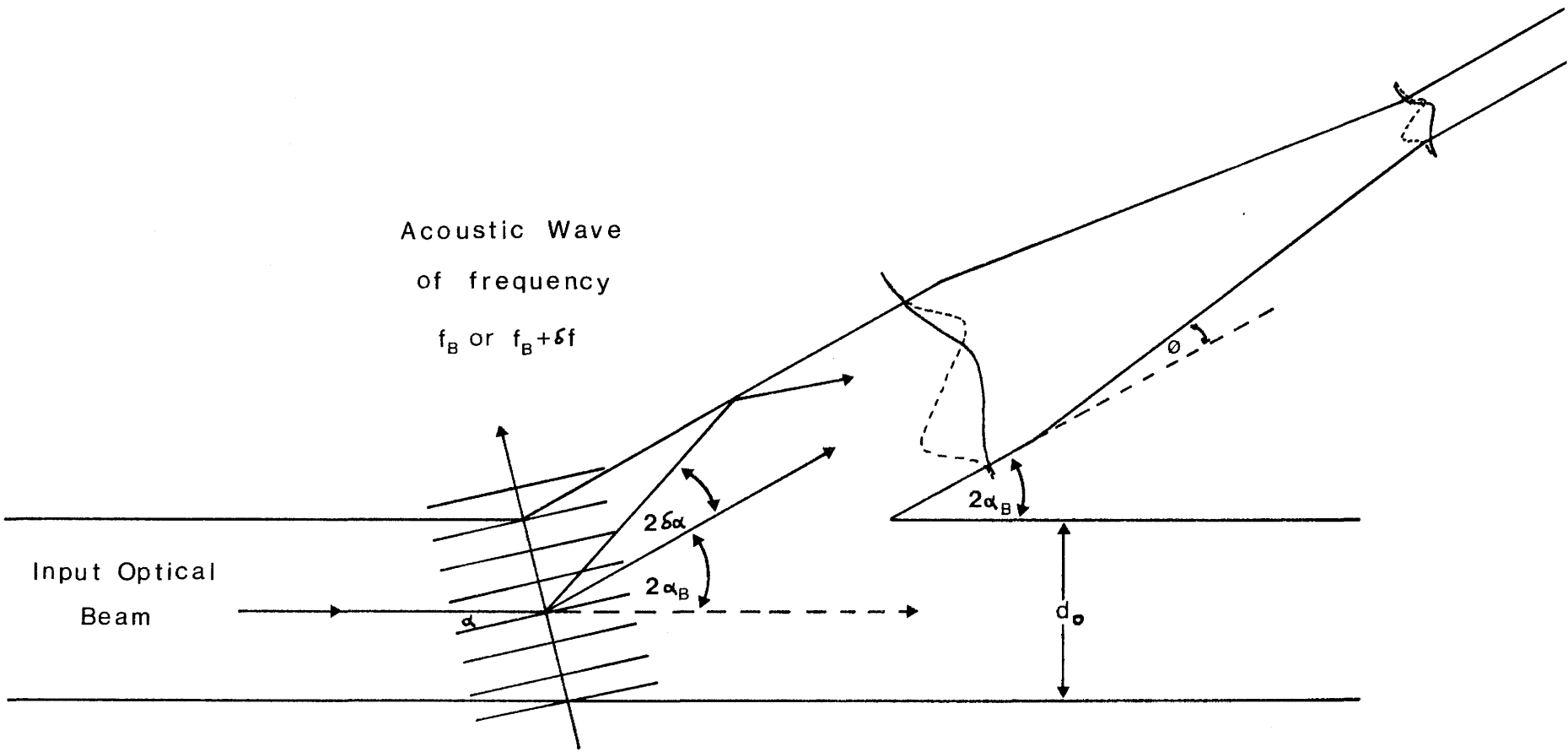

Figure 2.4 Acousto – optic channel waveguide demodulator

taper would follow the branch waveguide to ensure that unwanted higher order modes, possibly excited during the interaction, would be radiated into the substrate and only the fundamental and first order modes would propagate to the end of the waveguide. For efficient power transfer, the taper angle would have to be sufficiently small so that no additional modes were excited as a result of variations in the waveguide width. This section presents a simple analysis which predicts, for a given waveguide width, the change in acoustic frequency required to excite alternatively two adjacent modes in such a channel waveguide device.

Figure 2.4 depicts the structure under consideration. The waveguide refractive index n is taken to be a constant throughout the structure and it is assumed that no higher order transverse modes are excited by imperfections in the waveguide. In addition, it is assumed that, in the absence of a SAW grating, there is negligible coupling between the principal waveguide and the branch waveguide. (In the following section it is shown that for a branch angle of 2° and without deflection from a grating, ~5% of the optical power leaks from the main waveguide into the branch.) The SAW grating and the waveguide branch are both aligned at the Bragg angle α_B so that, when the grating is operated at the Bragg frequency, the fundamental mode of the principle waveguide will transfer directly into the branch and propagate as the fundamental mode of the branch waveguide. Any change in the diffraction angle of the SAW grating would result in a phase mismatch at the guide input and the generation of additional transverse modes.

For a SAW grating operating at the Bragg angle, the acoustic frequency can be expressed by (see equation 2.2)

$$f_1 = \frac{2V}{\lambda} \alpha_B \qquad \ldots.2.11$$

Now consider frequency f_2 ($>f_1$) such that $f_2=f_1+\Delta f$. This would imply that, for fixed λ and V,

$$f_1 + \Delta f = \frac{2V}{\lambda}\{\alpha_{B1} + \Delta\alpha_B\} \qquad \ldots.2.12$$

If for a given f_1 and α_{B1}, the deflected light beam excites the fundamental mode of the waveguide then it is possible to calculate the required angular separation between it and a second deflected beam, if that second beam is to predominantly excite the next order transverse mode.

The change in input coupling angle required to provide the necessary change in phase shift is given by λ/d_o, where d_o is the waveguide width.* To achieve this angular separation in the waveguide the deflection angle at the grating would be required to change by

$$\Delta\alpha = \frac{\lambda}{2d_o} \qquad \ldots.2.13$$

Thus substituting equation 2.13 into equation 2.12 gives

$$f_1 + \Delta f = \frac{2V}{\lambda}\{\alpha_{B1} + \lambda/2d_o\} \qquad \ldots.2.14$$

where Δf represents the minimum frequency shift for the second order transverse mode of the waveguide to be predominantly excited and equation 2.14 reduces to

$$\Delta f = V/d_o \qquad \ldots.2.15$$

Therefore, the change in frequency is independent of optical

* See Appendix 2, p34a.

wavelength and is governed primarily by the waveguide width d.

Table 2.1 Frequency separation

d_o	Δf	$\Delta\alpha$
10μm	349.4MHz	0.813°
20μm	174.7MHz	0.406°
50μm	69.9MHz	0.1623°
100μm	34.9MHz	0.0813°
874μm	4.0MHz	0.0093°

Thus, if a propagating optical beam is deflected by an acoustic grating into a channel waveguide branch, such that the fundamental transverse mode of the branch is excited, then Table 2.1 gives examples of the acoustic frequency change which would be necessary to alter the phase of the input light beam so that the next order transverse mode was predominantly excited. The analysis has considered proton-exchanged $LiNbO_3$ channel waveguides of various widths d, and the angular shift $\Delta\alpha$ has been calculated from equation 2.13, for λ_o=0.6328μm and n=2.23. The value Δf=4.0MHz corresponds to the desired frequency resolution of the IOSA[27]. For an acoustic frequency of 425MHz, α_B=0.989°.

If, for a given waveguide width d, the change in acoustic frequency Δf was not as large as that given in Table 2.1 then a complex wave interference pattern would exist in the branch waveguide which was the superposition of all the excited modes. For small changes in the acoustic frequency the complex waveform would be dominated by the approximately gaussian profile of the fundamental mode. In the following section the BPM is used to show that as the frequency is increased, up to the maximum value of Table 2.1, the proportion of power in the fundamental mode decreases and power transfers to the next order transverse mode.

2.6. Investigations of Mode Filtering using the Beam Propagation Method

The BPM is a numerical modelling method for the scalar wave equation in the paraxial propagation and small index variation approximation. The method involves propagating an input beam through a small distance Δz, in a homogeneous medium using Fourier optics, then correcting the phase for any index variations seen by the beam during the propagation step. The phase correction term simply involves using the lens law as for thin lenses. The BPM has been applied to a number of integrated optic structures in recent years and several review papers on the method have been published[28,29]. In this section the BPM is used to investigate the predictions of the simple analysis for mode conversion in channel waveguides given in the previous section.

The method has been used initially to calculate the power loss in branching waveguide structures in the absence of an acoustic field. Figure 2.5 shows the variation in optical field distribution along a branching channel waveguide structure for a gaussian input beam. The waveguides are 20μm wide and the 1/e points of the input gaussian beam co-incided with the walls of the guide. For a branching angle of 2.0°, ~5.02% of power launched at the input leaked into the branch. For the device presented in Figure 2.3, a deflection angle of 2.0° corresponds to an acoustic frequency of 425MHz.

A tapered waveguide with width variation from 20μm to 2μm has been modelled. The taper angle was 1.0° and a long 2μm wide channel waveguide followed the taper. The refractive index change between the waveguide and the substrate was 0.0275 at λ_0 = 0.6328μm and at its narrowest width the structure supported three transverse modes. Figure 2.6(a) shows the optical field distribution along the structure for a gaussian input. The input beam was launched on-axis and excited all the possible symmetrical transverse modes of the waveguide. It can be seen from Figure 2.6(a) that the optical wave distribution is symmetrical throughout the structure indicating that little of the optical

Figure 2.5 Optical field distribution along a branch waveguide structure. In the absence of an acoustic wave 5.02% of the power coupled into the branch. Branch angle = 2.0°

* Field distribution at input, as shown above, corresponds to steady state conditions established after input gaussian beam is allowed to propagate for an appropriate distance.

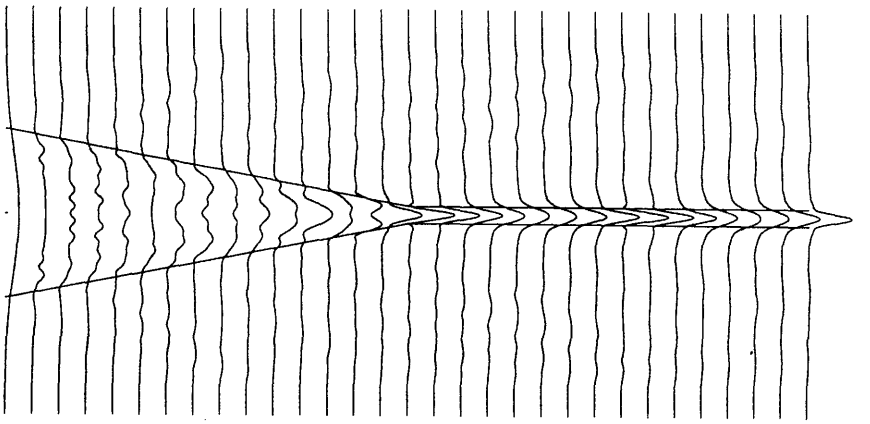

(a)

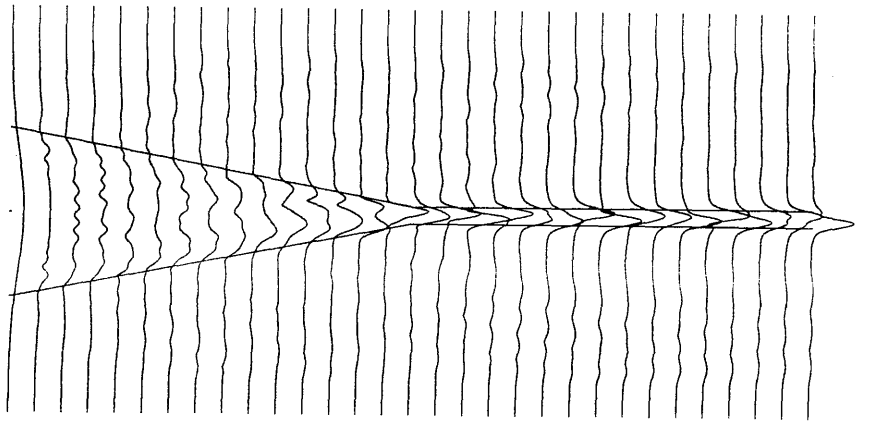

(b)

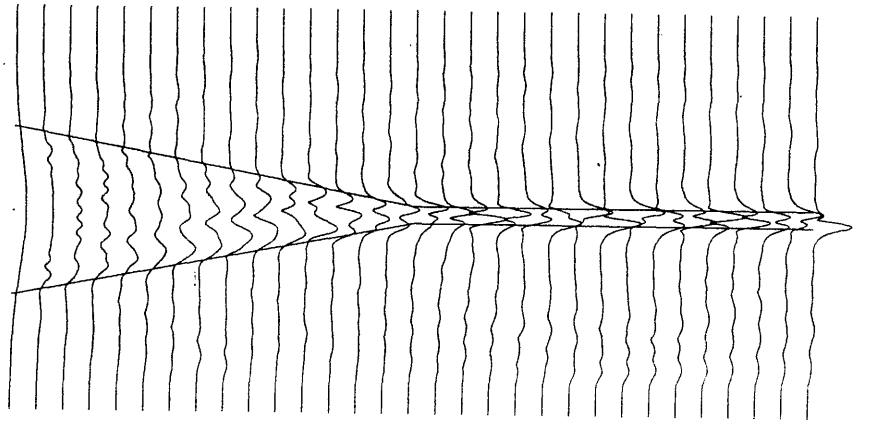

(c)

Figure 2.6 Optical field distribution along a branch waveguide for a gaussian input launched at an angle corresponding to an acoustic frequency shift of (a) 0MHz, (b) 87MHz and (c) 174MHz.

power coupled into asymmetric modes as a result of the taper action. In addition, the ripple evident outside the structure is indicative of radiative power loss as successive cut-off dimensions within the taper are reached. The modal content of the field in the output channel waveguide is presented in Figure 2.7(a). The output waveform is predominantly composed of the fundamental mode of the waveguide with a small contribution remaining in the third order mode.

Variation in the mode content of the waveguide was examined as a function of the phase of the gaussian input beam. Figures 2.6(b) and (c) show the optical field distribution in the structure for variations in input angle corresponding to changes in acoustic frequency of 87MHz and 174MHz respectively. It can be seen that the asymmetry of the optical field distribution increases with acoustic frequency, corresponding to an increase in the proportion of optical power which propagates in the asymmetrical modes. The modal content of the fields in the output waveguides of Figures 2.6(b) and (c) are presented in Figures 2.7(b) and (c) respectively. As predicted in the previous section the power in the first order asymmetric mode increases with increasing angle and the acoustic frequency required to produce this angular variation can be predicted by equation 2.15.

This section has shown that, in theory, it is possible to perform frequency filtering using modal variations in channel optical waveguides. However, there are many practical problems involved with the device design. The initial proposal for this device envisaged a frequency filtering performance comparable with that proposed for the IOSA. In addition, it was thought that this performance could be achieved without the need for either expensive geodesic lenses or complicated IDT structures. This analysis indicates that a very large frequency shift is required before a significant difference in the modal content of the branch waveguide is obtained. To achieve large changes in the acoustic frequency and still retain interaction at the Bragg angle, complicated wide-band IDT structures would be required, thus negating one of the original aims of the project. For modest frequency changes very slight changes in the modal content which

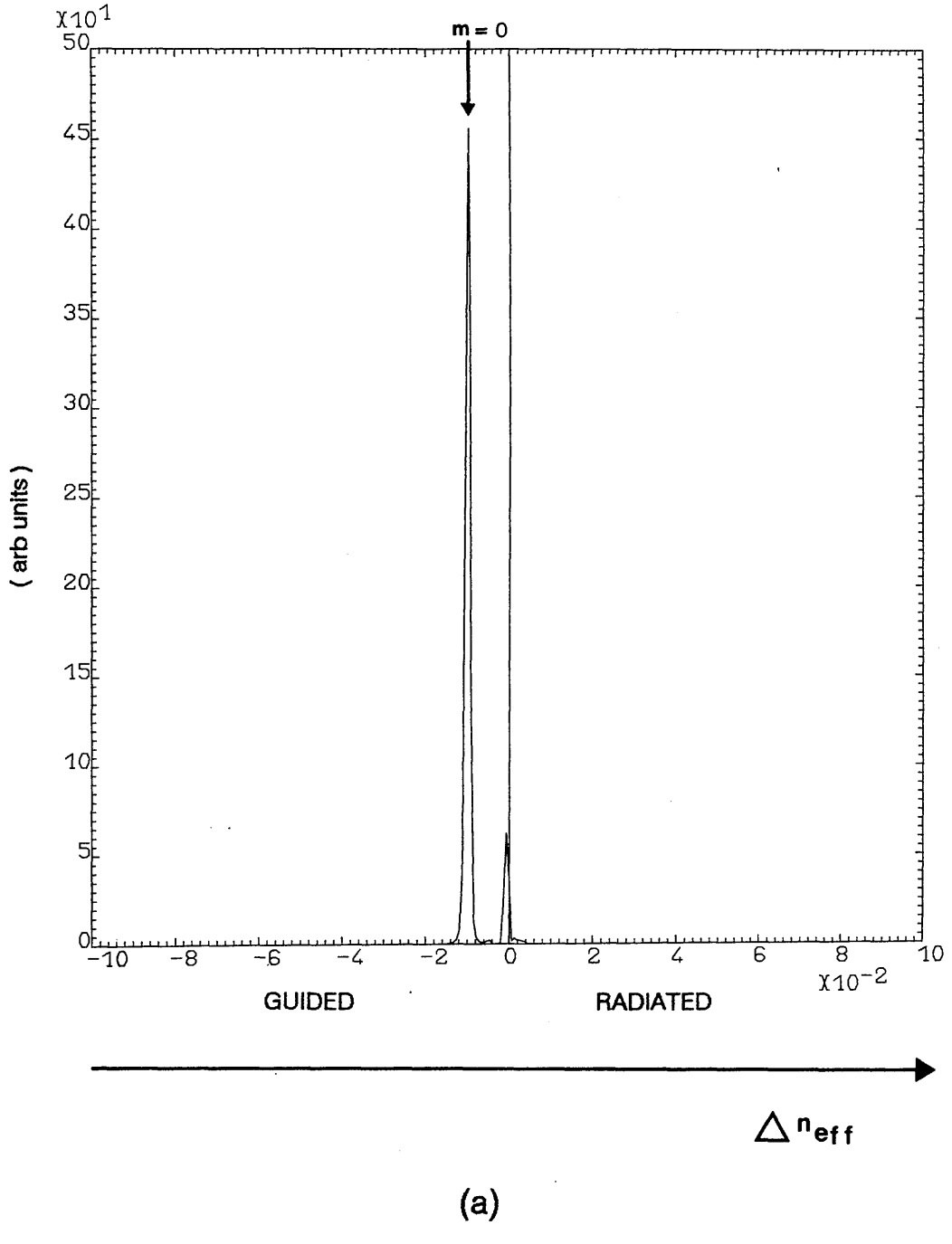

Figure 2.7 Modal content of the field for the output waveguide of Figure 2.6 for (a) 0MHz, (b) 87MHz and (c) 174MHz.

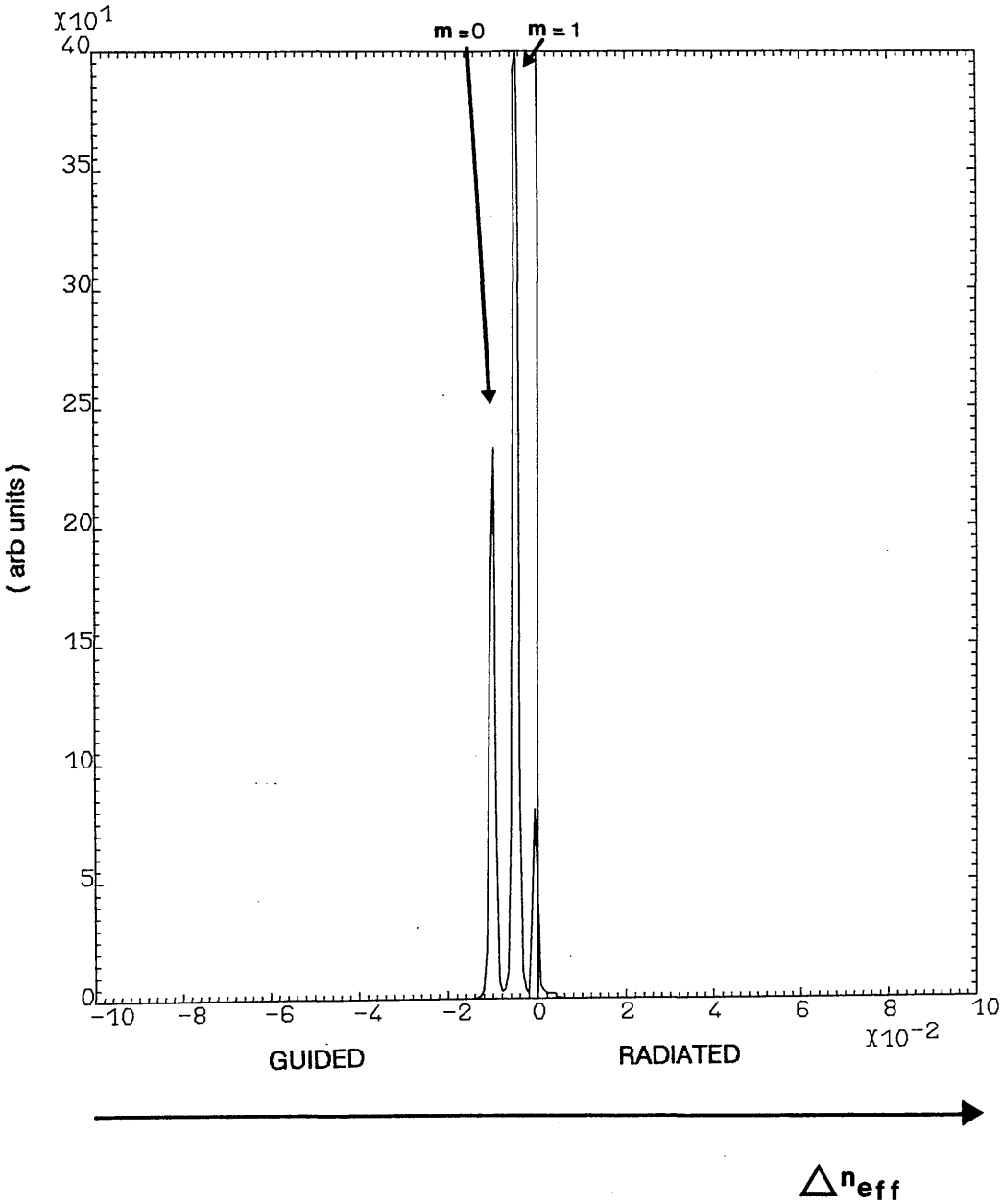
X10^1
40
35
30
25
20
15
10
5
0
m = 0
m = 1
(arb units)
-10
-8
-6
-4
-2
0
2
4
6
8
10
X10^-2
GUIDED
RADIATED
Δn_eff

(c)

would exist would be very difficult to detect. In addition, although the tapers would be designed to reduce power loss a significant amount of power would be radiated because of multi-mode excitation at the interaction region. It is possible to reduce the required frequency separation by increasing the width of the interaction region. However, wide waveguides would make it very difficult, if not impossible, to retain power in the fundamental mode and light deflected into the waveguide would no longer excite the fundamental mode only.

2.7. Fabrication of channel waveguide tapers

2.7.1. Introduction

In this section the experimental equipment and procedures used in fabrication of proton-exchanged optical waveguides formed in $LiNbO_3$ are presented. Shadow masks for the fabrication of linear waveguide tapers have been defined on $LiNbO_3$ substrates using the method of 'aluminium wet-etch'.

2.7.2. Diffusion mask fabrication

The most common method used in the fabrication of aluminium diffusion masks is the 'aluminium-etch' method (shown schematically in Figure 2.8). This method uses conventional photolithographic techniques which must be carried out in the dust free atmosphere of a clean-room. The clean-room facilities used in this work include individual laminar flow work stations of class 100 standard situated within a larger area of class 10,000. The substrate cleaning, resist deposition, exposure, and development were carried out within the workstations, each of which had its own supply of deionised (Reverse Osmosis) RO-water, analar grade solvents, and filtered nitrogen dispensers, to clean and blow dry substrates. Aluminium deposition, chemical etching, and acid cleaning were carried out in the larger area where deposition units and extraction cupboards were available.

Clean substrate.

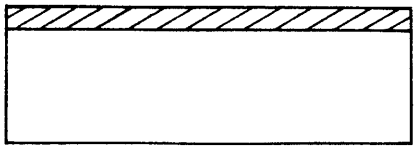

Aluminium evaporated onto substrate surface.

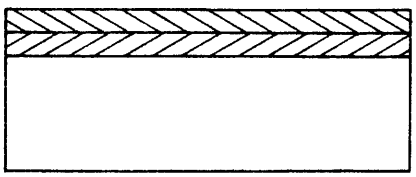

Photoresist spun onto aluminium surface.

Shadow mask

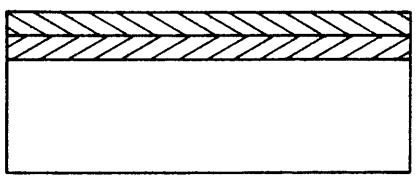

Photoresist exposed with UV light through dark field shadow mask.

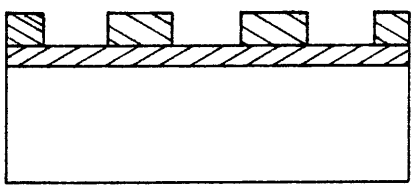

Photoresist developed giving raised ridges of resist on aluminium surface.

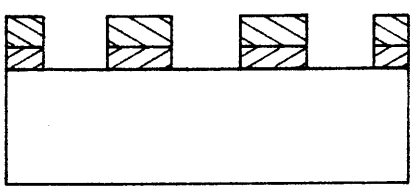

'Aluminium-etch' used to remove aluminium not covered by resist.

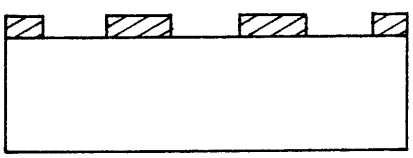

Resist removed to leave desired aluminium pattern on surface of substrate. Apertures define areas where waveguides are formed.

Figure 2.8 Fabrication procedure for aluminium diffusion mask.

2.7.3. Substrate cleaning

It was essential to remove all contaminants from the $LiNbO_3$ surface or the thin aluminium film used as a mask to benzoic acid would not adhere properly. The substrates were initially placed in a solution of warm trichlorethylene for 24 hours, which dissolved any wax which remained after cutting, followed by a rinse in methanol. The substrates were then cleaned ultrasonically alternately in acetone and methanol, thoroughly rinsed in deionised RO-water and blow dried using filtered nitrogen. $LiNbO_3$ tended to heat up during the cleaning process, due to its strong pyroelectric properties, which resulted in the sample charging up and attracting dust. To eliminate this problem a deionising gun was used at all stages of the fabrication process to discharge the substrates. (This problem was more acute with $LiTaO_3$ due to its much stronger pyroelectric properties).

2.7.4. Aluminium deposition

Thin aluminium films (0.2-0.3μm) were deposited on the substrates by evaporation from a hot electric filament in a high vacuum. A rotary pump was used for the initial roughing out and a liquid nitrogen cooled oil diffusion pump to obtain the high vacuum. The aluminium source was a high purity aluminium wire, which was degreased with acetone before being placed in the filament. The aluminium film thickness was measured using a Taylor-Hobson stylus surface plotter, though exact control of the thickness was not necessary at this stage since anything greater than 300Å was sufficient to stop penetration of benzoic acid during the exchange process. At no stage was the ion bombardment facility on the evaporation unit used as this charged up the substrates and resulted in poor film deposition. Upon removal from the evaporation unit the aluminium surface was immediately coated with photoresist to avoid any subsequent contamination.

2.7.5. Delineation of resist pattern and 'aluminium etch'

The positive photoresist 'Microposit AZ1350' was used exclusively throughout this work. The resist was dispensed from a

syringe with a 0.2μm filter to remove any large particles. All work involving photoresist was carried out under yellow light. The resist was spun at 2000rpm for 20 seconds on a standard resist spinner to give an even layer approximately 0.9μm thick. The thin layer of resist was especially useful when fabricating fine grating structures like an IDT where accurate line and spacing widths were required. Coated samples were then placed in an oven at 80-90°C and baked for 30 minutes to drive off solvent from the resist.

The resist was exposed by UV light through a dark field chrome shadow mask using either a quartz-halogen contact printer or a mercury vapour lamp Dage Precima mask aligner. (The shadow mask was pre-cleaned in an H_2SO_4 : H_2O_2 solution). The contact printer arrangement involved pressing the sample down on top of the shadow mask by means of a large weight and exposing the resist for 3 minutes. The mask aligner was used whenever two patterns had to be aligned accurately or in the case when a pattern had to be aligned relative to a crystal axis. Here the sample was held in one chuck and the shadow mask, held above by another, was aligned using micromanipulator movements and optical objectives. When aligned the mask was lowered carefully onto the sample and the resist was exposed for 12 seconds. In both cases the chrome mask and the sample had to be free from dust to ensure perfect contact.

The exposed resist was developed in a 1:1 solution of Microposit AZ positive photoresist developer and deionised RO-water. The development time was 35 seconds with the solution kept at a temperature of 20°C. The developed resist was rinsed in deionised RO-water for 5 minutes to remove any chemical residue. The sample was then dried and inspected using an optical microscope to see if the desired pattern has been successively reproduced. Successful samples had their unprotected aluminium film removed using an aluminium etchant (80% H_3PO_4 : 15% H_2O : 5% HNO_3). The process normally took between 1 and 2 minutes, depending on the thickness of the aluminium film and the temperature of the etchant (normally kept at 20°C). Keeping the samples wet prior to immersion in the etchant was found to prevent the formation of air bubbles on the surface which hinder the

etching process. The samples were then rinsed thoroughly in deionised RO-water and blown dry. Excess resist was dissolved using acetone, leaving the aluminium diffusion mask ready for the exchange process.

2.8. Design and fabrication of waveguide tapers

2.8.1. Design of shadow mask

Following the analysis of section 2.4, waveguide tapers were designed to provide adiabatic transfer of optical power from single mode to multimode channels (or vice-versa) with a minimum amount of cross coupling between transverse modes.

A shadow mask was designed which contained seven linear waveguide tapers with a range of taper angles of 0.4° to 1.0° with a 0.1° gradual increase. Each waveguide expanded from 2μm to 10μm with progressively shorter taper lengths for correspondingly larger taper angles. The maximum and minimum taper lengths were 573μm and 229μm respectively. A straight waveguide section existed at either end of the taper. Due to the high change in refractive index possible with proton-exchange on $LiNbO_3$, the 2μm width was chosen to ensure single mode propagation. Waveguides produced using the above design allowed investigations into the behaviour of waveguide tapers to be carried out.

2.8.2. Waveguide fabrication

Fabrication conditions were chosen to ensure single mode guiding in the 2μm channel waveguide and multimode guiding in the 10μm channel. A computer analysis based on the effective index method for channel waveguides[30,31] provided cut-off conditions for the modes in the 2μm channel which were used in equation 2.16 (see equation 3.7 in chapter 3) to obtain the correct fabrication conditions for dilute melt proton-exchange on $LiNbO_3$.

$$d = 3.347\ 10^3 (t)^{1/2} \exp(-4.39\ 10^3/T)\ \mu m \qquad ....2.16$$

where d is the diffusion depth, t the exchange time, and T the exchange temperature. In practice the diffusion rates in channel waveguides were slightly slower than for planar waveguides[32] so slightly longer exchange times were required to produce the same index change. For all subsequent results in this section the waveguide was proton-exchanged in 0.5% dilute melt for 11 minutes at 220°C. The waveguides were post-annealed at 400°C in an atmosphere of wet flowing O_2 to relieve strain in the lattice structure of the waveguide[33]. Full details of the procedures used for fabricating waveguides on $LiNbO_3$ by proton-exchange can be found in the following chapter.

2.9. Analysis of Taper Behaviour

'End-fire coupling' was employed to couple He-Ne laser light (λ_0 = 0.6328μm) into the polished end of an X-cut $LiNbO_3$ tapered waveguide via X40 microscope objectives. The input coupling angle was varied by rotation of the sample in a horizontal plane and the near field radiation pattern was detected by a Hamamatsu camera and displayed as an intensity distribution on a TV monitor.

Figure 2.9(a) and (b) show guiding in a 2μm and 10μm wide channel guide respectively. The waveguide had been annealed for 10 minutes and each guide supported the fundamental transverse mode. The taper angle was 0.9° and in both cases the properties of shallow waveguide tapers are displayed where, in Figure 2.9(a) multimode guiding in the wide guide has been reduced to single mode output as successive cut-off dimensions are reached and, in Figure 2.9(b), single mode guiding has been preserved from 2μm to 10μm due to the shallow taper angle.

In comparison with Figure 2.9(b), Figures 2.10(a) and (b) show that the preservation of single mode output in the wide waveguide can be disturbed by changing the input coupling conditions. In both cases the coupling conditions were varied by rotating the sample and such results were evident regardless of taper angle. When the sample was reversed only single mode propagation was observed in the narrow waveguide.

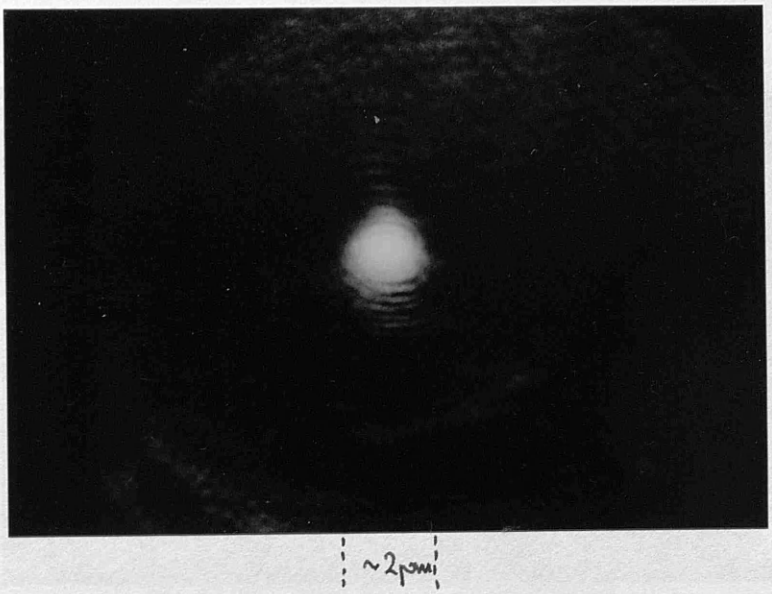

(a)

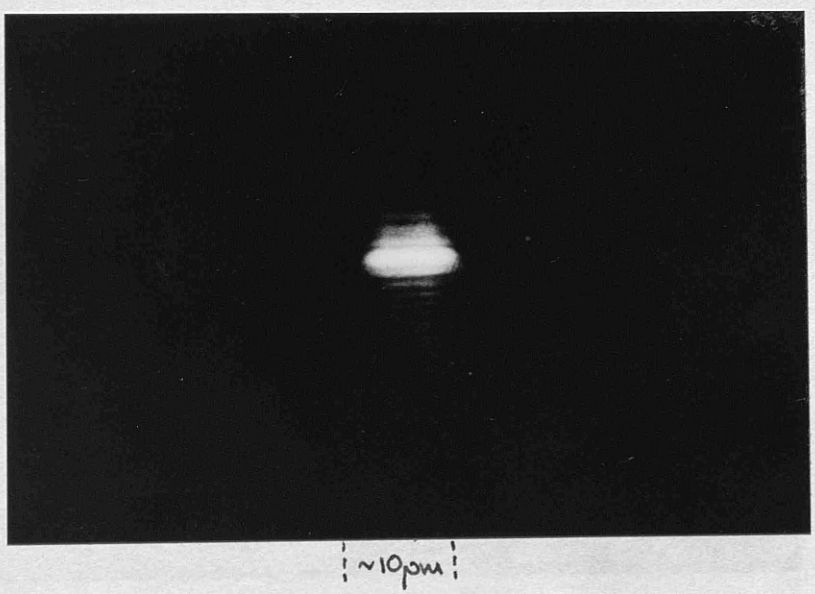

(b)

Figure 2.9 Output intensity of the guided light in a waveguide taper which varies in width from 2μm to 10μm with a taper angle of 0.9^{o}. Light was 'end-fire' coupled into and out of the waveguides and (a) indicates the output from the 2μm waveguide while (b) indicates output from the 10μm waveguide.

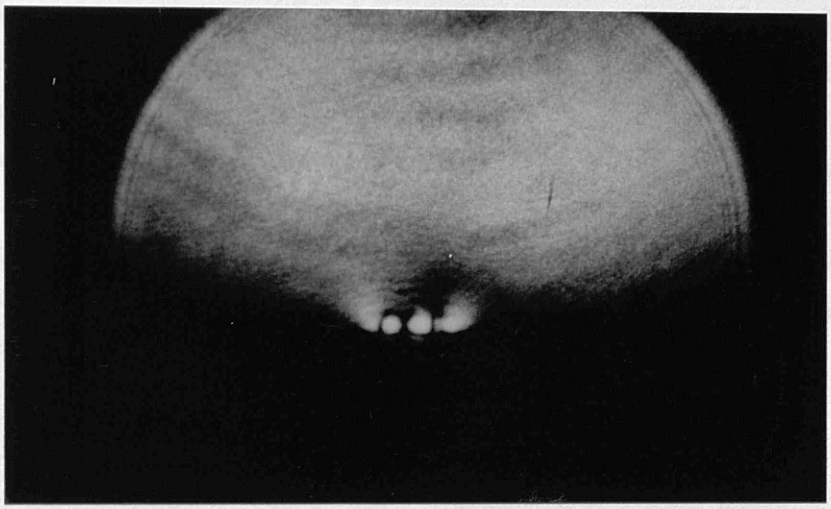

(a)

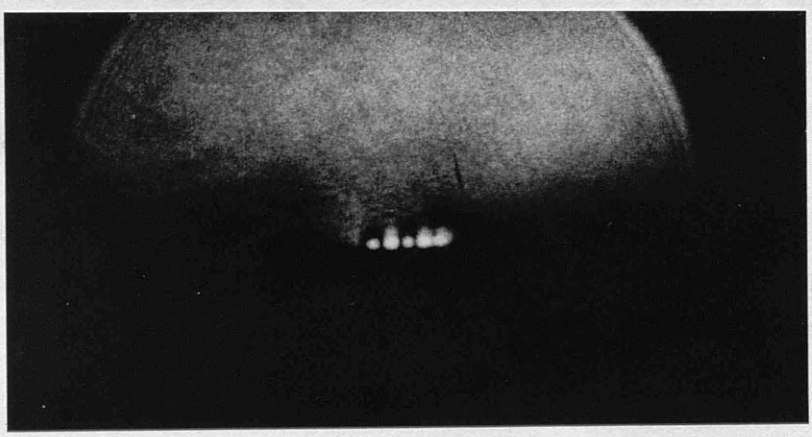

(b)

Figure 2.10 Symmetric multimode propagation in the 10μm wide waveguide of Figure 2.9 for variations in input coupling conditions.

In an attempt to obtain multimode propagation in the narrow waveguide the structure was annealed for a further 20 minutes. Figure 2.11 shows asymmetric mode propagation in the wide waveguide implying the presence of multimode propagation in the narrow waveguide. However, asymmetric mode propagation could not be detected in the narrow waveguide and subsequent annealing of the sample only resulted in a deterioration in the waveguide and a loss of the mode confinement.

2.10. Discussion

The simple experiments which have been performed on the tapered waveguides demonstrate the capabilities of the waveguide taper both as a mode stripper and as a means of conserving power in the lower order modes as the waveguide width is varied. The experimental procedure employed did not, however, allow for very sensitive measurements which could detect the presence of additional modes close to the fundamental. In order to make more sensitive measurements input and output prism coupling should be employed.

Acknowledgement

The BPM analysis used in this chapter was performed by Dr. T.J. Cullen. I am very grateful to Dr. Cullen for all his help during this work and for kindly providing the above mentioned data.

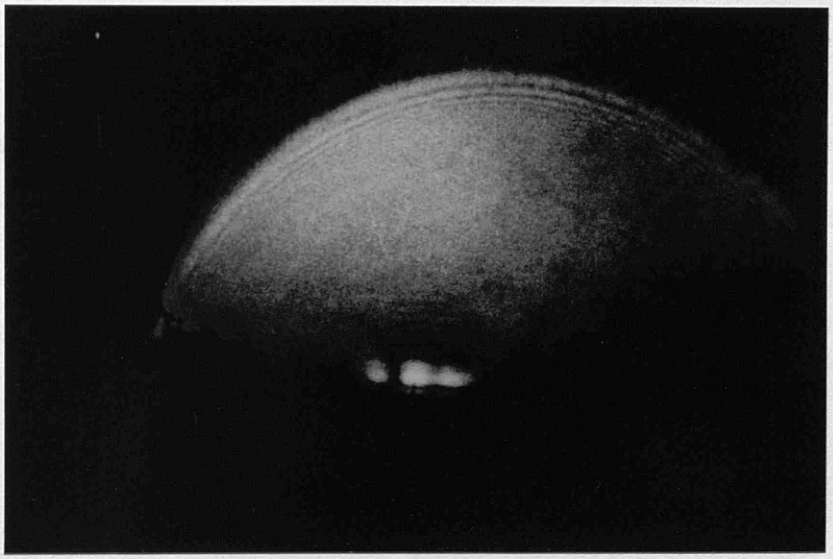

Figure 2.11 Asymmetric mode propagation in the 10μm waveguide of Figure 2.9 (see text).

PPENDIX TO CHAPTER 2

n a simple representation of a waveguide, ignoring the phase hanges at the boundaries, which is reasonable for very wide uides the waveguide modes can be written as:

$$kn_1 d_0 \sin\phi = m\pi$$

here kn_1 represents the wavevector of the wave zig-zagging across he guide. n_1 can thought of as the effective of the slab mode in he vertical direction. The difference angle between the waves hich make up adjacent modes is therefore given by :

$$\delta\phi = \frac{\pi}{kn_1 d_0 \cos\phi}$$

$$= \frac{\lambda_0}{2n_1 d_0} \qquad \text{for small } \phi.$$

References to Chapter 2.

1. R. Adler, 'Interaction between light and sound', IEEE Spectrum, Vol. 4, No. 5, pp.42-54, May 1967.

2. C.V. Raman and N.S. Nagendra Nath, 'The diffraction of light by high frequency sound waves: Part II', Proc. Indian Acad. Sci., Vol. 2A, pp.413-420, 1935.

3. G.W. Willard, 'Criteria for normal and abnormal ultrasonic light diffraction effects', J. Aco. Soc. Amer., Vol. 21, No. 2, pp.101-108, 1949.

4. W.R. Klein and W.D. Cook, 'Unified approach to ultrasonic light diffraction', IEEE Trans. Sonics and Ultrasonics, Vol. SU-14, No. 3, pp.123-134, 1967.

5. N. Uchida and N. Niizeki, 'Acousto-optic deflection materials and techniques', Proc. IEEE, Vol. 61, No. 8, pp.1073-1092, 1973.

6. E.G.H. Lean, J.M. White and C.D.W. Wilkinson, 'Thin-film acousto-optic devices', Proc. IEEE, Vol. 64, No. 5, pp.779-787, 1976.

7. A. Korpel, 'Acousto-optics - A review of fundamentals', Proc. IEEE, Vol. 69, No. 1, pp.48-53, 1981.

8. A. Korpel, R. Adler, P. Desmares and W. Watson, 'A television display using acoustic deflection and modulation of coherent light', Proc. IEEE, Vol. 54, No. 10, pp.1429-1437, 1966.

9. R.M. De La Rue, C. Stewart, C.D.W. Wilkinson and T.R. Williamson, 'Frequency-controlled beam steering of surface acoustic waves using a stepped transducer array', Elec. Lett., Vol. 9, No. 15, pp.326-327, 1973.

10. C.S. Tsai, 'Guided-wave acousto-optic Bragg modulators for wide-band integrated optical communications and signal

processing', IEEE Trans Circuits and Systems, Vol. CAS-26, No. 12, pp.1072-1098, 1979.

11. M.K. Barnoski, B. Chen, T.R. Joseph, J.Y. Lee and O.V. Ramer, 'Integrated-optic spectrum analyser', IEEE Trans. Circuits and Systems, Vol. CAS-26, No. 12, pp.1113-1124, 1979.

12. B. Chen and C.M. Meijer, 'Bragg switch for optical waveguides', Appl. Phys. Lett., Vol. 33, No. 1, pp.33-35, 1978.

13. C.S. Tsai, C.L. Chang, C.C. Lee and K.Y. Liao, 'Acousto-optic Bragg deflection in channel optical waveguides', Tech. Digest Top. Meet. Integrated and Guided Wave Optics., PE-7, Incline Village, Nevada, 1980.

14. P.K. Tien and R. Ulrich, 'Theory of prism-film coupler and thin-film light guides', J. Opt. Soc. Amer., Vol. 60, No. 10, pp.1325-1337, 1970.

15. C.H. von Helmolt, R.T. Kersten, W. Auch and W. Stendle, 'Bragg switch/SSB modulator with integrated optical single-mode waveguides', 2nd Euro. Conf. on Integrated Optics, pp.132-135, Florence, 1983.

16. R.T. Kersten, 'Integrated optical acousto-optic switching', Proc. Photo-opt. Soc. Inst. Eng., Vol. 517, pp.517-536, 1984.

17. C.H. von Helmolt, 'Integrated optic strip waveguides driven by SAW', J. Opt. Commun., Vol. 2, No. 4, pp.142-152, 1981.

18. R.H. Rediker, T.A. Lind, R.A. Becker and L.M. Johnson, 'Design, Fabrication and characterisation of horn antennas in Ti:indiffused $LiNbO_3$ channel waveguides', Proc. 7th Top. Meet. on Integrated and Guided Wave Optics, Orlando, Florida, PDP-71, 1984.

19. W.K. Burns and A.F. Milton, 'Optical waveguide parabolic coupling horns', Appl. Phys. Letts., Vol. 30, No. 1, pp.28-

30, 1977.

20. J. Marcou, R. Attia and N. Gremillet, 'Analysis of Bragg grating coupling between two channel waveguides intersecting at a right angle', IEEE J. Quantum Elect., Vol. QE-22, pp.1557-1567, 1986.

21. D. Marcuse, 'Radiation losses of tapered dielectric slab waveguides', B.S.T.J., Vol. 49, pp.273-290, 1970.

22. R.K. Winn and J. Harris, 'Coupling from multimode to single-mode linear waveguides using horn-shaped structures', IEEE Trans. Vol. MTT-23, No. 1, pp.92-97, 1975.

23. F. Sporleder and H.G. Unger, 'Waveguide tapers, transitions and couplers', Chapt. 9, Peter Peregrinus, Stevenage, 1979.

24. A.R. Nelson, 'Coupling optical waveguides by tapers', Appl. Opts. Vol. 14, No. 12, pp.3012-3015, 1975.

25. A.F. Milton and W.K. Burns, 'Mode coupling in optical waveguide horns', IEEE J. Quantum Elect., Vol. QE-13, No. 10, pp.825-835, 1977.

26. R. Baets and P.E. Lagasse, 'Calculation of radiation loss in integrated-optic tapers and Y-junctions', Appl. Opts., Vol. 21, No. 11, pp.1972-1978, 1982.

27. G.F. Doughty, R.B. Wilson, J. Singh, R.M. De La Rue and S. Wright, 'Aspheric geodesic lenses in an integrated optics spectrum anslyser', Proc. Photo-opt. Soc. Instr. Eng. Vol. 235, pp.35-41, 1980.

28. J. Van Roey, J. Van der Donk and P.E. Lagasse 'Beam-propagation method: analysis and assessment', J. Opt. Soc. Amer., Vol. 71, No. 7, pp. 803-810, 1981.

29. P.E. Lagasse and R. Baets, 'The beam propagation method in integrated optics', NATO Advanced Research Workshop, 1983.

30. H. Kogelink and V. Ramaswamy, 'Scaling rules for thin-film optical waveguides', Appl. Opts., Vol. 13, No. 8, pp.1857-1862, 1974.

31. A.C.G. Nutt, K.K. Wong, D.F. Clark, P.J.R. Laybourn and R.M. De La Rue, 'Proton-exchange $LiNbO_3$ slab and stripe waveguides: characterisation and comparisons', 2nd Euro. Conf. Integrated Optics., pp.53-56, Florence, 1983.

32. N.A. Sanford and W.E. Lee, 'Analysis of proton-exchanged channel waveguides in $LiNbO_3$', Proc. Photo-opt. Soc. Instr. Eng., Vol. 578, pp.7-11, 1985.

33. C. Canali, A. Carnera, G. Della Mea, R.M. De La Rue, A.C.G. Nutt and J. Tobin, 'Proton-exchanged $LiNbO_3$ waveguides: materials analysis and optical characteristics', Proc. Photo-opt. Soc. Instr. Eng., Vol. 460, paper 7, 1984.

CHAPTER 3. Characterisation of Dilute Melt Proton-exchange Waveguides

3.1. Introduction

Since its discovery in 1982[1], the proton-exchange process for waveguide fabrication in $LiNbO_3$ has gained considerable interest because of the various advantages it offers over the titanium indiffusion process such as fabrication simplicity, large index difference and the relatively low temperature at which it can be carried out. The technique has been used to fabricate various types of guided wave device including high efficiency beam deflectors, optical frequency translators[2], second harmonic generators[3,4], planar lenses[5] and integrated optical polarisers[6,7]. The process produces a maximum index change (+0.12) along the extraordinary axis (at optical wavelength λ_o= 0.6328μm) and a reduction of -0.04 along the ordinary axis[8]. This implies that, for X and Y-cut $LiNbO_3$ and $LiTaO_3$, the guided mode is TE polarised while, for Z-cut, it is TM polarised. In addition, for waveguide devices such as the integrated optical ring resonator[9], which require isotropic waveguides, Z-cut $LiNbO_3$ or $LiTaO_3$ substrates must be used and, for acousto-optic devices which utilise the strong electromechanical coupling coefficients of Y- and X-cut $LiNbO_3$ or $LiTaO_3$, the waveguide surface will be anisotropic.

The proton-exchange process from a pure melt has proved to be generally unsuitable for acousto-optic devices, due to damage caused to Y-cut crystals[10], aging effects on X and Y-cut crystals[11] and the reduction in electro-optic activity[2,12]. Efficient acousto-optic devices fabricated on Y-cut $LiNbO_3$ have required very short exchange times and post annealing[13] or have been produced by the combined titanium indiffusion proton-exchange (TIPE) process[14,15]. In both cases, the acousto-optic diffraction efficiency was found to fall with diffusion depth. By the use of the process of proton-exchange from dilute melts, many of the problems associated with pure melt exchange can be overcome and the process has the potential for efficient acousto-optic device fabrication.

This chapter deals with the characterisation of dilute melt proton-exchanged planar optical waveguides on both X and Y- cut $LiNbO_3$ as well as X-cut $LiTaO_3$. Waveguide properties such as index change, waveguide dispersion, diffusion coefficients and material disorder are discussed. In addition, problems inherent in this type of waveguide are outlined and, where appropriate, comparisons with pure melt waveguides are made.

3.2. Waveguide Fabrication Procedure

An important consideration in the characterisation of an optical waveguide fabrication process is the reproducibility of the waveguide performance for given fabrication conditions. One method is to perform the exchange in a sealed ampoule[16,17] at the boiling temperature of the acid. Although reports indicate that exchange at elevated temperatures produces a far better quality of waveguide[18], doubts remain about the reproducibility of this method. In addition, waveguides produced by this method are multi-mode and are not suitable for most device designs. This method, therefore, has not been considered for this work and the process outlined below has been found to be suitable for consistent waveguide reproduction.

Unlike the case of pure melt proton-exchange, where exchange time and temperature were extremely critical parameters, the most crucial part of the process with dilute melt proton-exchange was the preparation of the exchange melt. The desired molar percentages of lithium benzoate and benzoic acid were mixed in a stainless steel beaker which was placed in an oil-bath of high temperature, controlled to within $\pm 0.25^{o}C$. The stainless steel beaker ensured that there was good thermal contact between the oil and the acid. Once melted, the acid was thoroughly stirred to ensure that a good mixture between the benzoic acid and lithium benzoate was formed.

Single crystal $LiNbO_3$ or $LiTaO_3$ substrates were degreased and cleaned thoroughly, using a series of organic solvents, before

being mounted in a stainless steel basket and placed in the molten acid mixture. The temperature of the acid was directly monitored via an external thermocouple and the acid and the bath were both covered to ensure temperature stability and to minimise acid evaporation. The stainless steel beaker contained ~150ml of molten acid which was considered large enough to provide an effectively infinite source diffusion for a given dilution.

Due to the sensitivity of the process to acid dilution, the mixture was replaced after approximately 6 hours at a temperature of approximately 235°C. Benzoic acid is an organic material which, in general, tends to decompose on melting and when retained at high temperature for a long time. This decomposition impaired the acidity and, as a result, the acid required to be regularly changed. Figure 3.1 shows Rutherford Back-Scattering Spectrometry (RBS)[19] measurements performed on two Y-cut $LiNbO_3$ waveguides notionally exchanged for 20 minutes in 0.5% dilute melt at 200°C. The variation in exchange depth of 0.043μm indicates that the exchange melts were not identical. Waveguide (a), with an exchange depth of 0.268μm was fabricated in an unused melt, while waveguide (b), with a depth of 0.255μm was fabricated in a melt which had been in use previously for a number of hours. If an exchange melt is used continuously, then the lithium ions, which leave the substrate during exchange, contribute to the dilution of the benzoic acid. Therefore, in addition to the degradation of the acid, prolonged use of an exchange melt could result in an increase in the dilution ratio. Figure 3.1 indicates how severe this combined effect may be.

Later in this chapter (see Figure 3.7), a comparison is made between a series of $LiNbO_3$ waveguides which were fabricated, at the same time and temperature, over a range of dilution ratios. The comparison indicates that the RBS backscattering yield, which can be associated with the lattice disorder[19], falls with increased melt dilution. Figure 3.1 shows a similar trend indicating that, in comparison with waveguide (a), waveguide (b) was formed from a melt with a reduced acidity. This example emphasises the care which must be taken to ensure that the composition of each protonic source is the same.

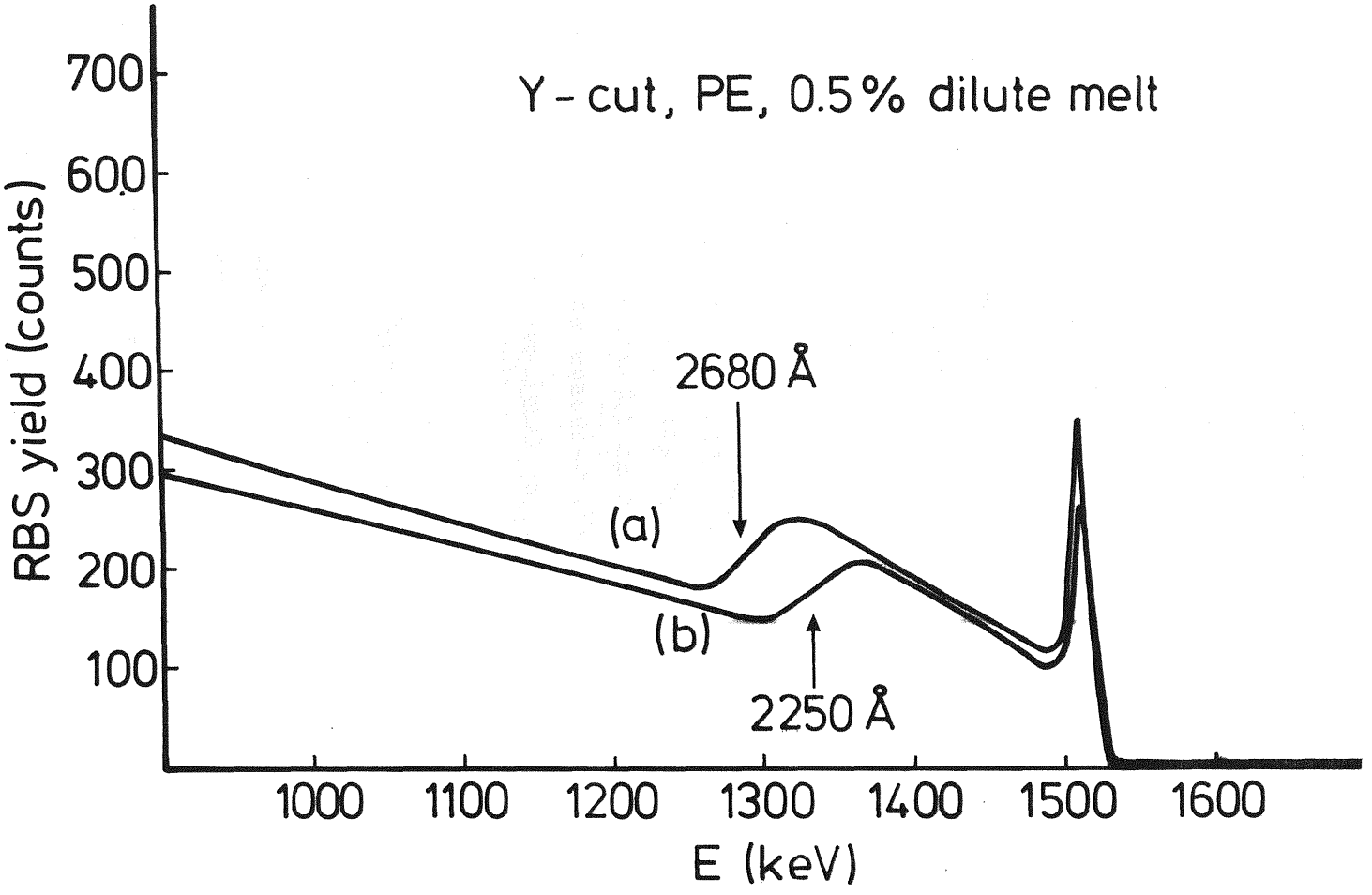

Figure 3.1 RBS data for two Y – cut $LiNbO_3$ waveguides, notionally exchanged under the same fabrication conditions (see text).

Exchange temperatures ranged from 180° to 235°C (benzoic acid has a melting point of 122°C and boiling point of 249°C) and upon removal from the acid, the crystallised benzoic acid, which formed on the substrates during cooling, was removed by rinsing in methanol. After exchange, the samples were ready for immediate use since dilute melt proton-exchange waveguides did not suffer from instabilities or ageing problems.

3.3. Optical Characterisation

3.3.1. Introduction

For all experiments outlined in this thesis, the source of lithium niobate was Barr and Stroud Ltd. while the lithium tantalate was made by Union Carbide and supplied by Roditi. In addition, unless otherwise stated, all samples were exchanged in a diluted melt of 0.5% (molar) lithium benzoate, and all optical measurements were carried out at a wavelength of λ_o= 0.6328μm. The prism coupling technique[20] with single crystal rutile prisms was employed to evaluate the optical characteristics of the waveguides. Equation 3.1 is the basic prism coupling equation which relates the measured coupling angle θ to the waveguide effective refractive index (n_{eff}).

$$n_{eff} = n_p\{\alpha_p - \sin^{-1}(\sin\theta/n_p)\} \qquad ....3.1$$

α_p is the prism angle and n_p is the index of the prism. For TE polarised light with λ_o=0.6328μm, n_p=2.8719. The effective refractive index (n_{eff}) of each observed TE mode was calculated from the measured mode angle using equation 3.1.

3.3.2. Lithium Niobate Waveguides

The calculated effective indices of the lithium niobate waveguides were used as data input for a computer program based on the inverse WKB method[21] which estimated the shape of the refractive index profile verses depth. The method takes as input the effective index measurements of the proton-exchange waveguides and uses an area minimising technique to work out the best-fit effective depth for each mode, as well as an estimation of the waveguide depth. The IWKB method requires a waveguide to support at least three modes and, as a result, is not necessarily suitable for the analysis of waveguides of practical interest (since for most applications single-mode waveguides are strongly preferred). However, the method is invaluable in determining the index profile for a particular waveguide fabrication method.

Figure 3.2(a) shows the step-like refractive index profile for an X-cut $LiNbO_3$ waveguide exchanged at 230°C for 6 hours. The second curve (Figure 3.2(b)) shows the same waveguide after a very short (5 minutes) annealing at 400°C in an atmosphere of flowing wet O_2. The immediate effect of this short annealing was to produce a deeper waveguide with a slightly reduced index yet retain the overall step-like profile. The importance of this result will be shown in a later chapter. A detailed explanation of the effects of annealing on proton-exchanged lithium niobate waveguides can be found in references 22 and 23.

The step-like index profile of dilute melt proton-exchanged waveguides was to be expected from the results of previously published work[1,24] on pure melt proton-exchange waveguides. On the basis of the step-like profile, the depth of the waveguides was determined by computational methods using the prism coupled mode angles[24,25,26]. The program was based on the effective index theory presented by Kogelnik and Ramaswamy[27] and using the normalised curves and the measured effective indices, the waveguide depth and surface index was estimated.

For TE modes a normalised waveguide effective index b is defined:

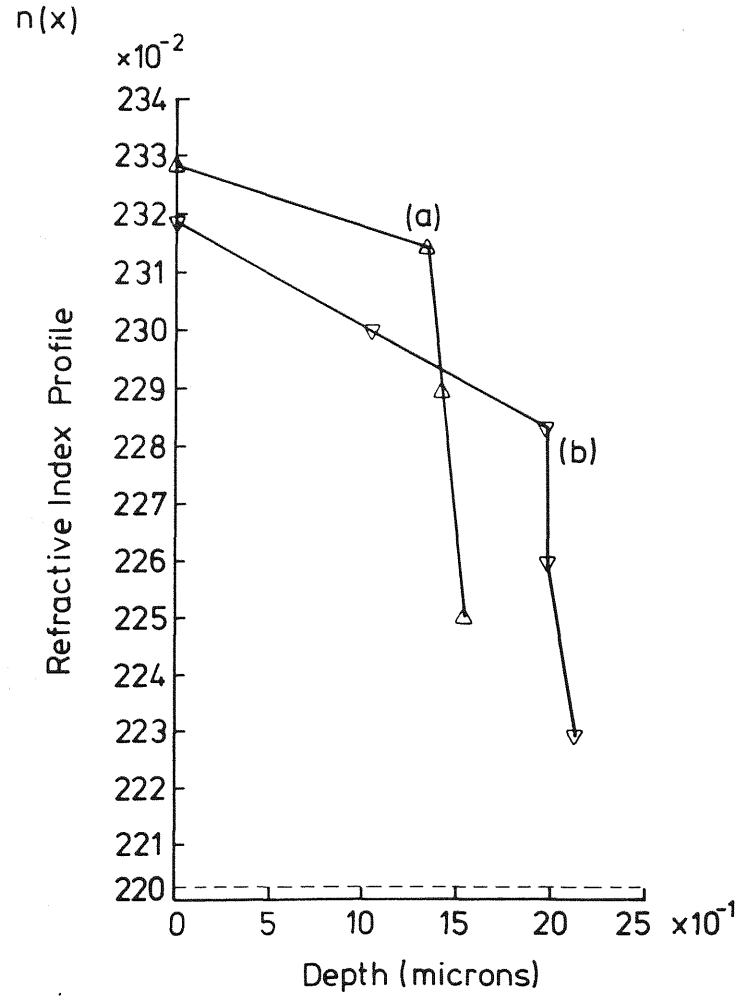

Figure 3.2 Refractive index variation with exchange depth for 0.5% dilute melt proton – exchange waveguides on X – cut $LiNbO_3$ 6hrs at 230°C:
(a) before annealing
(b) 5 mins annealing at 400°C

$$b = \frac{(N^2 - n_f^2)}{(n_f^2 - n_s^2)} \qquad \ldots.3.2$$

where N is the guided-mode effective index (which is obtained using equation 3.1), n_s is the substrate refractive index (which is known), and n_f is the (unknown) guiding region refractive index. A normalised guide thickness V is defined:

$$V = kf(n_f^2 - n_s^2)^{1/2} \qquad \ldots.3.3$$

where f is the guiding region thickness and k is the free-space propagation constant. Plots of b versus V are obtained from solutions of the normalised dispersion equation with an asymmetry parameter $\bar{a}$ given by:

$$\bar{a} = \frac{(n_s^2 - n_c^2)}{(n_f^2 - n_s^2)} \qquad \ldots.3.4$$

where n_c is the cover region refractive index.

From a knowledge of the number of modes which the guide supports, an appropriately restricted range of values for V is determined. Within this range, a computer scan is carried out to obtain an estimate of n_f for each mode, given an initial estimate of the asymmetry parameter $\bar{a}$. b-values from an initial choice of V are obtained from the theoretical plots, and, together with N-values from measurement, are used to obtain sets of estimated n_f values. V is then adjusted (and consequently the set of b-values) until the standard deviation over a set of n_f-values is reasonably small (typically 10^{-4} for guides supporting several modes). The

value for the asymmetry parameter $\bar{a}$ given by equation 3.4 is also refined at the same time. Having obtained an estimate of n_f and its corresponding value of V, the waveguide depth, f, then follows immediately from equation 3.3.

Proton-exchange waveguides may be characterised by their depth and guiding layer index, assuming that they have a step-index profile. The values of effective index of each waveguiding mode and the corresponding depth of the waveguide were plotted on to theoretical dispersion curves based on a step-index model but assuming the average film index. Figure 3.3(a) and (b) are plotted dispersion curves for dilute melt proton-exchanged waveguides on X-cut and Y-cut $LiNbO_3$ respectively. The experimental points agree closely with the superimposed 'theoretical' dispersion curves, supporting the step-index assumption.

It is possible to relate the proton-exchange process to a diffusion model[24]. To relate the exchange parameters to the estimated waveguide depth, the diffusion parameters must be calculated. Figures 3.4(a) and (b) show plots of diffusion depth versus exchange time for X-cut and Y-cut $LiNbO_3$ waveguides respectively. These figures show that the experimental points all lie on a straight line, indicating that the process is diffusion dominated. The gradient of each line yields the diffusion coefficients, D(T) ($\mu m^2/h$) at each exchange temperature, T.

For a diffusion limited process, the depth is given by the relationship[28]:-

$$d = 2(tD(T))^{1/2}\ \mu m \qquad ....3.5$$

where t is the exchange time in hours.

In equation (3.5) the dependence of D on temperature is given by the Arrhenius Law[28]

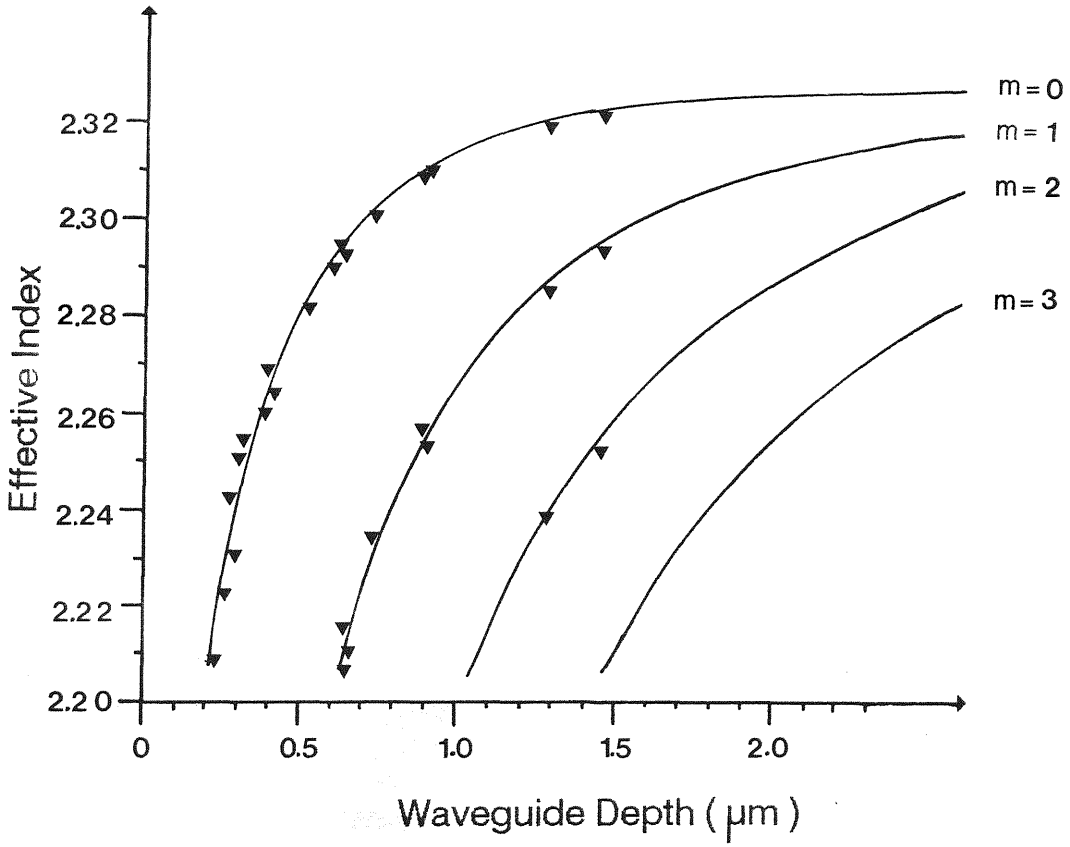

Figure 3.3 (a) Experimental points on theoretical dispersion curves for a step – index waveguide at a wavelength of 0.6328μm. Taken from X – cut dilute melt $LiNbO_3$ proton – exchanged waveguides.

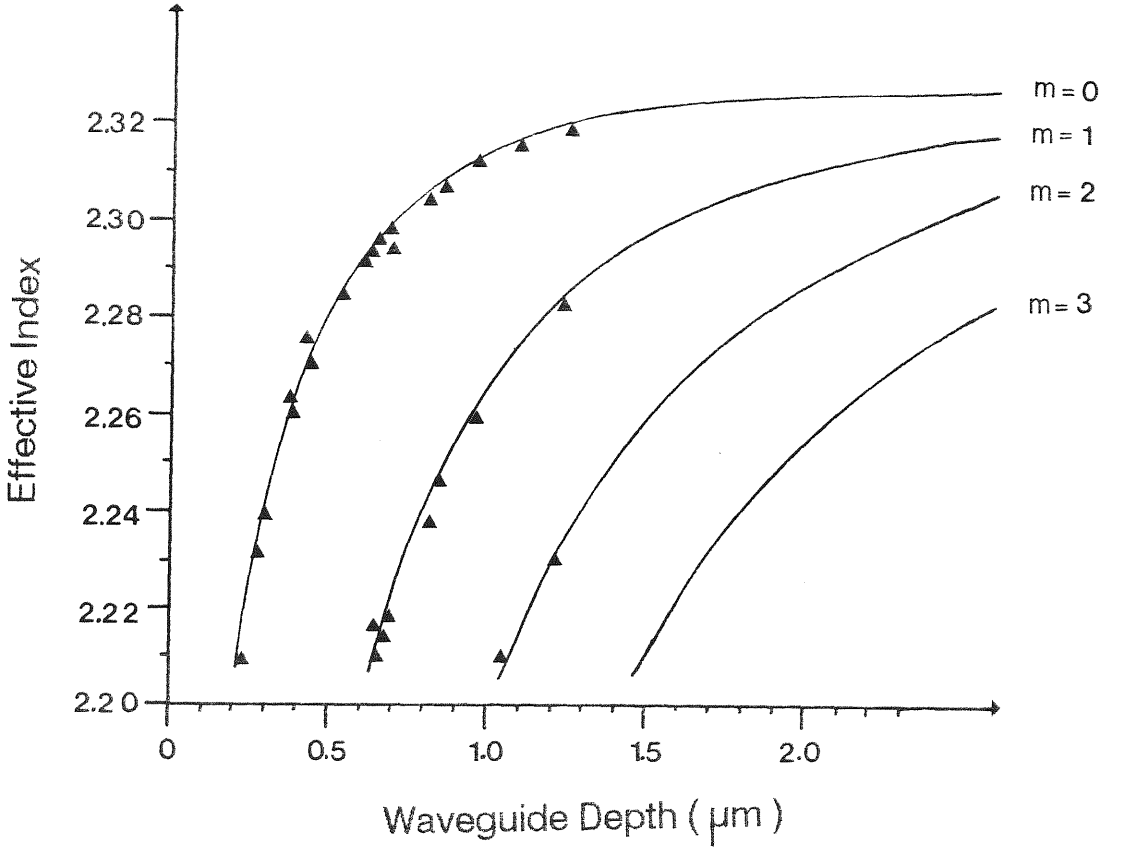

Figure 3.3 (b) Experimental points on theoretical dispersion curves for a step – index waveguide at a wavelength of 0.6328μm. Taken from Y – cut dilute melt $LiNbO_3$ proton – exchanged waveguides.

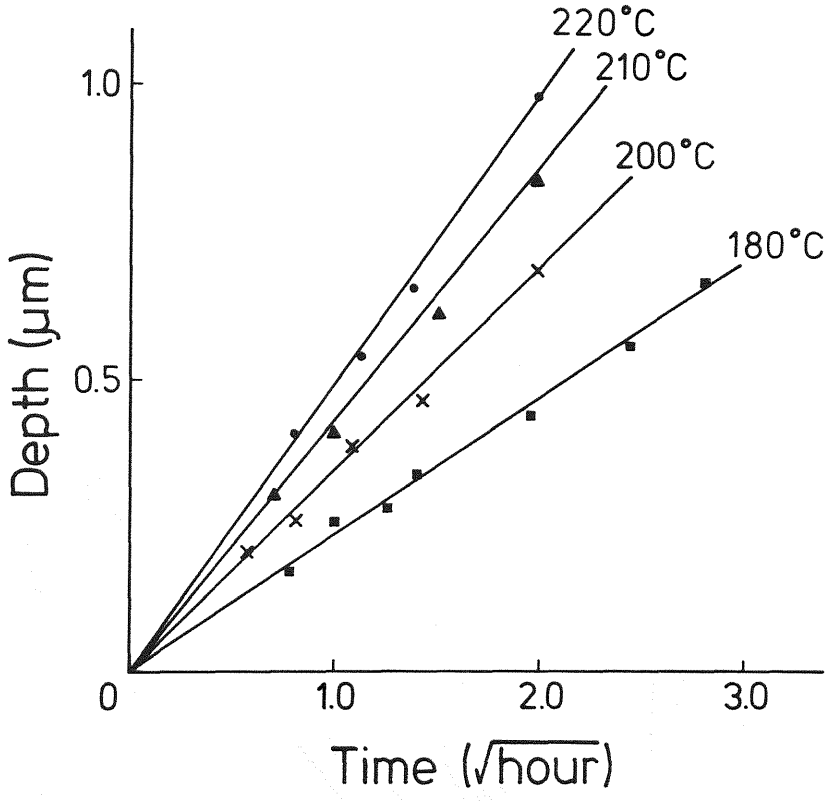

Figure 3.4(a) Dependance of waveguide depth on $(\text{time})^{1/2}$ for X – cut $LiNbO_3$ for 0.5% dilute melt proton – exchange at various temperatures.

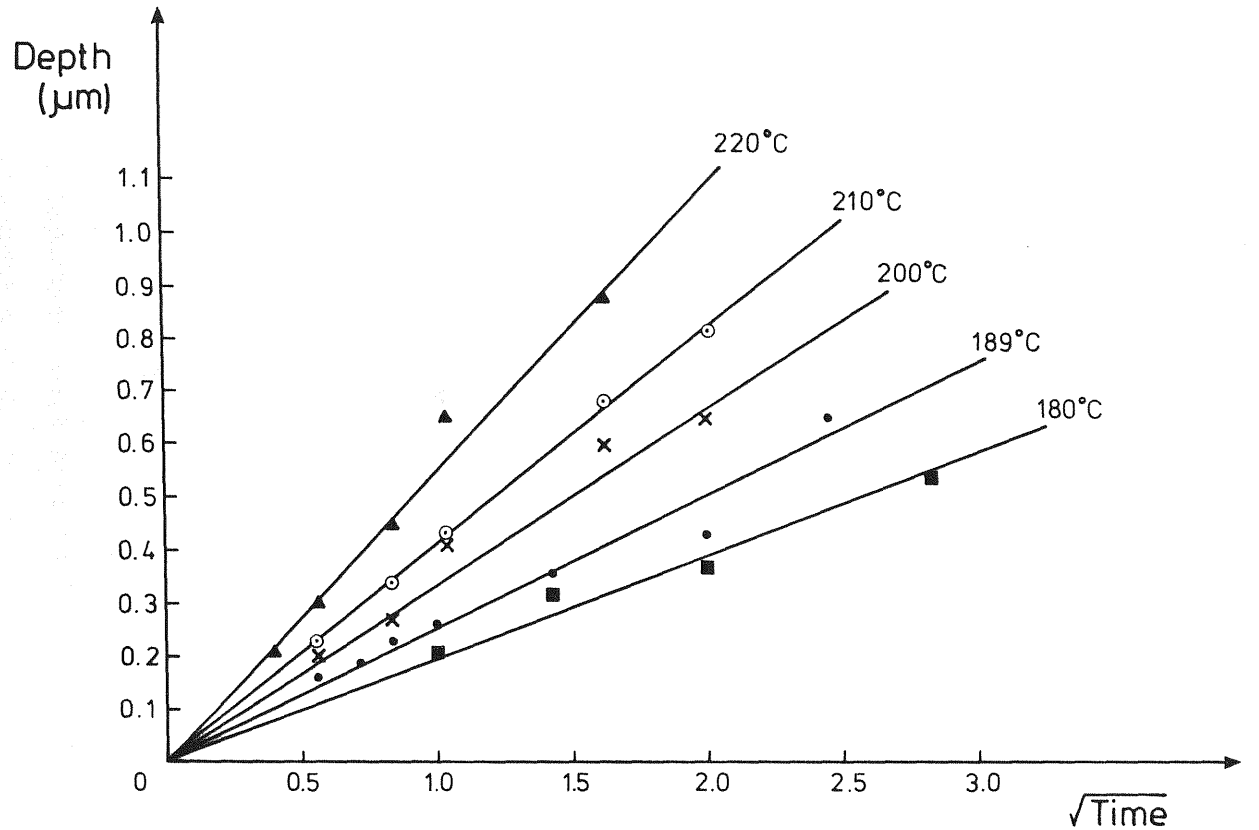

Figure 3.4(b) Dependance of waveguide depth on $(\text{time})^{1/2}$ for Y – cut $LiNbO_3$ for 0.5% dilute melt proton – exchange at various temperatures.

$$D(T) = D_o \exp(-Q/RT) \qquad \ldots.3.6$$

where D_o is the diffusion constant for the dilute melt proton-exchange process for the given crystal orientation, R the universal gas constant, T the absolute temperature and Q is an activation energy for the process.

If the dilute melt proton-exchange process is diffusion dominated (of the form of equation (3.6)), then, plotting the natural logarithm of the diffusion coefficients against the inverse of the exchange temperature, should give straight-line plots.

Figure 3.5 illustrates the relationship between 1/T and lnD(T) and, from these plots Q_x, Q_y, D_{ox} and D_{oy} (the activation energy and diffusion constant for the respective crystal cuts) for 0.5% dilute melt proton-exchange waveguides have been obtained.

For X-cut lithium niobate: 1 Q_x = 73KJ/mole (29)
$D_{ox} = 2.8 \times 10^6$ μm^2/hour.

For Y-cut lithium niobate: 2 Q_y = 93.3 KJ/mole
$D_{oy} = 5.47 \times 10^8$ μm^2/hour.

As shown in Figure 3.5, the diffusion of protons into Y-cut $LiNbO_3$ happens at a faster rate than into X-cut. In both cases, the diffusion rate is considerably reduced compared with that for pure melt proton-exchange.

An important point here is the sensitivity of equation (3.6) to slight changes in exchange temperature and/or time. Experience has shown that very slight changes in temperature or time can result in very large changes in estimated values of Q and D_o. To obtain accurate values of Q and D_o the experiment would have to be performed over a very large temperature range (e.g., >100°C) and for a large number of samples. However, these values are not so crucial when one comes to calculate the final fabrication

conditions for a given waveguide. Instead of quoting values of Q and D_o a full version of equation (3.2) is given.

For dilute melt proton-exchange in X-cut $LiNbO_3$ the relationship is

$$d = 3.3467\ 10^3 (t)^{1/2} \exp(-4.39\ 10^3/T)\ \mu m \quad [29] \quad \ldots.3.7$$

and for Y-cut $LiNbO_3$

$$d = 4.678\ 10^4 (t)^{1/2} \exp(-5.611\ 10^3/T)\ \mu m \quad \ldots.3.8$$

The information given in this section is sufficient to allow dilute melt proton-exchange waveguides to be fabricated on X and Y-cut $LiNbO_3$ with reasonable precision. Given the device design and desired optical depth the appropriate fabrication conditions can be chosen.

3.3.3. Lithium Tantalate Waveguides

The first optical waveguides fabricated by proton-exchange on lithium tantalate substrates were reported by Spillman et al.[30] in 1983. 10μm wide channel waveguides were produced by 3 hours exchange in a pure benzoic acid melt at 249°C, followed by an annealing process of 18 hours at 250°C and 17 hours at 325°C. Recently, a thorough examination of the process was carried out on planar X-cut substrates, using a somewhat similar procedure to the above but with greatly reduced fabrication times[31]. Single-mode planar waveguides (at λ_o = 0.6328μm) were formed by proton-exchange in a pure melt at 210°C, for a range of times from one hour to four hours, followed by annealing at 325°C for one hour. Further annealing, for an aggregate of two hours, produced a single-mode waveguide for the one hour exchange sample but two-mode waveguides for two hours and more. Fabrication conditions and

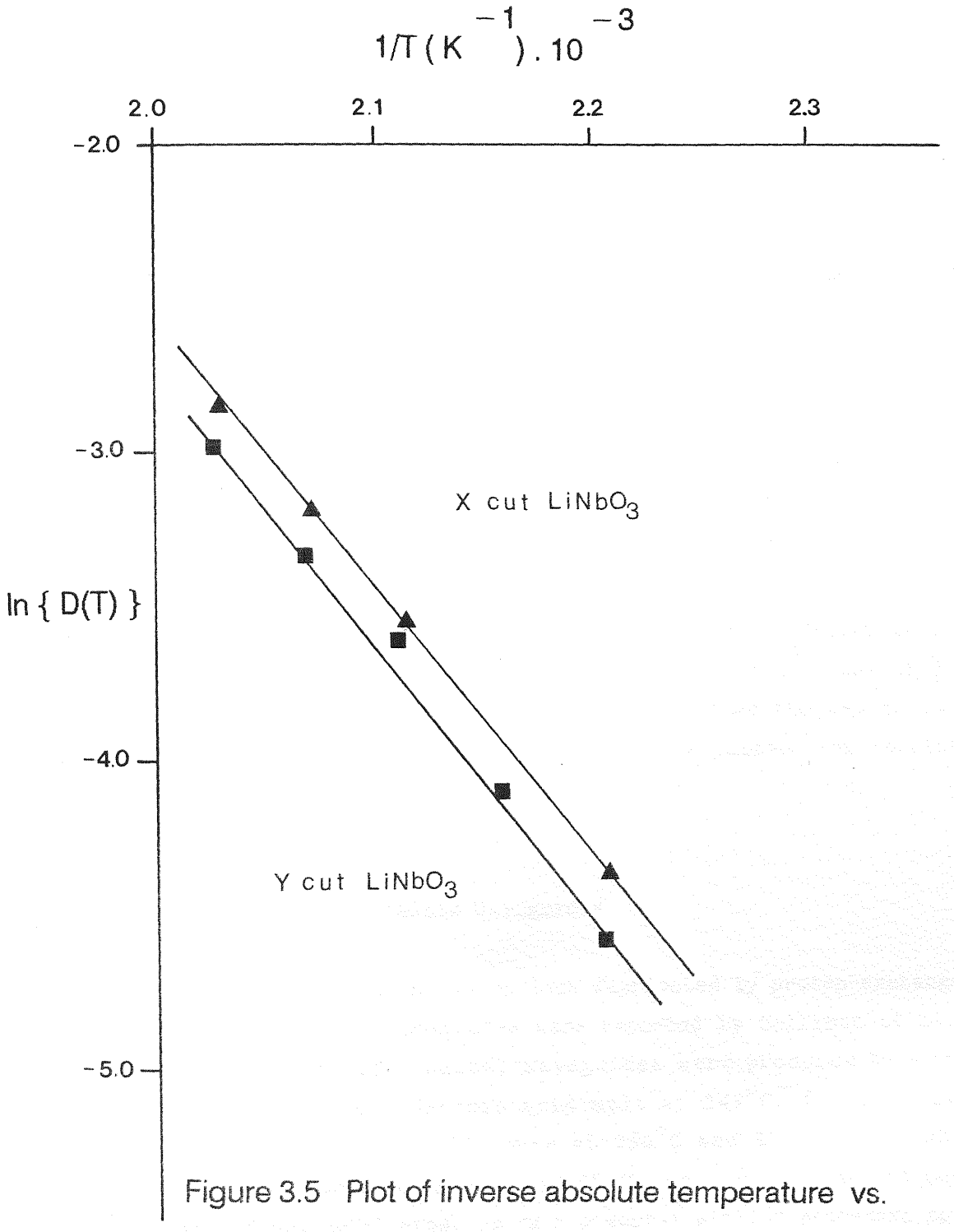

Figure 3.5 Plot of inverse absolute temperature vs. the natural log of the diffusion coefficient for X – and Y – cut 0.5% dilute melt proton – exchanged waveguides. (see text)

the modal effective refractive index (n_{eff}) results for this series of waveguides are summarised in Table 3.1.

Table 3.1 X-cut planar waveguides on $LiTaO_3$ at 210°C and λ_o = 0.6328μm

Time	Anneal Conds	n_{eff}	Anneal Conds	n_{eff}
1 hr.	325°C/1 hr.	2.1905	325°C/2 hr.	2.1900
2 hr.	325°C/1 hr.	2.1951	325°C/2 hr.	2.1944,2.1875
3 hr.	325°C/1 hr.	2.1978	325°C/2 hr.	2.1970,2.1878
4 hr.	325°C/1 hr.	2.1987	325°C/2 hr.	2.1994,2.1873

The largest n_{eff} obtained on $LiTaO_3$ was +0.0174 (n_o = 2.182 at λ_o = 0.6328μm) for polarisation along the extraordinary axis. For the range of X-cut samples given in Table 3.1, single-mode waveguiding was also observed at λ_o = 1.15μm and these results are given in Table 3.2.

Table 3.2 X-Cut planar waveguides on $LiTaO_3$ at λ_o = 1.15μm with n_o = 2.1360.

Fabrication conditions	n_{eff}
1 hr./210°C + anneal 2hr./325°C	2.1428
2 hr./210°C + anneal 2hr./325°C	2.1458
3 hr./210°C + anneal 2hr./325°C	2.1461
4 hr./210°C + anneal 2hr./325°C	2.1465

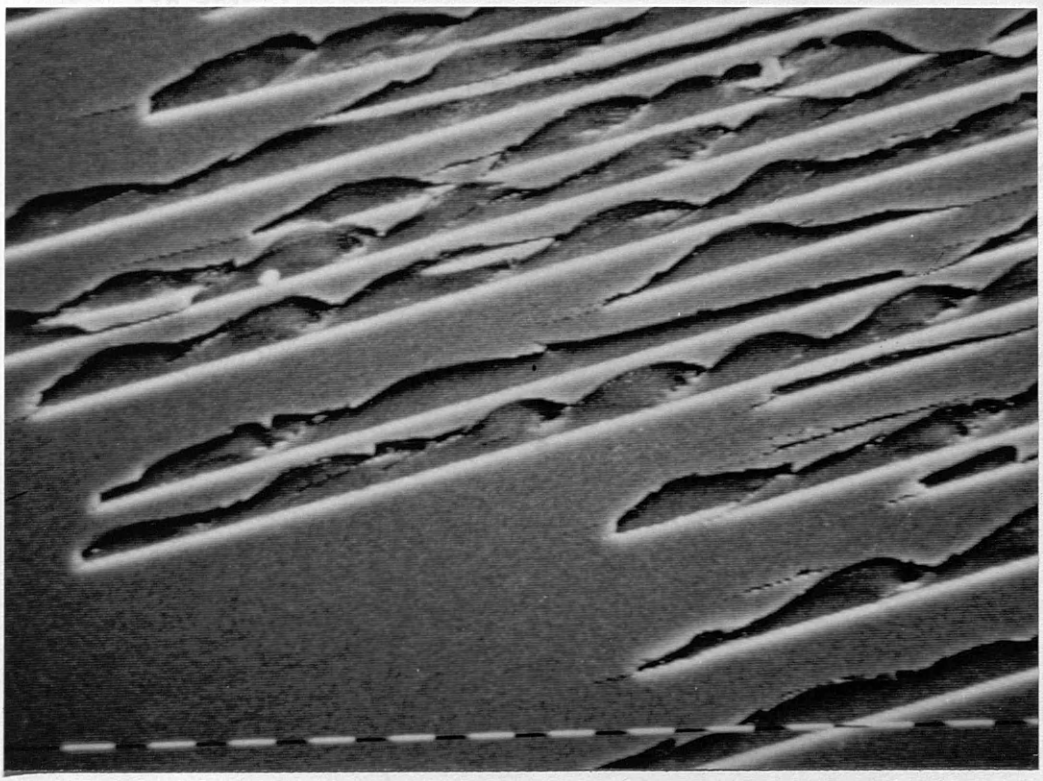

Figure 3.6 Scanning Electron Microscope image of surface damage on Y-cut $LiTaO_3$ proton-exchanged in pure melt for 3 minutes at 200°C. The damage is similar to that previously reported for Y-cut $LiNbO_3$. (Markers indicate 10μm steps).

It was found that waveguides could not be formed on Y-cut $LiTaO_3$, since severe surface damage occurred during the first few minutes of exchange, even at a low temperature (e.g., 200°C). Figure 3.6 indicates the resultant surface damage on Y-cut $LiTaO_3$ substrates. The damage is similar to that experienced with Y-cut $LiNbO_3$[10,32].

It was also found that use of dilute melts allowed waveguide formation without annealing and without subsequent damage to the crystal. Single mode guiding was observed in an X-cut sample produced at 230°C for six hours. Small amounts of annealing at 325°C of up to 20 minutes gave a systematic trend so that single-mode guiding could be observed in an X-cut sample exchanged for only two hours, but annealed for 20 minutes. A summary of these results is given in Table 3.3.

Table 3.3 X-cut planar $LiTaO_3$ waveguides from dilute melt proton-exchange at λ_o = 0.6328μm.

	Annealing Conditions[2]			
Exchange Conds.[1]	0 mins.	5 mins.	10 mins.	20 mins.
2hr./230°C	-	-	-	2.1928
4hr./230°C	-	2.1879	2.1892	2.1924
6hr./230°C	2.1879	2.1894	2.1902	2.1912
8hr./230°C	2.1881	2.1898	2.1910	2.1888

[1] For melt dilution of 0.5%

[2] Annealing at 325°C in wet O_2 with a flow rate of 1/2 l/min.

Computational characterisation similar to that described in

section 3.3.2 could not be carried out due to the small modal content and index change, although RBS results, presented in the following section, appear to indicate that the exchange process on $LiTaO_3$ is similar to that with $LiNbO_3$. In particular, $LiTaO_3$ samples show a change in the back-scattering yield which, for $LiNbO_3$ waveguides, is normally regarded as indicative of a step-change in the index profile. There is not, however, enough evidence to say whether $LiTaO_3$ waveguides exhibit a similar step-index profile.

3.4. Material Analysis

Rutherford Back-Scattering Spectrometry (RBS) has been used as the primary microanalytical non-destructive tool to study waveguides fabricated in dilute melts[19]. RBS can detect the presence of a distorted region by the associated increased alpha-particle back scattering yield in comparison with the yield for the underlying virgin crystal substrate, in the aligned (i.e. enhanced channeling) condition. Results have shown close agreement between optical waveguide measurements and RBS data[19]. In particular, in $LiNbO_3$ the waveguides have been shown to have nearly a step-index profile to the same depth as obtained by calculation from the energy at which there is a step change in the back-scattering yield. For $LiNbO_3$, this depth increases as a $t^{1/2}$ function of the exchange time, so that a temperature dependent diffusion coefficient can be assigned to the process and, furthermore, this coefficient can be fitted to an Arrhenius Law, (as discussed in section 3.3.2).

RBS data obtained for proton-exchange in $LiNbO_3$ from various dilution percentages of lithium benzoate in benzoic acid are shown in Figure 3.7. In all cases, exchange was carried out at 220° for 2 hours. The reduction in lattice disorder produced in all the dilute melt samples, up to 2.0% lithium benzoate, in comparison with the concentrated melt sample is apparent. Figure 3.8 shows estimates of the depth of the proton-exchange region obtained both from RBS data and from (in most cases) multimode optical waveguide measurements at $\lambda_o = 0.6328\mu m$, using both inverse WKB model[21] and dispersion curve calculations for step-index waveguides[27],

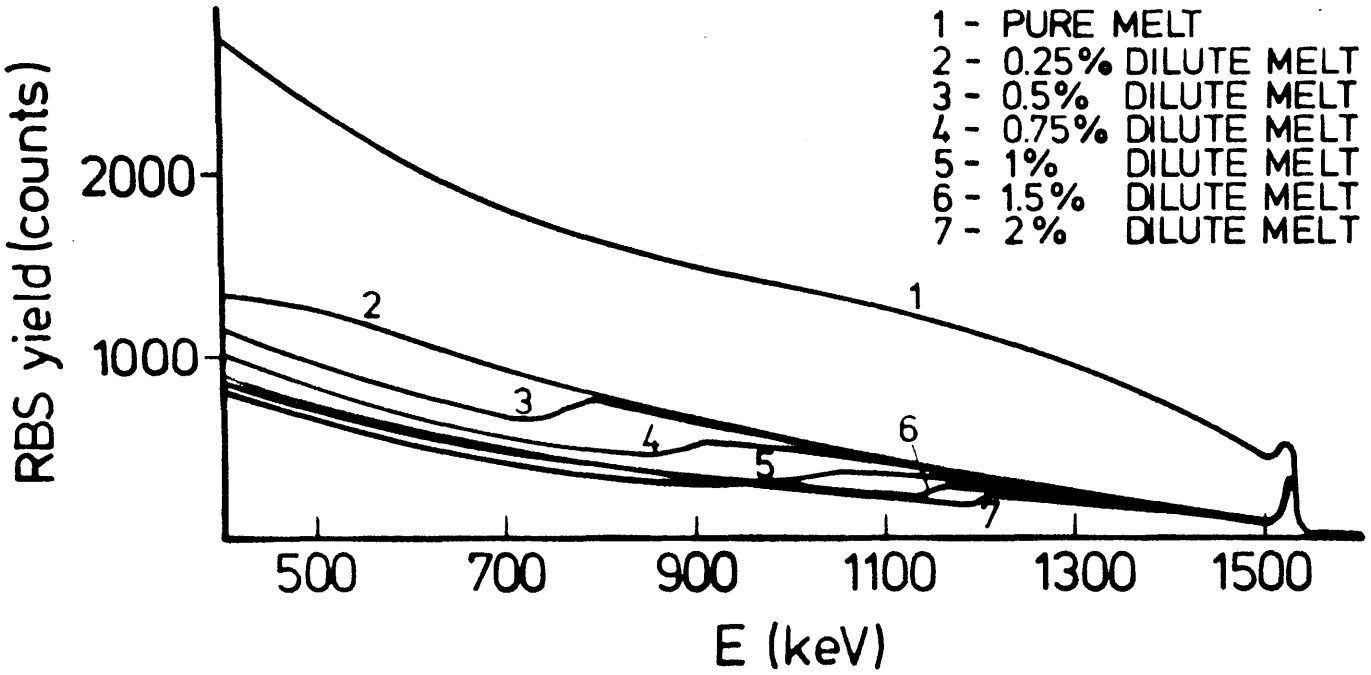

Figure 3.7 RBS data for dilute melt proton – exchange on X – cut $LiNbO_3$ with melt temperature of 220 ^{o}C for 2 hours.

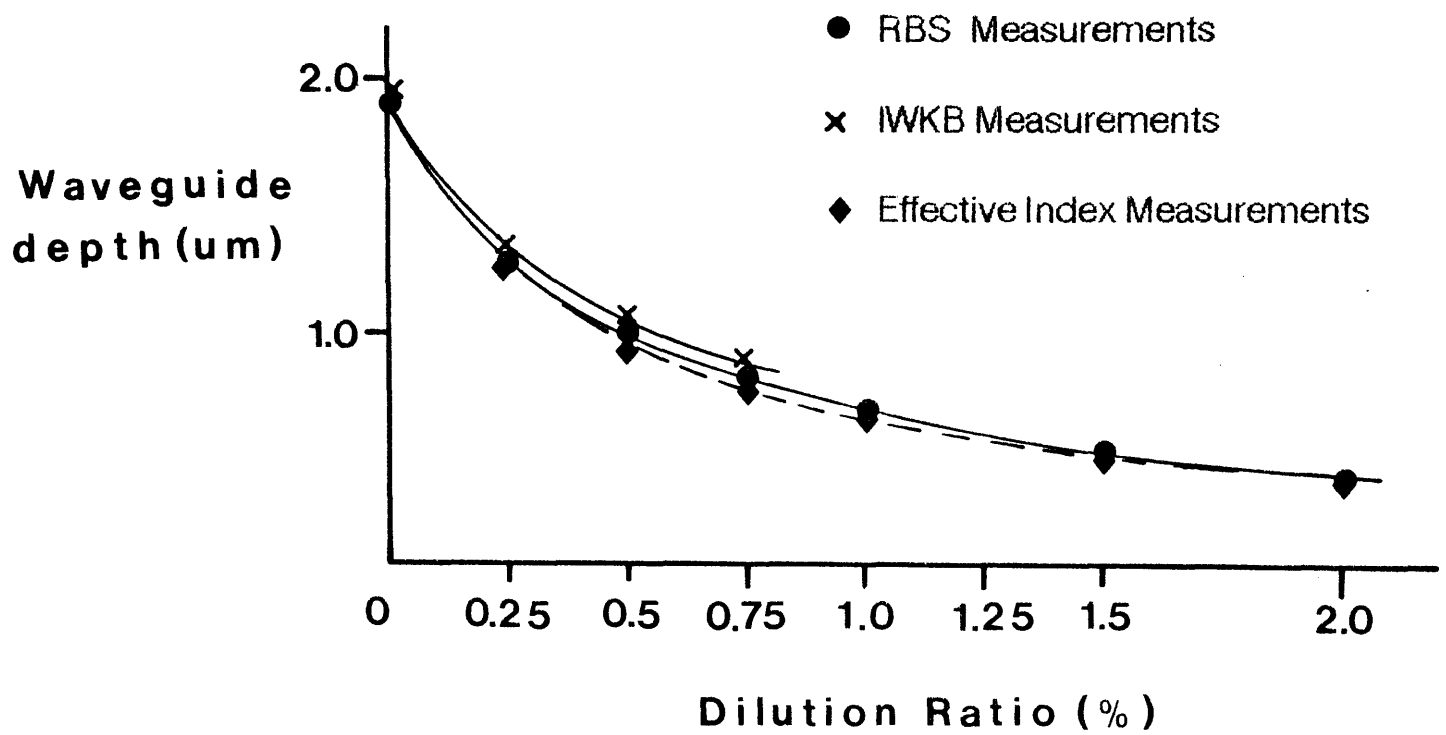

Figure 3.8 Estimated waveguide depth verses acid melt dilution in X – cut $LiNbO_3$ Exchange conditions: 2 hours, 220°C

as a function of melt dilution. The agreement is very good, giving support for a simple step-index model as an approximate profile for the refractive index.

Figure 3.9 shows typical RBS data obtained on X-cut $LiNbO_3$. It can be seen that, in comparison with the waveguides produced from a dilute benzoic acid melt, the pure melt waveguide produced a far greater back-scattering yield, indicating greater structural disorder. The maximum index change, Δn, is similar for pure and dilute melts and therefore Figure 3.9 indicates that the height of the RBS curve cannot be directly related to the index change. However, the position of the step change in height is, in all cases, an indication of both the existence of the exchanged region and its depth. Figure 3.10 gives similar results for Y-cut $LiNbO_3$ waveguides. In comparison with the X-cut data, the back-scattering yield is slightly larger for Y-cut $LiNbO_3$, possibly indicating a slightly greater lattice disorder, yet still far below that measured for the sample produced in a pure benzoic acid melt. These results clearly indicate that, in comparison with pure melt proton-exchange, waveguides produced from dilute melts are of a far better quality and suffer less from lattice disorder.

The narrow peak observed in all RBS data very close to the surface (and typically ~100Å wide) is present for all samples, including a virgin substrate. The reason for this peak is not known. However, it may be due either to a small amount of surface damage caused by mechano-chemical polishing of the substrates or to chemical reactions occurring at the sample surface during the exchange process[19].

Available RBS data for $LiTaO_3$ is somewhat limited but from that which does exist some general comments about the quality of the waveguides in comparison with $LiNbO_3$ can be made. Figure 3.11 shows RBS data obtained from $LiTaO_3$ samples exchanged in pure melt and subsequently annealed. In both cases, annealing was required to produce an optical waveguide, since prolonged exchange (>4 hours) led to surface damage. The region of lattice distortion produced by proton-exchange is clearly visible, though the limited data which exists indicates that the depth of the distorted region

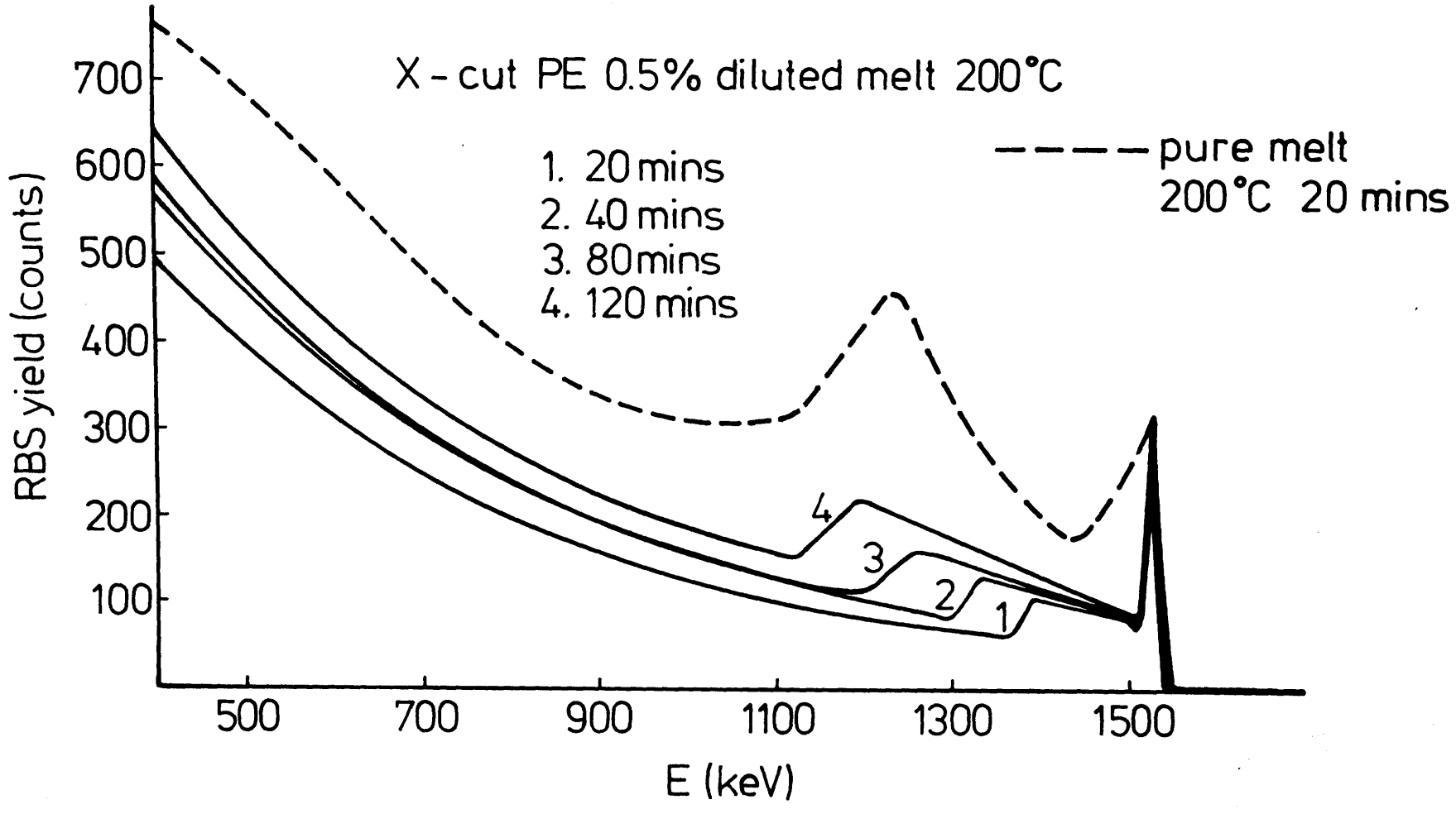

Figure 3.9 RBS Data for proton – exchange on X – cut $LiNbO_3$

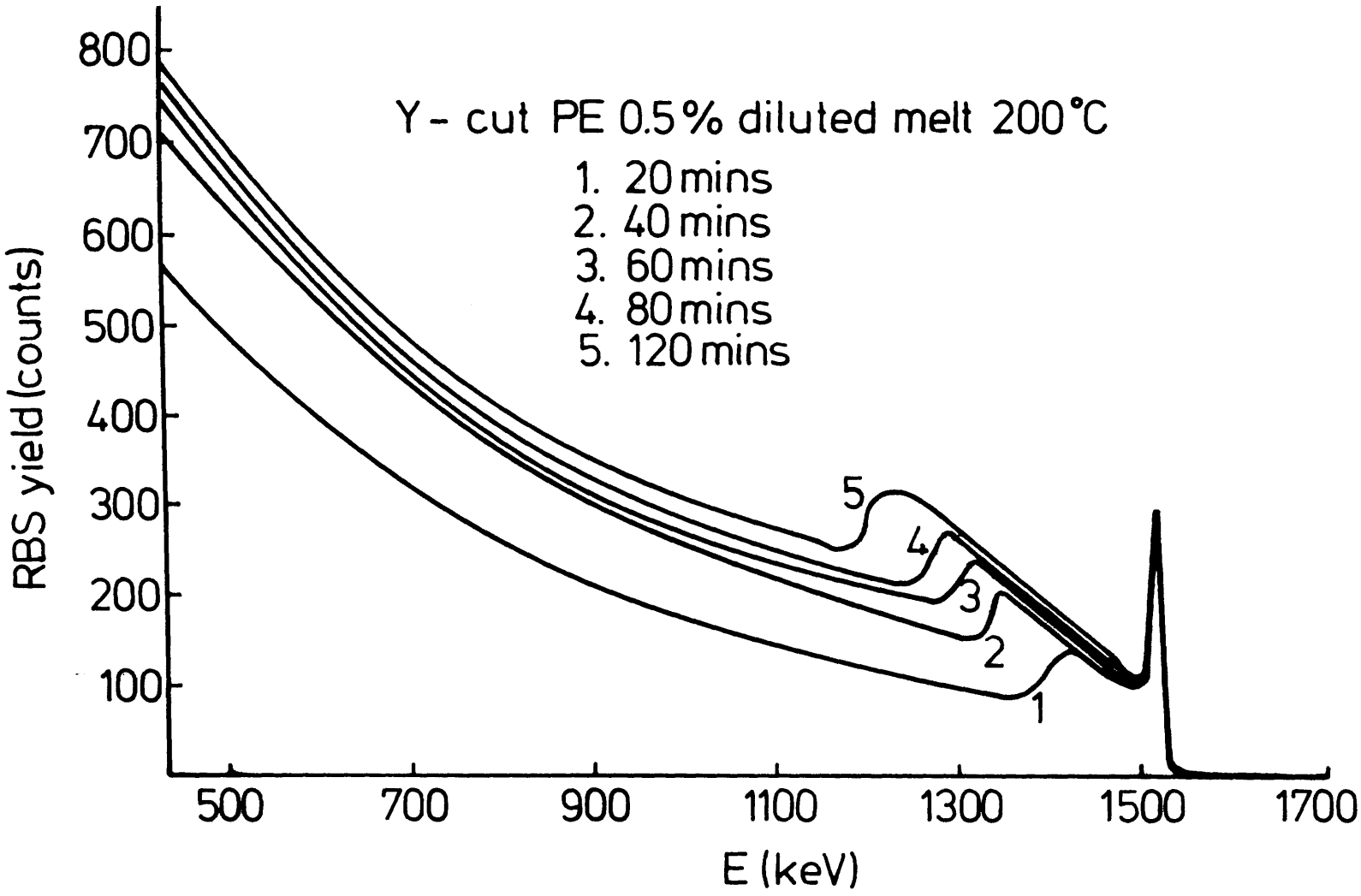

Figure 3.10 RBS Data for proton – exchange on Y – cut $LiNbO_3$

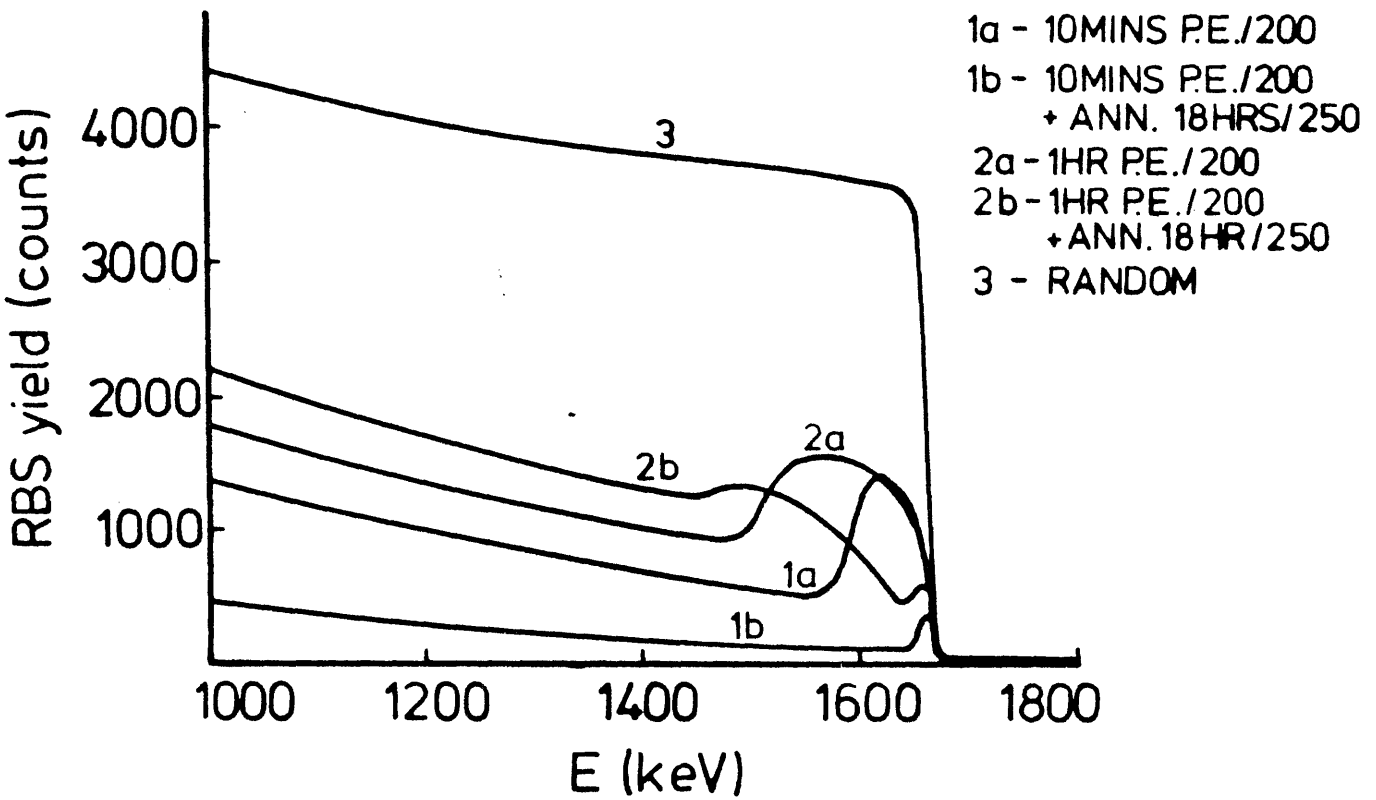

Figure 3.11 RBS data for pure melt proton – exchange on X – cut $LiTaO_3$

(and possibly the waveguide depth) does not follow the $(t)^{1/2}$ time dependence law established for proton-exchange in $LiNbO_3$. Results for samples 2a and 2b show an increase in the depth of the lattice distortion region with annealing, but a reduction in the level of distortion. However, results for samples 1a and 1b show that lattice distortion becomes undetectable after annealing when a much shallower initial exchange region has been produced.

Similar results obtained from dilute melt samples are shown in Figures 3.12 and 3.13. In Figure 3.12 the effect of annealing is to make the lattice distortion undetectable (see samples 1a and 1b in Figure 3.11) while Figure 3.13 again implies that the $(t)^{1/2}$ time dependence law could no longer be valid. Although this investigation is by no means thorough, initial results seem to suggest that qualitatively $LiTaO_3$ behaves like $LiNbO_3$ but with lower activation energies both for the H diffusion and the defect annealing process. Optical waveguide measurements indicated that the magnitude of the refractive-index change produced by proton-exchange in $LiTaO_3$ was considerably smaller than that in $LiNbO_3$. It is possible that $LiTaO_3$ is less affected than $LiNbO_3$ by lithium depletion during exchange and that this could be why there is a relatively small index change. It has been shown previously, for Li_2O out-diffused waveguides[33], that the effective index of $LiNbO_3$ was more affected by stoichiometric changes than $LiTaO_3$. In addition, the diffusion constants and activation energies for $LiTaO_3$ out-diffused waveguides were far less than those of $LiNbO_3$. It is, therefore, possible that this same effect occurs with proton-exchanged waveguides. However, detailed optical experiments and materials investigations are required before this process is fully understood. As with $LiNbO_3$, the use of dilute melts helps to produce a better quality waveguide, in terms of lattice distortion, than with pure melt and waveguides can even be produced directly from the exchange melt without post annealing.

Initial OH absorption measurements on proton-exchange $LiTaO_3$ waveguides[30] indicated that they showed a higher absorption peak than $LiNbO_3$, implying that in theory the waveguide index change should be higher in $LiTaO_3$. Initial experiments did not support this argument, returning either a smaller Δn or a damaged crystal.

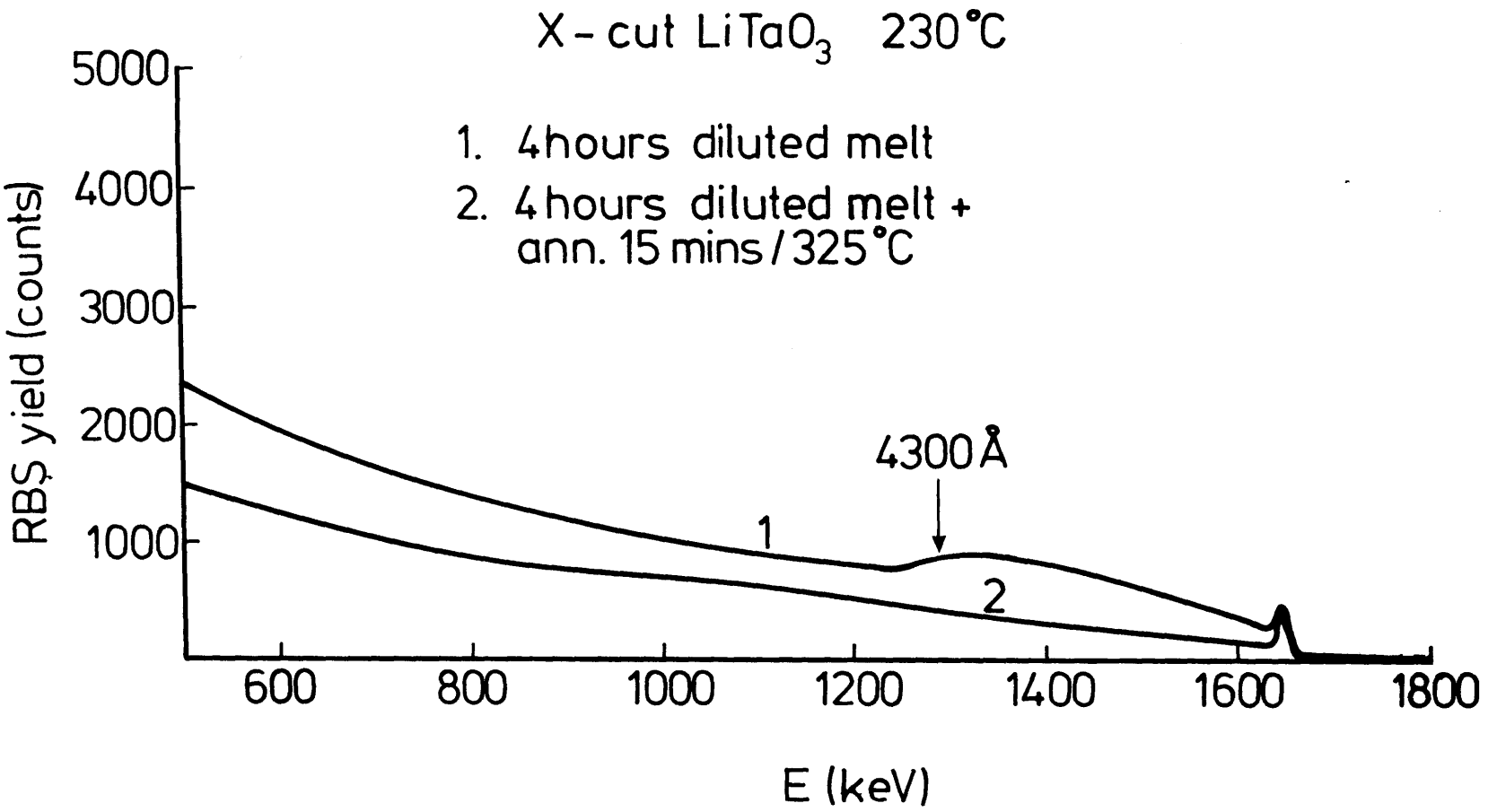

Figure 3.12 RBS Data for dilute melt proton – exchange on X – cut $LiTaO_3$ before (1) and after (2) annealing

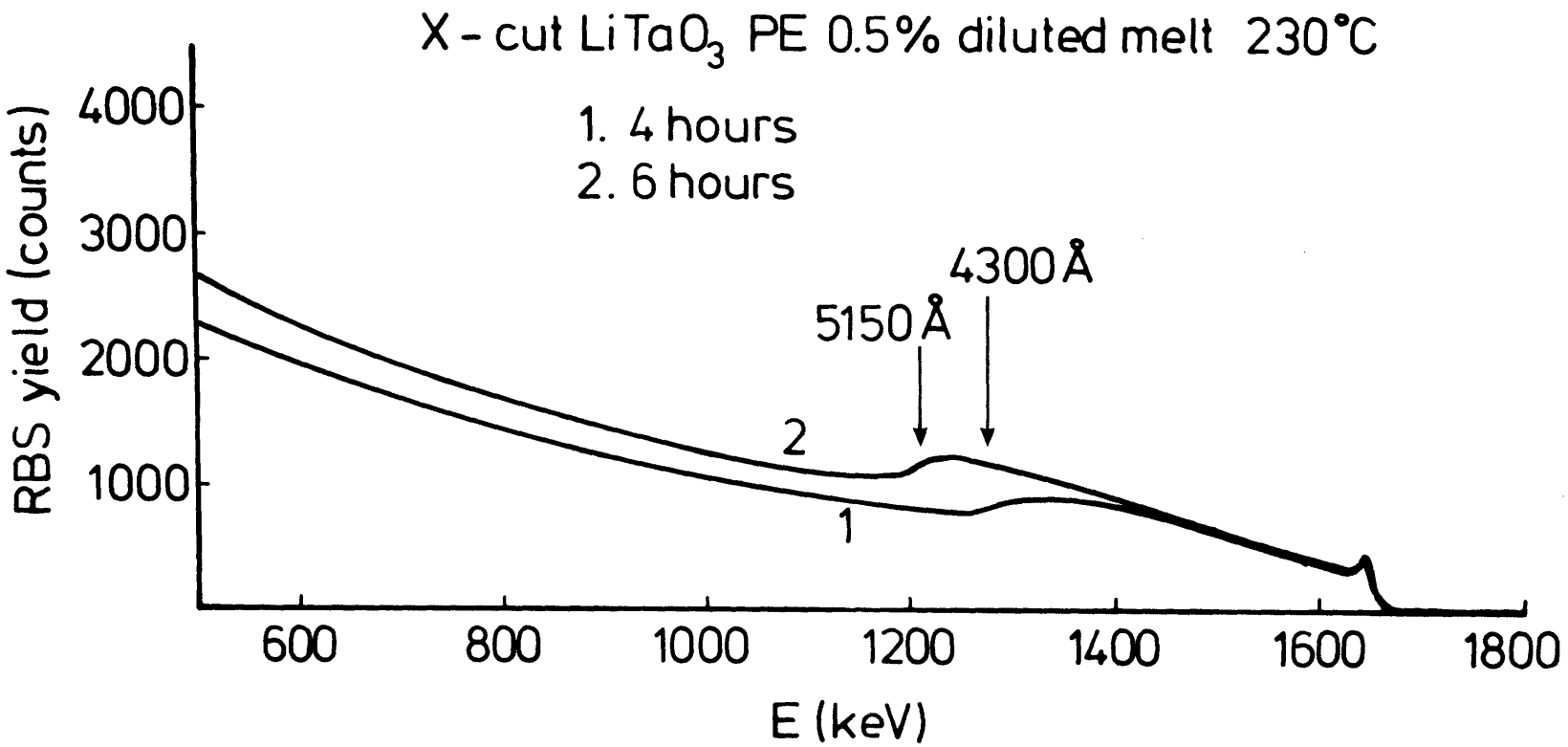

Figure 3.13 RBS data for dilute melt proton – exchange on X – cut $LiTaO_3$

Infrared transmission absorption spectra have been obtained previously on proton-exchanged $LiNbO_3$ waveguides to determine the effect of the exchange process upon the OH absorption spectra[19]. The results found a correlation between the increased OH absorption and the exchange depth. They also indicated the possibility of interstitial Hydrogen atoms within the host lattice. A repeat of this analysis for $LiTaO_3$, coupled with lithium depletion level profiles, is required before a full understanding of the exchange process and the refractive index, can be obtained.

3.5. In-plane Scattering Measurements

Rutile prism coupler observations of in-plane scattering[34] were carried out with a scanning photodetector on X-cut, dilute melt, proton-exchanged $LiNbO_3$ and $LiTaO_3$ waveguides. In-plane scattering measurements were based on the assumption that the amount of light scattered laterally in a planar optical waveguide is a measure of the quality of the waveguide. This measurement is extremely important for planar acousto-optic devices such as the IOSA, where severe in-plane scattering could limit the dynamic range of the device.

The scattered light, as well as the unscattered light, can be made available for measurement by output prism coupling. The output coupled light is commonly known as a mode- or m-line. Figure 3.14(a) shows m-lines for a multimoded X-cut $LiNbO_3$ waveguide fabricated for 4 hours in a 0.5% dilute melt at 235°C followed by 5 minutes annealing at 400°C. Figure 3.14(b) shows an m-line for an X-cut $LiTaO_3$ waveguide fabricated for 4 hours in a 0.5% dilute melt at 230°C, followed by 10 minutes annealing at 325°C. In contrast to pure melt proton-exchange waveguides, the greater amount of power in the central spot in comparison with that of the scattered-line is evident. Waveguide 'm-lines' were scanned with a photodiode and, at +/-1° in air (corresponding to approximately 1/2° in the waveguide) waveguides in X-cut $LiNbO_3$ gave in-plane scattering levels typically around -25dB while in X-cut $LiTaO_3$ values were -30dB. In general, with $LiTaO_3$, the lowest

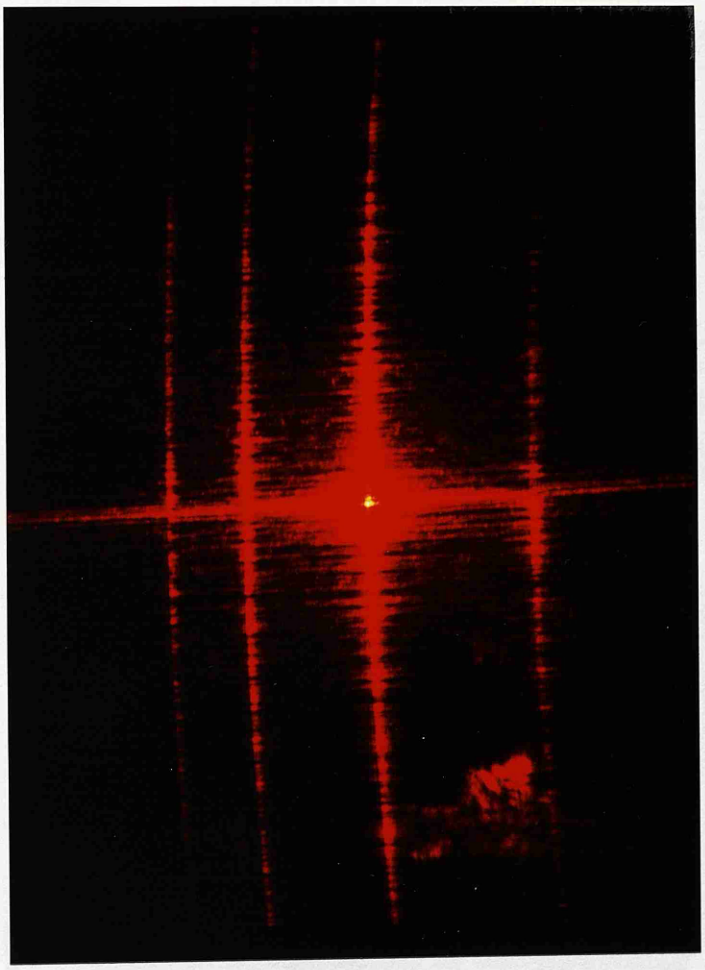

Figure 3.14 (a) Output coupled m-line for a multi-mode X-cut $LiNbO_3$ waveguide exchanged for 4 hours in 0.5% dilute melt at 325°C followed by 5 minutes annealing at 400°C in wet flowing O_2.

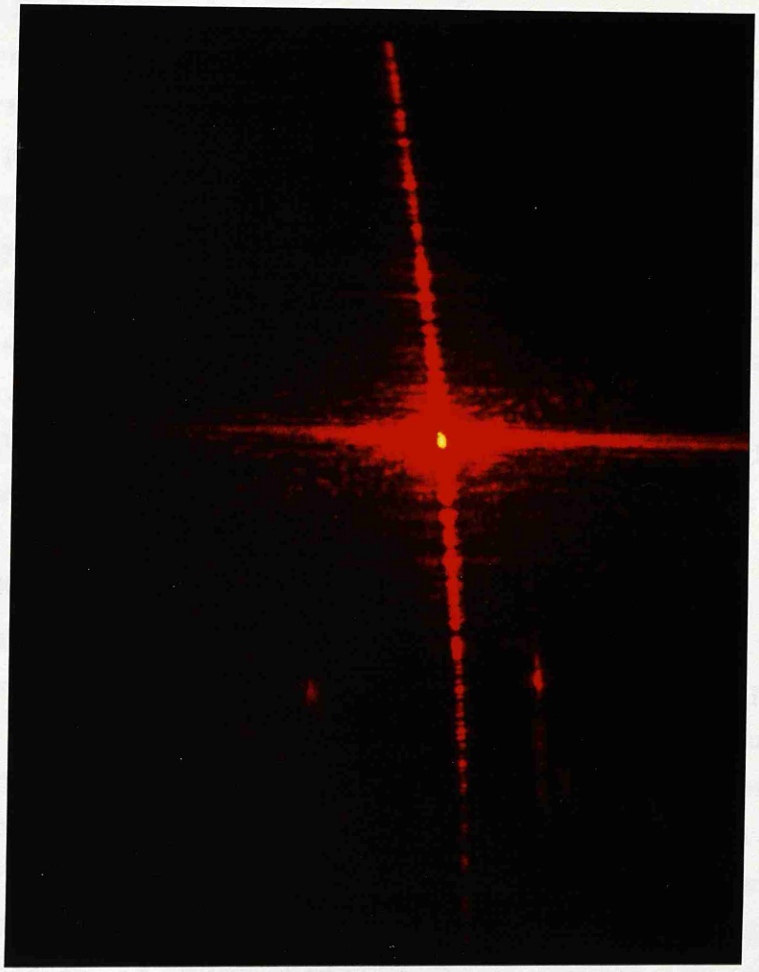

Figure 3.14 (b) Output coupled m-line for an X-cut $LiTaO_3$ waveguide exchanged for 4 hours in 0.5% dilute melt a 230°C followed by 10 minutes annealing at 325°C in wet flowing O_2.

in-plane scattering levels resulted from the shortest exchange time.

Wong et al.[35] have reported in-plane scattering levels below -40dB for the same angle of $1/2^{o}$ in multimode guides formed by 5 hours exchange at 239°C in a 1% diluted melt. Comparison of the two results is not really possible due to differences in the exchange process and measurement technique. In particular, the measurement system employed by Wong et al. had a detection capability of -50dB while the capability of the system used in the present discussion was -30dB. Beyond this value, the results were unreliable. However, in comparison with 0.5% dilute waveguides on $LiNbO_3$, waveguides produced in 1% dilute melts exhibited much less in-plane scattering and were similar to the very high quality waveguides produced on X-cut $LiTaO_3$ from 0.5% dilute melts.

De Micheli et al.[18] have performed RBS and in-plane scattering measurements on highly multi-mode pure melt $LiNbO_3$ waveguides fabricated in a vacuum-sealed ampoule at temperatures above the boiling temperature of the acid. The RBS spectrum for an exchange temperature of 300°C was the same as that of virgin $LiNbO_3$ indicating no lattice distortion. In addition, a correlation was found between increased exchange temperature and reduced in-plane scattering. In general, the authors conclude that proton-exchange in pure benzoic acid melts, at elevated temperatures, results in low loss optical waveguides while the addition of lithium benzoate was still required to produce stable waveguides. However, further investigation is still required to test the reproducibility and accuracy of this method.

With the levels of lattice distortion in waveguides made by dilute melt proton-exchange being much lower than those for pure melt proton-exchange waveguides[29,31], it was expected that the in-plane scattering measurements would be improved on dilute melt waveguides since there is a direct relationship between lattice distortion and in-plane scattering[29,22]. A systematic comparison of the optical and propagation losses between pure and dilute melt proton-exchange waveguides has not yet been carried out. However, the in-plane scattering results obtained so far are very

promising, with levels measured being comparable with Ti-indiffused $LiNbO_3$ waveguides.

3.6. Dilute Melt Proton-exchanged Waveguides on Y-cut $LiNbO_3$

One of the major drawbacks of proton-exchange waveguide fabrication in pure melts is that, after a very short time, Y-cut substrates invariably suffer surface damage and the guiding properties are consequently severely degraded[10]. In fact it has been shown that this damage is present in any proton-exchanged waveguide on Y-cut $LiNbO_3$ with an exchange depth of 0.2μm or more and that the damage originates mainly from the large strain induced in the exchange layer by the $Li^+ \rightleftharpoons H^+$ process[19]. This damage can be avoided by Ti-indiffusion[36] or by slowing down the H^+ diffusion process at higher proton-exchange temperatures[37]. The rate of diffusion can be reduced by increasing the Li-concentration in the source. Both methods in fact reduce the lattice strain in the waveguide region.

Bringing the diffusion process under control while still retaining the major advantages of proton-exchange can be effected by using dilute melt proton-exchange. Diluting the pure benzoic acid melt is usually performed by ensuring, in the melt, excess of Li ions which resist the out-diffusion of Li^+ from the wafer ($LiNbO_3$) and therefore slow down the H^+ diffusion process. Proton-exchange using dilute melts also ensures an improved structure in the waveguide region. Dilute melts have been used successfully to fabricate multimode optical waveguides on Y-cut substrates[37,29]. However, it has been observed, in experiments performed by the author, that these waveguides suffer from very abrupt attenuation of the propagating mode and severe scattering into mixed polarisations. This effect and the subsequent conclusions are outlined below.

When TE polarised light was prism coupled into waveguides fabricated by dilute melt proton-exchange on Y-cut $LiNbO_3$, the propagating light was observed to show an abrupt increase in scattering out of the waveguide at a distance from the input prism

(see Figure 3.15(a)). This distance was independent of prism position but dependent upon the effective index of the propagating mode, with the distance being greatest for the largest n_{eff}. When the scattered light was observed through a polariser, it was evident that it contained both TE and TM polarisations.

Further investigation included positioning of the input prism so that the scattering region coincided with a polished end of the waveguide. It was found that the light which scattered into the substrate was substantially TM polarised. In addition, it was noticed that a portion of the light behaved essentially like a substrate mode, moving along the edge of the waveguide as the input coupling angle was altered. This phenomenon occurred only close to the coupling angle of a TE mode and was present only when light was being guided. Further observations showed that when the waveguide was rotated about a normal to the substrate plane (i.e. light was no longer propagating along the X axis of the Y-cut substrates) the guided light split into two distinct beams. The splitting of the guided light into two distinct beams has been observed on the polished end of the waveguide substrate, on the output coupled m-line and directly from scattered light. Both beams were a mixture of TE and TM polarised light and there was an optimum position where the two beams joined together to propagate as one. In addition, positioning of an output prism beyond the enhanced scattering region indicated that no significant propagating light remained in the waveguide.

This phenomenon has also been observed by Chen and Chang[38] who have attempted to make a systematic study of the effect and detail its cause. They conclude that the effect is present only for modes with n_{eff} less than the ordinary index n_o of $LiNbO_3$ substrates (where $n_o = 2.286$ for $\lambda_o = 0.6328\mu m$). They define the distance between the front edge of the input prism and the scattering region as the 'walk-off' distance and have found that, for a given mode, $n_{eff} = n_o \sin\theta_s$ (where θ_s = arctangent of the ratio of the substrate thickness to the 'walk-off' distance). In addition, an abrupt attenuation of the propagating mode of ~25dB/cm was measured. The effect was related to the coupling angle and investigations of the polished end indicated that the

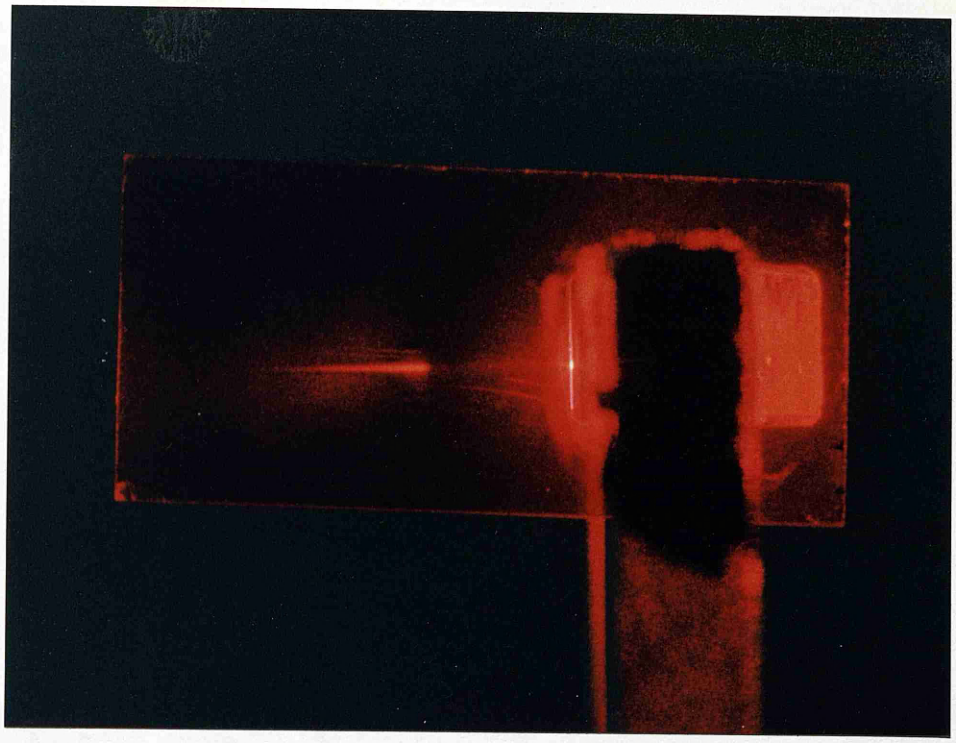

Figure 3.15 (a) Abrupt scattering of the guided wave in a waveguide fabricated by 0.5% dilute melt proton-exchange in Y-cut $LiNbO_3$

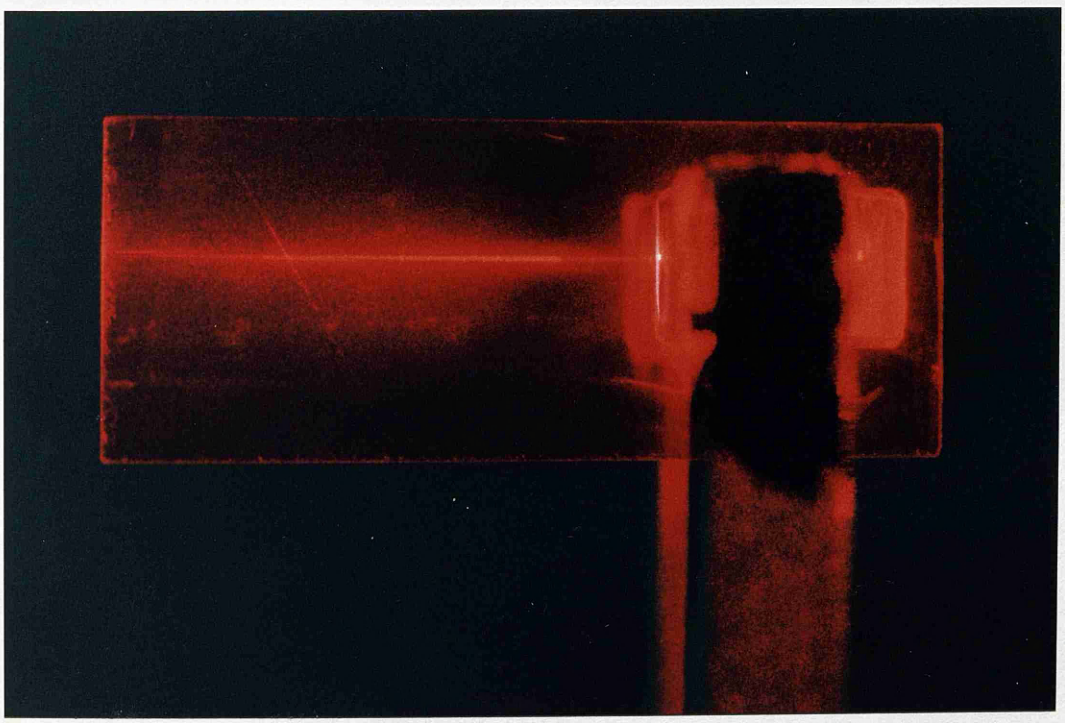

Figure 3.15 (b) Propagation of optical wave in a 0.5% dilute melt proton-exchange Y-cut $LiNbO_3$ waveguide which was annealed for 10 minutes at 400°C. In contrast with Figure 3.15 (a), no abrupt scattering was observed after annealing.

light guided at the surface was purely TE while that scattered into the substrate was purely TM. Chen and Chang[38] have interpreted this phenomenon as being 'random scattering of TE polarised radiation into TM polarised radiation'. They conclude that for $n_{eff} < n_o$, the TM radiation from the random scattering is phase matched to the TM substrate mode and power is transferred from the TE guided wave to the TM substrate mode, thereby creating a large attenuation rate.

Inspection by a Scanning Electron Microscope (SEM) has shown that the surfaces of these waveguides were not damaged in the way that Y-cut substrates immersed in pure proton-exchange melts were. This implied that this phenomenon was not due to surface damage but was most probably due to an increase in strain at the crystal substrate surface as a result of the exchange process. Evidence that there is an amount of strain (lattice constant change) induced lattice distortion present in similar waveguides is given by the RBS data (see Figure 3.10). Although the present level of strain was not sufficient to cause surface cracking it was possible that it was substantial enough affect propagation significantly. This theory is supported by the work by Yamanouchi et al.[39] where strain induced polarisation rotation was demonstrated on $LiNbO_3$ using periodic gratings and externally induced strains.

The increase in lattice strain in Y-cut $LiNbO_3$ after pure melt proton-exchange has been determined previously using X-ray double crystal (030) rocking curves(XRC)[32]. It was shown that after 20 minutes exchange at 180°C, the strain normal to the crystal surface increased by $\Delta a/a = 1.56\%$. The waveguide depth was 0.2μm and the increase in strain was sufficient to cause cracks on the crystal surface aligned parallel to the X-axis. Proton-exchanged Y-cut $LiNbO_3$ waveguides have been fabricated from 0.5% dilute melts with exchange depths in excess of 1.5μm. None of the waveguides suffered surface damage, indicating that the increase in strain due to the exchange process, $\Delta a/a$, was less than 1.56%. This conclusion is supported by Minakata et al.[40] who performed XRC analysis on Z-cut $LiNbO_3$, proton-exchanged in dilute melts for 6 hours at 220°C. For pure melt exchange, a maximum increase in

strain along the c-axis of $\Delta c/c = 0.46\%$ was measured and, more importantly, the value of strain was shown to decrease with increased lithium dilution of the exchange melt. Further evidence that the power loss described above was related to strain or stress was found at the input coupling prism where the principle of operation is based upon an artifically applied strain[39]. It was observed that a large proportion of the light was lost at the prism itself and the phenomenon of two output spots which were related to the coupling conditions could support this theory.

Post exchange annealing has been performed previously on proton-exchanged waveguides to relieve induced strains and improve the waveguide quality[22,23]. In order to examine the structural properties of the Y-cut dilute melt proton-exchanged waveguides, post exchange annealing was carried out. A Y-cut $LiNbO_3$ waveguide was formed by proton-exchange in a 0.5% dilute melt for 4 hours at 190°C. After exchange, the waveguide supported only one TE-mode, with $n_{eff} = 2.232$ and exhibited the anomalous scattering properties described above. After annealing at 400°C for 10 minutes, the waveguide supported two TE-modes with $n_{eff1} = 2.205$ and $n_{eff2} = 2.221$. Both modes propagated evenly to the end of the waveguide (regardless of prism position) and mode lines with very low in-plane scattering were observed. No visible attenuation of the propagating mode was observed and, although evidence of some very weak scattering centres existed, none of the anomalous effects described previously was observed (see Figure 3.15(b)). These results, which suggest that induced strain was the main cause of the attenuation and depolarisation scattering, are contrary to those obtained by Chen and Chang who concluded that annealing did not improve the waveguide performance. In addition, the mode effective indices were both less than n_o which, according to Chen and Chang, implies that random depolarisation scattering should have occurred. However, initial waveguide fabrication conditions in the two experiments differ to such an extent that the results are not comparable in many respects.

Again contrary to Chen and Chang's conclusions, a similar effect has been observed with X-cut $LiNbO_3$ waveguides but to a far lesser degree than on Y-cut. As a precaution however, during the

fabrication of acousto-optic devices, which will be detailed in later chapters, X-cut $LiNbO_3$ substrates were chosen for waveguide fabrication and all waveguides were annealed for very short periods (a maximum of 10 minutes at 400°C for $LiNbO_3$). Annealing these waveguides for short periods seemed to relieve the induced strain while still retaining the overall step-index profile of the waveguide structure (see Figure 3.2).

3.7. Discussion

This chapter has described investigations of waveguide fabrication by proton-exchange from dilute melts. It has dealt with the necessary characterisation of the process with $LiNbO_3$ and $LiTaO_3$ substrates, looked at the structural quality of the waveguides and assessed their suitability for acousto-optic devices.

In comparison with pure melt proton-exchange, the main effect of buffering the melt with excess lithium was to reduce the rate of depletion of lithium ions from the substrate and in effect slow down the diffusion rate of the protons. This allowed a greater proportion of hydrogen atoms to substitute directly for lithium atoms, thus reducing the amount of interstitial hydrogen and resulting in an overall reduction in the lattice distortion. Hence, in contrast with pure melt waveguides, dilute melt waveguides were stable immediately after exchange and showed very low levels of in-plane scattering, even before annealing.

Two of the major concerns with the use of pure melt proton-exchanged waveguides for acousto-optic devices were the difficulty in fabricating Y-cut $LiNbO_3$ waveguides and the reported loss in electro-optic activity. Dilute melt waveguides go a long way towards solving these problems. Y-cut waveguides could be produced, even if they required short annealing periods to relieve induced strain, and the reported preservation of electro-optic activity[35] in a 1% dilute waveguide structure is very encouraging. In addition, Minakata et al.[40] report, for dilute melt proton-exchanged $LiNbO_3$ waveguides, a direct relationship

between an increase in the r_{33} coefficient and an increase in the percentage of lithium in the exchange melt. This implies that dilute melt proton-exchange has the potential to resolve the problems of reduced electro-optic activity.

Subsequent chapters in this thesis will deal more formally with proton-exchanged acousto-optic devices and will explain how the acoustic parameters are affected by the choice of fabrication process.

References to Chapter 3.

1. J.L. Jackel, C.E. Rice and J.J. Veselka, 'Proton-exchange for high-index waveguides in $LiNbO_3$', Appl. Phys. Letts., Vol. 41, No. 7, pp.607-608, 1982.

2. K.K. Wong, R.M. De La Rue and S. Wright, 'Electro-optic waveguide frequency translator in $LiNbO_3$ fabricated by proton-exchange', Opt. Letts., Vol. 7, No. 11, pp.456-458, 1982.

3. S. Neveu, J.P. Barety, M. de Micheli, S. Sibillot, D.B. Ostrowsky and N. Papuchon, 'Phase matched SHG using the d_{33} coefficient in proton-exchanged $LiNbO_3$ guides', Proc. 7th Topical Meeting on Integrated and Guided Optics, Orlando, Florida, U.S.A., PDP-6, April 1984.

4. M. de Micheli, J. Botineau, S. Negeu, P. Sibillot, D.B. Ostrowsky and M. Papuchon, 'Extension of second-harmonic phase-matching range in lithium niobate guides', Opts. Letts., Vol. 8, No. 2, pp.116-118, 1983.

5. D.Y. Zang and C.S. Tsai, 'Titanium-indiffused proton-exchanged waveguide lenses in $LiNbO_3$ for optical information processing', Appl. Opts., Vol. 25, No. 14, pp.2264-2271, 1986.

6. M. Papuchon and S. Neveu, 'Integrated optical polariser on $LiNbO_3$:Ti channel waveguides using proton-exchange', Elect. Letts., Vol. 19, No. 16, pp.612-613, 1983.

7. T. Findakly and B. Chen, 'Single-mode transmission selective integrated-optical polarisers in $LiNbO_3$', Elect. Letts., Vol. 20, No. 3, pp.128-129, 1984.

8. A.C.G. Nutt, 'Experimental observations of light propagation in proton-exchanged $LiNbO_3$ waveguides', J. Opt. Commun., Vol. 6, No. 1, pp. 8-9,1985. See also: J. Ctyroky, 'Rigorous calculation of light propagation in proton-exchanged $LiNbO_3$

waveguides', J. Opt. Commum., Vol. 16, No. 3, pp. 100-102, 1985.

9. A. Mahapatra and W.C. Robinson, 'Integrated-optic ring resonator made by proton-exchange in lithium niobate', Appl. Opts., Vol. 24, No. 15, pp. 2285-2286, 1985.

10. M. Goodwin and C. Stewart, 'Proton-exchanged optical waveguides in Y-cut $LiNbO_3$', Elect. Letts., Vol. 19, No. 6, pp.223-225, 1983.

11. A. Yi Yan, 'Index instabilities in proton-exchanged $LiNbO_3$ waveguides', Appl. Phys. Letts., Vol. 42, No. 8, pp 633-635, 1983.

12. R.A. Becker, 'Comparison of guided wave interferometric modulators fabricated on $LiNbO_3$ via Ti:indiffusion and proton-exchange', Appl. Phys. Letts., Vol. 43, No. 2, pp.131-133, 1983.

13. A.L. Dawar, S.M. Al-Shukri and R.M. De La Rue, 'Guided wave acousto-optic interaction in proton-exchanged Y-cut $LiNbO_3$', Appl. Phys. Letts., Vol. 48, No. 23, pp. 1579-1581, 1986.

14. R.L. Davis, 'Acousto-optic Bragg diffraction in proton-exchanged waveguides', Proc. Soc. Photo-opt. Inst. Eng., Vol. 517, pp.74-81, 1984.

15. V. Hinkov, E. Ise and W. Sohier, 'Low frequency collinear acoustooptic TM_o-TE_o mode conversion and single sideband modulation in proton-exchanged $LiNbO_3$ optical waveguides', Proc. 3rd Europ. Conf. Integrated Optics, Berlin, pp.169-173, 1985.

16. M. de Micheli, J. Vollmer, J.P. Baretti and S. Neveu, 'Proton-exchange in $LiNbO_3$: temperature and water influence during the process', Proc. 2nd Europ. Conf. Integrated Optics, Florence, PDP-1, October 1983.

17. V. Hinkov and E. Ise, 'Surface acoustic waves velocity perturbation in $LiNbO_3$ by proton-exchange', J. Phys. D: Appl. Phys., Vol. 18, L31-34, 1985.

18. M. de Micheli, D.B. Ostrowsky, J.P. Barety, C. Canali, A. Carnera and M. Papuchon, 'Crystalline and optical quality of proton-exchanged waveguides', IEEE Vol. JLT-4, No. 7, pp.743-745, 1986.

19. C. Canali, A. Carnera, G. Della Mea, P. Mazzoldi, S.M. Al-Shukri, A.C.G. Nutt and R.M. De La Rue, 'Structural characterisation of proton-exchanged $LiNbO_3$ optical waveguides', J. Appl. Phys., Vol. 59, No. 8, pp.2643-2649, 1986.

20. P.K. Tien and R. Ulrich, 'Theory of prism-film and thin-film light guides', J. Opt. Soc. Amer., Vol. 60, No. 20, pp.1325-2337, 1970.

21. J. Finak and H. Jerominik, 'Planar diffusion glass waveguides obtained by immersing in molten KNO_3', Optica. Applicata, Vol. X11, No. 1, pp.11-17, 1982.

22. S.M. Al-Shukri, A.L. Dawar, R.M. De La Rue, A.C.G. Nutt, M. Taylor, J.R. Tobin, G. Mazzi, A. Carnera and C. Summonte, 'Analysis of annealed proton-exchanged waveguides in $LiNbO_3$ by optical waveguide measurements and microanalytical techniques', Proc. 7th Topical Meeting on Integrated and Guided Optics, Orlando, Florida, U.S.A., PDP 71-4, April 1984.

23. C. Canali, A. Carnera, P. Mazzoldi and R.M. De La Rue, '$LiNbO_3$ optical waveguide fabrication by Ti diffusion and proton-exchange: process, performances and stability', Proc. Soc. Photo-opt. Inst. Eng., Vol. 517, paper 15, 1985.

24. D.F. Clark, A.C.G. Nutt, K.K. Wong, P.J.R. Laybourn and R.M. De La Rue, 'Characterization of proton-exchange slab optical waveguides in Z-cut $LiNbO_3$', J. Appl. Phys., Vol. 54, No. 11,

pp.6218-6220, 1983.

25. A.C.G. Nutt, K.K. Wong, D.F. Clark, P.J.R.Laybourn and R.M. De La Rue, 'Proton-exchange $LiNbO_3$ slab and stripe waveguides: characterisation and comparisons', Proc. 2nd Europ. Conf. Integrated Optics, Florence, pp.53-56, 1983.

26. C. Canali, A. Carnera, G. Della Mea, R.M. De La Rue, A.G. G. Nutt and J.R. Tobin, 'Proton-exchanged $LiNbO_3$ waveguides: materials analysis and optical characteristics', Proc. Soc. Photo-opt. Inst. Eng. Vol. 460, paper 7, 1984.

27. H. Kogelnik and V. Ramaswamy, 'Scaling rules for thin-film optical waveguides', Appl. Opts., Vol. 13, No. 8, pp.1857-1862, 1974.

28. J. Crank, 'The mathematics of diffusion', Oxford University Press, Chapter 1, 1979.

29. S.M. Al-Shukri, J.F. Duffy, R.M. De La Rue, M.N.Armenise, C. Canali and A. Carnera, 'Proton-exchange optical waveguides on lithium niobate: devices, characterisation and future prospects', Proc. Soc. Photo-opt. Inst. Eng., Vol. 578, pp2-6, 1985.

30. W.B. Spillman, Jr., N.A. Sanford and R.A. Soref, 'Optical waveguides in $LiTaO_3$ formed by proton-exchange', Opts. Letts., Vol. 8, No. 9, pp.497-499, 1983.

31. S.M. Al-Shukri, J.F. Duffy, R.M. De La Rue, G. Mazzi, A. Carnera and M.N. Armenise, 'Single mode planar and stripe waveguides by proton-exchange in lithium tantalate and lithium niobate', Proc. Soc. Photo-opt. Inst. Eng., Vol. 651, pp 20-25, 1986.

32. A. Campari, C. Ferrari, G. Mazzi, C. Summonte, S.M. Al-Shukri, A.L. Dawar, R.M. De La Rue and A.C.G. Nutt, 'Strain and surface damage induced by proton-exchange in Y-cut $LiNbO_3$', J. Appl. Phys., Vol. 58, No. 12, pp.4521-4524, 1985.

33. J.R. Carruthers, I.P. Kaminow and L.W. Stulz, 'Diffusion kinetics and optical waveguiding properties of out diffused layers in lithium niobate and lithium tantalate', Appl. Opts., Vol. 13, No. 10, pp. 2333-2342, 1974.

34. M.N. Armenise, M. De Sario, C. Canali, P. Franzosi, J. Singh, R.H. Hutchins and R.M. De La Rue, 'In-plane scattering in titanium-diffused $LiNbO_3$ optical waveguides', Appl. Phys. Letts., Vol. 45, No. 4, pp.326-328, 1984.

35. K.K. Wong, N.J. Parsons, A.R. Oldroyd and A.C. O'Donnell, 'High quality optical waveguides in $LiNbO_3$ by dilute melt proton-exchange', Proc. IOOC/ECOC '85, pp.59-62, Venice, 1985.

36. M. De Micheli, J. Botineau, P. Sibillot, D.B. Ostrowsky and M. Papuchon, 'Fabrication and characterisation of titanium indiffused proton-exchange (TIPE) waveguides in $LiNbO_3$', Optics. Comm., Vol. 42, No. 2, pp.101-103, 1982.

37. J.L. Jackel, C.E. Rice and J.J. Veselka, 'Composition control in proton-exchanged $LiNbO_3$', Elect. Letts., Vol. 19, No. 10, pp.387-388, 1983.

38. R. Chen and W.S.C. Chang, 'Anomalous attenuation and depolarisation scattering in Y-cut $LiNbO_3$ proton-exchanged waveguides', IEEE, Vol. QE-22, No. 6, pp.980-982, 1986.

39. K. Yamanouchi, K. Wakazono and K. Shibayama, 'Optical surface wave mode converters and modulators utilizing static-optic effects', IEEE J. Quant. Elect., Vol. QE-16, No. 6, pp 628-634, 1980.

40. M. Minakata, K. Kumagai and S. Kawakami, 'Studies on lattice constant changes and electro-optic effects in proton-exchanged $LiNbO_3$ optical waveguides', First Optoelectronics Conf., paper A2-2, Tokyo, 1986.

CHAPTER 4. Analysis of Proton-exchanged Waveguides Using the Scanning Acoustic Microscope

4.1. Introduction

There have been several reports of investigations of the acoustic and acousto-optic properties of proton-exchanged lithium niobate ($LiNbO_3$) since the paper by Handa et al[1-9]. A wide variety of fabrication conditions has been used but, in general, results indicating increased acoustic wave propagation loss, a reduced piezoelectric effect and reduced acousto-optic interaction efficiency have all been obtained. These results, taken together with earlier evidence of a reduced electro-optic effect[10,11], reduced nonlinear optical coefficients[12], and relaxation from the initial value of index change[13], suggested the need for further studies of the properties of proton-exchanged $LiNbO_3$. Recent evidence indicated that some of the problems previously encountered were eliminated, or at least, greatly reduced by using dilute melts[14,15] and so experiments have been carried out using a line-focus-acoustic microscope[16] to determine the acoustic properties of the exchanged region produced from a dilute melt.

4.2. Acousto-optic Proton-exchange

Handa et al.[1] reported greatly increased insertion loss (approximately 30dB greater) for a surface acoustic wave (SAW) delay line in which the transducers were deposited directly on the proton-exchanged region. They attributed this, primarily, to reduced piezoelectricity and were unable to detect acousto-optic diffraction. Successful acousto-optic diffraction in proton-exchanged waveguides, was first reported by Korablev et al.[6] and by Dawar et al.[7] (later revised to Ref. 5). In the work by Dawar et al., the SAW transducers were deliberately placed on regions which were not proton-exchanged because it was suspected that ionic conductivity might affect transducer performance. Although reasonably efficient acousto-optic diffraction could be obtained, annealing of the waveguides led to greatly diminished acousto-optic diffraction efficiency. A possible reason for this is that the effect of the annealing was to change the original

step-index profile of the waveguide to a graded-index profile, resulting in a reduction in the overlap between the optical and acoustic waves (see chapter 5). Subsequent work by Hickernell et al.[4] indicated that acousto-optic propagation losses, under favourable circumstances, make a relatively small contribution to delay line insertion loss and that, for Y-cut $LiNbO_3$ with Z-propagating surface waves, there was only a small perturbation of the acoustic propagation velocity.

Hinkov et al.,[3] have used Brillouin scattering to investigate samples in which the combined titanium diffusion proton-exchange (TIPE) process was used and found as much as 20% relative velocity changes. With Brillouin scattering, relatively high-frequency phonons are involved, so that the properties of the 4μm deep proton-exchanged regions alone were observed. Hinkov et al.[8] have used very multimode TIPE waveguides on Y-cut $LiNbO_3$ to obtain phase matched TE-TM conversion but required large input power levels (4.0W) to obtain even quite small conversion efficiencies (5%).

4.3. Material Characterization by Line-Focus-Beam Acoustic Microscope

4.3.1. Line-Focus-Beam Acoustic Microscope

Recently, in the field of acoustic microscopy, a new technique for the determination of SAW velocity and attenuation has been developed[17,18]. Here it was found that if a large opening-angle (typically $> 30^{\circ}$ semiangle) acoustic lens was moved towards the surface of a material along the z-axis direction (i.e., the beam axis) without scanning in the x- or y-axes then the resulting voltage signal V(z) at the transducer showed oscillations whose periodicity could be simply related to the SAW velocity on that material[16]. Further, by use of a line-focus (cylindrical surface) lens[19] rather than the point-focus (spherical surface) lens used in imaging scanning acoustic microscopy[18], the SAW velocity in a particular propagation direction could be determined. Anisotropies of solid materials, which were previously determined in acoustic microscopy as a mean

value, with use of a circularly focussed beam, could now be unambiguously determined using a line-focus lens[20], since SAW were now only excited along one axis.

Figure 4.1 shows, schematically, the acoustic transducer and lens used in the line-focus-beam technique. The lens is translated towards the sample along the z-axis direction with the x- and y-directions being in the plane. The line-focus beam was realised by constructing a sapphire acoustic lens (chosen for its low attenuation of acoustic waves at high frequencies) with a cylindrical concave surface. The cylindrical concave surface was formed, with a curvature of 1.0mm radius and an aperture half-angle of $\theta_M = 60^o$, on one end of a z-cut sapphire rod[21]. The dimensions and shape of the sapphire rod were designed to suppress spurious signals caused by internal reflection in the rod[19]. On the concave surface, a chalcogenide glass film with a film thickness of a quarter acoustic wavelength was deposited, by vacuum evaporation, as an acoustic antireflection coating for efficient transmission of acoustic waves across the sapphire/water interface[16]. On the flat surface of the lens, a ZnO-film transducer with dimensions 1.73 x 1.73mm^2 was fabricated to radiate and detect longitudinal acoustic waves[16]. Acoustic plane waves, radiated from the ZnO-film transducer, were converted into a linearly focussed acoustic beam through the cylindrically concave acoustic lens, and water coupled to the specimen under investigation. A radio frequency (r.f.) signal of appropriate frequency, and ~ 200mW C.W. power[22], was fed from a pulse measurement system to the ZnO transducer. Pulsed acoustic waves of typical width 0.5μsec propagated along the lens rod. The transducer also acted as a receiver and picked up reflected pulses, which were fed to a pulse wave measurement system via a circulator. Electronic filtering was used to extract the V(z) signal from the detected pulse which also contained reflected signals due to the impedance mismatch at the sapphire/water interface. Distilled water maintained at a temperature of 20^{o}C was used as the coupling liquid. This also served as a reference source for all subsequent measurements.

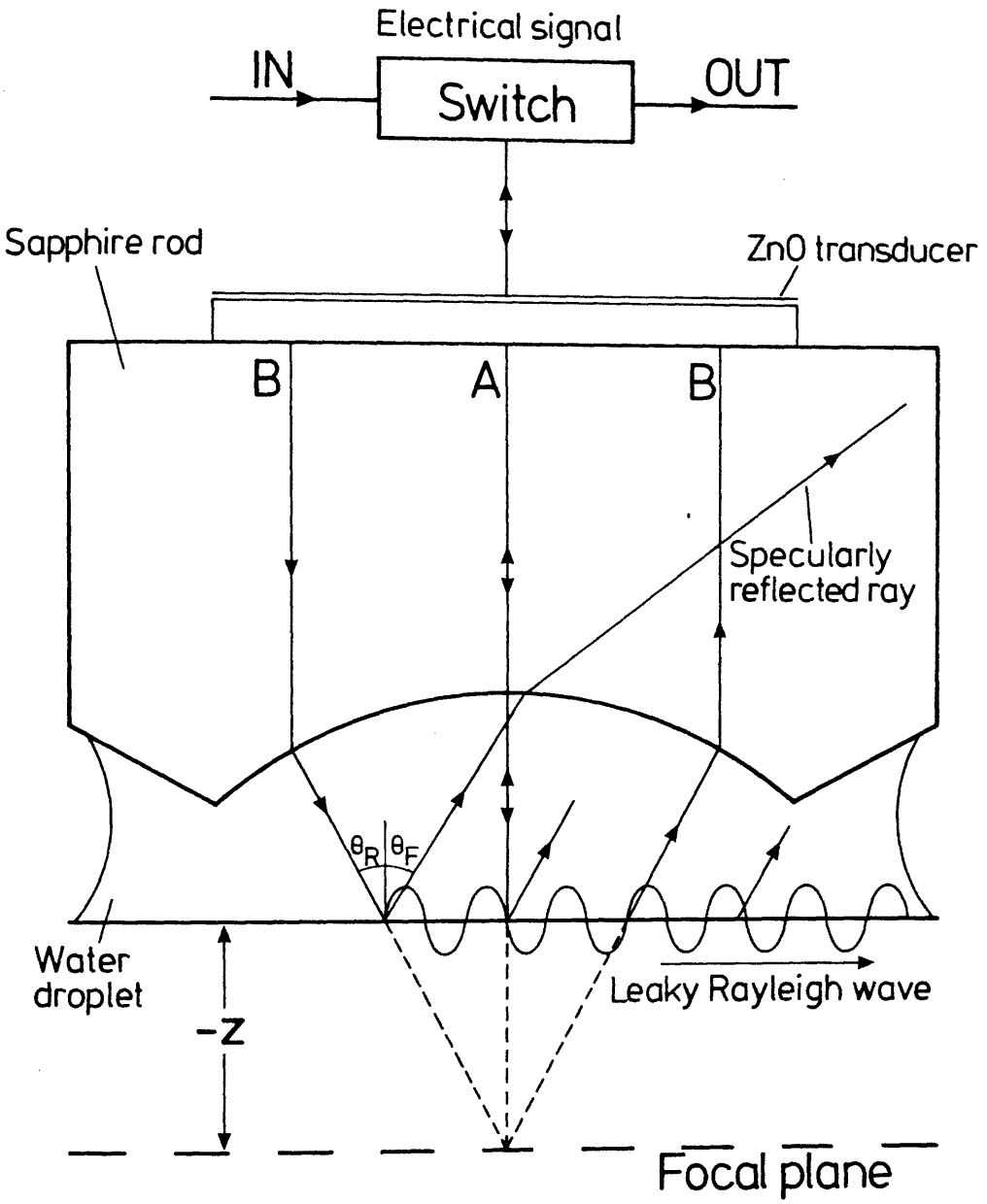

Figure 4.1 Cross – sectional geometry of acoustic line – focus – beam lens.

4.3.2. Principle of Material Characterisation

The determination of the acoustic properties and anisotropy of materials by the line-focus beam technique is carried out through V(z) curve analysis, where the V(z) curves are records of signal variations in the piezoelectric transducer output, as a function of distance along the z-axis between the lens and the sample surface (see Figure 4.1). This V(z) curve variation is caused by the interference of two components of the acoustic waves detected by the transducer, i.e. one component due to acoustic waves, near to the z-axis, directly reflected normal to the sample and the other component associated with waves reradiated from the sample into water through leaky acoustic waves (typically modified SAW) excited on the water/sample boundary[16]. Hence V(z) contains acoustic data characteristic of the sample under investigation. A simple ray theory interference model has been recognised for the determination of characteristics of leaky waves that propagate along the water/sample boundary[23] and excellent agreement has been found between acoustic properties derived from measurements and theoretical calculations[16]. From this model, the acoustic velocity is calculated from the quasi-periodic dip interval appearing in the V(z) curves, while the attenuation, if possible, is calculated from the overall shape of the curve.

Figure 4.2(a) shows the raw V(z) data obtained from a sample of $LiNbO_3$. The raw V(z) data can be represented approximately by combining field theory for the directly reflected component and ray theory for the leaky SAW component in the negative z region as

$$V(z) = V_I(z) + V_L(z) \qquad \ldots.4.1$$

where $V_L(z)$ is the characteristic lens response, defined as the hypothetical transducer output with respect to z and where the response for the leaky SAW component is completely excluded. The lens response depends on the dimensions of the acoustic line-focus-beam lens and operating frequency i.e. the acoustic field distribution[16]. In practice, the characteristic lens response

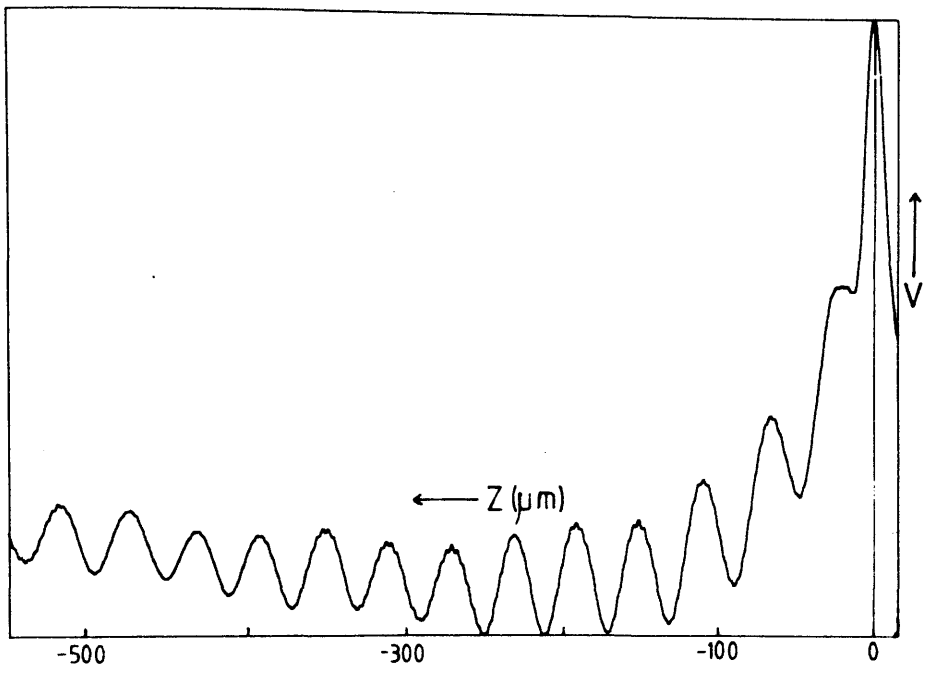

(a)

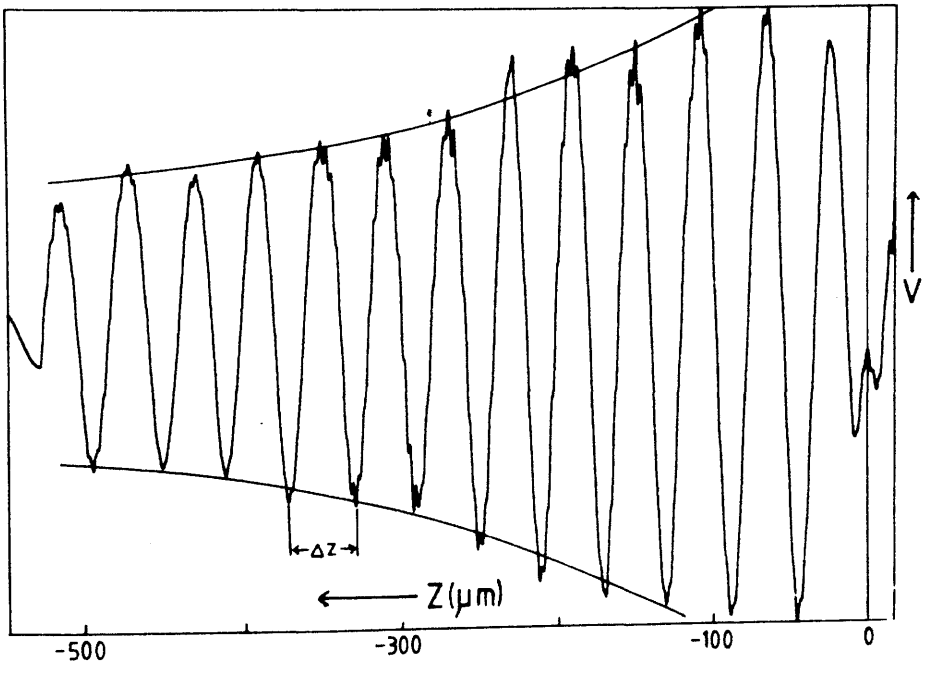

(b)

Figure 4.2(a) An example of unprocessed V(z) data
(b) The processed V(z) data showing the regular periodicity (z)

for a particular lens is obtained by measuring V(z) for a material where, in general, $\theta_{LSAW} > \theta_M$ (see Figure 4.3) where either no leaky SAW are excited or the wave excitation efficiency is very low.For example, for distilled water at 20°C with $V_w = 1483ms^{-1}$[16] and a lens angle in water of $\theta = 53^o$, it is desired that the velocity for the fastest leaky wave mode is smaller than or near to the value of $V = 1858ms^{-1}$. In this experiment lead (Pb) is such a material and its characteristic response is extracted from the raw V(z) data[16] of Figure 4.2(a) to yield the $V_I(z)$ curve for the $LiNbO_3$ alone. This curve is shown in Figure 4.2(b).

Figure 4.3 shows the ray model for the simplest case, where only one leaky SAW is excited along the water/sample boundary. (It is possible to excite multiple modes along the boundary, e.g., leaky pseudo-SAW modes and harmonic modes of leaky waves. In such a case, an FFT analysis may be used on the raw V(z) data to separate out each mode. The FFT analysis gives mode spectra which have maxima in the frequency domain corresponding to different characteristic dip intervals Δz[24]). Only the waves due to normal reflection from the sample (#0) and reradiation from the water/sample boundary (#1), take part in the analysis. The latter correspond to a portion of the reradiated waves propagating the distance $\overline{BC}$ on the boundary. The remaining reradiated waves cannot effectively reach the transducer due to refraction at the lens surface. The translation of a sample by a distance z from the focal plane to the lens gives rise to phase variations $\phi_0(z)$ for (#0), and $\phi_1(z)$ for (#1) as follows:

$$\phi_0(z) = -2\overline{OF}k_w = -2k_w z \qquad \text{....4.2}$$

and

$$\phi_1(z) = (\overline{BC}\, k_{LSAW}) - (\overline{BOC}\, k_w)$$

$$= 2z\left(k_{LSAW} \tan\theta_{LSAW} - \frac{k_w}{\cos\theta_{LSAW}}\right) \qquad \text{....4.3}$$

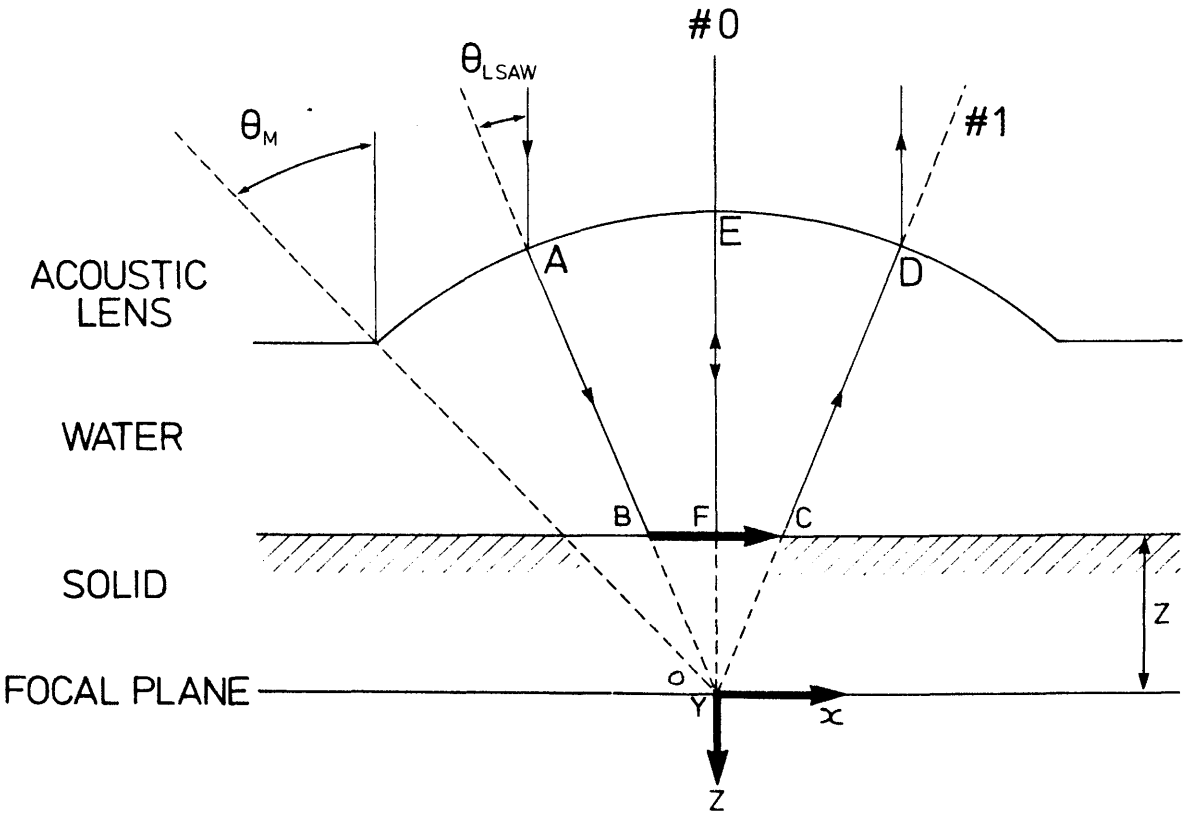

Figure 4.3 Ray model for determining the periodicity in V(z).

where $k_w = 2\pi f/V_w$, $k_{LSAW} = 2\pi f/V_{LSAW}$ and

$$\theta_{LSAW} = \sin^{-1}(V_w/V_{LSAW}) \qquad \ldots.4.4$$

V_w is the longitudinal velocity in water and V_{LSAW} is the phase velocity of the leaky SAW on the boundary. The relative phase change $\phi_t(z)$ between a normal reflection (#0) and a water/sample boundary reflection (#1) per unit translation distance z is given by

$$\phi(z) = \frac{(\phi_1(z) - \phi_0(z))}{z} = 2k_w(1 - \cos\theta_{LSAW}) \qquad \ldots.4.5$$

Thus, for rays of both the #0 and #1 reflection paths, $V_I(z)$ can be represented by[16]:

$$V_I(z) = \text{Const.}[\alpha \exp(j(\phi_t(z) + \gamma))] \qquad \ldots.4.6$$

where γ = initial phase difference between reflections (#0) and (#1) at focus, and α = attenuation factor of leaky SAW propagating on the boundary. The attenuation factor takes into account attenuation due to water loading, acoustic bulk absorption and structural scattering. The amplitude constant (Const) depends on the acoustic field distribution and the excitation efficiency for a leaky SAW[16].

A phase change of 2π in the relative phase difference $\phi_1(z) - \phi_0(z)$ corresponds to the dip interval Δz in the $V_I(z)$ curves (see Figure 4.2(b)). Hence from equation 4.5

$$\Delta z = \frac{2\pi}{2k_w(1 - \cos\theta_{LSAW})} \qquad \ldots.4.7$$

Equation 4.6 can also be expressed in terms of V_{LSAW} as follows:

$$V_{LSAW} = \frac{V_w}{\{1 - [1 - (V_w/2f\Delta z)]^2\}^{1/2}} \quad \ldots.4.8$$

Thus, this simplified theory representing the V(z) curves states that, if the $V_I(z)$ function is extracted from experimental data, the velocity and attenuation of a leaky SAW can be directly determined. The velocity is determined from the dip interval Δz of the interference and the attenuation from the gradient of the interference amplitude. In practice, a Fourier analysis is performed on all data and values of α and Δz are extracted, using digital signal processing[16].

In the present quantitive measurements, distilled water is employed as the reference material with the longitudinal velocity V_w and the acoustic attenuation coefficient α_w. The acoustic properties of distilled water, i.e., the values of the velocity, attenuation coefficient and density, are exactly known as a function of temperature and they are found to be stable both physically and chemically. The determination of the leaky wave velocity is made using the velocity of water corresponding to the temperature at which the V(z) curve measurements are performed.

4.4. Waveguide Fabrication Conditions

Lithium niobate crystal plates approximately 1mm thick were used throughout these experiments. For all samples, the proton-exchange process was carried out in air using 'dilute' melts in a manner previously described in Chapter 3 of this thesis. The time and melt temperature used for preparing samples of each crystal cut are shown in Table 4.1. The choice of 0.25% molar dilution allowed reasonably large exchange-region depths to be obtained without excessively long fabrication times, while giving substantial modification to the acoustic velocity. Table 4.1

includes the estimated depths of the proton-exchanged regions, while Table 4.2 shows the corresponding modal effective indices and guiding region indices.

Table 4.1 Proton-exchange conditions

Crystal cut	Crystal plane	Proton exchange		Waveguide Depth (μm)
		Temp(°C)	Time(h)	
X	X-Y	200	16	2.03
Y	X-Z	220	5	1.36
Z	X-Y	200	16	1.46

Table 4.2 Modal refractive indices of proton-exchange waveguides

Crystal cut and polarisation	Effective ref. indices	Extrapolated layer ref. index[1]
X-cut (TE)	2.3196	2.3233
	2.3060	
	2.2839	
	2.2531	
	2.2155	
Y-cut (TE)	2.3145	2.3231
	2.2870	
	2.2432	
Z-cut (TE)	2.3173	2.3252
	2.2921	
	2.2521	

[1]Substrate refractive index at 0.6328μm is 2.2025.

V(z) data acquisition was carried out at 215MHz, using the arrangement and measurement techniques described earlier in this chapter. The specimens were mounted on a rotating two-axis goniometer to allow both accurate levelling of the specimen (with respect to the z-axis of the lens) and selection of the propagation direction on the crystal surface. V(z) data were acquired and processed for both virgin and proton-exchanged $LiNbO_3$ in the azimuthal angle ranges (propagation directions) 0-180°, 0-90° and 0-60° for the X-, Y- and Z-cut crystals, respectively.

4.5. Line-Focus-Acoustic Measurements on $LiNbO_3$: Results and Analysis

The variation of SAW velocity with azimuthal angle for all cuts of virgin and proton-exchanged $LiNbO_3$ is shown in Figure 4.4, together with previously published data[25]. The V(z)-derived SAW velocities for all cuts of virgin $LiNbO_3$ agree well with the data available in the literature, giving a high degree of confidence in the results yielded by this technique. The acoustic microscope measures the Rayleigh (SAW) velocity in the presence of fluid loading, which will cause a small perturbation on the unloaded velocity reported for virgin $LiNbO_3$ in reference 26. For most propagation directions, the combined mechanical and electrical effects of the water loading caused a reduction in the Rayleigh velocity of not more than $50ms^{-1}$[27]. The measured values in the principal directions are summarised in Table 4.3. The estimated error is $5ms^{-1}$.

It can be seen from Figure 4.4 that proton-exchange has markedly altered the 215MHz SAW velocity (by up to 5% in some cases) for all crystal cuts, despite the thickness of the exchanged regions (1.5 - 2.0μm) being much less than the wavelength of the SAW (typically ~20μm). Proton-exchange can result not only in decreases in SAW velocity (as reported previously by Hinkov et al.[3]) but, for some cases, in increases in the SAW velocity. This is observed for azimuthal angles in the range 50-130° (Figure 4.4(a)). for X-cut crystal and 40-90°

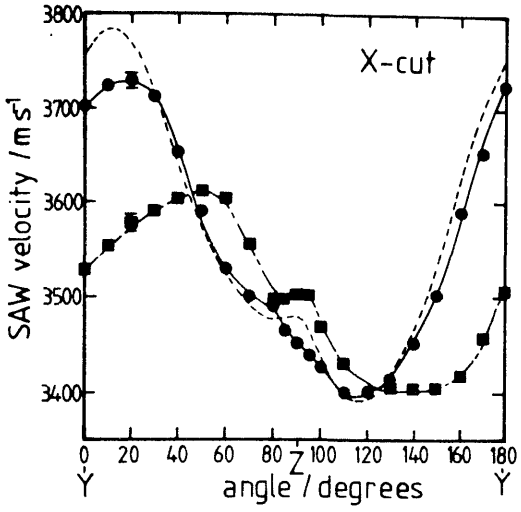

(a)

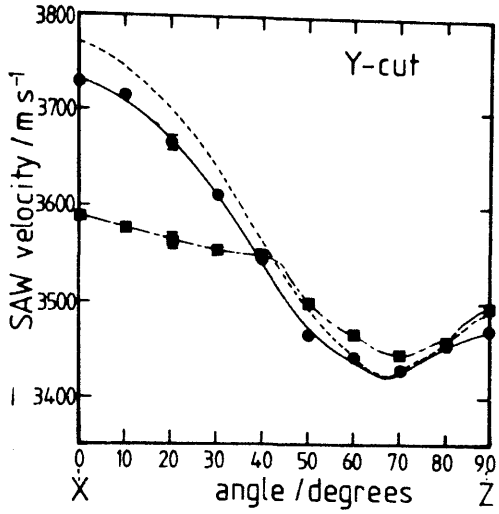

(b)

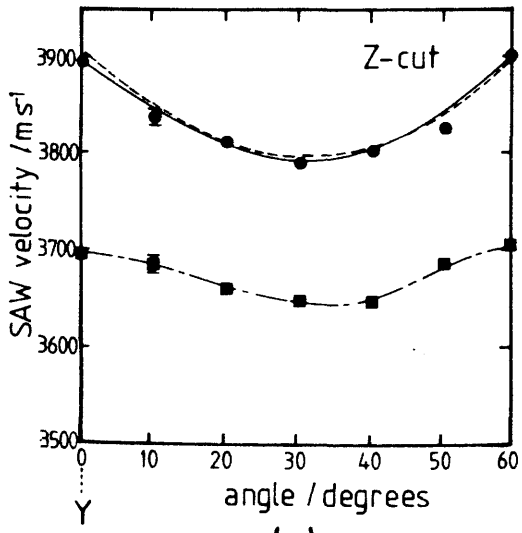

(c)

Figure 4.4 The experimentally obtained variation of SAW velocity with propagation direction for virgin (●) and proton – exchanged (■) $LiNbO_3$ (a) X – cut, (b) Y – cut and (c) Z – cut. Also shown is the published data (broken line) from Ref. 25.

(Figure 4.4(b)) for the Y-cut crystal. The SAW velocity was reduced by proton-exchange for all propagation directions on the Z-cut crystal (Figure 4.4(c)). It can also be seen that proton-exchange generally reduced SAW propagation velocity along the X- and Y-directions and generally resulted in (smaller) increases in velocity for waves propagating along the Z-direction.

Table 4.3 Velocity measurements in symmetry directions.

Crystal Cut	Propagation direction	Velocity/ms^{-1} ($\pm 5ms^{-1}$)	
		unexchanged	exchanged
X	Y	3700	3528
X	Z	3451	3519
Y	X	3729	3590
Y	Z	3468	3494
Z	X	3788	3646
Z	Y	3893	3694

It is possible to calculate the theoretical 'true' SAW velocity for an infinitely thick proton-exchange layer on a $LiNbO_3$ crystal[21], i.e., to calculate the SAW velocity for a proton-exchange region only, without the influence of a virgin $LiNbO_3$ base, as in the previous experiments. A detailed analysis of this kind is extremely complicated. However, a simplified version, using isotropic layered media wave propagation theory, has been carried out[21] and the results are presented in Figure 4.5. For X-cut proton-exchanged $LiNbO_3$, the angles of maximum and minimum SAW velocity were shifted by approximately 50°. Similarly, the maxima and minima of the SAW velocity on Y-cut and Z-cut crystals were shifted by 40° and 30°, respectively. In addition, the degree of acoustical anisotropy exhibited by the X- and Y-cut proton-exchanged $LiNbO_3$ appears greater than that of virgin $LiNbO_3$ (the variation of SAW velocity increasing from ~$200ms^{-1}$ to ~$2000ms^{-1}$ for X-cut). Due to the simplified computation analysis

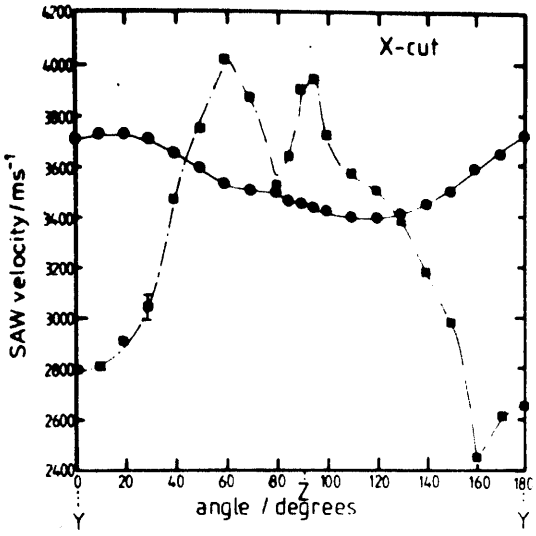

(a)

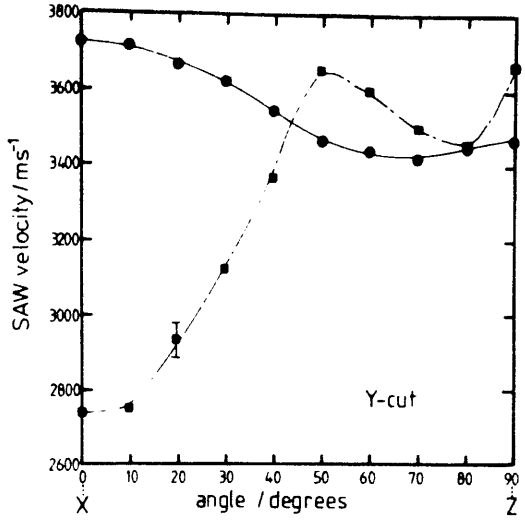

(b)

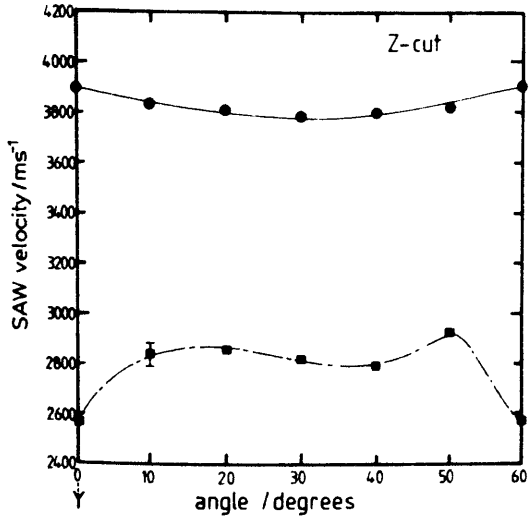

(c)

Figure 4.5 The variation of 'true' SAW velocity with propagation direction from virgin (●) and proton – exchanged (■) $LiNbO_3$ (a) X – cut, (b) Y – cut and (c) Z – cut.

employed in this section, the values of SAW velocities presented in Figure 4.5 should not be taken as absolute. Rather, the results should be used as a guide to the changes in acoustical properties occurring as a result of proton-exchange.

Measurement of SAW attenuation on these samples has proved to be difficult since the attenuation measured by the acoustic microscope was due both to the fluid loading and to losses within the material, with the former tending to dominate using this technique. The acoustic microscope does permit the determination of attenuation due to material losses alone, by means of an inverse transform technique[28], but this requires a knowledge of the phase of V(z) and has not yet been implemented at frequencies as high as those used here.

The variations of SAW attenuation with propagation direction derived for X- and Y-cut $LiNbO_3$ are shown in Figure 4.6 (for some propagation directions, multiple modes were excited, making the calculation of SAW attenuation practically impossible[21]). Figure 4.6 shows that, for Z-propagating SAW, the attenuation is similar to that of the bulk, pure $LiNbO_3$. However, for Y- and X-propagating SAW on X- and Y-cut $LiNbO_3$, respectively, an increase in attenuation accompanied the decrease in SAW velocities noted above. Finally, on the Z-cut surface only data for the attenuation of Y-propagating SAW could be obtained: this also showed increases in attenuation.

4.6. Discussion

The variations of SAW velocity with orientation for virgin $LiNbO_3$ showed in all cases good agreement with the literature[25] and the discrepancies that were present may have been artefacts of the V(z) technique. However, good agreement between these results and those obtained by Hinkov et al.[3] on Y-cut $LiNbO_3$ was not found and, in particular, Hinkov et al. obtained SAW velocities consistently lower than those obtained in the present study. This could have been due to (i) loading of the substrate due to the presence of the 400-Å Aluminium film required for the Brillouin scattering technique or (ii) the modification of the electrical

boundary condition by this conducting film. The former effect is expected to be small, since the SAW velocities of $LiNbO_3$ and aluminium are similar. However, the latter effect is large and similar in magnitude and sign to that reported in the literature[29]. The acoustic anisotropy observed in the proton-exchanged Y-cut $LiNbO_3$ by Hinkov et al.[3] (and reproduced in Figure 4.7) indicated that, for all orientations, the proton-exchanged material was slower than the virgin material. Conversely, Davis[2] has indicated that no velocity changes were present for Z-propagating waves after proton-exchange (though this was probably due to his measurement technique not being sensitive enough to detect the slight velocity perturbations that can be detected using the V(z) technique). This was clearly not the case in the present study. The discrepancy between the results of Hinkov et al.[3] and those presented here was probably due to differences in the proton-exchange treatment used in the experiments. Hinkov et al.[3] used a significantly different exchange treatment involving a pure benzoic acid melt rather than the dilute melts used in the present study. Furthermore, an exchange region ~3.5μm deep was obtained using their treatment, about 60% greater than that used in the present study. However, despite these differences the changes in the sign of the acoustic birefringence reported by Hinkov et al.[3] (see Figure 4.7) agree qualitatively with those obtained in the present study.

Acknowledgement

The work presented in this chapter has been performed in collaboration with Dr. P.J. Burnett and Dr. G.A.D. Briggs at the Department of Metallurgy and Science of Materials, University of Oxford. The Scanning Acoustic Microscope is housed in the above department and the SAM experiments were performed on the optical waveguides by Dr. Burnett. I would like to thank Dr. Burnett and Dr. Briggs for their help and for many valuable discussions about the operation of the SAM. I would also like to thank Dr. J. Roe for demonstrating the operation of the SAM.

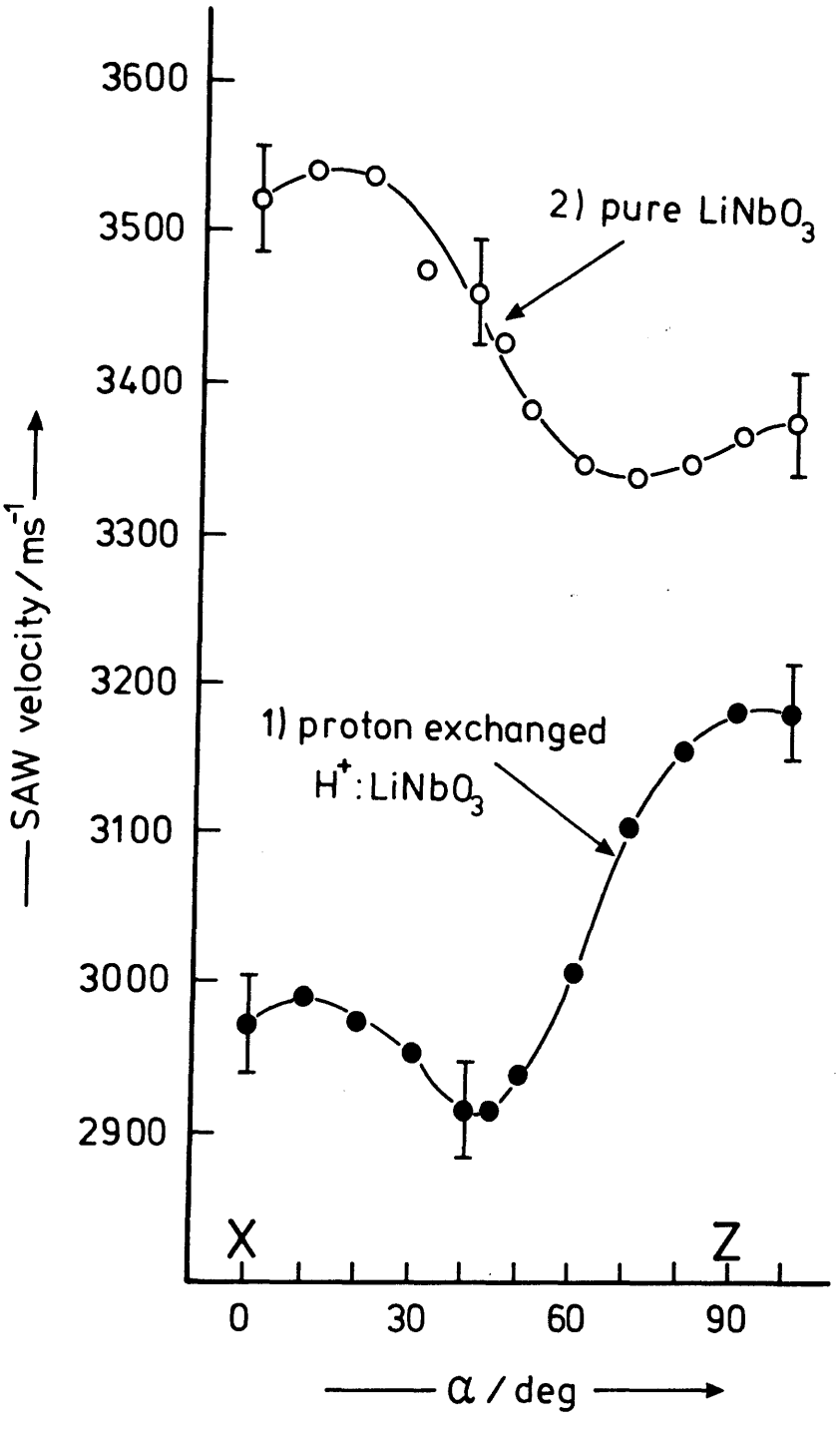

Figure 4.7 Variation of the SAW velocity in the X-Z plane of a $LiNbO_3$ crystal with angle α. Curve 1 refers to the exchanged part of the sample, curve 2 to the non-exchanged part. The wavelength of the SAW was 0.251 μm (after 3).

References to Chapter 4.

1. Y. Handa, M. Miyawaki and S. Ogura, 'Guided-wave characteristics and optical damage in $LiNbO_3$ waveguides', Proc. Soc. Photo-opt. Inst. Eng., Vol. 460, pp. 101-108, 1984.

2. R.L. Davis, 'Acousto-optic Bragg diffraction in proton-exchanged waveguides', Proc. Soc. Photo-Opt. Inst. Eng., Vol. 517, pp. 74-81, 1984.

3. V. Hinkov, M. Barth and K. Dransfeld, 'Acoustic properties of proton-exchanged $LiNbO_3$ investigated by Brillouin scattering', Appl. Phys. A. Vol. 38, pp. 269-273, 1985.

4. F.S. Hickernell, K.D. Ruehle, S.J. Joseph, G.M. Reese and J.F. Weller, 'The surface acoustic wave properties of proton-exchanged YZ lithium niobate', Proc. IEEE Ultrasonics Symposium, pp. 110-113, San Francisco, 1985.

5. A.L. Dawar, S.M. Al-Shukri and R.M. De La Rue, 'Guided wave acousto-optic interaction in proton-exchanged Y-cut $LiNbO_3$', Appl. Phys. Letts., Vol. 48, No. 23, pp. 1579-1581, 1986.

6 E.M. Korablev, Yu L. Kopylov and V.V. Proklov, 'Acousto-optic investigations of proton-exchanged waveguides in $LiNbO_3$', IEEE Workshop on Optical Signal Processing and Related Technologies, PD-4, Florence, 1984.

7. A.L. Dawar, S.M. Al-Shukri and R.M. De La Rue, 'Surface acoustic wave-guided optical wave interaction in Y-cut $LiNbO_3$ annealed proton-exchanged waveguides', ibid, PD-3, Florence, 1984.

8. V. Hinkov, E. Ise and W. Sohier, 'Low frequency collinear acousto-optic TM_o-TE_o mode conversion and single sideband modulation in proton-exchanged $LiNbO_3$ optical waveguides', Proc. 3rd Euro. Conf. on Integrated Optics, pp. 169-173, Berlin, 1985.

9. M.M. Miyawaki and S. Ogura, 'Efficient, damage resistant $LiNbO_3$ acousto-optic waveguide deflector', Appl. Phys. Letts. Vol. 47, No. 9, pp. 918-920, 1985.

10. K.K. Wong, R.M. De La Rue and S. Wright, 'Electro-optic waveguide frequency translator in $LiNbO_3$ fabricated by proton-exchange', Opts. Letts. Vol. 7, No. 11, pp. 456-458, 1982.

11. R.A. Becker, 'Comparison of guided wave interferometric modulators fabricated on $LiNbO_3$ via Ti:indiffusion and proton-exchange', Appl. Phys. Letts., Vol. 43, No. 2, pp. 131-133, 1983.

12. S. Neveu, J.P. Barety, M. De Micheli, S. Sibillot, D.B. Ostrowsky and M. Papuchon, 'Phase matched SHG using the d_{33} coefficient in proton-exchanged $LiNbO_3$ waveguides', Proc. 7th Topcial Meeting on Integrated and Guided Optics, Orlando, Florida, PDP 71-4, 1984.

13. A. Yi Yan, 'Index instabilities in proton-exchanged $LiNbO_3$ waveguides', Appl. Phys. Lett. Vol. 42, No. 8, pp. 633-635, 1983.

14. S.M. Al-Shukri, J.F. Duffy, R.M. De La Rue, M.N. Armenise, C. Canali and A. Carnera, 'Proton-exchanged optical waveguides on lithium niobate: devices, characterisation and future prospects', Proc. Soc. Photo-opt. Inst. Eng., Vol. 578, pp. 2-6, 1985.

15. K.K. Wong, N.J. Parsons, A.R. Oldroyd and A.C. O'Donnell, 'High quality optical waveguides in $LiNbO_3$ by dilute melt proton-exchange', Proc. IOOC/ECOC '85, pp. 59-62, Venice, 1985.

16. J. Kushibiki and N. Chubachi, 'Material characterisation by line-focus-beam acoustic microscope', IEEE Trans. Sonics and Ultrasonics, Vol. SU-32, No. 2, pp. 189-212, 1985.

17. A. Atalar, C.F. Quate and H.K. Wickramsinghe, 'Phase imaging in reflection with the acoustic microscope', Appl. Phys. Lett., Vol. 31, No. 12, pp.791-793, 1977.

18. R.D. Weglein, 'A model for predicting acoustic material signatures', Appl. Phys. Letts., Vol. 34, No. 3, pp. 179-181, 1979.

19. J. Kushibiki, A. Ohkubo and N. Chubachi, 'Linearly focused acoustic beams for acoustic microscope', Elect. Letts. Vol. 17, No. 15, pp. 520-522, 1981.

20. J. Kushibiki, A. Ohkubo and N. Chubachi, 'Anisotropy detection in sapphire by acoustic microscope using line-focus-beam', Elect. Letts., Vol. 17, No. 15, pp. 534-536, 1981.

21. P.J. Burnett, G.A.D. Briggs, S.M. Al-Shukri, J.F. Duffy and R.M. De La Rue, 'Acoustic properties of proton-exchanged $LiNbO_3$ studied using the acoustic microscope V(z) technique', J. Appl. Phys., Vol.60, No. 7, pp. 2517-2522, 1986.

22. G.A.D. Briggs, 'An introduction to scanning acoustic microscopy', Royal Microscopical Society Handbook, No. 12, Oxford University Press, 1985.

23. W. Parmon and H.L. Bertoni, 'Ray interpretation of the material signature in the acoustic microscope', Elect. Letts. Vol. 15, No. 21, pp. 684-686, 1979.

24. J. Kushibiki, K. Horri and N. Chubachi, 'Velocity measurements of multiple leaky waves on germanium by line-focus-beam acoustic microscope by FFT', Elect. Letts., Vol. 19, No. 11, pp. 404-405, 1983.

25. A.J. Slobodnik Jr., R.J. Delmonico and E.D. Conway, Microwave Acoustics Handbook, Vol. 1A, Air Force Research Labs., Mass., U.S.A. 1973.

26. J. Kushibiki, A. Ohkubo and N. Chubachi, 'Propagation characteristics of leaky SAW on water/$LiNbO_3$ boundary measured by acoustic microscope with line-focus-beam', Elect. Letts. Vol. 18, No. 1, pp. 6-7, 1982.

27. J.J. Campbell and W.R. Jones, 'Propagation of surface waves at the boundary between a piezoelectric crystal and a fluid medium', IEEE Trans. Sonics and Ultrasonics, Vol. SU-17, No. 2, pp. 71-76, 1970.

28. K.K. Liang, G.S. Kino and B.T. Khuri-Yakub, 'Material characterisation by the inversion of V(z)', IEEE Trans. Sonics and Ultrasoncis, Vol. SU-32, No. 2, pp. 213-224, 1985.

29. J.J. Campbell and W.R. Jones, 'A method of estimating optimal crystal cuts and propagation directions for excitation of piezoelectric surface waves', IEEE Trans. Sonics and Ultrasonics, Vol. SU-15, No. 4, pp. 209-217, 1968.

CHAPTER 5. Analysis of the Acousto-optic Overlap in Proton-exchange Waveguides

5.1. Introduction

The efficiency of acousto-optic interaction on proton-exchanged $LiNbO_3$ waveguides has been related previously[1] to the index profile of the waveguide. Dawar et al[2] found a correlation between the change in index profile from step to graded, due to post exchange annealing, and a reduction in the acousto-optic diffraction efficiency, while Davis[1] concluded that the optical field distribution associated with diffused waveguides (e.g., Titanium indiffused $LiNbO_3$) was not optimal to the acousto-optic interaction. This chapter describes an investigation of the overlap between the propagating acoustic wave distribution and the optical field distribution for proton-exchanged waveguides on $LiNbO_3$. Acoustic wave propagation was in the z-direction and the optical field distribution was determined primarily by the waveguide index profile. The analysis looked at the contribution to the diffraction efficiency of both the photoelastic and electro-optic effects and investigated how each term was affected by changes in acoustic wavelength and optical field distribution. In particular, the effect of reduced electro-optic activity, which has been suspected in proton-exchange waveguides[3,4], was examined and results are presented for a 'piezoelectrically deficient' region.

Experimental results obtained from both pure and dilute melt proton-exchanged waveguides were used as input data for the optical field distribution and the variation in the overlap was due primarily to a variation in the optical field distribution as a result of index profile variations. The dilute melt waveguides had step-index profiles[5] while the pure melt waveguides had index profiles which varied from step to graded, depending upon annealing time[6]. No attempt was made to quantify any possible effects on the acoustic and elastic properties of the proton-exchanged $LiNbO_3$ waveguide since this information is not available at the moment. The analysis did, however, include the reduction in

acoustic velocity for z-propagating acoustic waves predicted by the acoustic microscopy analysis of chapter 4 for proton-exchanged $LiNbO_3$. It is hoped that in the future, the acoustic microscopy analysis might be used to predict more detailed variations in the elastic constants.

5.2. Elastic Waves in Solids

Waves of particle displacement propagate in elastic solids as a result of applied time-varying mechanical stresses[7]. Two types of elastic wave exist in solids: bulk elastic waves which propagate in any direction in a solid, whether the solid be elastically isotropic or anisotropic, and surface elastic waves, which propagate along the stress free surface of a solid with particle displacement concentrated near the surface, moving in elliptical paths.

Three independent bulk waves can propagate in a given direction. One of these, the longitudinal bulk wave, has a particle motion along the direction of propagation. The other two bulk waves have particle displacements purely transverse to the direction of propagation. The motion of surface acoustic waves can be decomposed into at least two orthogonal components, one in the direction of propagation and one normal to the free surface . There are both longitudinal and transverse strains associated with the motion. In the ideal case, up to microwave frequencies[7], the wave is non-dispersive (i.e. its velocity does not vary with frequency), its phase velocity is somewhat slower than the slowest elastic bulk wave in the medium and its penetration depth into the interior is comparable to a wavelength. For a layered refractive index medium, e.g., proton-exchanged or titanium indiffused $LiNbO_3$ waveguides, the non-dispersive nature of the SAW no longer holds. In such cases, a SAW propagates with a phase velocity which is frequency-dependent for frequencies such that the wavelength is comparable with the layer thickness[7].

5.3. Propagation of Elastic Waves.

5.3.1. Basic Elastic Equations

Consider an unbounded solid in which only bulk longitudinal and bulk transverse waves propagate. If the solid is perfectly elastic and is nonpiezoelectric, the stress (force per unit area) and the strain (dimensionless normalised particle displacement) are related simply by Hooke's Law.

$$T_{ij} = C_{ijkl}\, S_{kl} \qquad \ldots.5.1$$

where T_{ij} is the stress acting along the x_i co-ordinate direction on a surface whose normal is parallel to the x_j axis, and S_{kl} is the strain component defined by

$$S_{kl} = \frac{1}{2}\left\{\frac{\partial U_k}{\partial x_l} + \frac{\partial U_l}{\partial x_k}\right\} \qquad \ldots.5.2$$

where U_k denotes a particle displacement in the k direction and x_l is the lth position co-ordinate. The quantities C_{ijkl} are the elastic stiffness constants for the medium. The cartesian summation convention (over 1,2,3) for repeated indices is assumed throughout. From this law and Newton's force equation, one can derive the elastic wave equation for a homogeneous solid

$$\rho \frac{\partial^2 U_j}{\partial t^2} = \frac{\partial T_{ij}}{\partial x_i} \qquad \ldots.5.3$$

where ρ is the mass density. In addition, the electrical displacement D is uniquely related to the electric field E through the permittivity tensor ε, so that

$$D_i = \varepsilon_{ij} E_j \qquad \text{....5.4}$$

In a piezoelectric medium, an applied electrical signal will alter the polarisation of the crystal resulting in a distortion of the crystal. If the electric field is sinusoidally varied, then this will result in a distortion which will propagate away from the source. Thus supplementary stress components appear: ΔT_{ij} as well as electric polarisation ΔP_{ij} such that

$$\Delta T_{ij} = -e_{kij} E_k \qquad \text{....5.5}$$

$$\Delta P_{ij} = e_{ikl}\, S_{kl} \qquad \text{....5.6}$$

where e_{ijk} represents the piezoelectric tensor.

The stresses, as well as the electrical displacements, are functions of both strains and electric field, and the constitutive equations of a piezoelectric medium are written as

$$T_{ij} = C^E_{ijkl} S_{kl} - e_{kij}\, E_k \qquad \text{....5.7}$$

$$D_i = e_{ikl}\, S_{kl} + \varepsilon^S_{ij} E_j \qquad \text{....5.8}$$

where C^E_{ijkl} represents the elastic tensor in a zero electric field and ε^S_{ij}, the permittivity tensor at zero strain. A wave of electric field now accompanies the elastic wave, and the wave velocity depends upon elastic, piezoelectric, and dielectric properties. The medium behaves as if it were stiffer because of the additional potential energy resulting from the piezoelectric coupling, and the velocities are higher than without the coupling as a result of the 'piezoelectric stiffening'[7]. The effective elastic stiffness is increased to the value

$$C_{stiffened} = C(1 + k^2) \qquad \text{....5.9}$$

with $k^2 = e^2/C\varepsilon$, where the components of e, C, and ε used depend upon the propagation direction. The term k, the electromechanical coupling coefficient, is a convenient measure of the strength of piezoelectric coupling and is related to the perturbation of the wave ΔV caused by a change in the electric field boundary conditions. Typically for YZ-$LiNbO_3$, $k^2 = 0.045$[8].

5.3.2. Surface Waves Solutions

With an elastic solid which is not infinite in extent but is bounded by a plane y = 0, Rayleigh waves[9] propagate along the free surface. Waves propagating along the surface in the z direction with their amplitude decaying with the depth y have the form[10]

$$U_i = A_i \exp(\Omega_i k y) \exp[i(kz - \omega t)] \qquad \text{....5.10}$$

$$E_i = k\xi_i \exp(\Omega_i k y) \exp[i(kz - \omega t)] \qquad \text{....5.11}$$

for $y \leq 0$, i=1,2,3.

where A_i, ξ_i are amplitude constants, k is the wave number, and Ω_i is the dimensionless decay constant.

Equations 5.10 and 5.11 can be solved to give solutions where the non-vanishing displacements and electric fields are confined to the sagittal plane (defined as the plane perpendicular to the crystal surface and parallel to the propagation direction i.e. the YZ plane). A surface wave resulting from this solution, with its propagation on the plane free surface of the elastic solid, and disturbance confined to a thickness comparable with the wavelength, is referred to as a Rayleigh wave. With this solution $U_i = E_i = 0$, i.e. displacements and potentials are considered to be independent of the x co-ordinate.

Equations 5.10 and 5.11 are solutions to the equation of motion (equation 5.3) and to Maxwell's equations inside the elastic solid. The equation of motion is confined to particle displacement within the solid while Maxwell's equations extend to entire space. The equations for the electric field outside the solid have the same form as those inside, but with E_1 decoupled from E_2 and E_3[10].

The stresses and electric fields defined by equations 5.10 and 5.11 are subject to the following boundary conditions: the stress components which are normal to the surface vanish at y = 0, the tangential component of the electric field, and the normal component of the electric displacement are continuous at the surface, i.e.

$$T_{2j}(0) = 0 \qquad \text{where } j = 1,2,3$$

$$E_3(0-) = E_3(0+)$$

$$D_2(0-) = \varepsilon_0 E_2(0+) \qquad \text{....5.12}$$

5.4. Effect of Elastic Waves on the Refractive Index of a Medium

If a sinusoidally varying electrical potential is applied to a piezoelectric medium, two coupled waves propagate away from the source: an elastic displacement wave and an electrical wave. Both waves propagate as distortions in the solid and, associated with each of these waves, is a corresponding sinusoidally varying refractive index change. The change caused by the displacement is due to the photoelastic effect, while that caused by the electrical wave is due to the electro-optic effect. In practice, the waves are coupled, however, in the overlap analysis discussed in this chapter, the photoelastic and the electro-optic effects have been treated separately with the photoelastic constants used being those for zero electric field.

5.4.1. Photoelastic Effect

For an optically anisotropic crystal, the dielectric impermeability tensor can be defined in terms of an index ellipsoid such that[11]

$$B_{ij}\, x_i\, x_j = 1 \qquad \text{....5.13}$$

and where, using the Kronecker delta,

$$B_{ij}\varepsilon_{jk} = \delta_{ik} \qquad \text{....5.14}$$

and, along the principal axes only, $B_{ii} = 1/\varepsilon_{ii}$. By analogy with an isotropic medium

$$B_{ij} = (1/n^2)_{ij} \qquad \text{....5.15}$$

If the crystal undergoes a strain with components S_{kl} when under the effect of a stress T_{ij}, there is a resultant change in the dielectric impermeability due to the photoelastic effect. This change has the effect upon the index ellipsoid described by:

$$[\, B_{ij} + \Delta B_{ij} \,]\, x_i\, x_j = 1 \qquad \text{....5.16}$$

Pockels related this change to the strain component S_{kl} by a centrosymmetric photoelastic tensor P_{ijkl}

$$\Delta B_{ij} = P_{ijkl}\, S_{kl} \qquad \text{....5.17}$$

Due to symmetry, (5.17) reduces to

$$\Delta B_m = P_{mn} S_n \qquad \text{....5.18}$$

where $m = 1,2,...6$

$n = 1,2,3$

where the dimensionless photoelastic coefficients are defined in relation to the crystallographic axes. By assuming that the situation can be simplified greatly and because of the fact that relative variations of the index due to the photoelastic effect are always small compared with unity, the change in dielectric impermeability can be re-written in terms of the refractive index as

$$\Delta B_{ij} = -\frac{n^2}{2} P_{mn} S_n \qquad \text{....5.19}$$

5.4.2. The Electro-optic Effect

In a piezoelectric crystal, a change occurs in the dielectric impermeability due to the presence of an electric field. This is known as the electro-optic effect, and the linear part or Pockels effect is given by[11]

$$\Delta B_{ij} = r_{ijn} E_n \qquad \text{....5.20}$$

where r_{ijn} is the electro-optic tensor of rank 3.

Again, assuming a much simplified system and using the reduced notation, it is possible to re-express Equation (5.18) in terms of the refractive index such that

$$\Delta B_{ij} = -\frac{n^2}{2} r_{mn} E_n \qquad \text{....5.21}$$

where $m = 1,2,...,6$

$n = 1,2,3$

5.5. Interaction of a Surface Acoustic Wave and a Guided Optical Wave

The acousto-optic interaction mechanism in guided wave structures is the same as that in bulk wave structures. Propagating acoustic surface waves induce a periodic variation in the index of refraction of the substrate and incident guided optical waves, as they traverse the region of induced fluctuation in the index of refraction, will be diffracted provided that proper phase matching conditions exist.

It can be shown[12] that, under the proper phase matching conditions for Bragg diffraction, an incident guided optical beam can be converted efficiently into a diffracted beam propagating in another direction. The efficiency of this interaction is given by[13]

$$\eta = \sin^2\left\{\frac{\pi}{\lambda_o}\,\frac{|\Delta n|}{\cos\alpha_B}\,LF\right\} \qquad \ldots.5.22$$

with

$$F = \frac{\int v(x)\,|U(x)|^2\,dx}{\int |U(x)|^2\,dx} \qquad \ldots.5.23$$

where α_B is the Bragg angle for the phase matching condition between the incident and diffracted modes, λ_o is the free space optical wavelength and L is the interaction length. $U(x)^*$ represents the transverse variation of the electric field of the guided optical wave and v(x) represents the transverse dependence of the induced Δn due to the surface acoustic waves. It should be noted that for the bulk wave case $v(x) = U(x) = 1$ and $F = 1$[13].

The overlap integral F is a dimensionless quantity which has a value from 0 to 1 depending on the field distributions of the incident and diffracted optical waves and the acoustic waves.

There are three contributions to the change in refractive index at or near the surface of the crystal and, ultimately, to the overlap integral and diffraction efficiency. They are the photoelastic effect, the electro-optic effect and a surface ripple effect. This latter contribution causes a periodic thickness variation in the waveguide. Movement of the dielectric boundary produces a change in the effective index of refraction and, as a result, also contributes to the diffraction of a guided optical mode.

This parameter is given by

$$\Delta n = 1/2\ \delta_0\ \frac{(n^2 - 1)}{n}\ \frac{|U(0)|^2}{\int |U(x)|^2\ dx} \qquad ....5.24$$

and is a single constant which is very small and was ignored in comparison with the elasto-optic and electro-optic contributions[13,14].

It can be shown that[15], for Bragg diffraction of a TE mode in, for example, YZ-$LiNbO_3$ equation (5.22) can be re-expressed in the form

$$\eta = \sin^2\left\{\frac{2\pi\delta_0}{\lambda_0}\ \frac{n^3}{4\cos\alpha_B}\ \frac{2\pi L}{\lambda_a}\ |\bar{p}|\right\} \qquad ....5.25$$

where δ_0 is the amplitude of the surface displacement in the y or x_2 direction, λ_a the acoustic wavelength, n the waveguide mode effective index and $\bar{p}$ the effective photoelastic constant, taking into account the overlap integral. $\bar{p}$ includes contributions due to the acousto-optic (p_{ao}) and the electro-optic (p_{eo}) effects, i.e. $\bar{p} = \bar{p}_{ao} + \bar{p}_{eo}$.

In this notation

$$F|\Delta n| = \frac{n^3}{2} \frac{2\pi\delta_o}{\lambda_a} |\bar{p}| \qquad \ldots.5.26$$

where it can be shown that

$$\bar{p}_{ao} = \frac{\lambda_a}{2\pi\delta_o} p_{mn} S_n \qquad \ldots.5.27$$

and

$$\bar{p}_{eo} = \frac{\lambda_a}{2\pi\delta_o} r_{mn} S_n \qquad \ldots.5.28$$

For a TE wave on YZ-$LiNbO_3$, with the assumption that the acoustic wave is uniform in the x-direction, equations (5.27) and (5.28) expand to

$$\bar{p}_{ao} = \frac{\lambda_a}{2\pi\delta_o} [\, p_{32} S_2(y) + p_{33} S_3(y) \,] \qquad \ldots.5.29$$

$$\bar{p}_{eo} = \frac{\lambda_a}{2\pi\delta_o} r_{33} E_3(y) \qquad \ldots.5.30$$

where p_{32}, p_{33} and r_{33} are the photoelastic and electro-optic coefficients respectively. $S_2(y)$ and $S_3(y)$ are the strain components of the Rayleigh wave and $E_3(y)$ the electric field.

For the above orientation of optical and acoustic waves, the overlap integral can be expressed as follows

$$|\bar{p}| = |\bar{p}_{ao} + \bar{p}_{eo}|$$

where

$$\bar{p}_{ao} = \frac{\lambda_a}{2\pi\delta_o} \frac{\int [p_{s,2}S_2(y) + p_{s,3}S_3(y)] \, |U_m(y)|^2 \, dy}{\int |U_m(y)|^2 \, dy} \quad \ldots.5.31$$

and

$$\bar{p}_{eo} = \frac{\lambda_a}{2\pi\delta_o} \frac{\int r_{s,3}E_3(y) \, |U_m(y)|^2 \, dy}{\int |U_m(y)|^2 \, dy} \quad \ldots.5.32$$

where $U_m(y)$ is the amplitude of the m^{th} TE optical mode.

* For the situation where the incident and diffracted waves propagate as the same mode.

5.6. Implementation of Overlap Analysis

5.6.1. Introduction

The overlap integral equations 5.31 and 5.32 have been implemented for acousto-optic interaction in proton-exchanged $LiNbO_3$ waveguides. The optical field distribution was calculated, for each waveguide, from the refractive index profiles, and the stress and electric field terms were calculated from the displacement and electric field equations of 5.10 and 5.11. Proton-exchanged optical waveguides were fabricated, by various methods, on X-cut $LiNbO_3$ and the resultant refractive index profiles were determined from the measured modal refractive index values and the corresponding exchange depth.

5.6.2. Derivation of Elastic and Electric Field Equations

For surface waves propagating in the z-direction of a semi-infinite $LiNbO_3$ crystal with the y-direction normal to the surface, Spaight and Koerber[16] have derived non-uniform plane-wave solutions to the stress equation of motion and Maxwell's equation for the electric field. These equations have been used to derive the components of strain and electric field necessary to solve equations 5.31 and 5.32, and have been reproduced in

Appendix 5.1 with the associated numerical values for the decay and amplitude constants.

The equations were originally derived by Tseng and White[10] from the stress and strain relations for x-propagating acoustic waves on Hexagonal Class-6m crystals. $LiNbO_3$ is a Trigonal Class-3m crystal and Appendix 5.2 details the derivation of similar equations presenting also the stress and strain relationships for this type of crystal[11,17]. Appendix 5.2 also contains the exact strain equations for acoustic waves on YZ-$LiNbO_3$. These were derived from the displacement equations (see equation 5.2) and were used directly in the implementation of equations 5.31 and 5.32. Spaight and Koerber[16] provided the numerical values for the decay and amplitude constants, while values of elasto-optic and electro-optic constants were obtained from Pressley[18]. The numerical integration required to implement equations 5.31 and 5.32 was performed using Simpsons Rule.

To ensure the validity of the displacement and electric field equations presented in Appendix 5.1 and the calculated data of Spaight and Koerber[16], the boundary condition for a stress free surface at y = 0 was checked. The equations for the stress normal to the surface are presented in Appendix 5.3 (Equations 5.44). These equations were implemented using the definitions of strain and electric field of Appendix 5.2 and the elastic and piezoelectric constants for Trigonal Class-3m crystals[19]. In all cases, the condition was satisfied to an accuracy of 1 in 10^{-4}.

It has been shown for pure melt proton-exchange waveguides on Y-cut $LiNbO_3$[20], that a stress free surface does not exist and a large increase in induced strain has been measured along an axis normal to the crystal surface. This strain can, however, be relieved by post annealing[6] or by using dilute melts[21], and the present simple analysis assumes that the only strain present in the waveguide is due to propagation of elastic waves.

5.6.3. Determination of the Optical Field Profile

The value of the overlap integral defined by equations 5.31 and 5.32 was calculated numerically using a computer program written by the author. The electric field profile of the guided optical wave was obtained, for various refractive index profiles, using a computer program based upon the Vassel technique[22]. This program yielded both the theoretical mode effective indices of a waveguide, where the refractive index profile had been defined, and the resultant optical field distribution for either TE or TM polarisation. Measured IWKB[23] refractive index profiles were used as input data to the Vassel program and a comparison was made between the measured and theoretically calculated mode effective index values. Good agreement was found.

Proton-exchanged X-cut $LiNbO_3$ waveguides were fabricated from either pure or dilute Benzoic acid melts using the procedure outlined earlier in Chapter 3. 0.5% Dilute melt proton-exchange waveguides were fabricated at 220°C for a period of between 10 minutes and 7 hours, resulting in step-index waveguides of various depths up to 1.2μm. Pure melt proton-exchange waveguides were exchanged for 15 and 60 minutes at 210°C, resulting in single mode and multimode waveguides with step-index profiles. These waveguides were annealed, in an atmosphere of wet flowing O_2, at 400°C for 30 minutes, with subsequent samples being successively annealed for double the time period up to a maximum of 8 hours.

For each annealed waveguide, the modal effective indices were determined, using the prism coupling technique of equation 3.1. These effective index values were used as input data for the IWKB technique which returned refractive index profiles and exchange depths corresponding to the measured effective index values. This exact technique has been employed previously[6] to show that prolonged annealing of pure melt proton-exchanged waveguides results in waveguides with graded index profiles.

The modal refractive index values and their associated exchange depths were used as input data to a curve fitting procedure based upon the piecewise-polynomial (B-spline)

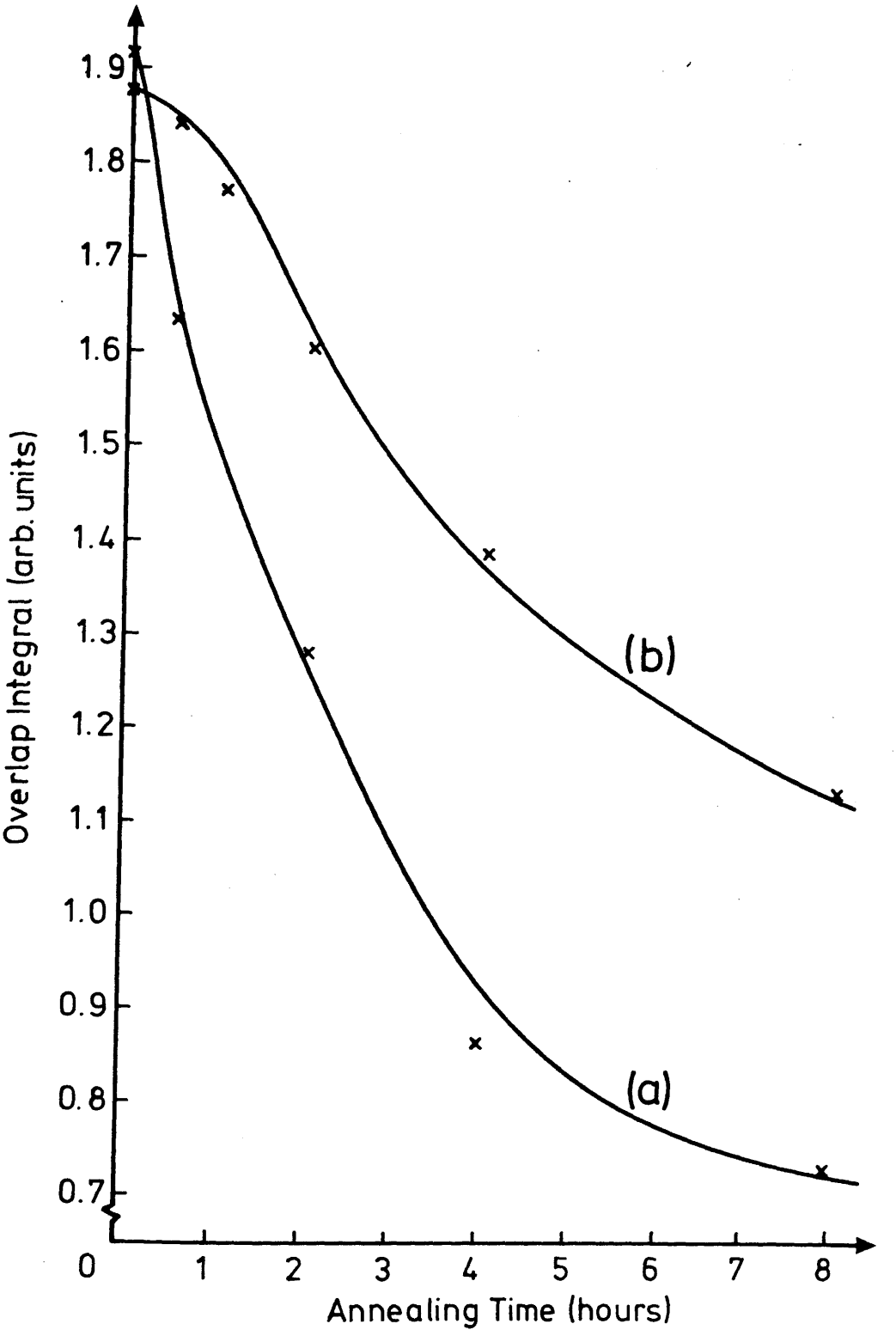

Figure 5.1 The variation in overlap integral with annealing time for pure melt proton exchanged waveguides at an acoustic frequency of 425MHz.
Waveguides fabricated for:
(a) 15 mins
(b) 60 mins
} at 210°C

5.7. Results and Analysis

5.7.1. Overlap Integral for Waveguides with Graded-index Profiles

Figure 5.1 shows the variation in the overlap integral with annealing time for two pure melt proton-exchange waveguides on X-cut $LiNbO_3$ which have undergone successive post-annealing. The waveguides were exchanged in a pure melt at 210° for 15 and 60 minutes and annealed in an atmosphere of wet flowing O_2 at 400°C for up to 8 hours. Originally, the waveguides had step-index profiles with depths of 0.44μm and 1.0μm respectively (calculated using IWKB method). However, after annealing for 8 hours the waveguides had graded index profiles with the WKB turning point of the highest order mode ~ 17μm. The acoustic frequency was 425 MHz, corresponding to an acoustic wavelength on proton-exchanged X-cut $LiNbO_3$ of ~ 8.28μm[26] and the analysis considered the TE_0 mode only.

The value of the overlap integral falls away dramatically with annealing time, corresponding to a change in the refractive index profile from a step-profile to a graded-profile[6]. This reduction in overlap is similar to the trend observed experimentally by Dawar et al.[2] where the acousto-optic diffraction efficiency, at 425MHz in Y-cut $LiNbO_3$, proton-exchanged for 3 minutes at 210°C, was observed to fall from 72% after 15 minutes annealing to 0.35% after 2 hours annealing. Dawar's device was fabricated in a pure melt for 15 mins at 210°C and was annealed at 400°C to reduce the in-plane scattering.

It can be seen from Figure 5.1 that the magnitude of the reduction in overlap integral is related to the exchange time. In fact, for 2 hours annealing, a waveguide exchanged for 60 minutes showed a reduction of 14% while the waveguide exchanged for 15 minutes was reduced by 33%. However, this relation cannot be directly applied to the waveguide exchanged for only 3 minutes since the rate of change of the overlap integral is not linear and increases with a corresponding reduction in the exchange time. It does, however, indicate that the reduction in the overlap integral for the waveguide exchanged for 3 minutes should be greater than

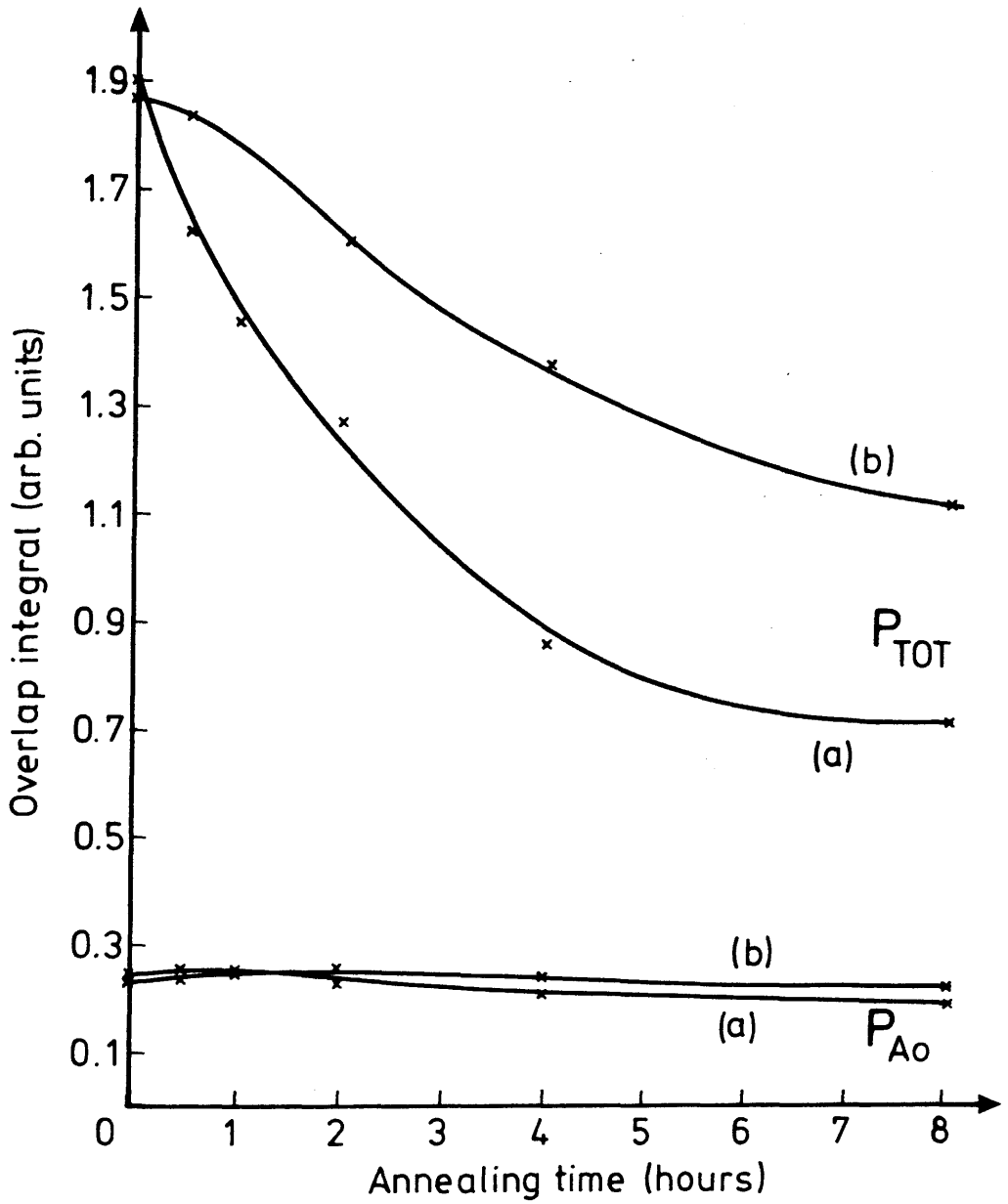

Figure 5.2 The variation in overlap integral with annealing time for pure melt proton exchange $LiNbO_3$ waveguides:- with (P_{TOT}) and without (P_{EO}) electrooptic contribution.

33%. Only once experimental data (e.g. refractive index profiles in relation to annealing time) for the waveguide exchanged for 3 minutes is analysed, using the overlap integral analysis, can a full comparison be made.

From the theoretical calculations for a TE mode on the stress free surface of a YZ-$LiNbO_3$ waveguide, the strain contributions (equation 5.29) approximately cancel for light propagating near the surface of the waveguide. The strong interaction that occurred was due almost entirely to the piezoelectrically induced field. This domination of the electro-optic contribution to the total overlap is emphasised in Figure 5.2, for X-cut $LiNbO_3$ waveguides, where a comparison between the overlap integral of Figure 5.1 and that of the same waveguides assuming zero electro-optic contributions is shown. Results here indicate that the electro-optic contribution to the overlap integral can be as much as 10 times greater than that of the elasto-optic contribution and, if indications of a reduced electro-optic effect in pure melt proton-exchange waveguides[3,4] were proved to be correct, then these results would show that the overall acousto-optic interaction efficiency would be severely reduced in such an electro-optically deficient crystal. This electro-optic domination of the acousto-optic interaction has also been found theoretically for titanium-indiffused waveguides on $LiNbO_3$ by Lean et al.[13] and for out diffused $LiNbO_3$ waveguides by Tsai et al.[14,27].

Figure 5.2 also indicates that for an electro-optically deficient crystal, the variation in overlap integral with index profile is constant and determined by the photoelastic properties of the waveguide. For non annealed waveguides the photoelastic contribution to the total overlap integral is 14% and this contribution increases with annealing time. Dawar et al.[2], however, reported almost total extinction of the acousto-optic diffraction after 2 hours annealing. Therefore, it is probable that the overlap analysis presented in this chapter does not describe fully the acousto-optic interaction process in pure melt proton-exchange waveguides and investigations are necessary to determine exactly how the electro-optic contribution is modified

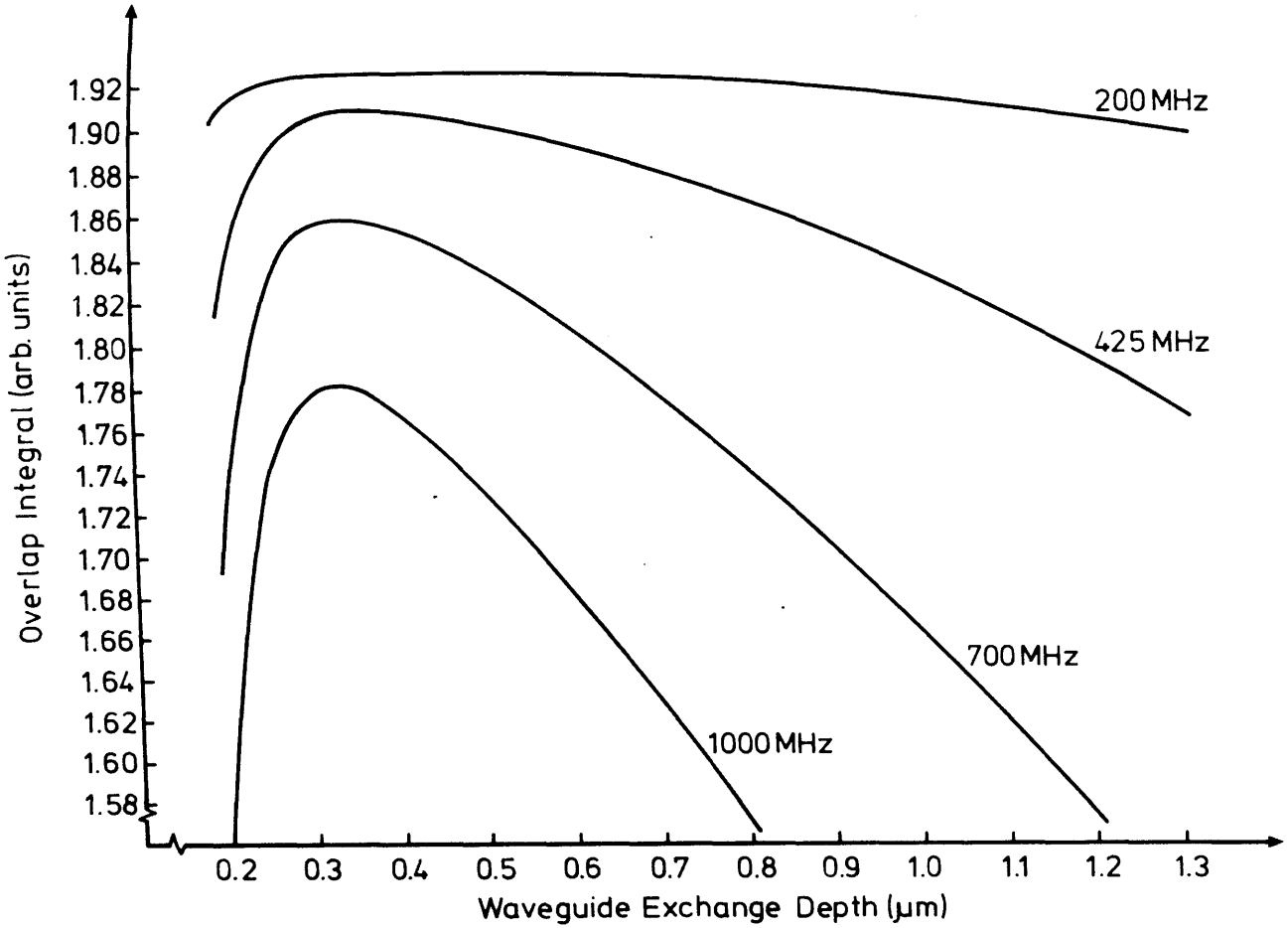

Figure 5.3 The variation in overlap integral with waveguide exchange depth for various values of acoustic frequency. Waveguides are produced by dilute melt proton exchange and have step index profiles.

as the annealing progresses i.e. is it eventually restored.

5.7.2. Overlap Integral for Waveguides with Step-index Profiles

Proton-exchange waveguides fabricated from dilute benzoic acid melts have step-index profiles and do not require post annealing to remain stable[28,5]. Waveguides of this kind have very low in-plane scattering losses and some quoted results indicate that the electro-optic properties of the crystal are preserved[29]. In general, dilute melt proton-exchange waveguides suffer less damage and are of far better quality than those fabricated from pure melts. In addition, since these waveguides no longer require to be annealed, the step-index profile is maintained. This section determines whether, in comparison with graded-index profiles, the step-index profile results in greater acousto-optic efficiency.

X-cut $LiNbO_3$ waveguides were proton-exchanged in 0.5% dilute melts at 220°C, for up to 7 hours, resulting in exchange depths of up to 1.2μm. Figure 5.3 shows the variation in overlap integral with the exchange depth for the TE_0 mode of step index proton-exchange $LiNbO_3$ waveguides for various values of acoustic frequency. A peak value of overlap was obtained in the region between 0.3μm and 0.35μm. This region was independent of acoustic frequency. However, the peak value of overlap was frequency dependent, falling steadily with increasing frequency. This increase in acoustic frequency corresponds to a reduction in acoustic wavelength and hence a reduction in the penetration of the acoustic wave. In fact, for all values of waveguide depth, the overlap integral value falls with increasing acoustic frequency, corresponding to a reduced interaction volume. This result concurs with that obtained by Tsai et al[27] on graded index out-diffused $LiNbO_3$ waveguides. In this work the authors noted that the interaction efficiency fell with increased acoustic frequency and concluded that 'the smaller the optical penetration depth the higher will be the optimum acoustic frequency and diffraction efficiency'.

The overlap integral variation presented in Figure 5.3 for

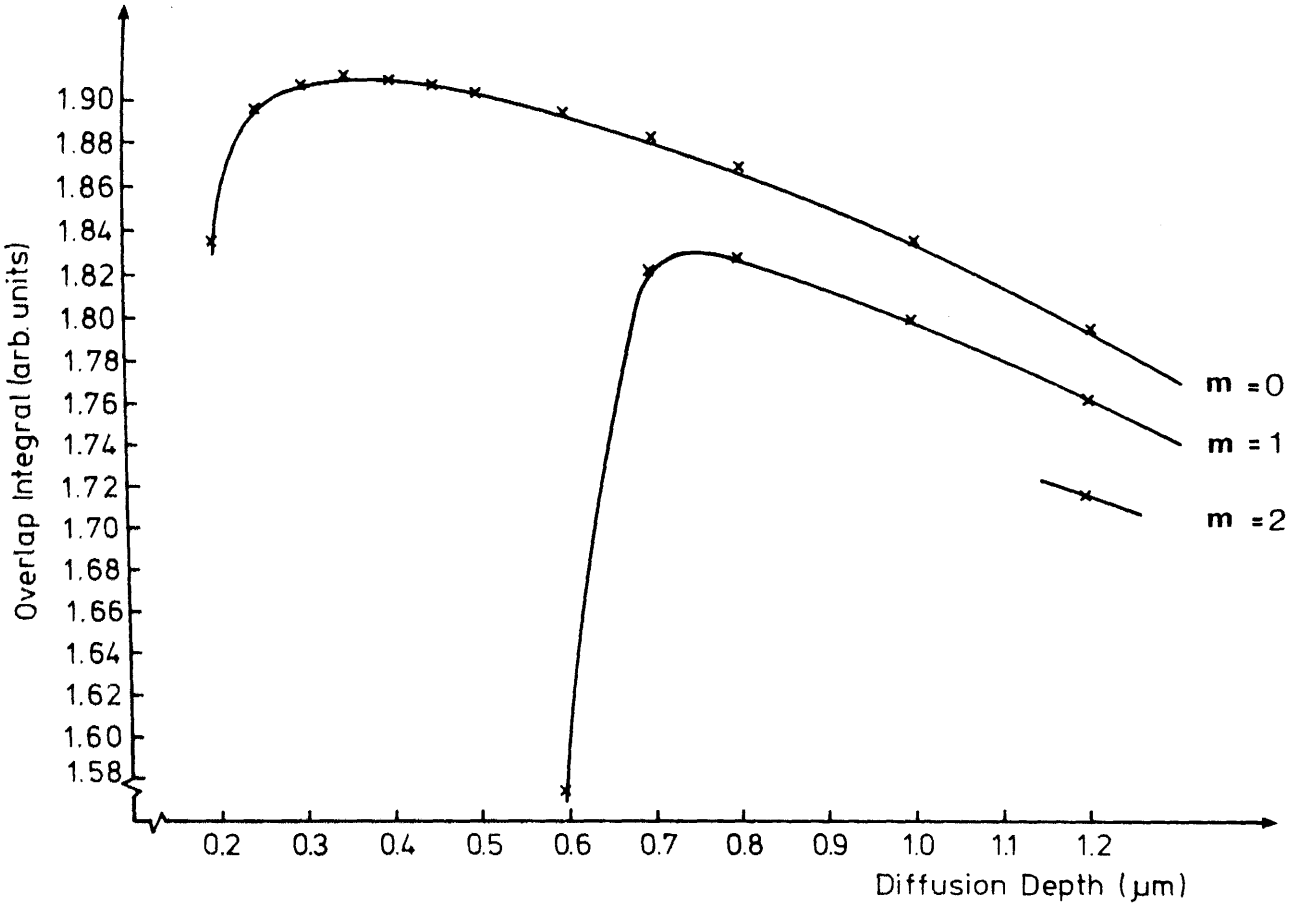

Figure 5.4 The variation in overlap integral with exchange depth for step-index proton exchange waveguides at 425 MHz

step-index waveguides at an acoustic frequency of 425 MHz can be compared with the variation of Figure 5.1 for graded-index waveguides. For the same acoustic frequency, the reduction in overlap integral with exchange depth is far more severe with graded-index waveguides than with step-index waveguides. This comparison is not ideal, since annealing times of only 2 hours result in waveguide depths far in excess of those used for the analysis of Figure 5.3. However, such annealing times have been required because of the poor condition of the pure melt waveguides[2] and, although, at annealing times of only a few minutes, the values of overlap were in theory equally as good as those of the step index waveguides, the quality of the waveguide did not allow for a practical device.

The variation in overlap against the waveguide mode order, m, is presented in Figure 5.4 for a step-index waveguide at an acoustic frequency of 425MHz. For a particular diffusion depth d, the peak value of overlap integral was obtained from the lowest waveguide mode. This was to be expected since higher order modes are less confined to the surface region and therefore are less affected by the surface acoustic waves[13]. For a 0.5% dilute proton-exchange X-cut $LiNbO_3$ waveguide and an acoustic frequency of 425MHz, the theoretical depth for maximum diffraction efficiency is 0.35μm. Experimental results presented in Chapter 6 of this thesis indicate however that the peak diffraction efficiency was in fact obtained at approximately 0.2μm. This indicates that results obtained in this chapter cannot be taken to be exact, numerically, and must be looked upon only as providing guidelines. The theoretical results do, however, indicate that step-index waveguides result in higher diffraction efficiencies than annealed waveguides and that the electro-optic contribution completely dominates the acousto-optic interaction.

A point which has not been considered in this analysis is the possible effect that additional stress, produced by the proton-exchange process, might have on the interaction efficiency. It has been shown[20] that the proton-exchange process causes an increase in strain along an axis normal to the waveguide surface and that this increase can cause stress fractures. It has also been shown

that this induced stress can be relieved either by post annealing[6] or by fabrication from dilute melts with large dilution ratios[21]. However, the above analysis has indicated that prolonged post exchange annealing can result in reduced interaction efficiencies. Therefore for high efficiency acousto-optic proton-exchanged devices, fabrication from dilute melts followed by, at most, a relatively short annealing period is desirable.

5.8. Conclusions

This chapter has investigated the overlap integral for acousto-optic interaction on proton-exchanged $LiNbO_3$ waveguides. A simple analysis has been used to examine the elasto-optic and electro-optic contributions to the interaction and the importance of the waveguide index profile to the interaction efficiency was assessed. In summary, the results indicate that shallow step-index waveguides are required for maximum interaction efficiency and that prolonged annealing results in reduced interaction efficiencies. Results obtained in this chapter are similar to investigations performed on out-diffused[14,27] and Titanium in-diffused[13] $LiNbO_3$ waveguides. Numerically, a comparison between the different results cannot be made, but the systematic trends relating to diffusion depth and acoustic frequency which were predicted by Tsai et al[14,27] have been repeated in this analysis. In addition, the magnitude and importance of the electro-optic contribution reported by these authors has been emphasised.

An important parameter in acousto-optic interaction is the ratio of diffraction efficiency to input power, which should be maximised. In theory, maximum diffraction efficiency can be obtained, regardless of index profile, if sufficient r.f. drive power is available. However, the importance of this kind of analysis is to indicate, for a fixed value of acoustic power, which interaction geometry is most suitable for high diffraction efficiency, and what would be the effect of a change in optical depth or acoustic frequency.

Appendix 5.1 Equations for displacement and electrical waves in YZ-$LiNbO_3$

The following equations describe displacement and electrical wave propagation on the surface of a Trigonal Class-3m crystal. The equations form solutions to the equations of motion for an infinite plane wave propagating in the z-direction of a y-cut crystal. For a general substrate, there exist six coupled wave equations, having three components of particle displacement (U_1,U_2,U_3) and three components of electric field (E_1,E_2,E_3) as dependent variables. For the case treated here, Maxwell's equations are solved to give two decoupled sets of equations having (U_2,U_3,E_2,E_3) and (U_1,E_1) as dependent variables. It is not possible to satisfy the free surface boundary conditions for the set (U_1,E_1)[10].

For the set (U_2,U_3,E_2,E_3), particular solutions which do satisfy the boundary conditions are of the form[16]:

$$U_2 = B_1(e^{i\alpha_1 ky} + m_{21}e^{i\alpha_2 ky} + m_{31}e^{i\alpha_3 ky})e^{i(kz - \omega t)},$$

$$U_3 = NB_1(e^{i\alpha_1 ky} + n_{21}e^{i\alpha_2 ky} + n_{31}e^{i\alpha_3 ky})e^{i(kz - \omega t)},$$

$$E_2 = kOB_1(e^{i\alpha_1 ky} + o_{21}e^{i\alpha_2 ky} + o_{31}e^{i\alpha_3 ky})e^{i(kz - \omega t)},$$

$$E_3 = kPB_1(e^{i\alpha_1 ky} + p_{21}e^{i\alpha_2 ky} + p_{31}e^{i\alpha_3 ky})e^{i(kz - \omega t)},$$

$$E_1 = U_1 = 0, \quad y <= 0, \qquad \text{....5.33}$$

where k is the wave number and B_1 represents the amplitude of the surface displacement at y = 0, i.e. $B_1 = \delta_0$ (see equation 5.25). (NB: 'O' is used in equation 5.33 to be consistent with the original equation definitions of Spaight and Koerber. This should

not be confused with zero.)

The dimensionless constants for a free surface on YZ-$LiNbO_3$ have been calculated by Spaight and Koerber[16] as follows:

$$v = 3.5105\ 10^3\ ms^{-1}$$
$$\alpha_1 = 0.06462 - i0.1217$$
$$\alpha_2 = 0.3804 - i1.0379$$
$$\alpha_3 = -0.3960 - i0.7738$$
$$N = -0.05180 + i0.09719$$
$$O = (-0.1826 + i0.1402)\ 10^9$$
$$P = (-1.5202 - i0.6931)\ 10^9$$
$$m_{21} = -0.02637 + i0.3719$$
$$m_{31} = 0.02740 - i0.5141$$
$$n_{21} = -1.9258 + i5.0939$$
$$n_{31} = -4.1164 - i1.4533$$
$$o_{21} = -32.435 - i22.191$$
$$o_{31} = 27.233 + i19.453$$
$$p_{21} = -3.6274 - i3.2912$$
$$p_{31} = -0.05632 + i5.3042$$

Values of elasto-optic and electro-optic constants used in equations 5.31 and 5.32, for $LiNbO_3$ are as follows[18]:

$$r_{33} = 30.8\ 10^{-12}\ mV^{-1}$$

$$p_{32} = 0.178$$

$$p_{33} = 0.088$$

Appendix 5.2 Piezoelectric Stress and Strain Relationships for Trigonal Class-3m Crystals

Throughout this section, the reduced notation (over 1,2,3) for repeated indices is employed,

e.g., $23,32 = 4$

$13,31 = 5$

$12,21 = 6$

Characteristic Equations

Solving equations 5.7 and 5.8, the piezoelectric equations for the Trigonal Class-3m crystal, with z the c-axis, are[11,18]:-

$$T_1 = c_{11}S_1 + c_{12}S_2 + c_{13}S_3 + c_{14}S_4 + e_{22}E_2 - e_{31}E_3,$$

$$T_2 = c_{12}S_1 + c_{11}S_2 + c_{13}S_3 - c_{14}S_4 - e_{22}E_2 - e_{31}E_3,$$

$$T_3 = c_{13}S_1 + c_{13}S_2 + c_{33}S_3 - e_{33}E_3,$$

$$T_4 = c_{14}S_1 - c_{14}S_2 + c_{44}S_4 - e_{24}E_2,$$

$$T_5 = c_{44}S_5 + 2c_{14}S_6 - e_{24}E_1,$$

$$T_6 = 2c_{14}S_5 + c_{66}S_6 - 2e_{22}E_1, \qquad \ldots.5.34$$

$$D_1 = e_{15}S_5 - 2e_{22}S_6 + \varepsilon_{11}E_1,$$

$$D_2 = -e_{22}S_1 + e_{22}S_2 + e_{15}S_4 + \varepsilon_{11}E_2,$$

$$D_3 = e_{31}S_1 + e_{31}S_2 + e_{33}S_3 + \varepsilon_{33}E_3. \qquad \ldots.5.35$$

From equation 5.2, the components of the strain are expressed in terms of the components of the displacement by[11]:-

$$S_1 = S_{11} = (\partial U_x/\partial x),$$

$$S_2 = S_{22} = (\partial U_y/\partial y),$$

$$S_3 = S_{33} = (\partial U_z/\partial z),$$

$$S_4 = 2S_{23} = (\partial U_z/\partial y) + (\partial U_y/\partial z),$$

$$S_5 = 2S_{13} = (\partial U_x/\partial z) + (\partial U_z/\partial x),$$

$$S_6 = 2S_{12} = (\partial U_y/\partial x) + (\partial U_x/\partial y). \qquad \ldots.5.36$$

and from equation 5.3 the stress equations of motion are

$$\rho(\partial^2 U_x/\partial t^2) = (\partial T_1/\partial x) + (\partial T_6/\partial y) + (\partial T_5/\partial z),$$

$$\rho(\partial^2 U_y/\partial t^2) = (\partial T_6/\partial x) + (\partial T_2/\partial y) + (\partial T_4/\partial z),$$

$$\rho(\partial^2 U_z/\partial t^2) = (\partial T_5/\partial x) + (\partial T_4/\partial y) + (\partial T_3/\partial z), \qquad \ldots.5.37$$

The electric fields associated with the elastic wave must also satisfy Maxwell's equation,

$$\text{curl}(\text{ curl } E) = -\mu_0(\partial^2 D/\partial t^2). \qquad \ldots.5.38$$

(Note: It must be understood that this is a quasi-static approximation which deals with electric waves which propagate in a crystal at a velocity determined by the velocity of the acoustic wave.)

Surface waves are considered which propagate in the z-direction with their amplitudes decaying with depth y. The nonuniform plane-wave solutions for equations 5.37 and 5.38 can then be assumed to have the following form[10]:-

$$U_x = A \exp(\Omega_x ky) \exp[i(kz - \omega t)],$$

$$U_y = B \exp(\Omega_y ky) \exp[i(kz - \omega t)],$$

$$U_z = C \exp(\Omega_z ky) \exp[i(kz - \omega t)],$$

$$E_x = k\xi \exp(\Omega_x ky) \exp[i(kz - \omega t)],$$

$$E_y = k\gamma \exp(\Omega_y ky) \exp[i(kz - \omega t)],$$

$$E_z = k\eta \exp(\Omega_z ky) \exp[i(kz - \omega t)], \quad \text{for } y <= 0, \qquad \ldots.5.39$$

where the complex dimensionless decay constant Ω, the wave number k, and the amplitude constants A,B,C,ξ,γ, and η have been determined for YZ-$LiNbO_3$ by Spaight and Koerber (see Appendix 5.1)

Formulation of Strain Equations

Using the strain relations for Trigonal Class-3m crystals given in equations 5.36 and the displacement equations for YZ-$LiNbO_3$ given in Appendix 5.1, it is possible to formulate the strain relations for acoustic waves on YZ-$LiNbO_3$ as follows:-

$$S_1 = 0,$$

$$S_2 = ikB_1(\alpha_1 e^{i\alpha_1 ky} + \alpha_2 m_{21} e^{i\alpha_2 ky} + \alpha_3 m_{31} e^{i\alpha_3 ky}) e^{i(kz - \omega t)},$$

$$S_3 = ikNB_1(e^{i\alpha_1 ky} + n_{21} e^{i\alpha_2 ky} + n_{31} e^{i\alpha_3 ky}) e^{i(kz - \omega t)},$$

$$S_4 = ikNB_1(\alpha_1 e^{i\alpha_1 ky} + \alpha_2 n_{21} e^{i\alpha_2 ky} + \alpha_3 n_{31} e^{i\alpha_3 ky}) e^{i(kz - \omega t)}$$

$$+ ikB_1(e^{i\alpha_1 ky} + m_{21} e^{i\alpha_2 ky} + m_{31} e^{i\alpha_3 ky}) e^{i(kz - \omega t)},$$

$$S_5 = 0,$$

$$S_6 = 0. \qquad \ldots.5.40$$

Appendix 5.3 Application of Boundary Conditions at a Stress Free Surface

Assuming that the crystal surface is stress free (which is dubious on proton-exchanged Y-cut $LiNbO_3$), the mechanical boundary conditions at each point on the surface of the crystal are

$$T_{2j}|_{y=0} = C^{E}_{2jkl}S_{kl} + e_{k,ij}E_k|_{y=0} = 0 \qquad ....5.42$$

The two boundary conditions on the electric potential (equation 5.35) are the continuity of the electric field E at y = 0 and the continuity of the normal component of the electric displacement across the surface of the crystal.

Using reduced notation, equation 5.42 can be re-expressed as

$$T_{6\,(21)}\,(y=0) = T_{2\,(22)}\,(y=0) = T_{4\,(23)}\,(y=0) = 0 \qquad ....5.43$$

For a Y-cut, trigonal class-3m crystal, with surface waves as defined in 5.39, equation 5.43 can be expanded using equation 5.34 to give

$$T_6(0) = 0$$

$$T_2(0) = c_{11}S_2(0) + c_{12}S_3(0) - c_{14}S_4(0) - e_{22}E_2(0) - e_{21}E_3(0) = 0$$

$$T_4(0) = -c_{14}S_2(0) + c_{44}S_4(0) - e_{24}E_2(0) = 0 \qquad ....5.44$$

References to Chapter 5.

1. R.L. Davis, 'Acousto-optic Bragg diffraction in proton-exchanged waveguides', Proc. Soc. Photo-opt. Inst. Eng., Vol. 517, pp 74-81, 1984.

2. A.L. Dawar, S.M. Al-Shukri and R.M. De La Rue, 'Guided wave acousto-optic interaction in proton-exchanged Y-cut $LiNbO_3$', Appl. Phys. Letts., Vol. 48, No. 23, pp 1579-1581, 1986.

3. K.K. Wong, R.M. De La Rue, and S. Wright, 'Electro-optic waveguide frequency translator in $LiNbO_3$ fabricated by proton-exchange', Opts. Letts., Vol 7, No. 2, pp 131-133, 1983.

4. R.A. Becker, 'Comparison of guided wave interferometric modulators fabricated on $LiNbO_3$ via Ti:indiffusion and proton -exchange', Appl. Phys. Letts., Vol. 43, No. 2, pp 131-133, 1983.

5. S.M. Al-Shukri, J.F. Duffy, R.M. De La Rue, G. Mazzi, A. Carnera and M.N. Armenise, 'Single mode planar and stripe waveguides by proton-exchange in lithium tantalate and lithium niobate', Proc. Soc. Photo-opt. Inst.Eng., Vol. 651, pp. 20-25, 1986.

6. S.M. Al-Shukri, A.L. Dawar, R.M. De La Rue, A.C.G. Nutt, M. Taylor, J.R. Tobin, G. Mazzi, A. Carnera and C. Summonte, 'Analysis of annealed proton-exchanged waveguides in $LiNbO_3$ by optical waveguide measurements and microanalytical techniques', Proc. 7th Topical Meeting on Integrated and Guided Optics, Orlando, Florida, U.S.A., PDP71-4, April 1984.

7. R.M. White, 'Surface elastic waves', Proc. IEEE, Vol. 58,No. 8, pp 1238-1275, 1970.

8. M.B. Schultz and J.H. Matsinger, 'Rayleigh-wave electro-mechanical coupling constants', Appl. Phys. Letts., Vol 20, No. 9, pp 367-369, 1972.

9. Lord Rayleigh, 'On waves propagated on the plane surface on an elastic solid', Proc. Lon. Math. Soc., Vol. 17, pp 4-11, 1885.

10. C.C. Tseng and R.M. White, 'Propagation of piezoelectric and elastic surface waves on the basal plane of hexagonal piezoelectric crystals', J. Appl. Phys., Vol. 38, No. 11, pp 4274-4280, 1967.

11. J.F. Nye, 'Physical Properties of Crystals', Oxford University Press, London, 1957.

12. R. Adler, 'Interaction between light and sound', IEEE Spectrum, Vol. 4, No. 5, pp 42-54, 1967.

13. E.G.H. Lean, J.M. White and C.D.W. Wilkinson, 'Thin-film acousto-optic devices', Proc. IEEE, Vol. 64, No. 5, pp 779-787, 1976.

14. C.S. Tsai, 'Guided-wave A.O. Bragg modulators for wide-band I.O. communications and signal processing', IEEE Trans Circuits and Systems, Vol. CAS-26, No. 12, pp 1072-1098, 1979.

15. J.M. White, P.F. Heidrich and E.G.H. Lean, 'Thin-film acousto-optic interaction in $LiNbO_3$', Elect. Letts., Vol. 10, No. 24, pp 510-511, 1974.

16. R.N. Spaight and C.G. Koerber, 'Piezoelectric surface waves on $LiNbO_3$', IEEE Vol. SU-18, No. 4, pp 237-238, 1971.

17. IEEE Standard on Piezoelectricity 1979, published in IEEE Trans on Sonics and Ultrasonics, Vol SU-31, No. 2,1984.

18. R.J. Pressley, Ed. Handbook of lasers and selected data of optical technology, pp 452-482, Chemical Rubber Co., 1971.

19. A.W. Warner, M. Onoe and G.A. Coquin, 'Determination of elastic and piezoelastic constants for crystals in class

(3m)', J. Aco. Soc. Amer., Vol. 42, No. 6, pp 1223-1231, 1967.

20. A. Campari, C. Ferrari, G.Mazzi, C. Summonte, S.M. Al-Shukri, A. Dawar, R.M. De La Rue, and A.G.C. Nutt, 'Strain and surface damage induced by proton-exchange in Y-cut $LiNbO_3$', J.Appl. Phys., Vol. 58, No.12, pp 4521-4524, 1985.

21. M. Minakata, K. Kumagai, and S. Kawakami, 'Studies on lattice constant changes and electro-optic effects in proton-exchanged $LiNbO_3$ optical waveguides', First Optoelectronics Conf., Paper A2-2, Tokyo, July, 1986.

22. M.O. Vassell, 'Structure of optical guided modes in planar multilayers of optically anisotropic materials', J. Opt. Socm. Am., Vol. 64, No. 2, pp 166-173, 1974.

23. J.M. White and P.F. Heidrich, 'Optical waveguide refractive index profiles determined from measurement of mode indices : a simple analysis', Appl. Opts. Vol 15, No.1, pp151-155, Jan 1976.

24. A.J. Slobodnik Jr., R.J. Delmonico and E.D. Conway, Microwave Acoustics Handbook, Vol. 1A, Air Force Research Labs., Mass., U.S.A. AFGL-TR-730597, 1973.

25. A.J. Slobodnik, Jr., 'Surface acoustic waves and SAW devices', Proc. IEEE, Vol. 64, No. 5, pp 581-595, 1976.

26. P.J. Burnett, G.A.D. Briggs, S.M. Al-Shukri, J.F. Duffy, R.M. De La Rue, 'Acoustic properties of proton exchanged $LiNbO_3$ studied using the acoustic microscopy V(Z) technique', J. Appl. Phys., Vol. 60, No.7, pp 2517-2522, 1986.

27. C.S. Tsai, M.A. Alhaider, Le. Trong. Nguyen, B. Kim, 'Wide-band guided-wave acoustooptic Bragg diffraction and devices using multiple tilted surface acoustic waves' Proc. IEEE., Vol. 64, No. 3, pp 318-328, 1976.

28. S.M. Al-Shukri, J.F. Duffy, R.M. De La Rue, M.N. Armenise, C. Canali and A. Carnera, 'Proton-exchanged optical waveguides on lithium niobate: devices, characterisation and future prospects', Proc. Soc. Photo-opt. Inst. Eng., Vol. 578, pp 2-6, 1985.

29. K.K. Wong, N.J. Parsons, A.R. Oldroyd and A.C. O'Donnell, 'High quality optical waveguides in $LiNbO_3$ by dilute melt proton-exchange', Proc. IOOC/ECOC '85, pp 59-62. Venice, 1985.

CHAPTER 6. Acousto-optic Surface Acoustic Wave Devices: Design and Operation

6.1. Introduction

In the previous chapter, the principles of acousto-optic interaction and the ways in which variations in the proton-exchange process affected the acousto-optic interaction were discussed. That chapter dealt also with the issue of the overlap between the acoustic wave and the optical wave and ways of determining fabrication conditions to optimise this interaction. This chapter deals, initially, with the design and fabrication of the electrode structure used to launch the acoustic waves on the piezoelectric material and, latterly, with the operation of proton-exchanged acousto-optic devices, detailing the conditions for maximum diffraction efficiency and minimum drive power. Resistive losses in the electrode structure also give rise to noticeable thermo-optic behaviour in proton-exchanged lithium niobate and lithium tantalate waveguides and comparison of the results obtained with results previously published for titanium indiffused lithium niobate waveguides will be made.

6.2. Acousto-optic Interaction using Surface Acoustic Waves

The use of surface acoustic waves (SAW) and planar optical waves for acousto-optic interaction provides distinct advantages over bulk wave interaction in terms of transducer design and power requirements[1,2], where the confinement of the optical and acoustical waves results in greater power densities. Such devices require materials which have low acoustic propagation loss, high electro-mechanical coupling coefficients, high electro-optic coefficients and are receptive to low loss optical waveguides. Two such materials are lithium niobate ($LiNbO_3$) and lithium tantalate ($LiTaO_3$). While many acousto-optic SAW devices have been reported[2,3,4] on $LiNbO_3$, a suitable waveguiding process (i.e. one which does not involve temperatures above the Curie temperature of the crystal) has only recently been developed[5,6] for $LiTaO_3$ and SAW acousto-optic diffraction has still to be demonstrated. $LiNbO_3$ and $LiTaO_3$ have very similar elastic and

electro-optic coefficients[7,8,9]. However, the electro-mechanical coupling coefficient for $LiTaO_3$ is approximately six times smaller than that of $LiNbO_3$[10] and, as a result, $LiTaO_3$ devices require more complicated transducer designs to provide comparable interaction efficiency.

Deposited metal electrode arrays, known as interdigital transducers (IDT), are the preferred method for SAW generation. The configuration of such an IDT structure is shown in Figure 6.1(a), while Figure 6.1(b) shows a schematic cross-section of the structure with the associated electric field distribution at some instant. Radio frequency (r.f.) signals are supplied to the IDT and there is a 3dB power loss at the input due to the bi-directionality of the structure[11]. Operating requirements such as input impedance and bandwidth will determine such parameters as finger width and spacing and the width of the acoustic aperture.

6.3. Design of the Interdigital Transducer

An IDT transforms a high frequency electrical signal into a sinusoidally propagating surface acoustic wave, utilizing the piezoelectric properties of the substrate. Ideally, this conversion takes place over a large frequency bandwidth and involves minimum power conversion loss due to impedance mismatch. Smith et al[12] have modelled the IDT as a series RLC circuit with acoustic radiation and reactance (see Figure 6.2) and have provided approximate equations for the radiation impedance as follows

$$R_a(\omega) \sim R_a \, (\sin(x)/x)^2 \qquad \ldots.6.1$$

$$X_a(\omega) \sim R_a \, (\sin(2x)-2x)/2x^2 \qquad \ldots.6.2$$

where

$$x = N\pi(\omega-\omega_o)/\omega_o \qquad \ldots.6.3$$

and

$$R_a = 4k^2/(\pi\omega_o C_s) \qquad \ldots.6.4$$

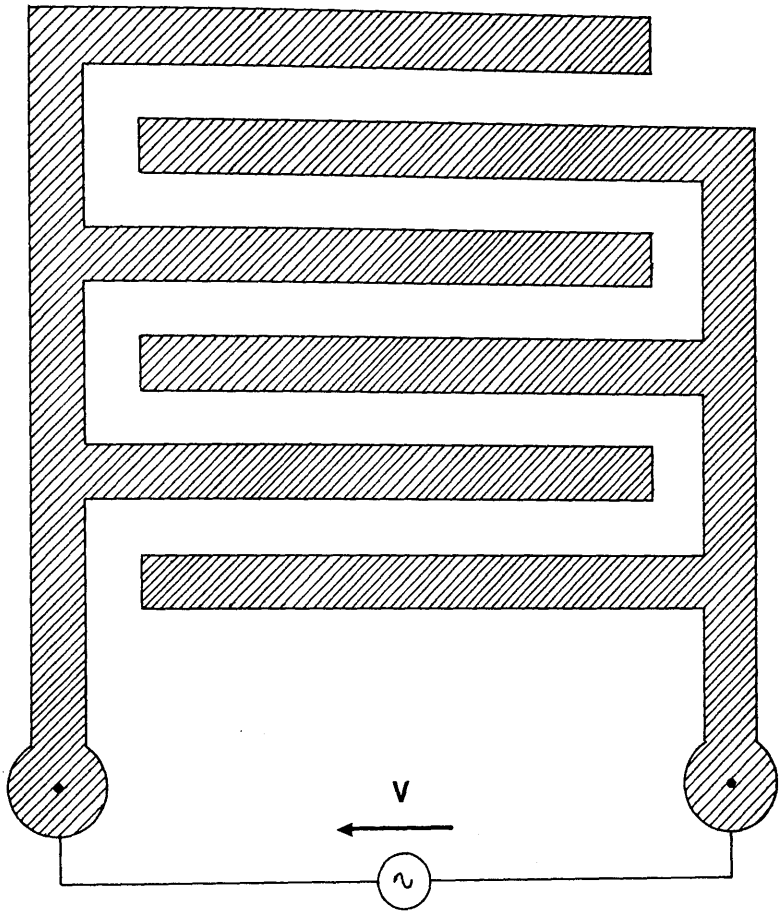

Figure 6.1(a) Plan view of IDT electrode structure.

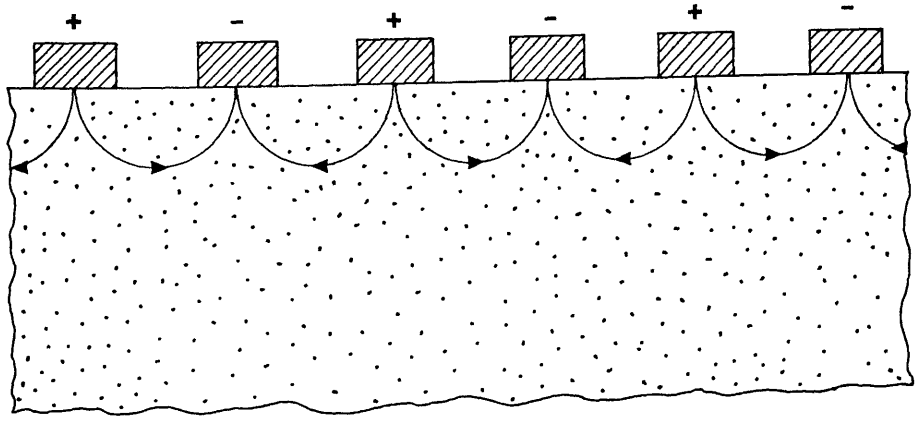

Figure 6.1(b) Cross – section of electrode structure.

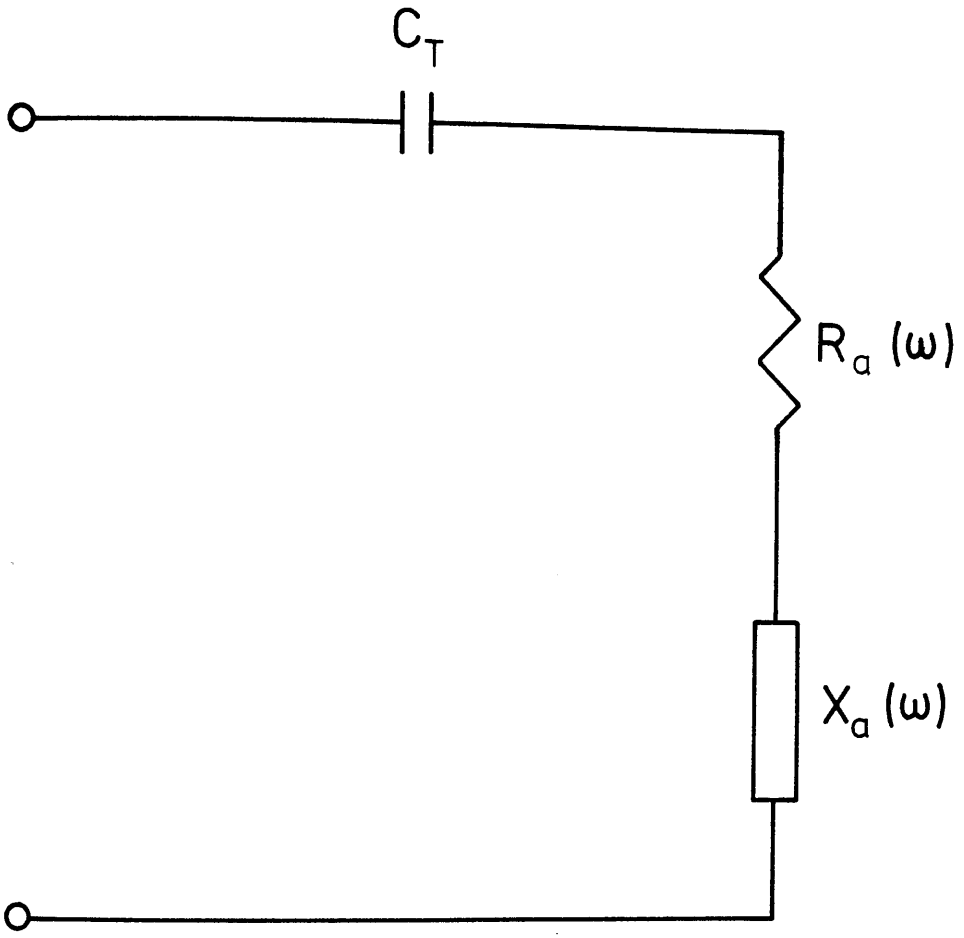

Figure 6.2 Series RLC representation for transducer electrical input impedance.

N is the number of interdigital periods, k the material electro-mechanical coupling coefficient, C_s the capacitance per periodic section and ω the synchronous frequency. With use of this simple RLC series circuit, it is possible to match the impedance of the IDT with the characteristic impedance of the supply circuit, typically 50Ω.

The overall bandwidth of the IDT is determined by the product of the transducer acoustic bandwidth and the electrical bandwidth of the RLC circuit and is, therefore, limited by the lower contribution. This quantity can be maximised by the following design criterion[11]:-

$$N^2 \sim \pi/(4k^2) \qquad \ldots.6.5$$

Hence, for a given IDT design, the maximum operating bandwidth is limited by the properties of the substrate material. However, this value can be increased by redesign of the IDT[13,14] and bandwidths in excess of 500MHz[15] have been reported.

The width of the acoustic aperture can be determined by the expression[16]

$$C_s = (2\pi C_{ff} V_s L)/\omega_o \qquad \ldots.6.6$$

where V_s is the velocity of the SAW, and C_{ff} is the capacitance per unit length. Using equations 6.4 to 6.6, optimum values of C_s, N, and L have been calculated for the IDT structures used in work described in this thesis on YZ $LiNbO_3$ and YZ $LiTaO_3$. The results are presented in Table 6.1.

From Table 6.1, it can be seen that the value of acoustic aperture L required for maximum bandwidth is approximately four times greater in $LiNbO_3$ than in $LiTaO_3$. This result means that, for a single IDT structure, the maximum possible acousto-optic diffraction efficiency in the $LiTaO_3$ device is reduced, in comparison with the $LiNbO_3$ device, by approximately a factor of 16.

Table 6.1 Design parameters for IDT on YZ $LiNbO_3$ and $LiTaO_3$

	$LiNbO_3$	$LiTaO_3$	Ref
V_s	$3488ms^{-1}$	$3230ms^{-1}$	(10)
V_{sp}	$3494ms^{-1}$	-	
k^2	0.045	0.0074	(16)
C_{ff}	$4.6438\ 10^{-10}Fm^{-1}$	$4.43523\ 10^{-10}Fm^{-1}$	(10)
N	4	10.5	
D_x	2μm	4μm	
f_o	425MHz	203MHz	
C_s	0.429125pF	0.147739pF	
L	$112\lambda_a$	$21\lambda_a$	

where D_x is the finger width, R_a=50Ω and L is measured in units of acoustic wavelength. V_{sp} is the SAW velocity on a proton-exchanged layer (see Table 4.3). The ratio of finger width to finger spacing is 1.

In order to make the acoustic apertures comparable, four simple IDT structures designed for operation on $LiTaO_3$ were connected in a series and parallel arrangement[17] to give a four times increase in the acoustic aperture L, yet to retain the characteristic 50Ω input impedance. The design is given in Figure 6.3.

The IDT structures defined in this section are designed for operation on YZ-$LiNbO_3$ and YZ-$LiTaO_3$ respectively. However, in practice, the crystal orientations which were used for acousto-optic device fabrication were XZ-$LiNbO_3$ and XZ-$LiTaO_3$. The choice of crystal orientations was governed by the waveguide fabrication conditions, as discussed earlier in Chapter 3. However, in Appendix 6.1, a comparison which is made between the acoustic parameters of each orientation indicates that the respective electrode structures are suitable for either orientation on the given material

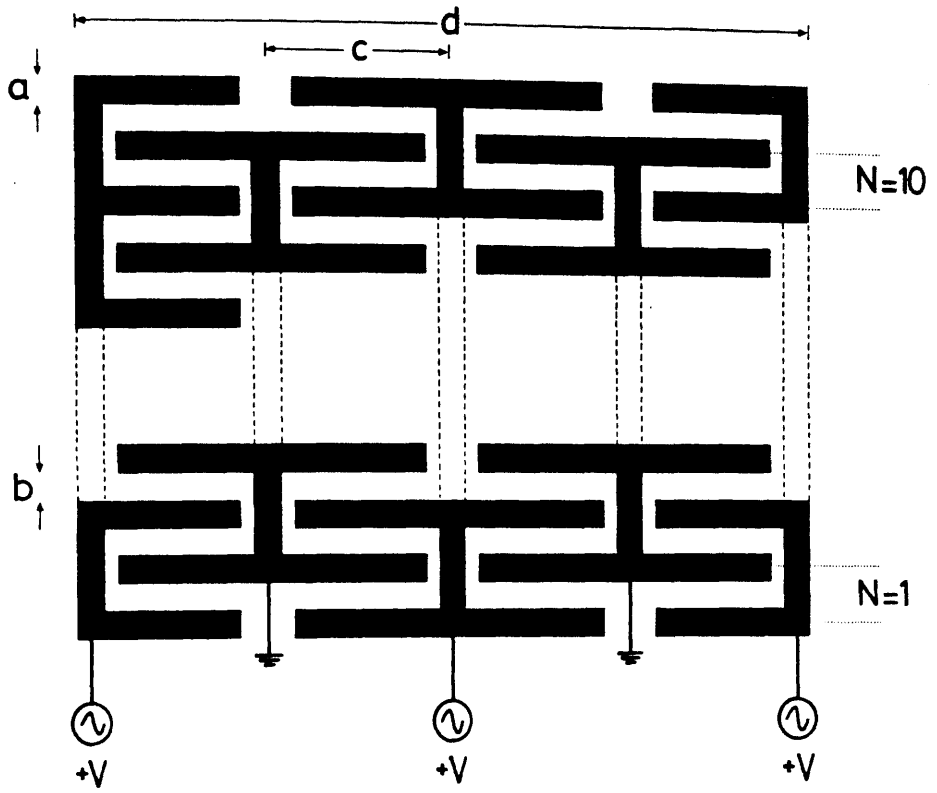

$a = b = 4\mu m$

$d = 4 * c = 100\Lambda$

$f_0 = 203\,MHz$

$N = 10.5$

Figure 6.3 Series/Parallel IDT structure for

$LiTaO_3$

6.4. Fabrication of Interdigital Transducer

Interdigital electrode patterns were fabricated on lithium niobate and lithium tantalate substrates on to which optical waveguides had been formed. Before optical waveguides were defined, a small rectangular area was covered with an arbitrary thickness of aluminium to protect it from the benzoic acid. It was on to this unexchanged area that the IDT was defined. This precaution was taken to ensure that the performance of the IDT was not impaired by the proton-exchange region. Once coated, waveguides were fabricated on the substrates, following the waveguide fabrication process of Chapter 3. After exchange, the solidified benzoic acid was removed using methanol and the aluminium protective layer removed using aluminium etch.

IDT patterns were photolithographically defined on the unexchanged areas by the 'aluminium etch' technique described in full in Chapter 4. In this instance light-field shadow masks were utilized to leave the desired pattern on the substrate. Figures 6.4(a) and 6.4(b) show IDT patterns on $LiNbO_3$ and $LiTaO_3$ waveguides respectively. The line widths were measured using an optical microscope and conformed very closely to the original mask design.

Once the sample had been thoroughly cleaned, it was mounted on a specially designed printed circuit (PC) board and the IDT were bonded to the PC board with 3μm thick gold wire, using a thermo compression bonding machine. Figure 6.5 shows a completed $LiNbO_3$ device, mounted and bonded as above. R.F. power was supplied to the device via a conhex connector mounted on the PC board and subsequently connected to the bonding pads via a lumped inductor. The overall copper covering on the PC board provided the ground plane for the device with the positive connection being isolated.

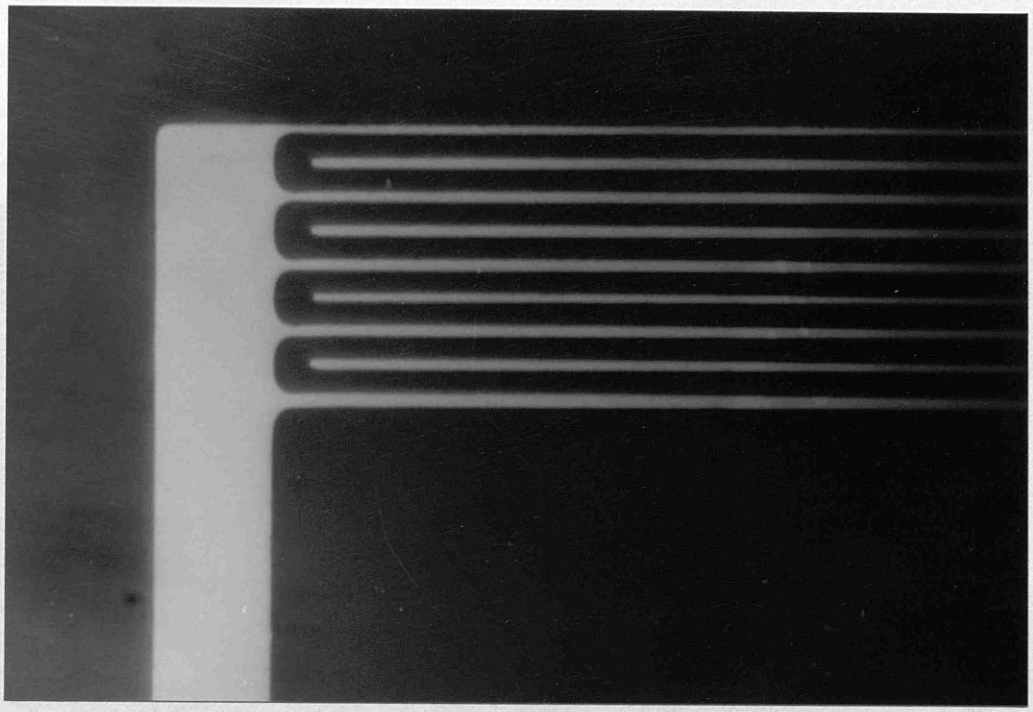

Figure 6.4 (a) IDT pattern on $LINbO_3$ with center frequency of 425MHz. Finger width = 2μm.

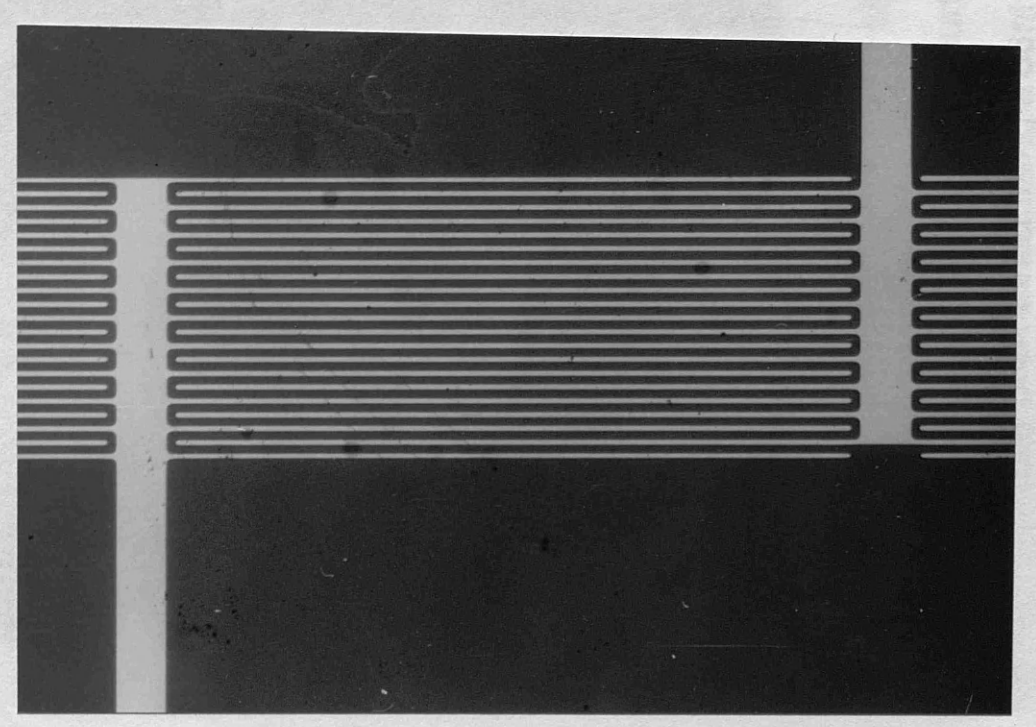

Figure 6.4 (b) IDT pattern on $LiTaO_3$ with center frequency of 203MHz. Finger width = 4μm.

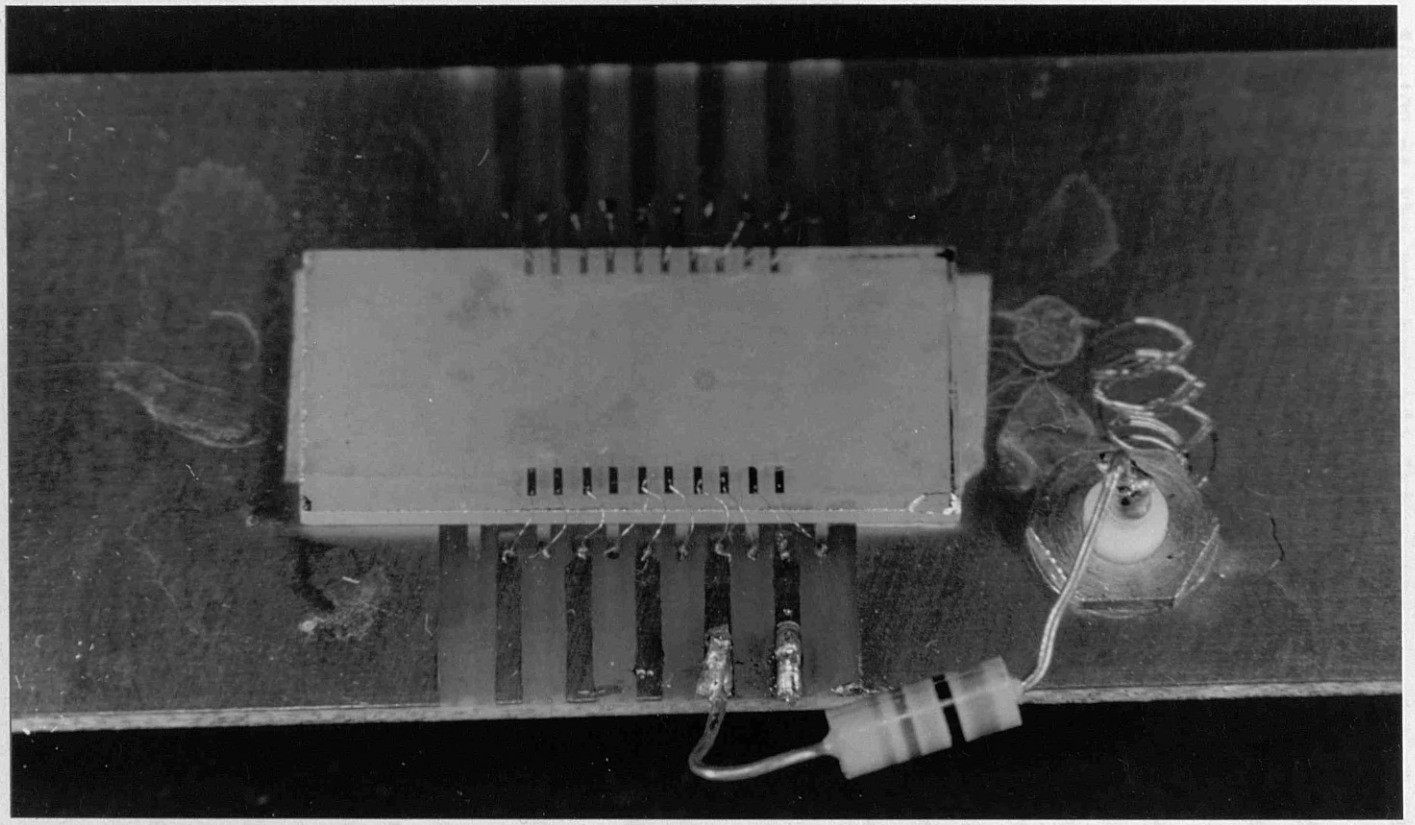

Figure 6.5 Example of a completed $LiNbO_3$ acousto – optic device. Five IDT pairs fabricated on the $LiNbO_3$ surface and bonded using 3μm thick gold wire has been tuned using a 56nH inductor.

6.5. Characterisation of an IDT

Although the IDT was designed to have an input impedance of 50+j0Ω at the synchronous frequency ω_o, it was very difficult to achieve this in practice due to stray capacitance in the circuit. The radiation resistance is not only frequency dependent but is also dependent upon the active capacitance of the electrodes and equation 6.6 defines a relationship for the active capacitance of an electrode finger pair at the synchronous frequency. It is possible using, for example, an inductor to tune the IDT structure at the synchronous frequency to achieve a resonant structure with an ideal input impedance of 50+j0Ω. In practice this is very difficult to achieve, especially at high frequencies, since stray capacitance in the bonding wires and the finite resistance of the electrodes contribute to the overall input impedance of the device.

A schematic diagram of the set-up used to tune the IDT is given in Figure 6.6. The arrangement consists of a network analyser system and an s-parameter test set which allow the observation of IDT input impedance variation with frequency. With the reference arm of the network analyser adjusted so that the test plane began at the ground plane of the IDT, the input power reflection coefficients were examined and displayed in terms of amplitude and phase on a polar display[18]. By simple adjustment of inductor value or length, it was possible to tune the IDT until the best possible value of input impedance was achieved. Figure 6.7(a) shows a typical polar display for an IDT on $LiNbO_3$. The frequency sweep was 200MHz around a centre frequency of 425MHz and the tuning inductance was 56nH. Figure 6.7(b) shows the initial response for an untuned IDT on $LiTaO_3$. The centre frequency was 203MHz and the low value of input impedance is evidence that the device was not fully tuned.

6.6. Optical Bench Arrangement

The set-up used to make optical measurements on the IDT is shown schematically in Figure 6.8(a). High index rutile prisms were used to couple light into and out of the waveguides[19] with

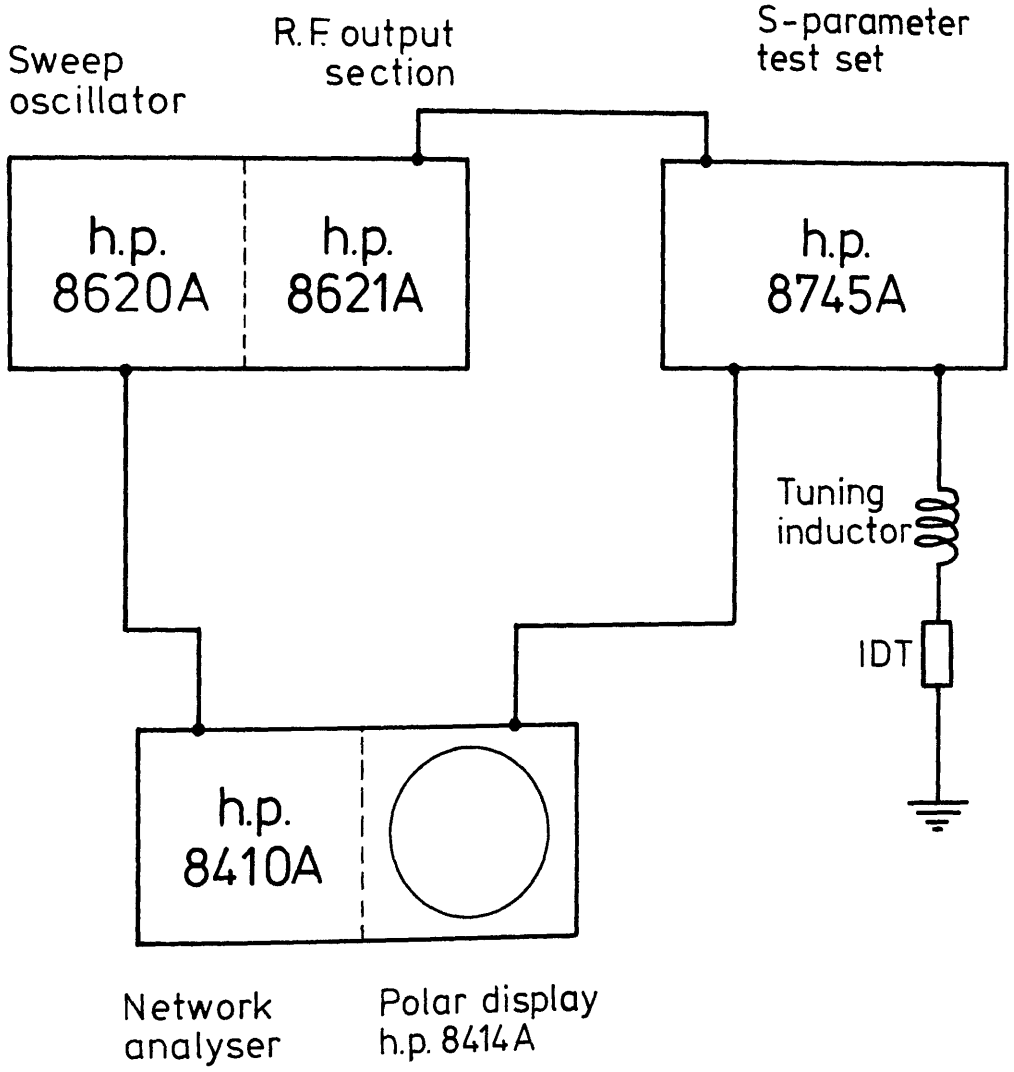

Figure 6.6 Electrical circuit for the measurement of radiation impedance of the IDT.

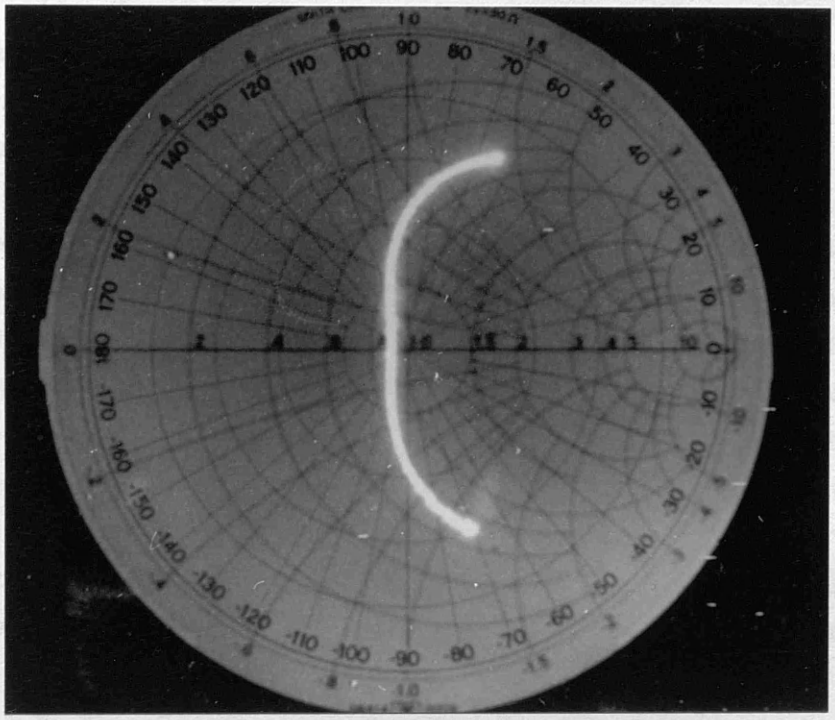

Figure 6.7 (a) Network analyser polar display of the input impedance of an IDT on $LiNbO_3$. The frequency sweep was 200MHz with a centre frequency of 425MHz.

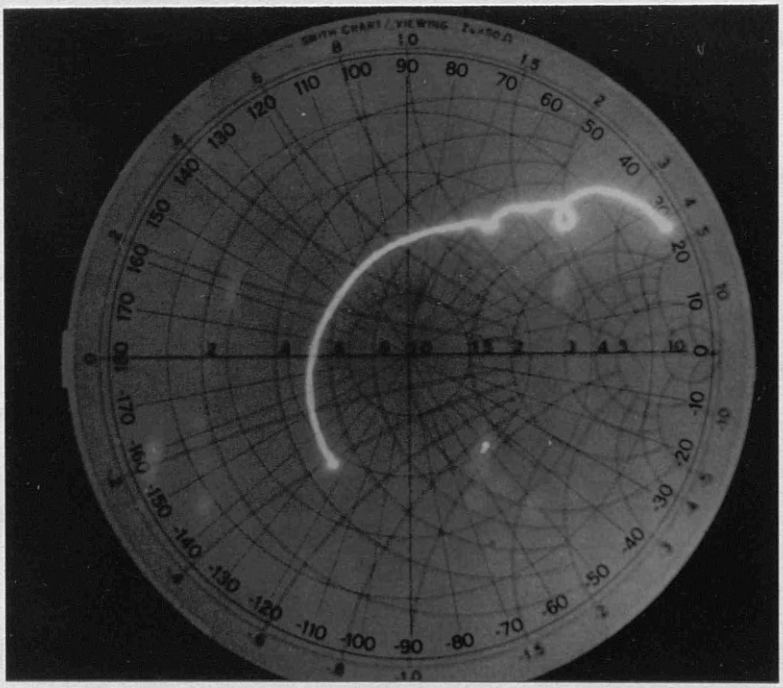

Figure 6.7 (b) Network analyser polar display of the input impedance of an IDT on $LiTaO_3$. The frequency sweep was 200MHz. with a centre frequency of 203MHz.

the IDT being mounted on a rotational movement to allow for independent excitation of the waveguide modes. Waveguide TE modes were excited by a vertically polarised He-Ne laser beam at a wavelength of 0.6328μm. TM modes were not considered.

Phase sensitive detection was employed to measure the diffracted light intensity. A square wave modulation was placed on the input laser beam and the diffracted light was detected by a silicon photodetector and supplied to a precision Lock-in amplifier (Brookdeal 9503-SC). The amplifier was tuned to the frequency of the initial modulation and detected only light which carried that same modulation. The silicon photodetector was mounted on a vertical movement which allowed intensity scanning detection of the main undiffracted beam or the diffracted beam.

The r.f. drive power required to generate acoustic waves was supplied to the IDT as indicated in Figure 6.8(a). Figure 6.8(b) shows schematically the electrical circuit used to supply and detect the levels of r.f. power to the IDT. The source of the power is a synthesized signal generator (Racal 9081) calibrated for an output range of 0dbm to -50dbm, over a frequency range of 0-500MHz. The signal was amplified via an r.f. power amplifier (ENI 305L) which produced a gain of 31dB at 425MHz up to a maximum output of 29dbm.(The amplifier saturated at a maximum gain of 29dbm and any power levels quoted in the range 500-700mW are subject to a slight error). Power was supplied to the IDT via a conhex connector with a power meter measuring the actual power level via a circulator. The values of r.f. power quoted in this thesis were the levels at the input to the conhex connector, not the acoustic power launched at the transducer.

6.7. Acousto-optic Measurements

Due to difficulties with the fabrication of dilute melt proton-exchange waveguides on Y-cut $LiNbO_3$ (as discussed in Chapter 3), $LiNbO_3$ acousto-optic devices discussed in this chapter were fabricated on XZ-$LiNbO_3$ (X-cut crystal, Z-propagating acoustic wave) only. Similary XZ-$LiTaO_3$ was used as the substrate material for the $LiTaO_3$ acousto-optic devices. Optical waveguides

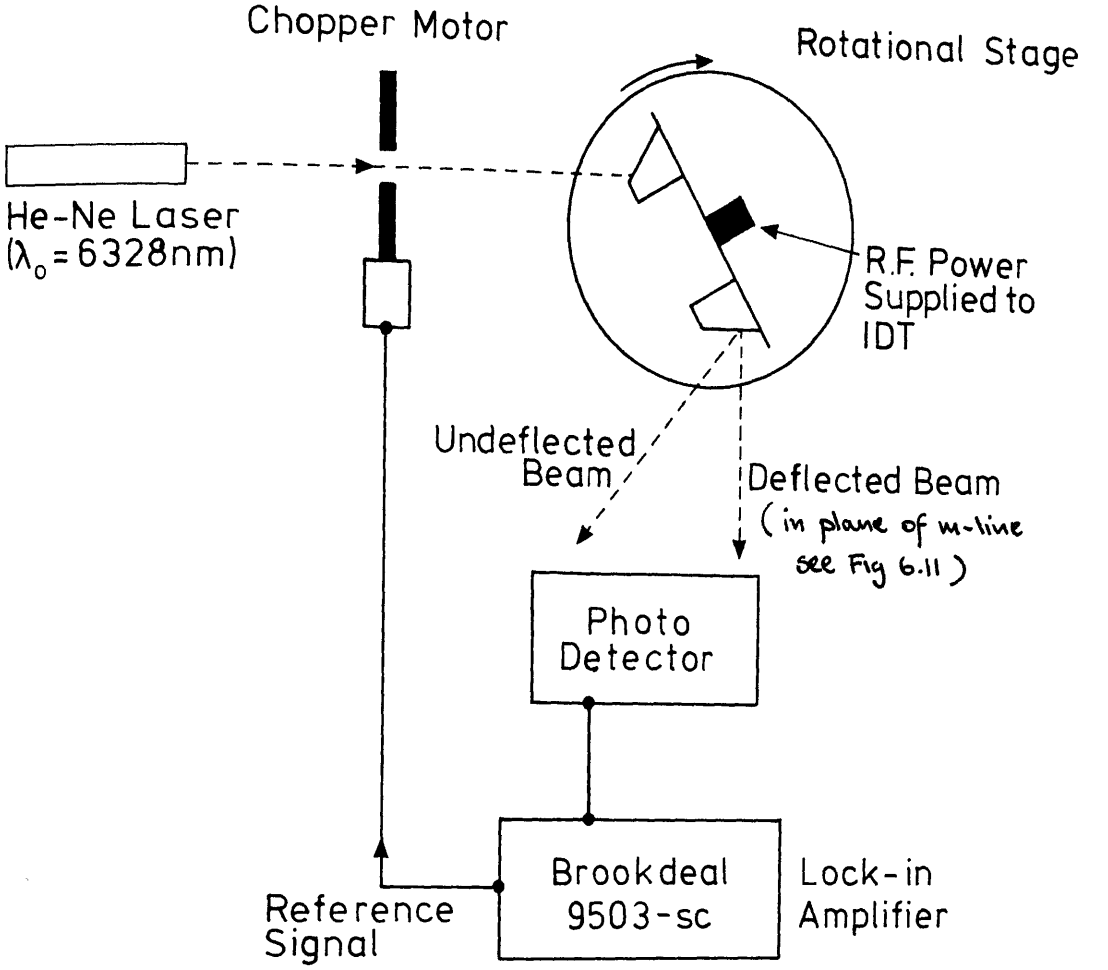

Figure 6.8(a) Optical bench arrangement for operation and detection of acousto-optic beam deflector.

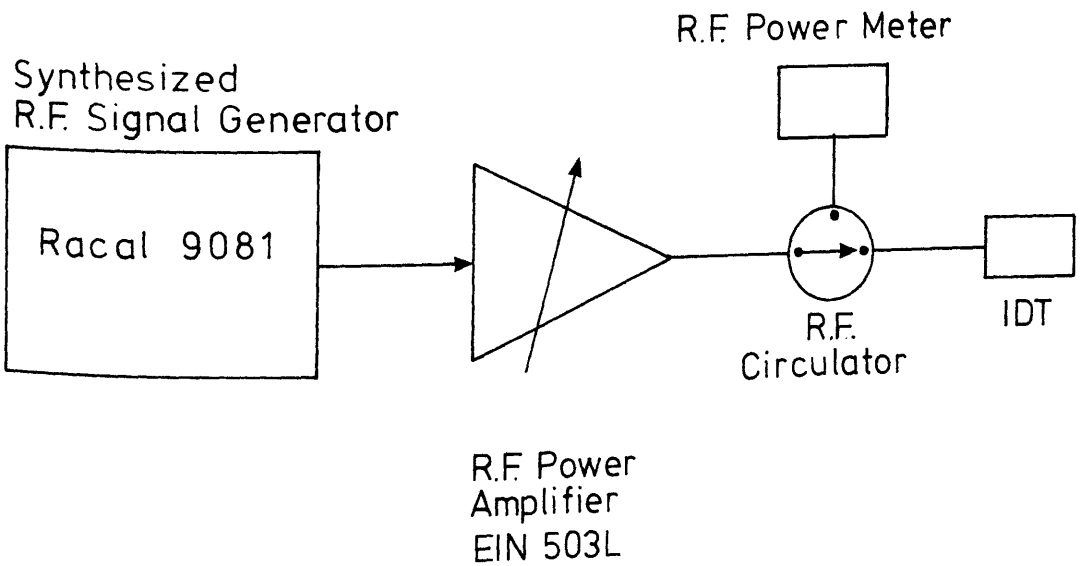

Figure 6.8(b) Electrical circuit for generation and measurement of r.f. power for IDT.

were fabricated by proton-exchange on both substrate materials using the methods detailed in Chapter 3. IDT structures were fabricated and all devices were electrically tuned using processes detailed earlier in this chapter.

This section discusses results obtained on four separate acousto-optical devices, three produced on $LiNbO_3$ and one on $LiTaO_3$. Table 6.2 lists, for each sample, the fabrication conditions and maximum obtained diffraction efficiency. For all samples, the melt dilution ratio was 0.5%. For the samples LN1,LN2, and LN3 discussed in Table 6.2, the IDT fabricated on each substrate surface were notionally identical. In each case the IDT design and IDT fabrication procedure was the same and no major differences in the electrical properties of the IDT were noted when the devices were electrically tuned using the network analyser arrangement. It was possible, however, that variations in the electrode thickness and finger width did exist but every precaution was taken to ensure that these variations were as small as possible and, for the particular comparisons which were being made in this chapter, it was not thought that these differences would effect the eventual outcome to any significant extent. Results presented show the effects of a change in the waveguide depth and the position of the IDT, in relation to the exchange region, on the maximum diffraction efficiency. In all cases, the maximum diffraction efficiency quoted is the maximum value obtained experimentally. (During the experiments the drive power was not taken above 640mW to protect the IDT from damage and therefore the maximum diffraction efficiency quoted is not necessarily the maximum theoretically possible).

Acousto-optic devices were originally produced using 0.5% dilute melt proton-exchange on YZ-$LiNbO_3$, but the quality of the waveguides was so poor (see Chapter 3) that acousto-optic measurements were very difficult to perform. It should be noted, however, that acousto-optic deflection did take place though it was very weak and barely visible to the eye. Also, the inplane scattering levels associated with these waveguides were so severe that detection of the diffracted light intensity was very difficult. Although work was then carried out exclusively on X-cut

substrates, subsequent results on annealed Y-cut waveguides indicate that high quality waveguides could be fabricated and that further attempts to produce high efficiency acousto-optical devices on dilute melt proton-exchanged Y-cut $LiNbO_3$ waveguides should prove successful.

Table 6.2 Summary of Fabrication Conditions for Acousto-optic Devices[1]

Sample	Temp	Time	Anneal Conds	N_{eff}	Depth	η_{max}[2]
LN1	220°C	12min	400°C/5min	2.2183	0.16μm	86%
LN2	220°C	7.5min	400°C/10min	2.2098	0.15μm	87%
LN3	234°C	6hrs	400°C/5min	2.2989	1.97μm	30%[3]
				2.2834		+
				2.2604		+
				2.2294		+
LT1	230°C	4hrs	325°C/10mins	2.1892	-	22%

+ Diffraction intensity lower than detection limit.

[1] all samples fabricated with a melt dilution of 0.5%

[2] maximum diffraction efficiency at a drive power of ~640mW

[3] for TE_0

6.7.1. Lithium Niobate

Figure 6.9 shows the variation in the first order diffraction efficiency with electrical input power obtained for sample LN1 (see Table 6.2). The diffraction efficiency is defined as the ratio of power in the first order diffracted beam to the peak power in the original undeflected beam. 86% of the optical power was deflected into the first order at 640mW r.f. power input to

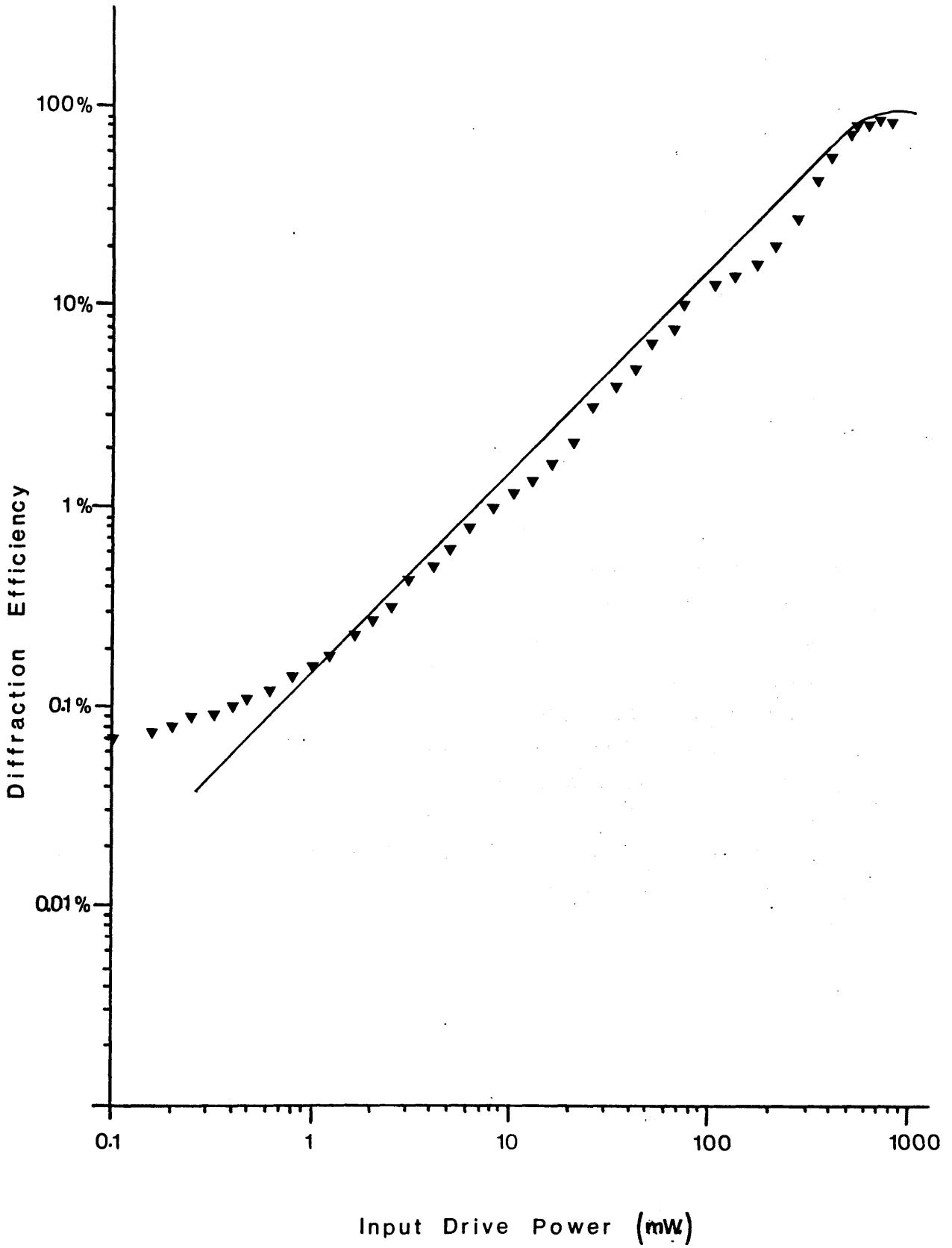

Figure 6.9 Acousto – optic diffraction efficiency vs. drive power for X – cut $LiNbO_3$ sample LN1. Solid line represents the relationship efficiency $\approx \sin^2[\text{ const } .\sqrt{p}]$

the transducer, giving a small signal efficiency of 0.25%/mW. This latter result is calculated from Figure 6.9 by extrapolating the linear small signal section of the curve out to a power value of 1000mW. (This method reduces to a minimum the effects of any errors associated with the power levels in the range 500-700mW). Figure 6.10 shows similar results for sample LN2, giving a maximum recorded diffraction efficiency of 87% at 640mW. Figure 6.10 can be extrapolated to give a small signal efficiency of 0.3%/mW. The two samples differ only marginally in fabrication conditions (sample LN1 is slightly deeper and IDT performance was assumed to be identical) and, within the limits of experimental error, they both return similar results. In sample LN2, the IDT was placed on the proton-exchanged area of the substrate surface and the high diffraction efficiency obtained seems to indicate that ionic conductivity problems[3] and reduced piezoelectric activity[20,21] observed with pure melt proton-exchanged waveguides, do not exist with dilute melt proton-exchange waveguides[22]. A third sample, LN3, with a comparatively deep waveguiding region (~2μm) was tested. This sample supported 4 TE modes, each of which could be independently excited via a prism coupler without any significant scattering between modes[19]. The maximum diffraction efficiency of the device was much lower than that measured for devices LN1 and LN2, indicating a reduction in acousto-optic activity with increased exchange depth, as shown theoretically in Figure 5.4. To achieve a given diffraction efficiency, the higher order modes require a greater drive power, indicating a less efficient interaction geometry[17]. This result was also shown theoretically in Figure 5.4.

With samples LN1 and LN2, the maximum measured diffraction efficiency of 86% corresponded to a measured depletion of the zero-order beam of 97%. Observations of the deflected signals indicated that the Bragg condition was not fully satisfied and the acousto-optic device could not suppress all other orders, in particular, the -1 order. The reason why total conversion of the diffracted signal from the zero order to the +1 order did not take place can be attributed, in part, to the acoustic beam not being wide enough totally to suppress Raman-Nath scattering. (Another possible reason, the existence of frequency harmonics in the

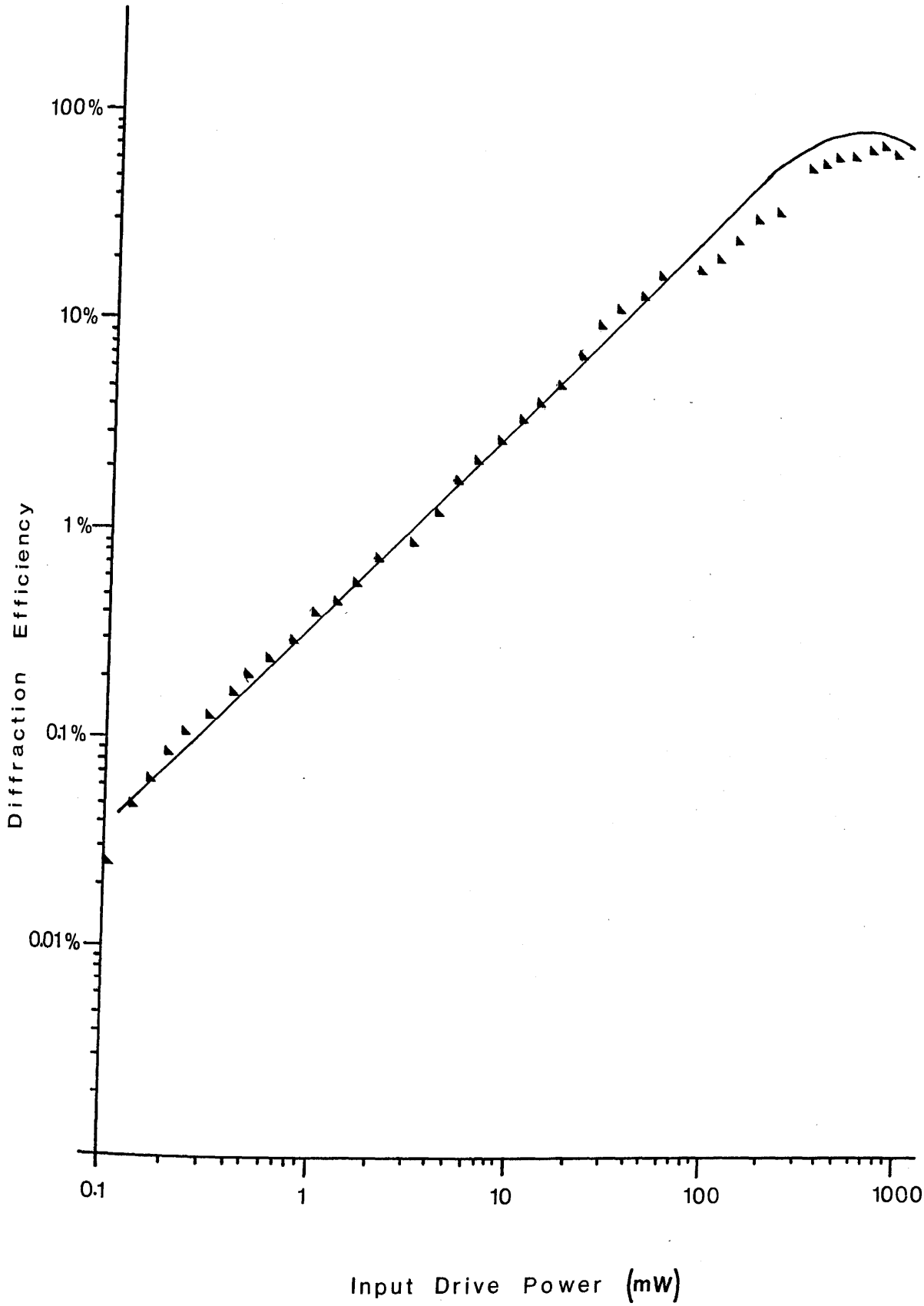

Figure 6.10 Acousto – optic diffraction efficiency vs. drive power for X – cut $LiNbO_3$ sample LN2. Solid line represents the relationship efficiency $\approx \sin^2[\text{const.}\sqrt{p}]$

signal, was reduced by the introduction of a low pass filter with f_L=500MHz). A major parameter in the performance of an acousto-optic interaction is the Q factor, defined as

$$Q = \frac{2\pi\lambda L}{\lambda_a^2} \qquad \ldots.6.7$$

where L is the width of the acoustic beam, λ_a the acoustic wavelength and λ the optical wavelength in the interaction medium. Q is linearly dependent upon the acoustic beam width and for Q<1 Raman-Nath (multiple scattering) interaction exists. Bragg diffraction becomes dominant when the Q factor is greater than or equal to 4π and for all values between unity and 4π a transition from multiple scattering to Bragg interaction takes place[23]. Another way to look at the problem is to realise that $Q=4\pi$ represents the situation where the optical wave traverses one complete acoustic wavelength and, for all values of $Q>4\pi$, the optical wave will traverse a greater number of acoustic wavelengths and the Bragg interaction of the grating will be enhanced[24].

With samples LN1 and LN2, $Q=7.7\pi$ or the optical beam traversed 1.9 acoustic wavelengths and, although Bragg interaction was taking place, it was probable that the interaction was not strong enough totally to surpress scattering into other orders. For fixed optical and acoustic wavelengths, Q can be increased only by increasing the acoustic beam width L. However, in samples LN1 and LN2, L was chosen so that the IDT structure would have an input impedance of 50Ω. Any variation of L would require either additional external impedance matching or a device re-design such as the series-parallel design[17] used to extend the width of the $LiTaO_3$ device.

The results detailed above are significant because they provide evidence of a simple method of fabricating highly efficient acousto-optical devices on $LiNbO_3$ waveguides. Dilute melt proton-exchange waveguides clearly do not have the problems previously associated with the pure melt proton-exchange waveguides, i.e. index instabilities[25] and high inplane

scattering[26], and therefore do not require the extensive annealing which reduces acousto-optic activity[3]. Complex processes devised by Handa et al.[20], and Miyawaki and Ogura[27] to avoid reduction of piezoelectric properties are no longer necessary, with efficient interaction being achieved with acoustic waves launched from proton-exchanged regions.

It would be an extremely difficult task to make a complete comparison between the performance of acousto-optic devices formed on proton-exchanged $LiNbO_3$ waveguides and similar devices formed by other fabrication methods such as Ti-indiffusion. To make such a comparison, a complete knowledge of the waveguide properties i.e.,propagation loss, optical field profile, refractive index profile, and modal content, would be necessary. The experiment would have to compare device performance over a whole range of acoustic frequencies, optical wavelengths and waveguide depths, taking into account the effect that each parameter might have on the interaction efficiency. Theoretical investigations for graded index waveguide devices[14,28] and for step index waveguide devices (see previous chapter) show the dependence of the diffraction efficiency on the acoustic frequency and waveguide depth. Tsai[28] shows also how the interaction efficiency varies with the choice of acoustic wave propagation direction. Hence full range comparisons are difficult and, in practice, a comparison is made only when a particular application is involved where the optical waveguide properties are as important (e.g., in relation to external coupling) as the interaction efficiency.

It is difficult to compare the results obtained for the dilute melt waveguides with published results for other waveguides because of the wide variation in fabrication conditions and frequency of operation. The peak diffraction efficiency of 86% at a drive power of 640mW compares with 70% at 540mW obtained by Dawar et al.[3] on pure melt proton-exchanged waveguides. These results were obtained using identical electrode designs and operating at the same acoustic frequency. However, results for indiffused waveguides[18] of 70% at 50mW, and outdiffused waveguides[29] of 50% at 200mW were obtained using complicated electrode designs and at considerably lower frequencies, making

a proper comparison very difficult. In addition, although bulk acousto-optic devices require considerably higher levels of drive power, (e.g. 30% per Watt for a 1.1GHz bandwidth device with a centre frequency of 2.7GHz[30]) comparison can be made only when the device application is taken into account, in which case the very large bandwidths available with bulk acousto-optic devices might be preferred. Despite the fact that it is difficult to make a comparison between dilute melt proton-exchange acousto-optic devices and other waveguide devices, the results presented in this chapter indicate that the method can be used to produce efficient devices which operate at low r.f. power levels.

6.7.2. Lithium Tantalate

Bragg interaction has been demonstrated previously on $LiTaO_3$ waveguides using static electro-optic gratings[31,32,33]. In each case, however, a different waveguide fabrication process was employed, and all three fabrication processes involved temperatures in excess of the Curie temperature of the crystal. For this reason, no surface wave acousto-optic devices have been demonstrated on $LiTaO_3$ waveguides although the crystal has a moderately large electro-mechanical coupling coefficient[16] and large electro-optic coefficients[9]; both properties which indicate the potential of the crystal for efficient acousto-optic interaction. The proton-exchange process has been used to fabricate optical waveguides on $LiTaO_3$ at temperatures below the Curie temperature (see Table 6.2) and an acousto-optic waveguide device, LT1, was developed using the IDT electrode structure described earlier in section 6.2.

Figure 6.11(a) shows the variation in diffraction efficiency against drive power for LT1. Without electrical tuning, 22% of the optical power was deflected into the first order for a drive power of 640mW. Figure 6.11(b) shows the output coupled m-line for LT1 with the diffracted power evident as the lower beam. In comparison with the $LiNbO_3$ devices previously mentioned, this performance is relatively poor. However, it is very likely that, with a thorough investigation of the acoustic and the optical properties of the crystal, an improvement on the present results might be obtained.

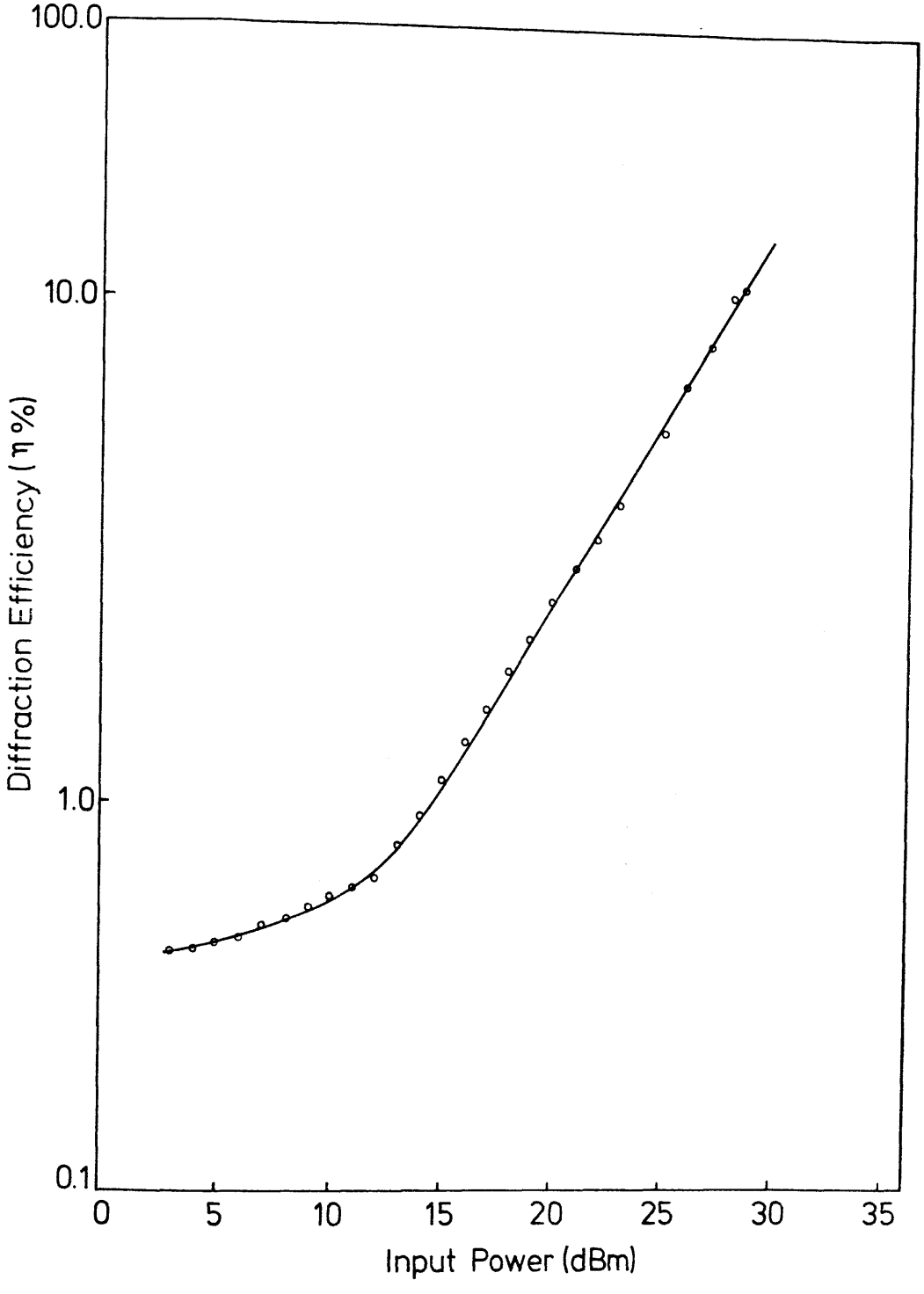

Figure 6.11(a) Acousto – optic diffraction efficiency against drive power for X – cut $LiTaO_3$ sample LT 1. Centre frequency = 203MHz.

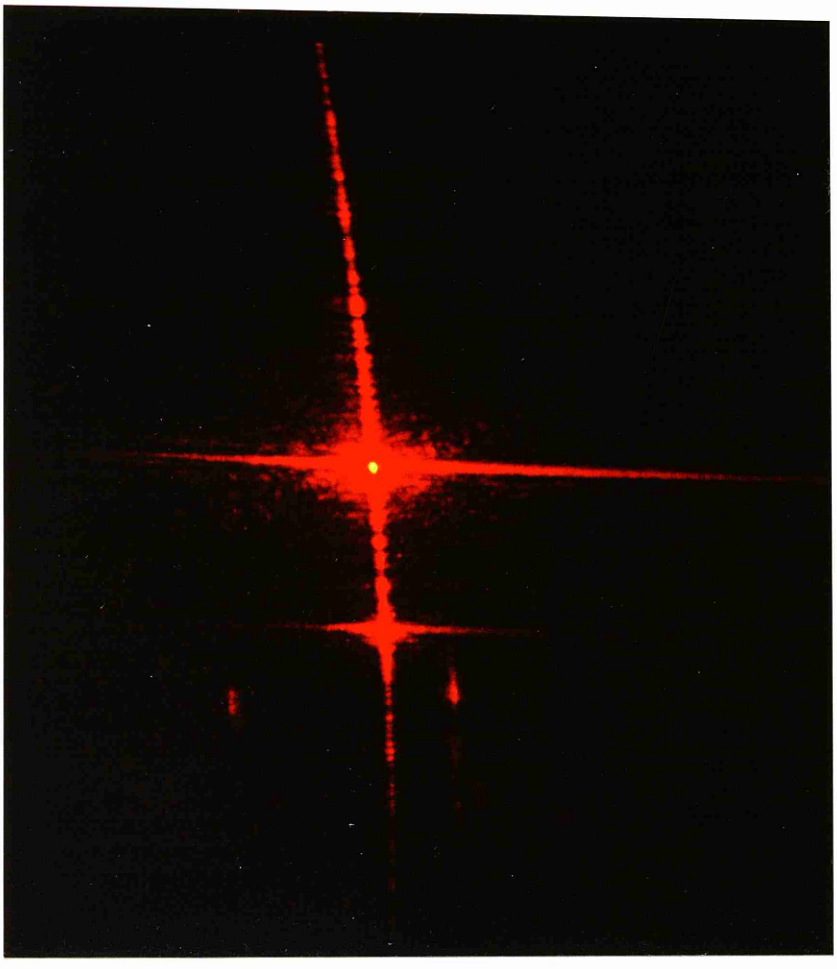

Figure 6.11 (b) Evidence of acousto-optic deflection on an output coupled m-line for $LiTaO_3$ sample LT1. For an r.f. drive power of 640mW, 22% of the main beam was deflected into the first order.

Due to equipment difficulties, it was not possible to take the investigation further and, an obvious step to take, is to tune the device electrically to see if any improvement is obtained. The fact that acousto-optic diffraction has been demonstrated in $LiTaO_3$ could prove significant in some applications where the use of $LiNbO_3$ is not desirable. The surface acoustic wave velocity is more susceptible to temperature change in $LiNbO_3$ than in $LiTaO_3$[34,35] implying, that in certain circumstances, one crystal could be favoured against the other. In addition, proton-exchanged waveguides on $LiTaO_3$ have a small index change and low in-plane scattering which could prove beneficial in certain applications.

6.8. Thermo-optic Behaviour

In the operation of a guided wave acousto-optic device at relatively high input r.f. power levels, it has been observed that the light intensity of a prism coupled output m-line decreases substantially with time. This decrease in the light intensity is caused by a change in the refractive index of the waveguide and can be overcome by readjusting the coupling angle at the input prism. This effect has been reported previously for Titanium indiffused waveguides[36] and has been attributed to resistive losses in the IDT[37] causing the waveguide surface temperature to rise. Additional evidence for substantial heating is that that the IDT tends to burn out at power levels exceeding 640mW. This increase in temperature results in a positive change in the effective index of the waveguide[38]. Upon removal of the temperature source, the waveguide properties eventually return to normal as the substrate surface cools down.

This effect, known as the thermo-optic effect, has been used in the past to construct a light deflection switch in Titanium indiffused $LiNbO_3$[39] and is an important consideration in the design of acousto-optic devices which depend on index stability. In a fully integrated optical spectrum analyser(IOSA), for example, where an injection laser and detector array are 'butt-coupled' after alignment of the detector array, any change in the refractive index due to r.f. power at the IDT will lead to a shift in the position of the main beam. According to Coquin et al.[37],

who considered acousto-optic devices for applications that required precise beam positioning, it is reasonable to assume that the beam should not wander by more that 10% of the spacing between adjacent resolvable positions. This change in the index due to r.f. power will be one of the effects (along with third-order modulation[40]) which will limit the maximum r.f. power that can be applied, without distorting the characteristics of the IOSA device. The variation of thermo-optic behaviour with crystal substrate and/or waveguide fabrication process is also a major consideration when acousto-optic devices are being designed.

This section discusses measurements of index change against temperature for dilute melt proton-exchange waveguides fabricated on $LiNbO_3$ and $LiTaO_3$ substrates, and compares the results obtained with those previously obtained on Titanium indiffused $LiNbO_3$ waveguides[36].

6.8.1. Experimental Arrangement

The experimental arrangement for the operation of the acousto-optic devices has been described earlier in this chapter. He-Ne laser light was prism coupled into and out of the waveguide and the IDT was driven at increasing input power levels upto a maximum of 640mW. A surface thermocouple (Digitron model no 1758-K) placed 4mm from the IDT was used to record the temperature change and a digital readout (accurate to +/- 0.01^{o}), attached to the rotation stage, was used to record the change in coupling angle as the light intensity changed. By the use of the simple prism coupling equation (equation 3.1), the change in the coupled angle was directly related to the change in the waveguide effective index.

6.8.2. Lithium Niobate

Figure 6.12 shows the variation in the waveguide surface temperature with r.f. power applied to the IDT for sample LN2. The variation is given on a logarithmic scale and from this the estimated dependence of waveguide surface temperature T on the r.f. power P is

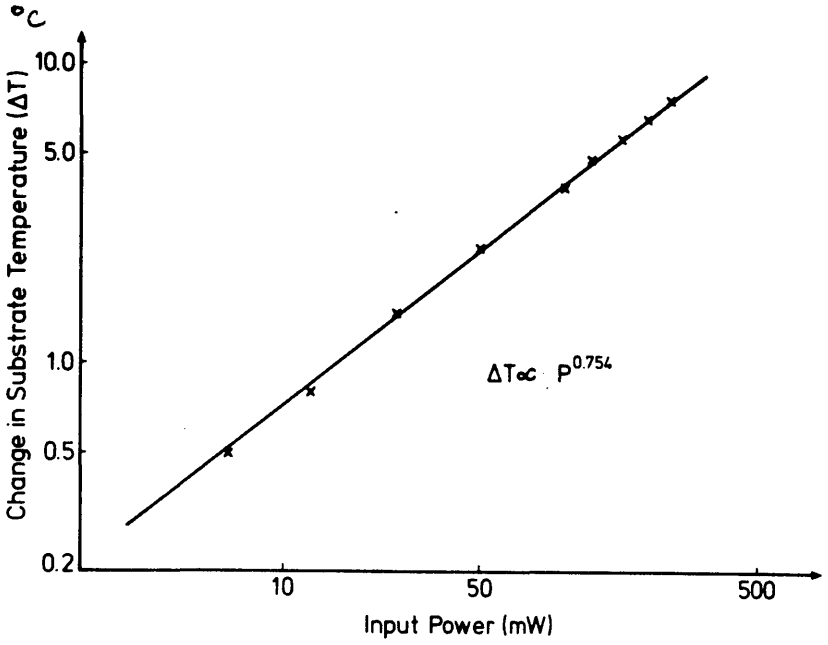

Figure 6.12 Variation in surface temperature against drive power for $LiNbO_3$

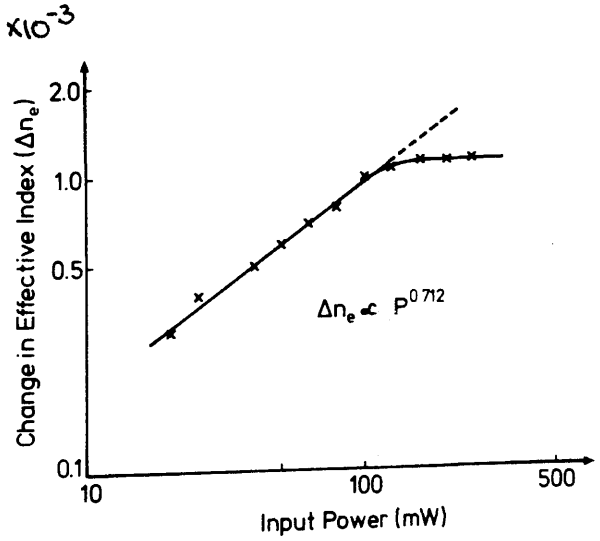

Figure 6.13 Variation in waveguide effective index against drive power for $LiNbO_3$

$$\Delta T \propto P^{0.754} \qquad \ldots.6.8$$

Similarly Figure 6.13 shows the logarithmic variation of the waveguide effective index n_e with r.f. power P, from which the estimated dependence of n_e on P is

$$\Delta n_e \propto P^{0.712} \qquad \ldots.6.9$$

From Figures 6.12 and 6.13 a relationship between the change in waveguide effective index and surface temperature is obtained as follows

$$\Delta n_e \propto \Delta T^{0.944} \qquad \ldots.6.10$$

Thus, within the limits of experimental error, a linear relationship exists, for dilute melt proton-exchange waveguides on $LiNbO_3$, between the change in waveguide temperature and the resultant change in waveguide effective index. This result is similar to that obtained by Singh et al.[36] for Titanium indiffused waveguides on $LiNbO_3$ where the relationship was reported to be

$$\Delta n_e \propto \Delta T^{1.067\ (37)} \qquad \ldots.6.11$$

In 1984 Dawar et al.[41] presented thermo-optic measurements on pure melt proton-exchanged Y-cut $LiNbO_3$ waveguides, where the variation between substrate surface temperature and index was reported to be

$$\Delta n_e \propto \Delta T^{1.099\ (42)} \qquad \ldots.6.12$$

In Dawar's experiment, similar variations were obtained between substrate surface temperature and index with power to those obtained by Singh[36] but with considerably larger log-log plot slopes. At the time, this could not be explained, however, it is now believed that Dawar made arithmetical errors which were self cancelling and so did not affect the final relationship repeated above. Thus, a comparison of the results presented previously for

titanium indiffused $LiNbO_3$ waveguides and pure melt proton-exchanged $LiNbO_3$ waveguides with results obtained on dilute melt proton-exchanged waveguides indicates that there is no significant difference between the thermo-optic properties of the waveguide fabrication processes.

This result apparently contradicts that obtained by Rottschalk et al.[42] in 1985, when the authors concluded that the thermo-optic coefficient of proton-exchanged lithium niobate waveguides was negative and equal to $-(0.65 +/- 0.5)10^{-5}K^{-1}$ [42]. However, upon careful examination of these authors' work, it can be seen that their experiment is not directly comparable with that which is described in this thesis. The work described in this section involves, essentially, heat-flow on a layered surface and concerns itself with the problems resulting from conductive losses in surface electrodes. Rottschalk et al[42], on the other hand, conduct an experiment in which they investigate the optical waveguide effects of heat applied uniformly to the whole of the substrate and waveguide.

6.8.3. Lithium Tantalate

The thermo-optic properties of $LiTaO_3$ optical waveguides measured under acousto-optic interaction are presented for the first time. Figure 6.14 shows the logarithmic variation in waveguide substrate temperature T with r.f. power P, from which the following relationship is derived

$$\Delta T \propto P^{0.943} \qquad ....6.13$$

Similarly, Figure 6.15 shows the logarithmic variation in waveguide effective index with r.f. power P, giving

$$\Delta n_e \propto P^{1.058} \qquad ....6.14$$

Both results were obtained on sample LT1 with the IDT placed on a region previously protected from proton-exchange. The larger change in surface temperature recorded for $LiTaO_3$ in comparison

with $LiNbO_3$ for a given r.f. power could be attributed to the larger physical size of the IDT used, resulting in greater resistive losses. The relationship between the surface temperature change and the resultant effective index change is given below

$$\Delta n_e \propto P^{1.12} \qquad \ldots.6.15$$

This relationship is approximately linear, implying that the thermo-optic behaviour on dilute melt proton-exchanged $LiTaO_3$ waveguides is in this respect, similar to that of $LiNbO_3$ waveguides. It has been demonstrated[34,35] that the velocity of surface acoustic waves in both $LiTaO_3$ and $LiNbO_3$ is temperature dependent, with XZ and YZ- $LiTaO_3$ having approximately one-third the temperature coefficient of delay of that found in YZ-$LiNbO_3$. Thus the information provided in the previous two sections of this chapter could prove to be very useful to an acousto-optic device designer where temperature variations are an important consideration.

6.9. Discussion

In this chapter, the design and operation of two types of acousto-optic waveguide device fabricated using the method of dilute melt proton-exchange have been discussed. Results have shown that high diffraction efficiencies can be obtained on lithium niobate waveguides with further work required to realise the full potential of lithium tantalate waveguides. Thermo-optic behaviour of waveguides fabricated on both substrates has been observed, indicating no apparent difference between proton-exchanged waveguides and those produced by Titanium indiffusion. The work also contains the first successful demonstration of acousto-optic interaction on lithium tantalate waveguides and demonstrated that, with suitable fabrication conditions, efficient acousto-optic interaction can be obtained on proton-exchanged lithium niobate waveguides whether the IDT is placed on or off the proton-exchanged area.

Appendix 6.1 Exact Determination of Design Parameters for IDT on XZ and YZ $LiNbO_3$ and $LiTaO_3$

Lithium Niobate

	YZ	XZ	Ref
V_s	$3488ms^{-1}$	$3483ms^{-1}$	(10)
V_{sp}	$3494ms^{-1}$	$3519ms^{-1}$	
k^2	0.045	0.048	(16)
C_{ff}	$4.6438\ 10^{-10}Fm^{-1}$	$6.1531\ 10^{-10}Fm^{-1}$	(10)
N	4.178	4.045	
C_s	0.429125pF	0.147739pF	
L	$112.26\lambda_a$	$98.9\lambda_a$	(10)

Lithium Tantalate

	YZ	XZ	Ref
V_s	$3230ms^{-1}$	$3226ms^{-1}$	(9)
k^2	0.0074	0.0069	(16)
C_{ff}	$4.4352\ 10^{-10}Fm^{-1}$	$5.3456\ 10^{-10}Fm^{-1}$	(10)
N	10.3	10.67	
C_s	0.429125pF	0.147739pF	
L	$20.94\lambda_a$	$16.3\lambda_a$	(16)

where $R_a=50\Omega$, and L is measured in units of acoustic wavelength. V_{sp} is the SAW velocity on a proton-exchanged layer (see Table 4.3).

References to Chapter 6.

1. R.M. White, 'Surface Elastic Waves', Proc. IEEE, Vol. 58, p. No. 8, pp. 1288-1276, 1970.

2. R.V. Schmidt, 'Acousto-optic interactions between guided optical waves and surface acoustic waves', IEEE Trans. Sonics and Ultrasonics, Vol. SU-23, No. 1, pp. 22-33, 1976.

3. A.L. Dawar, S.M. Al-Shukri and R.M. De La Rue, 'Guided wave acousto-optic interaction in proton-exchanged Y-cut $LiNbO_3$', Appl. Phys. Letts., Vol. 48, No. 23, pp. 1579-1581, 1986.

4. R.L. Davis, 'Acousto-optic Bragg diffraction in proton-exchanged waveguides', Proc. Soc. Photo-opt. Inst. Eng., Vol. 517, pp. 74-81, 1984.

5. W.B. Spillman Jr., N.A. Sanford and R.A. Soref, 'Optical waveguides in $LiTaO_3$ formed by proton-exchange', Opts. Letts., Vol. 8, No. 9, pp.497-499, 1983.

6. S.M. Al-Shukri, J.F. Duffy, R.M. De La Rue, G. Mazzi, A. Carnera and M.N. Armenise, 'Single mode planar and stripe waveguides by proton-exchange in lithium tantalate and lithium niobate', Proc. Soc. Photo-opt. Inst. Eng., Vol. 651, pp. 20-25, 1986.

7. R.S. Weis and T.K. Gaylord, 'Lithium Niobate: Summary of physical properties and crystal structure', Appl. Phys. A., Vol. 37, pp. 191-203, 1985.

8. J.T. Milek and M. Neuberger, 'Linear electro-optic modular materials', IFI/Plenum, New York, 1972.

9. A.J. Slobodnik Jr., R.J. Delmonico and E.D. Conway, Microwave Acoustics Handbook, Vol. 1A, Air Force Research Labs., Mass., U.S.A., 1973.

10. A.J. Slobodnik, Jr., 'Surface acoustic waves and SAW

devices', Proc. IEEE, Vol. 64, No. 5, pp. 581-595, 1976.

11. W.R. Smith, H.M. Gerard, J.H. Collins, T.M. Reeder and H.J. Shaw, 'Design of surface wave delay lines with interdigital transducers', IEEE, Vol. MTT-17, No. 1, pp. 865-873, 1969.

12. W.R. Smith, H.M. Gerard, J.H. Collins, T.M. Reeder and H.J. Shaw, 'Analysis of interdigital surface wave transducers by use of an equivalent circuit model', IEEE Vol. MTT-17, No. 1, pp. 856-864, 1969.

13. A. Korpel, R. Adler, P. Desmares and W. Watson, 'A television display using acoustic deflection and modulation of coherent light', Proc. IEEE, Vol. 54, No. 10, pp. 1429-1437, 1966.

14. C.S. Tsai, M.A. Alhaider, Le T. Nguyen and B. Kim, 'Wide-band guided-wave acousto-optic Bragg diffraction and devices using multiple tilted surface acoustic waves', Proc. IEEE, Vol. 64, No. 3, pp. 318-328, 1976.

15. C. Stewart, W.J. Stewart and G. Scrivener, '500MHz bandwidth guided wave L-band Bragg cell', Elect. Lett. Vol. 17, No. 25, pp. 971-973, 1981.

16. M.B. Schultz and J.H. Matsinger, 'Rayleigh-wave electromechanical coupling constants', Appl. Phys. Letts., Vol. 20, No., pp. 367-369, 1972.

17. R.V. Schmidt and I.P. Kaminow, 'Acousto-optic Bragg deflection in $LiNbO_3$ Ti: diffused waveguides', IEEE Jour. Quant. Elect., Vol. QE-11, No. 1, pp.57-59, 1975.

18. H.P. Application Note No. 117-1, 'Microwave network analyser application', 1970.

19. P.K. Tien and R. Ulrich, 'Theory of prism-film coupler and thin-film light guides', J. Opt. Soc. Amer., Vol. 60, No. 10, pp. 1325-1337, 1970.

20. Y. Handa, M. Miyawaki and S. Ogura, 'Guided-wave characteristics and optical damage in $LiNbO_3$ waveguides', Proc. Soc. Photo-opt. Inst. Eng., Vol. 460, pp. 101-108, 1984.

21. F.S. Hickernell, K.D. Ruehle, S.J. Joseph, G.M. Reese and J.F. Weller, 'The surface acoustic wave properties of proton-exchanged YZ-Lithium Niobate', Proc. IEEE Ultrasonics Symp., pp. 110-113, San Francisco, 1985.

22. K.K. Wong, N.J. Parsons, A.R. Oldroyd and A.C. O'Donnell, 'High quality optical waveguides in $LiNbO_3$ by dilute melt proton-exchange', Proc. IOOC/ECOC '85, pp. 59-62, Venice, 1985.

23. W.R. Klein and W.D. Cook, 'Unified approach to ultrasonic light diffraction', IEEE Trans. Soncis and Ultrasonics., Vol. SU-14, No. 3, pp. 123-134, 1967.

24. G.W. Willard, 'Criteria for normal and abnormal ultrasonic light diffraction effects', J. Aco. Soc. Amer., Vol. 21, No. 2, pp. 101-108, 1949.

25. A. Yi Yan, 'Index instabilities in proton-exchanged $LiNbO_3$ waveguides', Appl. Phys. Letts., Vol. 42, No. 8, pp.633-635, 1983.

26. S.M. Al-Shukri, A.L. Dawar, R.M. De La Rue, A.C.G. Nutt, M. Taylor, J.R. Tobin, G. Mazzi, A. Carnera and C. Summonte, 'Analysis of annealed proton-exchanged waveguides in $LiNbO_3$ by optical waveguide measurements and microanalytical techniquesπ, Proc. 7th Topical Meeting on Integrated and Guided Optics, Orlando, Florida, U.S.A., PDP71-4, April 1984.

27. M. Miyawaki and S. Ogura, 'Efficiency, damage resistant $LiNbO_3$ acousto-optic waveguide deflector', Appl. Phys. Letts., Vol. 47, No. 9, pp. 918-920, 1985.

28. C.S. Tsai, 'Guided-wave A.O. Bragg modulators for wide-band

integrated optical communications and signal processing', IEEE Trans. on Circuits and Systems, Vol. CAS-26, No. 12, pp. 1072-1098, 1979.

29. C.S. Tsai, Le. T. Nguyen, S.K. Yao and M.A. Alhaider, 'High performance acousto-optic guided-light beam device using two tilting surface acoustic waves', Appl. Phys. Letts., Vol. 26, No. 4, pp. 140-142, 1975.

30. J.M. Bagshaw and T.F. Willats, 'Anisotropic Bragg cells', G.E.C. Journal of Research, Vol. 12, No. 2, pp.96-103, 1984.

31. J.M. Hammer and W. Phillips, 'Low-loss single-mode optical waveguides and efficient high-speed modulators of $LiNb_xTa_{1-x}O_3$ on $LiTaO_3$', Appl. Phys. Letts., Vol. 24, No. 11, pp.545-547, 1974.

32. Y. Okamura, S. Yamamoto and T. Makimoto, 'Electro-optic guided-to-radiation mode conversation in Cu-diffused $LiTaO_3$ waveguide with periodic electrodes', Appl. Phys. Lett., Vol. 32, No. 3, pp.161-163, 1978.

33. A.L. Tangonan, D.L. Persechini, J.F. Lotspeich and M.K. Barnoski, 'Electro-optic diffraction modulation in Ti-diffused $LiTaO_3$', Appl. Opts., Vol. 17, No. 20, pp.3259-3263,. 1978.

34. M.B. Schultz and M.G. Holland, 'Temperature dependence of surface acoustic wave velocity in lithium tantalate', IEEE Trans. on Sonics and Ultrasonics, Vol. SU-19, No. 3, pp.381-384, 1972.

35. J.D. Maines, E.G.S. Paige, A.F. Saunders and A.S. Young, 'Simple technique for the accurate determination of delay-time variations in acoustic-surface-wave structures', Elect. Letts., Vol. 5, pp. 678-680, 1969.

36. J. Singh, J.R. Tobin and R.M. De La Rue, 'Observation of thermo-optic and photorefractive effects during acousto-optic

interaction in Ti:$LiNbO_3$ waveguides', J. Appl. Phys., Vol. 58, No. 5, pp.1990-1995, 1985.

37. G.A. Coquin, D.A. Pinnow and A.W. Warner, 'Physical properties of lead molybdate relevant to acousto-optic device applications', J. Appl. Phys., Vol. 42, No. 6, pp. 2162-2168, 1971.

38. D.S. Smith, H.D. Riccius and R.P. Edwin, 'Refractive indices of lithium niobate', Opts. Commun., Vol. 17, No. 3, pp.332-335, 1976.

39. M. Haruna and J. Koyam, 'Thermo-optic effect in $LiNbO_3$ for the light deflection and switching', Elect. Letts. Vol. 17, No. 22, pp.842-844, 1981.

40. D.L. Hecht, 'Multifrequency acousto-optic diffraction', IEEE Trans. Soncis and Ultrasonics, Vol. SU-24, No. 1, pp.7-18, 1977.

41. A.L. Dawar, S.M. Al-Shukri and R.M. De La Rue, 'Surface acoustic wave-guided optical wave interaction in Y-cut $LiNbO_3$ annealed proton-exchanged waveguides', IEEE Workshop on Optical Signal Processing and Related Technologies, PD-4, Florence, 1984.

42. M. Rottschalk, A. Rasch and W. Karthe, 'Temperature dependence of the extraordinary refractive index in proton-exchanged $LiNbO_3$ waveguides', J. Opt. Commun., Vol. 6, No. 1, pp.10-13, 1985.

CHAPTER 7. Conclusions

The objectives of the work described in this thesis were twofold. Firstly to investigate the design of an acousto-optic filter device based on a channel waveguide structure and secondly to investigate dilute melt proton-exchange as a method of waveguide fabrication and, in particular, to determine the suitability of the waveguides for acousto-optic interaction.

It was proposed that a simple acousto-optic channel waveguide device could be designed which could demodulate a frequency shift key (FSK) r.f. signal. The device, based loosely on the Integrated Optical Spectrum Analyser, would act as a beam deflector and deflect an optical signal at an angle determined by the r.f. signal frequency. Complicated IDT and waveguide lenses were not desired and it was proposed that the deflected beams, propagating at different angles, would excite adjacent transverse modes of a channel waveguide and hence allow their identification. It has been shown, for such a device, that the variation in frequency can cause the partial excitation of two alternative modes. However, very wide waveguide structures and very large frequency changes are required before any detectable mode variation occurs. These limitations make this particular device design impractical.

In the past few years, much interest has centred on the method of proton-exchange for waveguide fabrication on $LiNbO_3$. The simplicity of the fabrication process and the very large refractive index changes possible were two reasons why interest was so great. In terms of acousto-optic device fabrication, however, the method has not proven so advantageous. Y-cut $LiNbO_3$, which has been the most widely used crystal orientation for acousto-optic applications, suffers from severe surface damage for exchange depths in excess of 0.2μm. In addition, pure melt proton-exchange waveguides suffer from index instability and high levels of in-plane scattering. These problems have been overcome previously by post annealing. However, it has been shown that prolonged annealing results in a significant reduction in the acousto-optic diffraction efficiency. This reduction has been

attributed to the change in the waveguide index profile from step to graded resulting from annealing.

Dilute melt proton-exchange waveguides have been investigated, with emphasis being placed on their suitability for acousto-optic interaction. It has been shown that low loss, stable index waveguides can be fabricated from dilute melts and that post annealing is no longer necessary. In addition, waveguides have been fabricated on Y-cut $LiNbO_3$, although short annealing periods were required to improve on their quality. A characterisation of dilute melt proton-exchange waveguide fabrication on both X- and Y-cut $LiNbO_3$ has been carried out and equations have been presented which can be used to calculate the required fabrication conditions for a given waveguide. Optical waveguides have also been fabricated on $LiTaO_3$ substrates and very low levels of in-plane scattering were observed.

The acoustic properties of dilute melt proton-exchange waveguides were determined in a novel way using a line-focus-beam scanning acoustic microscope (SAM). Here acoustic waves were focussed on to the surface of the waveguide and the SAW velocity along a particular crystal direction was determined from the period of the reflected signal. Examination of the SAW velocity on X- Y- and Z-cut $LiNbO_3$ waveguides indicated that the acoustic velocity was, in some cases, greatly affected by the fabrication process. Along the principal axes, however, it was shown that the variation was not large and particular values of SAW velocity were calculated. A theoretical analysis of the effect of changes in the index profile on the acousto-optic overlap integral was performed. Results indicated that, as the index profile changed from step to graded, there was a corresponding reduction in the overlap integral. These calculations supported the experimental observations of a reduction in diffraction efficiency with annealing. Dilute melt proton-exchange waveguides do not, however, require prolonged post annealing and as a result retain the step-index profile and should, therefore, have an improved acousto-optic performance. The theoretical calculations have indicated that, for a given acoustic frequency, the maximum diffraction efficiency can be obtained from a shallow (~0.3μm) step-index

waveguide.

Finally, 85% acousto-optic diffraction efficiency was demonstrated on an X-cut $LiNbO_3$ dilute melt proton-exchanged waveguide using a very simple, non-optimum structure, which had a Q value of only 24.2. The waveguide had a step-index profile and required a short annealing period to relieve induced strain. In addition, acousto-optic interaction was demonstrated on a $LiTaO_3$ waveguide and it was shown that the thermo-optic behaviour of both samples was similar to that of titanium diffused waveguides.

Future Work

In comparison with the established Titanium indiffusion process, the proton-exchange method for optical waveguide fabrication is still in its infancy and its future depends upon whether suitable fabrication conditions for low loss optical waveguides can be determined. The work presented in this thesis contributes to this objective with a demonstration of the suitability of dilute melt proton-exchange for acousto-optic and integrated optical device fabrication. However, work is still required in a number of areas before complete acceptance of the proton-exchange process is achieved.

De Micheli[1], for example, has indicated that very high quality waveguides can be produced by using exchange temperatures in excess of 300°C. Therefore, if a process could be devised whereby single-mode waveguides were reproduced at these high temperatures (possibly by using large dilution ratios), future device fabrication might use this method. The present analysis has concentrated on 0.5% dilute melts. However, there are indications that the use of higher dilution ratios may provide further improvements to waveguide quality, although, in practical applications, fabrication time must be taken into consideration before the optimum melt dilution is determined. In addition, the possibilities of using alternative protonic sources to Benzoic acid are being investigated and preliminary results[2] indicate

that step-index waveguides with $\Delta n_e = +0.145$ can be produced on Z-cut $LiNbO_3$ using Phosphoric acid. This index change is somewhat greater than that possible with Benzoic acid. However, although good quality waveguides have been reported[2] additional work is required before the validity of the process can be fully assessed.

The true cause of the 'depolarisation scattering' problems which were evident in dilute melt Y-cut $LiNbO_3$ proton-exchange waveguides is still unknown and although induced strain is suspected a full materials analysis of the waveguides is required before this can be confirmed. In particular, X-ray double crystal analysis is required to measure the lattice strain and to determine whether that strain is removed during annealing.

One area which still requires some attention is the reported losses in the electro-optic coefficients of the crystal as a result of proton-exchange. Indications of the preservation of the electro-optic coefficients with dilute melts are encouraging. However, the coefficients have never been properly measured and work is required in this area if confidence in the process is to remain. Despite these doubts, the recently reported[3] highly efficient second harmonic generation by Cerenkov radiation in Z-cut $LiNbO_3$ indicates that practical devices can be made using proton-exchange.

The investigations of proton-exchange waveguides on $LiTaO_3$ are only preliminary and a concentrated effort is required in this area before the waveguides can become established. Insufficent evidence exists, at present, to determine the peak refractive index of the exchanged layer, whether the waveguides have a step-index profile similar to that of proton-exchanged $LiNbO_3$ waveguides and whether there is a $t^{1/2}$ dependence between the exchange time and the diffusion depth. A full materials analysis, similar to that performed on proton-exchanged $LiNbO_3$ waveguides may answer some of these questions. In particular, it may be possible to determine whether the $LiTaO_3$ crystal is less affected, than $LiNbO_3$, by lithium depletion during exchange and whether this is the reason for the relatively small index change.

The results of the investigation of the acoustic properties of proton-exchanged waveguides using the Scanning Acoustic Microscope can be applied not only to acousto-optic devices but also to purely acoustic wave devices. One such application is in a distributed acoustic reflector array[4] where an acoustic wave is incident upon a periodic grating which perturbs the acoustic velocity and leads to reflections. These reflector arrays have been used in radar to provide pulse compression or expansion and have have also been used in SAW resonators[5] where two arrays, placed either side of an IDT, allow constructive interference of the acoustic waves and form an acoustic Fabry-perot cavity. The most efficient arrays on $LiNbO_3$ have been formed by etching grooves into the material[5] with the reflection coefficient being controlled by the groove depth.

Schmidt[6] fabricated periodic gratings on $LiNbO_3$ using the indiffusion of Titanium and measured velocity perturbations as large as 1.4%. The advantage of using diffused regions instead of etched grooves is that they are simpler to fabricate and the smooth transition should result in a reduction in scattering loss. In addition, it would be possible to vary the reflection coefficients of the gratings by changing the diffusion parameters. These processes have not been fully evaluated and it is possible that proton-exchanged gratings, with velocity reductions as large as 5% (for an X-propagating acoustic wave on Y-cut $LiNbO_3$), could be fabricated. Such gratings could also be incorporated into certain collinear acousto-optic devices where the propagation direction of the acoustic wave, launched initially along the Z-axis of Y-cut $LiNbO_3$, could be rotated through 90^o to propagate parallel to the optical beam.

The SAM can provide valuable measurements of the acoustic properties of various crystals and waveguides. The work presented in this thesis can be developed further to investigate the properties of proton-exchanged $LiTaO_3$ waveguides and to determine whether the acoustic birefringence and the magnitude of the velocity change are dependent upon the exchange time and melt dilution. In addition, it might be possible to use the SAM to predict detailed variations in the elastic constants of the

proton-exchanged waveguides. With this detailed knowledge it would be possible to assess the accuracy of the overlap integral analysis and to predict the effects of a change in elastic and electro-optic variables on the acousto-optic interaction efficiency.

Finally, the preliminary results on the acousto-optic performance on $LiTaO_3$ should be extended to determine the full potential of the devices and to see if they can match the performance of the $LiNbO_3$ devices.